

CRANFIELD UNIVERSITY

School of Applied Sciences

PhD THESIS

Hydrogen Embrittlement Susceptibility of
Super Duplex Stainless Steels

Jalal Alsarraf

CRANFIELD UNIVERSITY

School of Applied Sciences

PhD THESIS

Academic Year 2006 - 2010

Jalal Alsarraf

Hydrogen Embrittlement Susceptibility of
Super Duplex Stainless Steels

Supervisor: Dr. M. J. Robinson

April 2010

ABSTRACT

This thesis describes the metallurgical and environmental factors that influence hydrogen embrittlement of super duplex stainless steels and presents a model to predict the rate at which embrittlement occurs. Super duplex stainless steel has an austenite and ferrite microstructure with an average fraction of each phase of approximately 50%. An investigation was carried out on the metallurgical and environmental factors that influence hydrogen embrittlement of super duplex stainless steels.

Tensile specimens of super duplex stainless steel were pre-charged with hydrogen for two weeks in 3.5% NaCl solution at 50° C at a range of applied potentials to simulate the conditions that exist when subsea oilfield components are cathodically protected in seawater. The pre-charged specimens were then tested in a slow strain rate tensile test and their susceptibility to hydrogen embrittlement was assessed by the failure time, reduction in cross-sectional area and examination of the fracture surface.

The ferrite and austenite in the duplex microstructures were identified by analysing their Cr, Ni, Mo and N contents in an electron microscope, as these elements partition in different concentrations in the two phases. It was shown that hydrogen embrittlement occurred in the ferrite phase, whereas the austenite failed in a ductile manner.

An embrittled region existed around the circumference of each fracture surface and the depth of this embrittlement depended on the hydrogen charging time and the potential at which the charging had been carried out. The depth of embrittlement was shown to correlate with the rate of hydrogen diffusion in the alloy, which was measured electrochemically using hydrogen permeation and galvanostatic methods. A two-dimensional diffusion model was used to calculate the hydrogen distribution profiles for each experimental condition and the model could be employed to provide predictions of expected failure times in stressed engineering components.

Keywords:

Ferritic-austenitic stainless steel, Hydrogen permeation, Diffusion, Hydrogen uptake, Cathodic protection, Cracking, Galvanostatic, Modelling, Austenite spacing.

ACKNOWLEDGEMENTS

It is difficult to overstate my gratitude to my Ph.D. advisor, Dr. Mike Robinson, for his advice and support throughout my research. His continuous enthusiasm, inspiration, and great efforts to explain things clearly and simply during the early parts of my graduate studies helped me understand the true values of research and set me on the right path to a smooth and easy journey to graduation. I would like to thank him for being such a great advisor, without him this work would not have been a success. I would also like to thank my committee members for their valuable input and guidance to improve this study.

I greatly appreciate and wish to thank all the technical and library staff at Cranfield University for their great assistance during this project. I would further like to thank my friends and colleagues in the department, especially members of the corrosion group, with whom it has been very enjoyable to work.

Furthermore, I must sincerely thank for the Public Authority for Applied Education and Training (PAEET, State of Kuwait) for their academic and financial support of the present thesis. Thanks to BÖHLER and Langley Alloys for partial support of the project.

Lastly, I like to thank my family for their support, love and encouragement all this time, their phone calls cheered me up whenever was needed. To my parents for all that they did and who unfortunately never got to see this work.

TABLE OF CONTENTS

ABSTRACT	i
ACKNOWLEDGEMENTS	iii
LIST OF FIGURES	ix
LIST OF TABLES	xviii
1 Introduction	1
2 Duplex Stainless steels	3
2.1 Types of Duplex Stainless Steels.....	6
2.2 Metallurgy of Duplex Stainless Steels	8
2.3 Alloy Design	8
2.3.1 Chromium	10
2.3.2 Molybdenum	11
2.3.3 Nickel.....	11
2.3.4 Copper.....	12
2.3.5 Nitrogen	14
2.3.6 Manganese	15
2.3.7 Tungsten.....	16
2.3.8 Silicon	16
2.4 Mechanical Properties of Duplex Stainless Steel	18
2.5 Applications of Duplex Stainless Steels	19
2.6 Limitations of DSS.....	20
2.6.1 Hydrogen Embrittlement Failures.....	21
2.6.1.1 BP	21
2.6.1.2 Shell	23
2.7 Segregation of Alloying Elements	24
2.7.1 Sigma Phase.....	25
3 Corrosion Behaviour of Duplex Stainless Steels	27
3.1 Types of Damage Due to Hydrogen.....	29
3.2 Hydrogen Embrittlement	29
3.2.1 Mechanisms of Hydrogen Embrittlement	30
3.2.1.1 The Internal Pressure.....	30
3.2.1.2 Surface Energy.....	30

3.2.1.3	Decohesion Theories	31
3.2.2	Methods for Hydrogen to Enter Metals	32
3.2.2.1	Pickling and Chemical metal Removal	33
3.2.2.2	Plating Operations (another cathodic Process)	33
3.2.2.3	Crevice Corrosion Conditions.....	33
3.2.2.4	Service Condition	33
3.2.3	Comparison of SCC and HE	33
3.2.4	Diffusion of Hydrogen in Duplex Stainless Steels	36
3.2.4.1	Diffusion	36
3.3	Pitting Corrosion.....	37
3.3.1	Effect of Alloying Elements on Epit	37
3.3.2	Pitting Mechanism.....	38
3.3.3	Pit Growth	39
3.3.4	Pit Initiation	41
3.3.5	Initiation Mechanism	42
3.3.5.1	Defect Theory.....	42
3.3.5.2	Chloride Ion Dissolutions.....	42
3.3.5.3	Peptisation.....	42
3.3.5.4	Local Cells.....	43
3.3.5.5	Stress Theory	43
3.3.5.6	Vacancy Theory	43
3.3.5.7	Breakdown and Repair.....	43
3.3.5.8	Inclusions	44
4	Experimental Methods.....	45
4.1	Materials	45
4.2	Specimen Preparation.....	46
4.3	Etching	47
4.4	Metallography	47
4.5	SEM	47
4.6	Hardness.....	48
4.7	Electrochemical Measurements	48
4.7.1	Polarization Behaviour	49

4.7.2	Potentiostatic Measurement.....	49
4.7.3	Electrochemical Cell	49
4.8	Scan Rate	51
4.9	Hydrogen Precharging Cell	52
4.10	Environmental Corrosion Cell	53
4.11	Slow Strain Rate Testing.....	57
4.12	Hydrogen Diffusion Measurements	59
4.12.1	Potentiostatic Hydrogen Charging	59
4.12.1.1	Steel Membranes	60
4.12.2	Galvanostatic Hydrogen Charging	61
5	Results and Discussion.....	66
5.1	Characterizing SDSS	66
5.2	Optical Metallography	66
5.3	SEM.....	74
5.4	Hardness.....	82
5.5	Polarization behaviour.....	82
5.6	Potentiostatic Test.....	89
5.7	Slow Strain Rate Testing.....	98
5.8	Analysis of SSRT Results	110
5.9	Comparison of SSRT	118
5.10	Fractography Analysis.....	123
5.11	Cracking Profile.....	124
5.12	Hydrogen Diffusion Coefficient.....	127
5.12.1	Hydrogen Permeation Measurements	127
5.12.1.1	Cold Rolled Carbon Steel Shim.....	127
5.12.1.2	Carbon Steel 1 mm	131
5.12.1.3	Super DSS Ferralium 255	132
5.12.1.4	Super DSS SAF 2507	134
5.13	Galvanostatic Method	141
5.13.1	Carbon Steel.....	141
5.13.2	Super DSS Ferralium 255.....	144
5.13.3	Super DSS SAF 2507	146

6	Modelling of Hydrogen Transport.....	153
6.1	Introduction	153
6.2	The Model	153
6.3	Consider an Example	156
6.4	Applications of the Model	158
6.4.1	Estimation of the Diffusion Coefficient	158
6.5	Depth of the Embrittlement Measured on the Fractured Surface	158
6.6	Predicted Hydrogen for each precharging potential and Profile	167
6.7	Crack Propagation Influence	171
7	General Discussion.....	179
7.1	Influence of Microstructure	179
7.2	Ranking of Alloys	180
7.3	Consideration of Pitting	183
7.4	Influence of Microstructure	188
7.5	Influence of Grain Size	190
7.6	Influence of Hydrogen Diffusion	192
8	Conclusion.....	205
9	Future Work	208
10	REFERENCES.....	209
	APPENDICES	223

LIST OF FIGURES

Figure 2.1 : Phase diagram for Fe / Cr / Ni alloys ³⁵	8
Figure 2.2: Relative strength of alloying elements as ferrite formers and austenite formers ³⁶	9
Figure 2.3: Corrosion rate profile with respect to Cr contents in intermittent water spray at room temperature ⁵⁸	10
Figure 2.4 : Nickel addition to stainless steel ⁶⁴	12
Figure 2.5: Corrosion Rate in 10% H ₂ SO ₄ + 500 ppm Cl ⁻ Aerated, at 80 ° C and 85 ° C ⁶⁷	13
Figure 2.6: Concentration profiles in the ternary Fe-Cr-Ni constitution diagram at 70% and 60%Fe. The effect of 0.25% of N addition is shown in (a) ⁶⁹	15
Figure 2.7 : stress strain curve for some stainless steel ⁸⁰	18
Figure 2.8 : Super duplex stainless steel hub forging with welded pipe connections ¹⁵	22
Figure 2.9: Cracking location ¹⁵	23
Figure 2.10: Fracture surface of in board side of parted subsea hub ¹⁶	24
Figure 2.11: Precipitation reactions which may occur in duplex grades ⁵¹	25
Figure 3.1 Basic electrochemical corrosion cell between anodic and cathodic region on the steel surface ⁵⁶	28
Figure 3.2 Schematic illustration of the adsorption model. The model requires that a specific ion from the environment, <i>B</i> , interacts and reduces the cohesive strength of the strained bond A-A ₀ at the tip of the brittle crack ⁹²	31
Figure 3.3: Schematic illustration of the decohesion model for hydrogen embrittlement ⁹³	32
Figure 3.4: Schematic differentiation of anodic stress corrosion cracking and cathodically sensitive hydrogen embrittlement ¹⁸	34
Figure 3.5: Hydrogen permeation rate, as a function of potential for carbon steel crevices in NaCl solution	35
Figure 3.6: Theoretical calculations based on alloys with 25% Cr and 4% Mo. Ni was varied to keep constant ferrite content ⁹⁹	38
Figure 3.7 A generalized picture of pit propagation in stainless steel in containing chloride ions ¹⁰²	41
Figure 4.1: Specimen mounted in epoxy resin	46
Figure 4.2: A typical set up for potentiodynamic measurements	50
Figure 4.3: Detail of the cell arrangements showing the ministat used potentiostatic test	51

Figure 4.4: Precharging cell to promote hydrogen uptake of SSRT specimens	53
Figure 4.5: Glass-Perspex environmental cell for SSRT	54
Figure 4.6: Glass-Perspex environmental cell for SSRT	55
Figure 4.7: Experimental set – up for slow strain rate testing (SSRT) in a Glass-Perspex environmental cell	56
Figure 4.8: Dimensions of slow strain rate testing specimen.....	58
Figure 4.9: Modified Devanathan and Stachurski ¹¹⁹ permeation cell.....	60
Figure 4.10: Effective area of the membrane for the hydrogen permeation cell	61
Figure 4.11 Galvanostatic Hydrogen charging cell	64
Figure 4.12: Typical potential as a function of time trend from galvanostatic charging method ¹²¹	65
Figure 5.1 Optical micrograph of the transverse section of SDSS.....	67
Figure 5.2: Optical micrograph of the longitudinal section of SDSS	67
Figure 5.3: Optical micrograph of the transverse section of SDSS SAF 2507 etched by 10M of NaOH solution	68
Figure 5.4 Optical micrograph of the longitudinal section of SDSS	68
Figure 5.5: Optical micrograph of the transverse section of SDSS.....	69
Figure 5.6: Optical micrograph of the longitudinal section of SDSS	69
Figure 5.7: Phase forming of super duplex stainless steel ¹²⁴	70
Figure 5.8: Schaeffler diagram showing composition range in which stainless steels exhibit a duplex structure	71
Figure 5.9 SEM image of the transverse section of DSS Ferralium 255 etched by 10M NaOH solution	74
Figure 5.10 SEM image of the longitudinal section of DSS Ferralium 255 etched by 10M NaOH solution	75
Figure 5.11 SEM Image for phase analysis Transverse Section of super DSS	75
Figure 5.12 SEM Image for phase analysis Longitudinal Section of super DSS Ferralium 255 etched by 10M NaOH solution	76
Figure 5.13: Analysis by SEM for the austenite and ferrite phase of the transverse and longitudinal sections for Ferralium 255 showing the range of composition for each phase	76
Figure 5.14 SEM image of the transverse section of DSS SAF 2507 etched by 10M NaOH solution.....	77
Figure 5.15 SEM image of the longitudinal section of DSS SAF2507 etched by 10M NaOH solution.....	77
Figure 5.16: Analysis by SEM for the austenite and ferrite phase of the transverse and longitudinal sections for SAF 2507 showing the range of composition for each phase	78

Figure 5.17 SEM image of the transverse section of super DSS.....	79
Figure 5.18 SEM image of the longitudinal section of super DSS	79
Figure 5.19: Analysis by SEM for the austenite and ferrite phase of the transverse and longitudinal sections for super DSS Zeron 100 showing the range of composition for each phase	80
Figure 5.20: Illustrated polarisation behaviour on the cathodic reaction for stainless steels.....	84
Figure 5.21: Potentiodynamic scan test for Ferralium 255 with a scan	85
Figure 5.22 Comparison of the 5 potentiodynamic scan tests for super DSS Ferralium 255 with a scan rate of 10 mV/min.....	85
Figure 5.23 Values of the pitting potentials of the austenite and ferrite phase for super DSS Ferralium 255 with a scan rate of 10 mV/min.....	86
Figure 5.24 Potentiodynamic scan test for super DSS SAF 2507 with a scan rate of 10 mV/min.....	86
Figure 5.25: Potentiodynamic scan test for super DSS Zeron 100 with a scan rate of 10 mV/min.....	87
Figure 5.26: Mean values from five measurements of the pitting potentials of the austenite and ferrite phase for super DSS alloys	88
Figure 5.27: SEM image for potentiostatic test of super DSS Ferralium 255 specimen at 800 mV (SCE) for weeks	90
Figure 5.28: SEM image for potentiostatic test of super DSS Ferralium 255 specimen at 800 mV (SCE) for 2 weeks (Austenite and Ferrite Phase)....	91
Figure 5.29: Optical images for potentiostatic test – pit initiation for super DSS Ferralium 255 specimen at 800 mV (SCE) for 2 weeks.	92
Figure 5.30: SEM image for potentiostatic test of super DSS Ferralium 255 specimen at 850 mV (SCE) for 2 weeks (Austenite and Ferrite Phase)....	93
Figure 5.31: SEM image for potentiostatic test of super DSS Ferralium 255 specimen at 850 mV (SCE) for 2 weeks (Austenite and Ferrite Phase)....	94
Figure 5.32: Electron beam penetration into the subsurface of ferrite grain ..	95
Figure 5.33: SEM image for potentiostatic test Super DSS Ferralium 255 specimen at 950 mV (SCE) for 2 weeks (Austenite and Ferrite Phase)....	96
Figure 5.34: SEM image for potentiostatic test of super DSS Ferralium 255 specimen at 950 mV (SCE) for 2 weeks (Austenite and Ferrite Phase)....	97
Figure 5.35: Stress / Strain curve for Ferralium 255 in air test condition showing the mechanical properties.	100
Figure 5.36: SSR Testing stress vs. strain for Ferralium 255	100
Figure 5.37: SSR Testing stress vs. time for Ferralium 255	101
Figure 5.38: SSR Testing - Ferralium 255 Effect of Baking.....	102

Figure 5.39: Macrographs at of the fracture surface of super DSS Ferralium 255 specimen showing the necking and microvoid coalescence resulting from the air test	102
Figure 5.40: The macrograph showing brittle nature of the fractured surface of super DSS Ferralium 255 specimen – 3.5% NaCl at 50 °C, -1000 mV (SCE) for 2 weeks Test	103
Figure 5.41: Composition analysis by SEM for the austenite and ferrite phase of the fracture surface specimen for Ferralium 255.....	104
Figure 5.42: The macrograph showing brittle nature of the fractured surface of super DSS Ferralium 255 specimen – 3.5% NaCl at 50 °C -1250mV (SCE) for 2 weeks Test.....	104
Figure 5.43: The macrograph showing brittle nature of the fractured surface of super DSS Ferralium 255 specimen – 3.5% NaCl at 50 °C -1250mV (SCE) for 4 weeks Test.....	105
Figure 5.44: The macrograph showing ductile nature of the fractured surface of super DSS Ferralium 255 specimen precharged at -1250mV (SCE) in – 3.5% NaCl at 50 °C, for 4 weeks Baked for 3 day at 200 °C after SSRT	105
Figure 5.45: The macrograph showing ductile nature of the fractured surface of super DSS Ferralium 255 specimen precharged in 3.5% NaCl at -1250mV (SCE) at 50 °C for 4 weeks – Baked for one day at 200 °C after SSRT.	106
Figure 5.46: SSR Testing Stress vs. Strain for SAF 2507	106
Figure 5.47: SSR Testing Stress vs. time for SAF 2507.....	107
Figure 5.48: Measuring the facture surface area of SDSS SAF 2507 after SSR testing in 3.5% NaCl without charging at 50° C temperature.....	108
Figure 5.49: Measuring the fracture surface area of SDSS SAF2507 after SSR testing in 3.5% NaCl without charging at 50° C temperature.....	108
Figure 5.50 SSR Testing Stress vs. Strain for Zeron 100.....	109
Figure 5.51: SSR Testing Stress vs. time for Zeron 100	109
Figure 5.52: Time to failure (TTF) of all SSR testing for SDSS Ferralium 255	111
Figure 5.53: Embrittlement index after SSR testing for SDSS Ferralium 255, calculated from time to failure (TTF)	112
Figure 5.54: Embrittlement index after SSR testing for SDSS Ferralium 255, calculated from the percentage of reduction of area (%RA).....	112
Figure 5.55: Percentage of the elongation (% Elong) of all SSR testing for SDSS Ferralium 255	113
Figure 5.56: Embrittlement index Vs. cathodic potentials after SSR testing for SDSS Ferralium 255	113
Figure 5.57: Time to failure (TTF) of all SSR testing for SDSS SAF 2507	114

Figure 5.58: Embrittlement index after SSR testing for SDSS SAF 2507, calculated from the time for failure (TTF)	114
Figure 5.59: Embrittlement index after SSR testing for SDSS SAF 2507 calculated from the percentage of reduction of area (%RA).....	115
Figure 5.60: Percentage of the elongation (% Elong) of all SSR testing for SDSS SAF 2507	115
Figure 5.61: Time to failure (TTF) of all SSR testing for SDSS Zeron 100	116
Figure 5.62: Embrittlement index after SSR testing for SDSS Zeron 100, calculated from the time for failure (TTF)	116
Figure 5.63: Embrittlement index after SSR testing for SDSS Zeron 100 calculated from the percentage of reduction of area (%RA).....	117
Figure 5.64: Percentage of the elongation (% Elong) of all SSR testing for SDSS Zeron 100	117
Figure 5.65: Comparison of Time to failure (TTF) for all three super DSSs after SSR testing	119
Figure 5.66: Comparison of embrittlement indices of all three super DSSs after SSR testing, calculated from time for failure (TTF)	120
Figure 5.67: Comparison of embrittlement indices of all three super DSSs after SSR testing calculated from the percentage of reduction of area (%RA)	120
Figure 5.68: Comparison of percentage of elongation (% Elong) of all three super DSSs after SSR testing	121
Figure 5.69: Comparison of Percentage of reduction in area (%RA) of all three super DSSs after SSR testing	121
Figure 5.70: Comparison of 0.2% proof stress of all three super DSSs after SSR testing	122
Figure 5.71: Comparison of ultimate tensile strength (UTS) of all three super DSSs after SSR testing	122
Figure 5.72: Optical micrograph of crack profile on failed cross section of super DSS SAF 2507 precharged at -1250 mV for 2 weeks	125
Figure 5.73: Optical micrograph of crack profile on failed cross section of super DSS Ferralium 255 precharged at -1250 mV for 2 weeks	125
Figure 5.74: Optical micrograph of sectioned fracture surface of SDSS specimen of Ferralium 255 precharged at -1250 mV (SCE) for 4 weeks in 3.5% NaCl at 50° C, the crack occurred in the ferrite phase and was blocked by the austenite phase.....	126
Figure 5.75: Optical micrograph of internal microcrack on failed cross section of super DSS SAF 2507 precharged at -1250 mV for 2 weeks	126
Figure 5.76: Optical micrograph of internal microcrack on failed cross section of super DSS SAF 2507 precharged at -1250 mV for 2 weeks	127

Figure 5.77: Hydrogen Depletion Transient for cold-rolled Low Carbon Steel Shim in 0.2 M NaOH Solution with different charging potentials vs. (SCE)	128
Figure 5.78: Hydrogen Permeation Transient for cold-rolled Low Carbon Steel Shim in 0.2 M NaOH Solution with different charging potentials vs. (SCE)	129
Figure 5.79: graphical illustration of the permeation curve at a potential of -1250 mV (SCE).....	129
Figure 5.80: Permeation transient for 1 mm thick of low carbon steel membrane cathodically charged at -1200 mV (SCE)	131
Figure 5.81: Hydrogen Permeation Transient for SDSS Ferralium 255 in 0.2 M NaOH Solution at 50° C with charging potential of -1200 mV vs. (SCE) .	133
Figure 5.82: Cross section of 1 mm thick membrane used in the permeation test for super DSS Ferralium 255 showing the direction of the austenite grains	134
Figure 5.83: Hydrogen Permeation Transient for SDSS SAF 2507 in 0.2 M NaOH Solution at 50° C with charging potential of -1200 mV vs. (SCE) .	135
Figure 5.84: Cross section of 1 mm thick membrane used in the permeation test for super DSS SAF 2507 showing the direction of the colonies of the austenite grains.....	136
Figure 5.85: Galvanostatic hydrogen charging method for low carbon steel membrane in 0.2M NaOH solution	142
Figure 5.86: Linear plot of potential (E) as a function of $t^{1/2}$ at the short time period ($t \ll L^2/D$) for low carbon steel specimen in 0.2M NaOH solution.	142
Figure 5.87: Linear plot of potential (E) as a function of time at the long time period ($t > L^2/D$) for low carbon steel specimen in 0.2M NaOH solution...	143
Figure 5.88: Galvanostatic hydrogen charging plot for super DSS Ferralium 255 specimen.....	144
Figure 5.89: Linear plot of potential (E) as a function of $t^{1/2}$ at the short time period for super DSS Ferralium 255 specimen in 0.2M NaOH solution ..	145
Figure 5.90: Linear plot of potential (E) as a function of time at the long time period for super DSS Ferralium 255 specimen in 0.2M NaOH solution ..	145
Figure 5.91: Cross section of 100 μ m thick membrane used in the galvanostatic test for super DSS Ferralium 255 showing the orientation of the colonies of the austenite grains.....	146
Figure 5.92: Galvanostatic hydrogen charging plot for super DSS SAF 2507 specimen.....	147
Figure 5.93: Linear plot of potential (E) as a function of $t^{1/2}$ at the short time period for super DSS SAF 2507 specimen in 0.2M NaOH solution.....	147
Figure 5.94: Linear plot of potential (E) as a function of time at the long time period for super DSS SAF 2507 specimen in 0.2M NaOH solution.....	148

Figure 5.95: Cross section of 100 µm thick membrane used in the galvanostatic test for super DSS SAF 2507 showing the direction of the colonies of the austenite grains.....	149
Figure 6.1: Different profiles of hydrogen concentration for cylinders obtained with different values of Dt/a^2	156
Figure 6.2: Profile of hydrogen concentration modelling in a 3 mm diameter gauge length for the tensile specimen of super DDS Ferralium 255 with different charging times using a measured D value of $1.38 \times 10^{-10} \text{ cm}^2/\text{sec}$	157
Figure 6.3: Fracture surface of super DSS Zeron 100 showing the depth of the embrittled region where the hydrogen travelled toward the centre precharged at a potential of -1250 mV (SCE) for 2 weeks at 50 °C	160
Figure 6.4: Fracture surface of super DSS Ferralium 255 showing the depth of the embrittled region where the hydrogen travel toward the centre and the boundary of ductile & brittle regions of SSR testing in 3.5% NaCl at 50 °C precharged at -1250mV (SCE) for 2 weeks.....	161
Figure 6.5 Fracture surface of super DSS Ferralium 255 Showing the boundary of ductile & brittle regions of SSR testing in 3.5% NaCl at 50 °C percharged at -1250mV (SCE) for 2 weeks (embrittled region is where the hydrogen travel toward the centre).....	161
Figure 6.6: Fracture surface of super DSS Ferralium 255 showing ductile region in centre of the specimen precharged at -1250mV (SCE) for 2 weeks in 3.5% NaCl at 50 °C	162
Figure 6.7 Fracture surface of super DSS Ferralium 255 after SSR test showing brittle region on the circumference of the specimen precharged at -1250mV (SCE) for 2 weeks in 3.5% NaCl at 50 °C	162
Figure 6.8 Profile of hydrogen concentration modelling in a 3 mm diameter gauge length for the tensile specimen of super DSS Ferralium 255 with different diffusion coefficient values for a period of 2 weeks (The area in the box shows the hydrogen distributions at higher magnification, for ease of comparison)	163
Figure 6.9 Profile of hydrogen concentration modelling in a 3 mm diameter gauge length for the tensile specimen of super DSS SAF 2507 with different diffusion coefficient values for a period of 2 weeks	164
Figure 6.10 Profile of hydrogen concentration modelling in a 3 mm diameter gauge length for the tensile specimen of super DSS Zeron 100 with different diffusion coefficient values for a period of 2 weeks	165
Figure 6.11: Illustration of measuring the threshold hydrogen concentration (C_{th}) for crack propagation	166
Figure 6.12: Profile of hydrogen concentration modelling in a 3 mm gauge length for the tensile specimen of super DSS Ferralium 255 at a range of applied cathodic potentials for a period of 2 weeks.....	169

Figure 6.13: Profile of hydrogen concentration modelling in a 3 mm gauge length for the tensile specimen of super DSS SAF 2507 at a range of applied cathodic potentials for a period of 2 weeks	170
Figure 6.14: Profile of hydrogen concentration modelling in a 3 mm gauge length for the tensile specimen of super DDS Zeron 100 at a range of applied cathodic potentials for a period of 2 weeks	171
Figure 6.15: Profile of hydrogen concentration modelling in a 3 mm gauge length for the tensile specimen of super DDS SAF 2507 at a range of applied cathodic potentials for a period of 2 weeks	173
Figure 6.16: Profile of hydrogen concentration modelling in a 3 mm gauge length for the tensile specimen of super DSS Ferralium 255 at a range of applied cathodic potentials for a period of 2 weeks	174
Figure 6.17: Profile of hydrogen concentration modelling in a 3 mm gauge length for the tensile specimen of super DDS Zeron 100 at a range of applied cathodic potentials for a period of 2 weeks	175
Figure 7.1: Comparison of Embrittlement Index (%RA) Vs. cathodic potentials from -1250 to -800 mV SCE after SSR testing for all three super DSSs .	181
Figure 7.2: Schematic summary of the effect of alloying elements in stainless steels on the anodic polarization curve ¹³⁹	185
Figure 7.3: PREN of the ferrite and austenite phases for the three alloys based on extended PRE number calculations	188
Figure 7.4: Effect of the alloy composition expressed as a ratio of Ni_{eq}/Cr_{eq} on the ferrite PREN number for the three alloys.....	190
Figure 7.5: Effect of the alloy composition expressed as a ratio of Ni_{eq}/Cr_{eq} on mean grain size of the ferrite phase for the three alloys.....	192
Figure 7.6 : Variation of the effective diffusion coefficient with volume fraction of Uranus B50 duplex stainless steel	193
Figure 7.7: Illustrated graph showing the ferrite length path and width for the hydrogen atoms diffusion through a permeation membrane	195
Figure 7.8: Effect of the ferrite PREN number on the hydrogen diffusion coefficient for the three alloys.....	197
Figure 7.9: Comparison of hydrogen diffusion coefficient and the mean embrittlement index (%RA) for the three alloys	198
Figure 7.10: Comparison of SSRT of the three tested super DSSs in air test condition.....	200
Figure 7.11: Effect of the grain size on the 0.2% Proof Stress	200
Figure 7.12: Comparison of the mean embrittlement index (TTF) for the three alloys at potentials of -900, -1000 and -1100 mV (SCE)	201
Figure 7.13: Comparison of Embrittlement Index (%RA) Vs. cathodic potentials from -1250 to -800 mV SCE after SSR testing for all three super DSSs .	202

Figure 7.14: The relation between the diffusion coefficient values and Ni_{eq}/Cr_{eq} ratio.	203
Figure 7.15: The relation between the austenite/ferrite ratio and Ni_{eq}/Cr_{eq} ratio.	203
Figure 10.1: Cross section of the 3mm gauge length of the super DSS Ferralium 255	223
Figure 10.2: Cross section of the 3mm gauge length of the super DSS SAF 2507	223
Figure 10.3: Cross section of the 3mm gauge length of the super DSS Zeron 100	224
Figure 10.4: Profile of hydrogen concentration modelling in a 3 mm gauge length for the tensile specimen of super DDS Ferralium 255 at a range of applied cathodic potentials for a period of 2 weeks showing D value.....	224
Figure 10.5: Profile of hydrogen concentration modelling in a 3 mm gauge length for the tensile specimen of super DDS SAF 2507 at a range of applied cathodic potentials for a period of 2 weeks Showing D value	225
Figure 10.6: Profile of hydrogen concentration modelling in a 3 mm gauge length for the tensile specimen of super DDS Zeron 100 at a range of applied cathodic potentials for a period of 2 weeks Showing D value	225
Figure 10.7: Measured crack length of the fracture surface after SSRT for tested materials.....	226

LIST OF TABLES

Table 2.1: Typical PREN for some stainless steels	6
Table 2.2: Chemical composition for the tested materials figure 3.4	13
Table 2.3: Influence of different alloying additions and microstructure on the pitting and crevice Resistance of Duplex Stainless Steels ⁷⁹	17
Table 4.1: Chemical composition of test materials super DSS (Ferralium 255, SAF 2507 and Zeron 100) investigated (after manufacturer's test certificate).....	45
Table 4.2: The mechanical properties of test materials super DSS (Ferralium 255, SAF 2507 and Zeron 100) investigated (after manufacturer's test certificate).....	46
Table 4.3: Average Diameters of the gauge length sections for a random specimen.....	57
Table 5.1: Phase ratio (Ferrite and Austenite) of super DSSs.....	72
Table 5.2: The area and length of the colonies of austenite grains of all three super DSS alloys.....	73
Table 5.3: Measured Vickers hardness for super DSSs.....	82
Table 5.4: Comparison of hydrogen diffusion coefficient using the permeation technique.....	137
Table 5.5: Summary of the effect of the austenite grain size on the hydrogen diffusion coefficient.....	140
Table 5.6: Comparison of hydrogen diffusion coefficient using the galvanostatic charging technique	149
Table 5.7: Hydrogen diffusion coefficient values (D) obtained from the hydrogen permeation and galvanostatic techniques	151
Table 5.8: Summary of the effect of the size of ferrite and austenite grain colonies thickness on the hydrogen diffusion coefficient measured by permeation method	152
Table 6.1: Values of maximum crack depth measured by SEM at a range of applied potentials in 3.5 % NaCl at 50 °C for 2 weeks.	159
Table 6.2: Estimated minimum diffusion coefficient D values from the hydrogen concentration graph for the three SDSSs materials	160
Table 6.3 Comparison of the hydrogen diffusion coefficients for the three super DSS materials measured by the permeation method and modeling	165
Table 6.4: Estimated mean minimum diffusion coefficients (D) from each potential corresponded to the crack depth from the hydrogen concentration graph for the three super DSSs materials	176

Table 6.5: Values for the hydrogen concentration obtained from the hydrogen profiles.....	177
Table 7.1: Degree of Embrittlement susceptibilities based on the reduction of area after SSR testing for the tested alloys	182
Table 7.2: Chemical composition and PRE of super DSSs	186
Table 7.3: Summary of volume fraction and grain size for both ferrite and austenite grains in the longitudinal section for the three alloys	189
Table 7.4: Heat treatment for the three tested super DSS	191
Table 7.5: Diffusion coefficient of hydrogen in different structure of stainless steel	194
Table 7.6: Summary of the length and width of the ferrite phase in the longitudinal section for the three alloys	196

1 Introduction

Super duplex (ferritic-austenitic) stainless steels have seen widespread application in the offshore oil, gas, paper and pulp, power and petrochemical industries¹⁻⁴ due to their attractive combination of high strength and excellent resistance to stress corrosion cracking and better weldability⁵⁻¹³. This excellent combination of mechanical properties and corrosion resistance of duplex stainless steel is the result of the presence of ferrite and austenite phases in the microstructure¹⁴. Presently, it is estimated that duplex stainless steels represent about 10 % of the world Fe:Cr:Ni stainless steels in the market and could grow up in the future. It has been recognized as a viable alternative to many other types of stainless steel and nickel based alloys in many of these technological applications. However, if this alloy is exposed to environments that can act as sources of hydrogen, severe problems may arise based on its susceptibility to hydrogen embrittlement. Recently, failures were reported on one of BP's North Sea platforms and a Shell sub-sea structure^{15, 16}. The main reason for these failures has been attributed to an unfortunate combination of load/stress and hydrogen embrittlement (HE) caused by ingress of hydrogen formed at the steel surface due to the cathodic protection technique which protects subsea structures from corrosion. This is sometimes called Hydrogen Induced Stress Cracking (HISC).

Super duplex stainless steels have no need for cathodic protection in subsea structures. But in sea water other less noble materials are frequently galvanically coupled with super duplex stainless steel and therefore cathodic protection is needed. The influence of cathodic protection can lead to evolution of hydrogen, which, if absorbed, may lead to embrittlement of metallic components with the resultant danger of failure. Failure of the component occurs when the residual ductile core is reduced in area by an encroaching hydrogen embrittlement front to a cross-section which cannot carry the load placed upon it. The threat of damage caused by hydrogen embrittlement of metals, has become a problem to the gas and oil industry where high concentrations of hydrogen are present.

In this study, an attempt was made to understand the factors that affect the susceptibility of super duplex stainless steel to hydrogen embrittlement in seawater. The aim was to investigate the influence of alloy composition on the hydrogen embrittlement susceptibility behaviour of super duplex stainless steels by comparing the behaviour of SDSS Ferralium 255 with that of other super duplex grades.

2 Duplex Stainless steels

Stainless steel was first developed around 1913, by researchers in Britain and Germany. This first true stainless steel was martensitic with 0.24% carbon and 12.8% chromium. Within a year, the first austenitic grades were developed in Germany by making a nickel addition. Almost simultaneously, ferritic stainless steel was discovered in the United States while investigating the content of low carbon. From these inventions, the martensitic, ferritic and austenitic stainless steel groups were developed just before World War I. The first duplex stainless steels were produced in Europe during 1930's for applications in the paper industry. These early alloys were found to have a poor balance of austenite and ferrite, thus producing poor mechanical properties and corrosion resistance. It is only recently that in the second generation of these alloys the austenite and ferrite balance was more stringently controlled, which led to increased performance due to the use of argon-oxygen decarburisation (AOD) refining technology combined with improved casting processes. During the 1970's, the control of alloy chemistry and the removal of oxygen and sulfur were significantly improved. Now, duplex stainless steels, which are considered to be industrial steels and no longer exotic alloys, have found widespread applications in the pulp and paper industry, chemical industry, transport/chemical tanks and pollution control equipment manufacture, marine offshore-gas and petroleum industry and a number of naval applications.

Duplex stainless steels (DSS) are defined as a set of iron-based alloys which contain nearly equal amounts of the ferrite (α -Fe) and austenite (γ -Fe) phases as a matrix (but not less than 30% each). DSS solidifies as ferrite, part of which transforms to austenite during subsequent cooling, yielding the prescribed mix of the two phases at room temperature. Generally, the austenite/ferrite ratio depends on the chemical composition of the alloy and the heat treatment. However, most alloys are designed to contain similar amounts of each phase at room temperature.

The austenite/ferrite matrix is attainable by combining various phase stabilizing elements. Chromium and Molybdenum are effective ferrite stabilizers, producing a wide ferrite field in phase diagrams. In general, stainless steels having ferrite as the predominant phase have excellent corrosion resistance due to the high solubility of Cr in ferrite. Chromium is one of the important elements in stainless steel because a passive layer (Cr_2O_3) can be formed on the metal surface.

In the 1980's, higher alloyed DSS grades came in favour, and developed into super DSS²⁰. They are made to withstand more aggressive environments, but also bearing higher risk of precipitation unfavourable phases due to the higher alloying element content. In the making of super DSS, Cr and Ni forming elements are balanced and more nitrogen is added. Super DSSs are usually characterized by having a Pitting Resistance Equivalent Number (PREN) greater than 40. The PREN has become as a part of the purchase specifications. The higher is the PREN, the better the predicted corrosion properties of a DSS. This is an increasingly common specification for certain offshore duties²¹. However, PREN numbers only provide an approximate grading of alloys and do not account for the microstructure of the material. An acceptance corrosion test on material in the supply condition is much more meaningful. The most common way of ranking stainless steels for their Pitting Resistance Equivalence Number (PREN) according to the relation between the amount of the essential elements and the corrosion properties can be formulated by using this relation²².

$$\text{PREN} = (\% \text{Cr}) + (3.3 \times \% \text{Mo}) + (16 \times \% \text{N})$$

However, some researchers have used numbers in between 10 and 30 in the last term of the formula in recognition of the extremely beneficial effects nitrogen²³. Nevertheless, the negative effects of undesirable constituents, such as inclusions, are generally not included in the PREN values published and therefore consideration of their influence should be taken when using these values²⁴.

However, for duplex stainless steel, it is necessary to consider the pitting resistance of ferrite and austenite individually due to the partitioning of the alloying elements between the phases, especially if the heat treatment is not optimized. Many researchers^{5,26-30} have pointed out that PREN calculated from the bulk alloy composition may be misleading in duplex alloys because they contain austenite and ferrite, which have different compositions. Austenite is enriched with N whereas ferrite is richer in Cr and Mo. In general, it has been found that austenite has a higher PREN than ferrite.

On the other hand, Okamoto³¹ showed theoretical calculation results that, by adjusting the ferrite/austenite balance via adjusting Ni and the heat treatment temperature, it is possible to achieve an equal PREN for both ferrite and austenite. With the introduction of tungsten as an active alloying element, the following expression has been proposed:

$$PRE_W = (\%Cr) + (3.3 \%Mo) + (0.5 \%W) + (16 \%N)$$

Therefore, higher PREN numbers mean higher resistance to pitting corrosion. Typical values of PREN for some stainless steel grades are shown in the following table:

Structure	Alloy	UNS Number	Selected Elements wt%				PREN*
			Cr	Ni	Mo	N	
Austenitic	AISI 304	S304	18	8	0	0	18
	AISI316L	S31603	17	12	2.6	0	25.6
	254 SMO	S21254	20	18	6.1	0.2	43.3
	AI 6XN	N08367	21	25	6.4	0.2	45.3
	1925hMo	N0925	20	25	6.4	0.2	44.3
Duplex	AL2003	S32003	22	3.7	1.7	0.16	30.2
	SAF 2205	S31803	22	5	3.2	0.12	34.5
	SAF 2507	S32750	25	7	4	0.25	42.2
	Ferralium 255	S32550	25	5	3.5	0.25	40
	Zeron 100	S32760	24	7.3	3.5	0.25	40.3
	SAF2707HD	S32707	27	6.5	5	0.4	49.9
	SAF 3207 HD	S33207	32	7	3.5	0.5	50
Ferritic	Sea Cure	S44660	27.5	1.2	3.5	0.02	39.4
	Monit	S44635	25.5	4	4	0.02	39

*Pitting Resistance Equivalent Number (PREN) = %Cr + 3.3 %Mo + 16 %N

Table 2.1: Typical PREN for some stainless steels

2.1 Types of Duplex Stainless Steels

Similar to the austenitic stainless steels, the development of duplex stainless steels has placed them into a family of grades, which range in corrosion performance depending on their alloy content. Duplex stainless steels are usually designed with four digits: the first two digits represent the weight percent of chromium, and the second two digits represent the weight percent of nickel. Therefore, 2507 supposedly has 25% Cr and 7% Ni by weight. However, a number of duplex stainless steels have registered trademarks associated with them such as Zeron 100, Uranus 50 and Ferralium 255. The more common alloys and their trade names are summarized in table 3.1. Nilsson³² has divided the modern Duplex Stainless Steel into four Different types:

Low Alloyed: This type, also called lean alloys DSS, has a low cost and Molybdenum free with a chemical composition of 23Cr – 4Ni – 0.1N. This Type of DSS was designed to replace and improve the resistance to stress corrosion cracking of AISI 304 and 316 which is often used for construction purposes. The PREN for this type is equal to 25.

Medium Alloyed: This second type of DSS, which also can be called standard 22% Cr alloys, has a chemical composition of 22Cr – 5Ni – 3Mo – 0.17N with corrosion resistance lying between AISI 316 and 6 wt% Mo + N super-austenitic stainless steel grades. In addition, they are the most popular and less expensive alloys in the duplex stainless steel family. They have a PREN ranging from 30 to 35.

High Alloyed: The chemical composition of this type of DSS is 25Cr with different weight percentage content of Molybdenum, Nitrogen, and addition of Copper and Tungsten as alloy elements. The value of PREN for this type of DSS is in the range of 35 to 39.

Super DSS: The chemical composition of this type is 25Cr – 7Ni – 3.7Mo – 0.27N with a PREN value greater than 40. It has almost the same Chromium content of High Alloyed DSS with increased Mo and N. Sometimes the third and fourth types of DSS are merged as one group.

A new hyper-duplex stainless steel, designed and developed to increase operating performance and extend service life in severely corrosive applications, such as heat exchangers, has been launched recently by Sandvik. These new alloys go beyond the first and second generations of these duplex stainless steel materials. Super duplex grade such as SAF 3207 HD which has a minimum PREN of 50, is a new hyper duplex stainless steel containing 32% (wt) of chromium and 7% (wt) of Nickel. Results from corrosion and mechanical testing show that SAF 3207 has better corrosion resistance and higher strength than super duplex stainless steel. The increase in strength is about 20% compared to SAF 2507^{33, 34}.

2.2 Metallurgy of Duplex Stainless Steels

2.3 Alloy Design

Secondary phases indicate precipitation of secondary particles involving chromium, molybdenum, nickel, tungsten, copper, nitrogen and other alloying elements. Therefore, it is essential to understand the importance that each element plays. Preventing secondary phases from forming is not the only worry when duplex is subjected to solution heat treatment or welding. A suitable ferrite and austenite level is also needed to get better corrosion resistance and mechanical properties. The following discussion is a brief review of the effect of the most important alloying elements on the mechanical, physical and corrosion properties of duplex stainless steels. The two phase microstructure of duplex stainless steel (ferrite and austenite) is formed during a very slow cooling. At temperature above 1200 °C, only ferrite phase is present and upon cooling the ferrite will start to transform into austenite till it reached the desired ferrite and austenite ratio. The ratio of the austenite/ferrite depends on the cooling rate and weight percentage of the alloying elements such as chromium and nickel (figure 2.1).

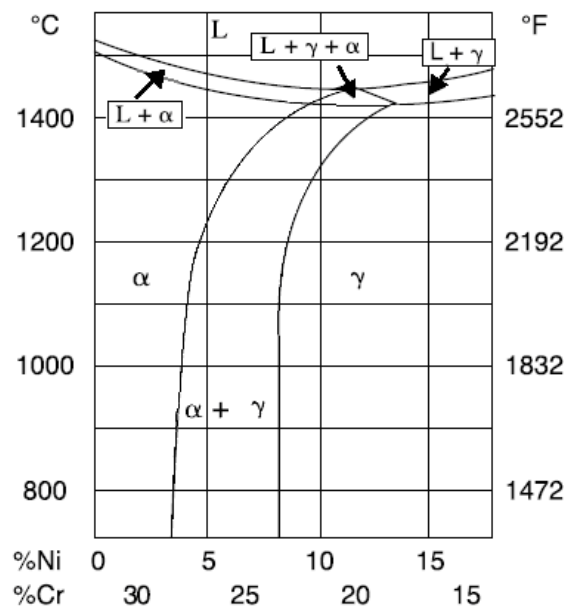


Figure 2.1 : Phase diagram for Fe / Cr / Ni alloys ³⁵

The addition of alloying elements affects the stability of the phases. Additions such as Cr, Si, and Mo are called ferrite stabilizers since they promote ferrite phase formation over wider composition and temperature ranges. In contrast, elements such as Ni, Mn and N promote austenite formation and are called austenite stabilizers. Figure 2.2 shows a basic diagram in term of ΔH (enthalpy change), which is equal to the heat absorbed per unit of solute dissolving in the austenite γ phase minus the heat absorbed per unit of solute in the ferrite α phase, i.e. $\Delta H = H_{\gamma} - H_{\alpha}$. ΔH is positive for ferrite stabilisers since H_{γ} is greater than H_{α} . For the austenite stabilisers, if H_{γ} is smaller than H_{α} , then ΔH becomes negative and the austenite region is expanded.

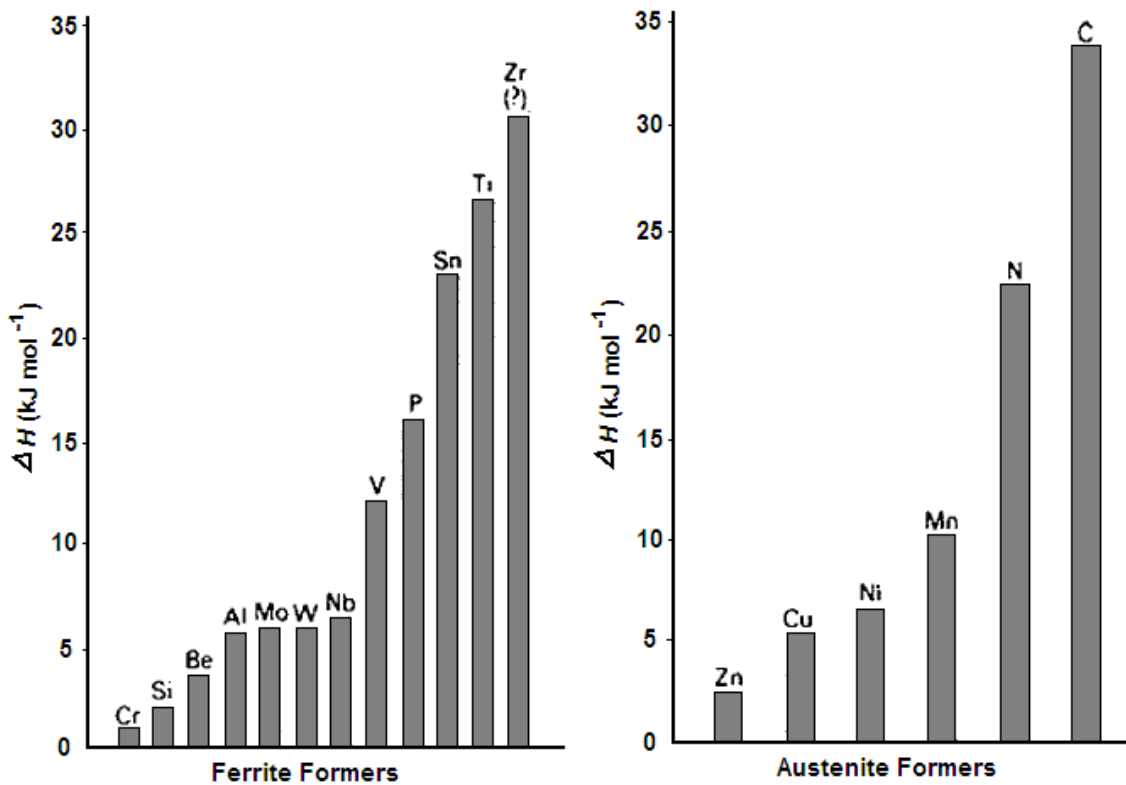


Figure 2.2: Relative strength of alloying elements as ferrite formers and austenite formers³⁶

2.3.1 Chromium

Chromium (Cr) is a strong ferrite former and stabiliser; it is the essential element for the excellent corrosion resistance improvement of stainless steels due to formation of a protective passive chromium rich oxy-hydroxide film ³⁷. This is achieved by electrochemically extending the passive range ³⁸ and reducing the rate of general corrosion. However, there is a limit to the level of Cr that can be added, as the beneficial effect of ever higher levels is negated by the enhanced precipitation of intermetallic phases, such as σ -phase, which will reduce the toughness and corrosion resistance. A minimum of about 12% Cr is necessary to establish the passivity for the stainless steel by the formation of the protective passive oxide film ³⁹. Figure 2.3 shows the important role of chromium in making the iron surface passive by forming a Cr-rich surface oxide film that protects the underlying metal from corrosion. The passive film becomes more stable with increasing chromium content of the alloy. In addition, the corrosion rate for more than 12% chromium addition appeared to be minimal in intermittent water spray at room temperature.

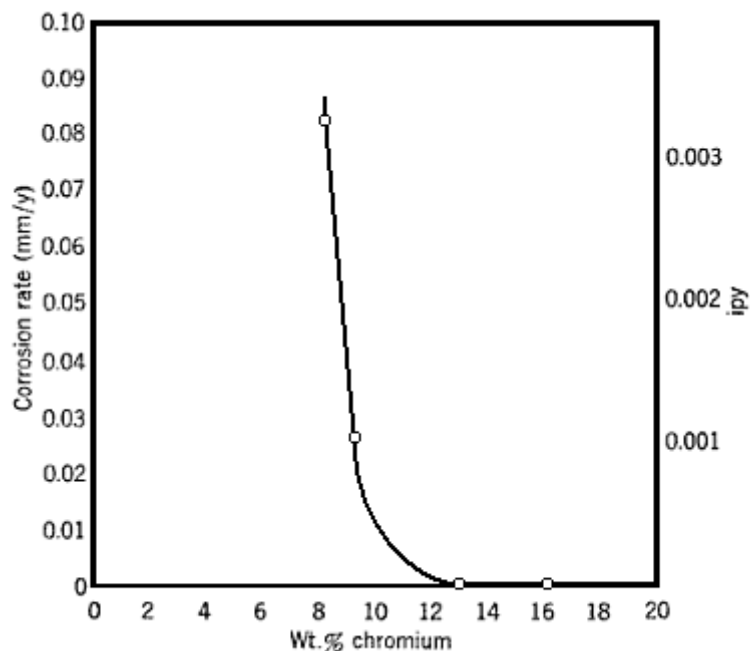


Figure 2.3: Corrosion rate profile with respect to Cr contents in intermittent water spray at room temperature ⁵⁸

2.3.2 Molybdenum

Molybdenum (Mo) has a similar effect on ferrite stability as Cr and increases the resistance against the local corrosion such as crevice, pitting and SCC corrosion. It extends the passive potential range and reduces the corrosion current density (I_{max}) in the active range⁵⁹. The mechanism by which Mo increases the pitting resistance has been found to be the suppression of active sites via formation of an oxy-hydroxide or molybdate ion⁶⁰. An addition of at least 3% is recommended while 4% is thought to be an upper limit to prevent crevice corrosion in high temperature sea water.

2.3.3 Nickel

Nickel (Ni) is a strong austenite former and is added to maintain the ferrite/austenite balance in DSS. Excessive Ni can enhance the precipitation of σ -phase (see section 2.7.1) by promoting greater concentrations of ferrite stabilizers such as Cr and Mo in the ferrite matrix. Higher Ni can also lead to highly alloyed ferrite which is more susceptible to the precipitation of intermetallic phases at the temperature range of 650-950°C. High Ni promotes the formation of alpha prime an embrittling intermetallic phase⁶¹. Low Ni levels can result in the formation of a high level of ferrite in the microstructure, thereby lowering toughness and corrosion resistance. Ni also supports the development of a strong passive chromium oxide film. It has a significant effect on the corrosion resistance and impact toughness as well as on the formation of secondary particles^{38, 62, 63}. Nickel addition as an austenite stabilizer, promotes a change of the crystal structure of stainless steel from body centred cubic (ferrite) to face centred cubic (austenite) as shown in figure 2.4. Austenite has the highest nickel content and the ferrite has the lowest. Usually, duplex stainless steels contain an intermediate amount of nickel between 4 to 7%.

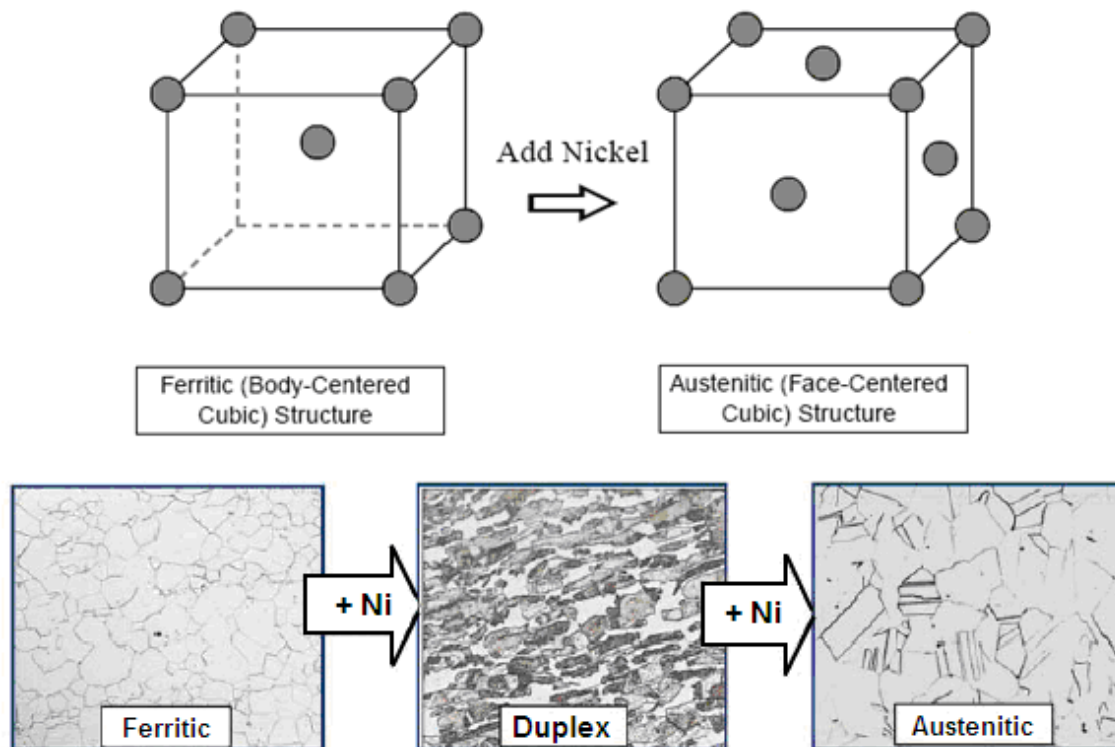


Figure 2.4 : Nickel addition to stainless steel ⁶⁴

2.3.4 Copper

Cu can increase the corrosion resistance when added not in excess of 2% In DSS, since higher level can reduce hot ductility and can lead to precipitation hardening ⁶⁵. However, Cu can be beneficial due to the formation of a Cu-rich layer on the surface during active dissolution. Unfortunately, no data from the field supports this mechanism. Additions of Cu can cause the super-saturation of ferrite due to the decrease in solubility at lower temperatures, which can lead to the precipitation of extremely fine Cu-rich ϵ -phase particles. The ϵ -phase has shown the ability to refine microstructure but the effect on toughness and corrosion properties has not been well documented. Cu addition to high alloy austenitic stainless steels is used to decrease the corrosion rate in non-oxidising environments such as sulphuric acid ⁶⁶. 1.5% Cu is added to some 25% Cr, 3.5% molybdenum duplex stainless steel to promote austenite formation and to obtain the optimum corrosion resistance in 70% H₂SO₄ at 60°C while for boiling HCl an addition of 0.5% Cu decreased both the active

dissolution and crevice corrosion rates. Figure 2.5 shows the effect of Cu on corrosion rate in sulphuric acid environment. Chemical compositions of the tested material are shown in table 2.2.

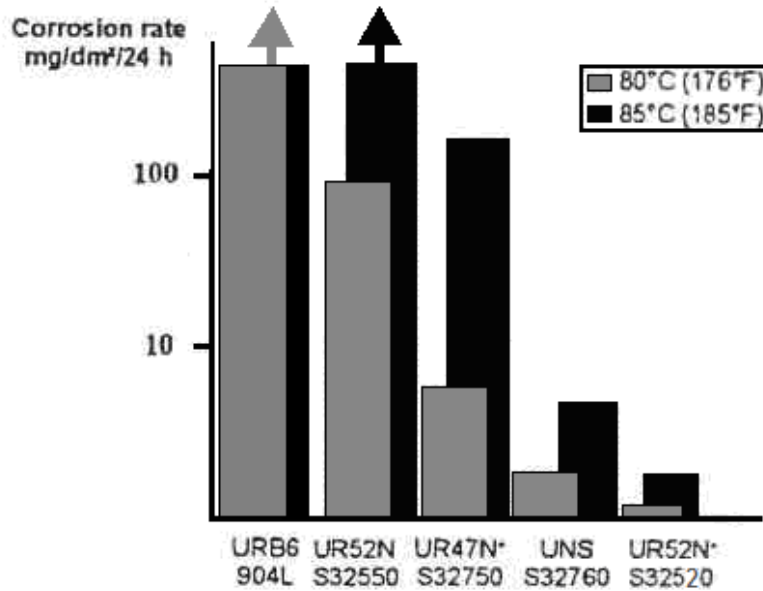


Figure 2.5: Corrosion Rate in 10% H₂SO₄ + 500 ppm Cl⁻ Aerated, at 80 ° C and 85 ° C ⁶⁷

Material	Chemical composition					
	C	Ni	Cr	Mo	Cu	N
904L	0.03	25	20	4-5	1.5	0.05
S32550	0.03	5	25	3.5	1.5	0.25
S32750	0.03	7	25	3.5	0.7	0.25
S32760	0.03	7	25	4	0.5	
UR52N ⁺	0.03	7	25	3.5	1.5	0.25

Table 2.2: Chemical composition for the tested materials figure 3.4

2.3.5 Nitrogen

N, like Ni, is a strong austenite former and can often be used in place of Ni for austenite stabilization since it is more effective than Ni. Nitrogen also effectively increases strength without the risk of sensitization, gives a good improvement in weldability, increases localized corrosion performance, and critical pitting temperature (CPT) more effectively than Cr³⁹.

There are several methods for determining CPT. It is often done in strongly oxidising conditions (FeCl₃ solution) at open circuit conditions. The CPT is also determined by measuring the anodic current of an alloy with increasing the solution temperature (room or above) at a selected potential applied to the alloy. At CPT, the current density increases abruptly. Lower CPT implies greater susceptibility. The determination of critical pitting temperature can be used for alloy development or selection, or both^{40, 41, 42}. ASTM G150 (Standard Test Method for Electrochemical Critical Pitting Temperature Testing of Stainless Steels) describes in detail how to perform such experiments. The suggested applied potential is +700 mV (SCE) and the starting temperature is deemed to be 0°C with an increase of 1°C/min.

Nitrogen increases the yield strength by solid solution strengthening, and unlike carbon does not promote any sensitization (i.e. susceptibility to intergranular corrosion). It partitions to the austenite due to the increased solubility in the phase and also concentrates at the metal passive film interface⁶⁸.

Nitrogen enhances pitting resistance, retards the formation of the chromium-molybdenum phase, and strengthens the steel. Nitrogen is essential in the newer duplex grades for increasing the austenite content, diminishing chromium and molybdenum segregation, and for raising the corrosion resistance of the austenitic phase. Figure 2.6⁶⁹ shows the effect of nitrogen in stabilizing the austenite by increasing the transformation temperature during casting or welding cooling cycle which can affect the ratio of the two phases⁷⁰. The addition of 0.25% N produce a ferrite volume fraction of approximately 50% at 1250 ° C, compared to about 80% ferrite with 0.18%N. However, predicting the

microstructure of a duplex alloy from simplified diagrams is difficult due to the effect of other alloying elements.

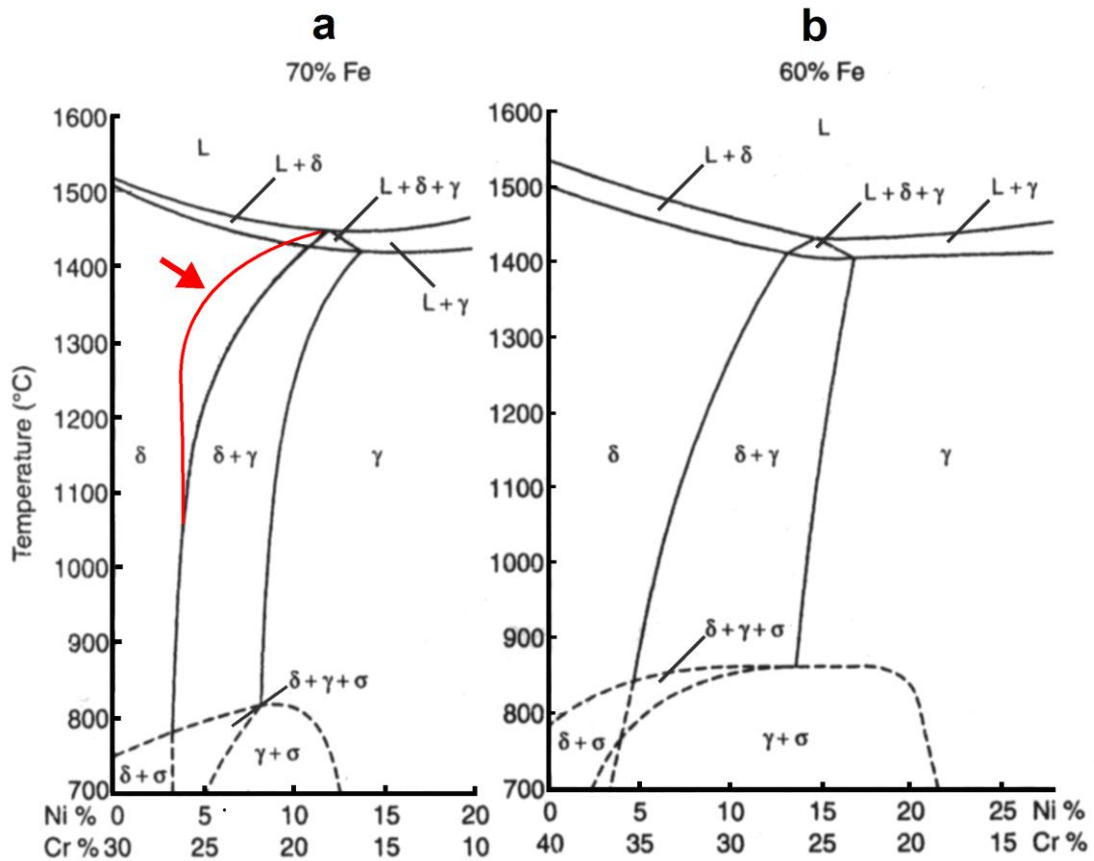


Figure 2.6: Concentration profiles in the ternary Fe-Cr-Ni constitution diagram at 70% and 60%Fe. The effect of 0.25% of N addition is shown in (a) ⁶⁹

2.3.6 Manganese

Mn increases abrasion, wear resistance, and tensile properties without a loss in ductility. However, Mn additions in excess of 3% and 6%, for nitrogen levels of 0.1% and 0.23% respectively, significantly decrease the CPT due to the increased likelihood of MnS inclusions, which can act as initiation sites for pits ³⁹. The combined addition of N and Mn in duplex improves pitting resistance and counteracts the singular problems associated with Mn ³⁹.

2.3.7 Tungsten

W additions of up to 2% in DSS improve the pitting resistance and crevice corrosion resistance^{71 - 73} due to the increase of the passive potential range and the reduction of the i_{pass} . W is known to encourage the formation of intermetallics in the 700 to 1000°C temperature range, and encourages secondary austenite formation in weld metal. Also, W has been shown to form chi phase more rapidly than otherwise similar chemical compositions without the W addition^{39, 74, 75}.

2.3.8 Silicon

Silicon is useful for concentrated nitric acid service and also enhances the high temperature oxidation resistance⁷⁶. Higher silicon level (3.5 - 5.5%) was developed in duplex stainless steel to improve the pitting corrosion resistance and immunity to stress corrosion cracking. Nevertheless, a high silicon level is a strong sigma phase former. Combination of silicon and molybdenum can be particularly dangerous. A recommended level of 0.5 - 0.6% Si content is the best selection for duplex stainless castings^{77, 78}.

The effect of alloying elements on the ferrite and austenite phases and on corrosion properties is summarized below (Table 2.3)

Alloying	Effect	Reason	Practical Limitation
C	Negative	Causes precipitation of chromium carbides with accompanying chromium depleted zones	About 0.03% maximum
Si	Positive	Si Stabilizes the passive film	About 2% maximum, due to its effect on structural stability and on nitrogen solubility
Mn	Negative	Mn-rich sulphides act as initiation sites for pitting. Mn may also destabilize the passive film	About 2%. Higher level may increase the risk of intermetallic precipitation
S	Negative	Sulphides if not Cr-Ti or Ce rich, tend to initiate pitting attack	About 0.003%, if maximum pitting resistance required. For reasonable machining, up to 0.02% allowed
Cr	Positive	Cr stabilizes the passive film	Between 25 and 28% maximum depending on the Mo content. Higher Cr content increases the risk of intermetallic precipitation
Ni	Negative	Increased Ni, other elements constant, dilutes the γ - phase with regard to N, which in turn decreases the PRE of the γ - phase. If the alloy is very sensitive to precipitation of chromium nitrides, Ni can have a positive effect	Ni should primarily be used to give the alloy desired austenite content.
Mo	Positive	Mo stabilizes the passive film, either directly or through enrichment beneath the film	About 4-5% depending on the Cr content. Mo enhances the risk of intermetallic precipitation
N	Positive	N increases the PREN of the γ phase, not only by increasing the N content of that phase, but also by increasing the Cr and Mo contents through their partitioning coefficients	About 0.15% in Mo free grades. About 0.3% in super duplex and some in 0.4% in 25%Cr, high Mo, high Mn alloys
W	Positive	Probably same as Mo	Increases the tendency of intermetallic precipitation
Cu	Disputed	Marginal positive and negative effect	About 2.5% maximum. Higher levels reduce hot workability and undesirable hardenability

Table 2.3: Influence of different alloying additions and microstructure on the pitting and crevice Resistance of Duplex Stainless Steels ⁷⁹

2.4 Mechanical Properties of Duplex Stainless Steel

The different stainless steel categories have different mechanical properties. This can be illustrated in stress-strain curve in figure 2.7. Martensitic steels have high yield and tensile strength but low ductility while austenitic grades have low yield strength and excellent ductility. Somewhere in between are both ferritic-austenitic (duplex) and ferritic steels. The advantage with duplex steels is their high strength due to the austenitic phase, and fairly high ductility, which is a result of the ferritic phase. The yield strength of DSS is higher than austenitic and ferritic stainless steel which is the results of small grain size, caused by mutual hindering of the growth of the ferrite and austenite grains, implying higher strength for the two phase structure than its constituents ³². Formation of hard secondary austenite and Interstitial and substitutional solution hardening is another reason for the high yield strength ⁸⁷.

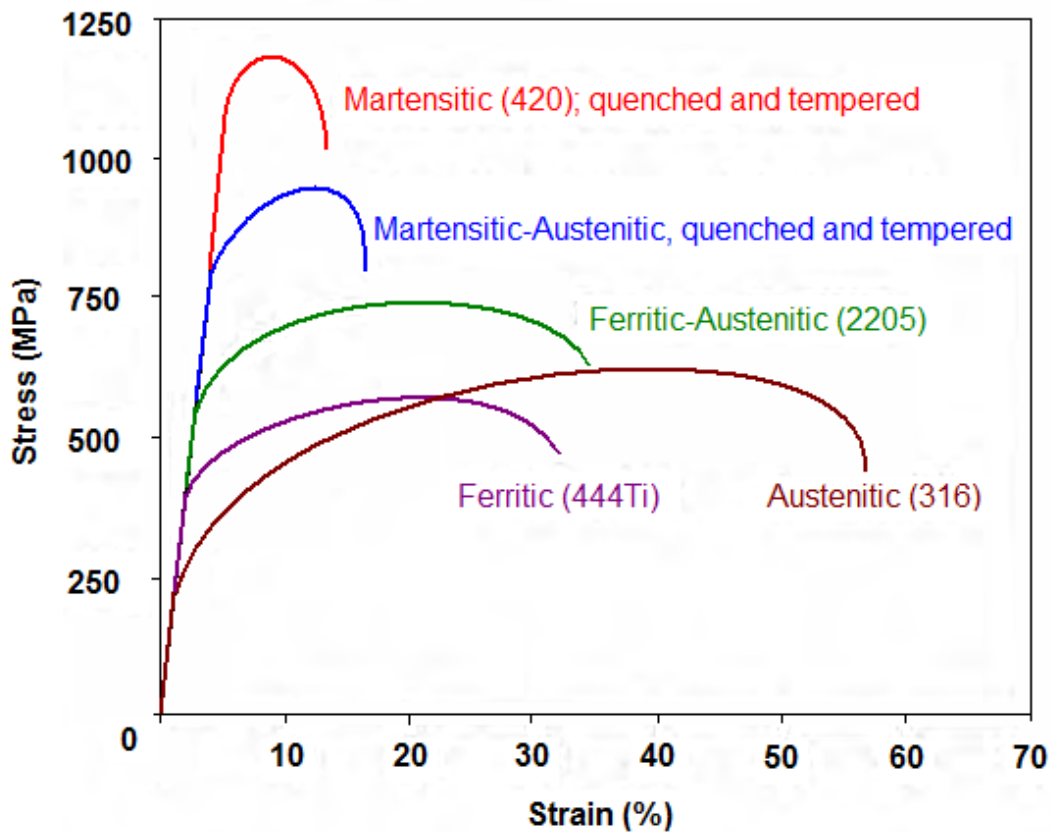


Figure 2.7 : stress strain curve for some stainless steel ⁸⁰

2.5 Applications of Duplex Stainless Steels

Offshore structures require special materials because of the highly corrosive environment in which they exist. The design of Duplex stainless steels has been found to be suitable to meet most of these condition needs due to their high strength and corrosion resistance to brine and carbon dioxide in variety of fields. Duplex stainless steel grades show excellent corrosion resistance when exposed to CO₂ (sweet corrosion) with low pH (2.5) and high concentration of chloride (150,000 mg/l) even with the presence of sand at a flow rate of 30 m/s.

In general, these alloys are widely utilised as a high strength material for critical applications in the offshore oil and gas industry. Their low thermal expansion and high thermal conductivity make them suitable for heat exchangers. Presently, they are used with thickness up to 100 mm and with design temperatures down to -50° C ³⁹. Duplex stainless steels can be supplied in all current forms such as bars, forgings, sheet, tubes and castings. These alloys are useful for a number significant fields of applications such as equipments for sour gas wells like tubes and valve castings, where H₂S, chlorides and elevated temperatures contribute to severe corrosion conditions and where operating pressures are high. Also, they have been used in the paper industry, process and desalination equipments where sulphate, sulphite, sulphuric and phosphoric acids are present. Super duplex stainless steels have been developed specifically to be used in the chemical processing, marine and oil industry for applications such as valves, pipes, vessels, shaft seals, pumps components and other mechanical parts.

The positive successful experience of duplex stainless steel applications over other type of stainless steel is well known. Duplex stainless steels offer cost saving for many aggressive environments including oil and gas industry, sea water applications, desalination plants, pulp and paper, chemical tankers, building and constructions. In most cases duplex stainless steels are selected because they combine high strength and excellent corrosion resistance

2.6 Limitations of DSS

Duplex stainless steel grades have been in use for many years. Their structure is usually 40 to 50% ferrite with the balance of the microstructure being austenite. They show complex behaviour in high temperature chloride containing media. Although they are sensitive to stress corrosion cracking in many cases they can offer a significant improvement comparing with austenitic grades. Their higher ferrite levels provide significantly better chloride stress corrosion cracking resistance than austenitic grades and higher chromium and molybdenum contents provide good localized corrosion resistance.

Welding is an important method of fabrication which needs understanding of transforming at different cooling rates and the effect of peak temperature in the HAZ and filler dilution. It may reduce corrosion resistance and ductility unless it is followed by a post-weld solution heat treatment. Duplex stainless steels can suffer from weld metal, hydrogen cracking but the reported incidences^{15, 81, 82} have been restricted to cases in which the alloy was heavily cold worked or weld metals experienced high levels of restraint or possessed very high ferrite contents in combination with very high hydrogen levels, as a result of poor flux controlled electrodes or the use of hydrogen-containing shielding gas.

None of the duplex stainless steels should be used in continuous service above 600°F (315°C) because of the potential for 885°F (475°C) embrittlement of the ferrite phase. The machinability of duplex stainless steels is limited by their high annealed strength level, and they are considered less machinable than most standard austenitic grades. Improved machinability can be achieved by introducing non-metallic inclusions, such as sulphides. Nevertheless high sulphur grades will be sensitive to weld metal cracking and have a lower resistance to pitting corrosion. Thus they should only be selected where welding is not envisaged and corrosion resistance is not paramount

At high temperatures, materials must be selected for resistance to pitting and stress corrosion cracking in the presence of chlorides media. Stress corrosion must be avoided in heat transfer applications, such as steam jacketing for

cooking or processing vessels or in heat exchangers. Cracking can occur from the process or water side or can initiate outside the unit under chloride containing insulation. Brewery applications of austenitic stainless steels have been generally successful except for a number of cases of SCC of high-temperature water lines. The use of ferritic or duplex stainless steels is an appropriate remedy for the SCC.

Duplex stainless steels are rarely used in heat resistant applications since they are embrittled by sigma phase precipitation between 600 and 1000 ° C and have very poor creep strength above this range.

2.6.1 Hydrogen Embrittlement Failures

Hydrogen damage can cause failure of steel in many industrial areas such as petrochemical, chemical, oil and gas production. In the late 1990s, over all 26% of failures of vessels inspected in refineries ⁸³ and even 75% of damage to pipelines containing hydrogen sulphide (H₂S) ⁸⁴ were attributed to the action of hydrogen. Unexpected failures were also reported due to cathodic protection used in subsea constructions. Hydrogen produced by cathodic protection has shown to be enough to cause hydrogen embrittlement of steels ^{85, 86}. Hydrogen embrittlement of duplex stainless steel did not attract much attention until some failures occurred under the effect of cathodic protection. The increasing numbers of failures were puzzling because there were designed and qualified to use under the desired operation conditions and also because currently similar components are still in operation.

2.6.1.1 BP

BP reported in paper submitted by Taylor ¹⁵, that heavily forged subsea manifolds fabricated from 25%Cr super duplex stainless steel had failed (Figure 2.8). The cracking occurred in machined nib regions adjacent to the weld to 6" pipe in water depth of about 400 meters. Leaks were discovered in two of these special connectors as shown in figure 2.9. The manifold was subjected to cathodic protection by aluminium, giving a potential around -1050 mV (SCE).

The hubs were solution annealed and quenched, had approximately a ratio of 50% of austenite and ferrite. The failure analysis had shown that cracking initiated and propagated in a coarse, aligned grain structure, produced by forging process. The cracking had occurred away from the weld and HAZ but was shown to be in the region with highest stress concentration. Although the microstructure had a good phase ratio it was shown to be susceptible to hydrogen embrittlement.



Figure 2.8 : Super duplex stainless steel hub forging with welded pipe connections ¹⁵

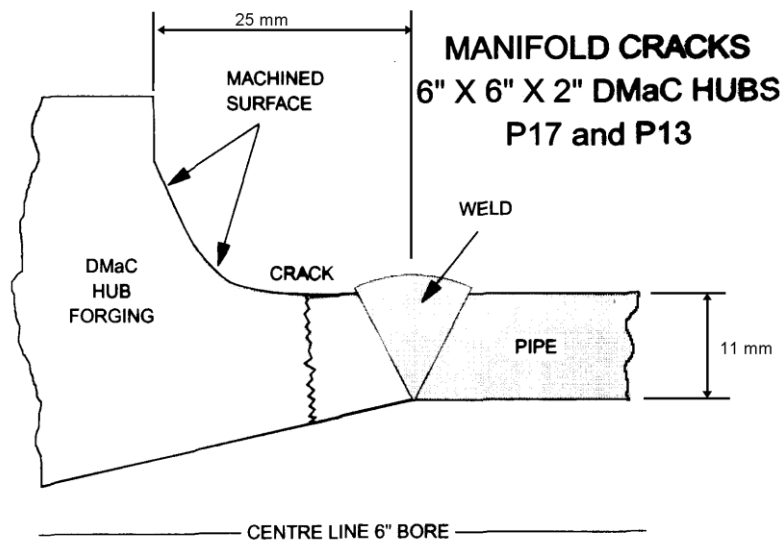


Figure 2.9: Cracking location ¹⁵

2.6.1.2 Shell

Shell reported a failure of subsea hub connection constructed from super duplex stainless steel Zeron 100 (UNS 32760) submitted in a paper by Huizinga et. al ¹⁶. The hub was used to connect the manifold pipe work with the transport pipeline and protected by a sacrificial anode with a potential of -1050mV (SCE). The flowing condition of the pipeline was about 50 ° C with a pressure of about 60 bars. During a start up following a planned shut down, crack was observed on the hub close to the weld to the manifold pipe. The fracture was around the full circumference of the hub as shown in figure 2.10. The cracking was identified as a case of hydrogen embrittlement mode occurred by the presence of a combination of a susceptible microstructure, hydrogen uptake and stress. The stress analysis studies showed that local stress (plus stress concentrated resulted from the geometry of the hub) and residual stress was likely to have exceeded 80% of yield stress. The value of this stress was below which failure occurred in laboratory tests. The sacrificial anode used as a cathodic protection was confirmed to be the source of hydrogen resulted in hydrogen embrittlement cracking.



Figure 2.10: Fracture surface of in board side of parted subsea hub ¹⁶

2.7 Segregation of Alloying Elements

Duplex stainless steels are produced by having a correct balance between ferrite forming elements (Cr, Mo, Ti, Nb, Si and Al) and austenite forming elements (Ni, Mn, C and N). To achieve a duplex structure it is necessary to increase the chromium content to above 20% ⁴³, whilst the exact ratio of ferrite and austenite phases is controlled by the heat treatment. The solidification of duplex stainless steel is entirely ferritic, with an austenitic phase formed through a solid-state phase transformation during post-solidification cooling ⁴⁴.

In addition to ferrite and austenite phases, a variety of undesirable phases may form on solidification of duplex stainless steels or during subsequent heat treatment, welding, plastic deformation, or ageing during their operational life. These secondary phases can have a pronounced effect on the workability of duplex stainless steels, impairing their mechanical and corrosion properties ⁴⁵, ⁴⁶. This is essentially a consequence of the instability of the ferrite phase ⁴⁹. Any large increase in temperature leads to a significant change in volume fractions and to partitioning of alloying elements within both the austenite and

ferrite phases. The ferrite phase, which is enriched in chromium and molybdenum, presents a high susceptibility to the formation of intermetallic phases. In addition, the solubilities of nitrogen, carbon, tungsten and copper in the ferrite phase fall sharply with a decrease in temperature, increasing the probability of precipitation during heat treatment ⁵⁰. A time-temperature-transformation (TTT) diagram for a typical duplex stainless steel, showing the possible metallurgical transformations at a range of temperatures (300 to 1000 °C) is depicted in figure 2.8 ⁵¹.

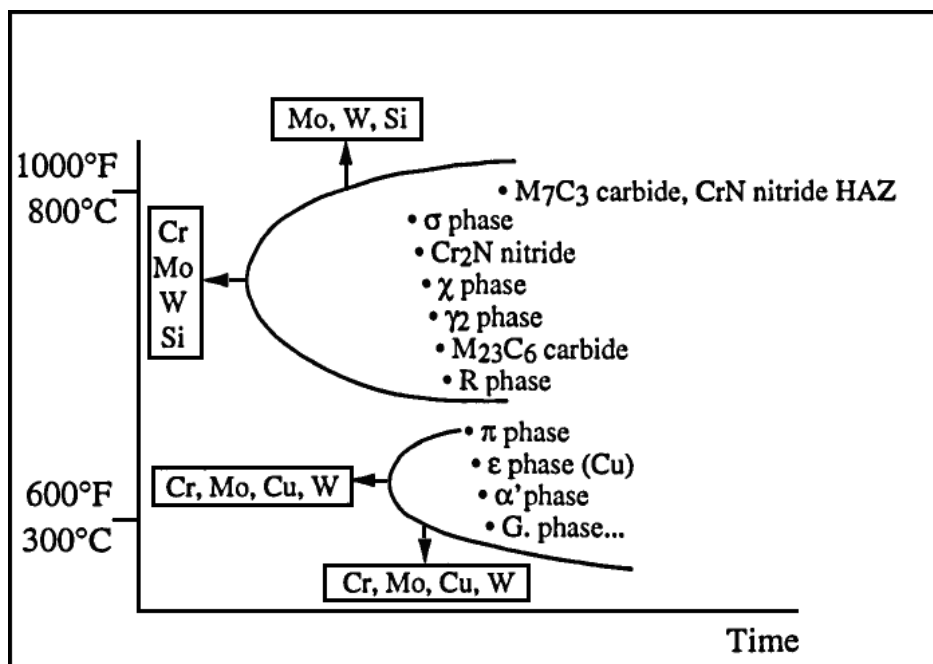


Figure 2.11: Precipitation reactions which may occur in duplex grades ⁵¹

2.7.1 Sigma Phase

Sigma phase is enriched with chromium and molybdenum and consider being the most important secondary phase in variety of duplex stainless steel ^{47 - 49} since it present in the highest volume fractions ⁵². It is a hard and brittle intermetallic phase that is normally forms adjacent to the ferrite phase ⁴⁵. Quantitative chemical analysis of the sigma phase showed that it enriched with Cr, Mo and Si, which are ferrite (bcc) stabilizing elements. This phase, which

often forms together with the chi (χ) phase, is clearly known for its particularly harmful effects on ductility and toughness, and corrosion resistance ⁵³. The precipitation can be influenced by heat treatment temperature that occurs between 600 and 1000 °C ⁵⁴ and often starts at triple junctions or grain boundaries and grows into the ferrite which will consequently be diluted by high solution temperature with respect to ferrite forming elements ^{53, 55}. Super duplex stainless steels with high additions of Cr and Mo are most prone to sigma precipitation, since these elements are enriched in sigma.

3 Corrosion Behaviour of Duplex Stainless Steels

However, some forms of corrosion do not involve such clear visual changes or material loss that can be observed. For example, a bright shiny stainless steel can break at stress level much below that predicted and the reason for that failure could be from a corrosion process. In many cases, it can be stress corrosion cracking or more likely hydrogen embrittlement. Another example of those dangerous forms of corrosion is crevice and pitting corrosion, which cannot be easily detected. These types of corrosion cannot always produce a clear visual change such as rust. Many other forms of corrosion reduce the stress bearing capability of the material, such as stress corrosion cracking, corrosion fatigue, fretting fatigue and hydrogen embrittlement. These types of corrosion are very difficult to detect and will lead the material to fail below the expected stress. Furthermore, if these types of corrosion are not detected, a failure may occur without any warning.

Corrosion of steel can be explained as an electrochemical process associated with at least two reactions when immersed in aqueous solution. Throughout this process, the anode and cathode reactions occur simultaneously. Therefore it is possible to control corrosion by slowing down the rates of either reaction ¹⁸. One of the methods to reduce the flow rates from the anodic is by using cathodic protection techniques. As described in figure 3.1, the anode (1) is the region of the metal surface that deteriorates and produces electrons which migrate to the surface and react with dissolved oxygen. The anode reaction is also called oxidation which means loss of electrons ¹⁹. During this process, electrons flow from the anode region to the cathode region. The driving force that allows the current to flow is the energy that is accumulated in the metal, which is also known as the potential of the metal. Each metal has different corrosion resistance characteristics due to the amount of the energy that is required during its refining process. Therefore, every metal has a different tendency to deteriorate. However, offshore environment is considered by many as the most severe of the environments.

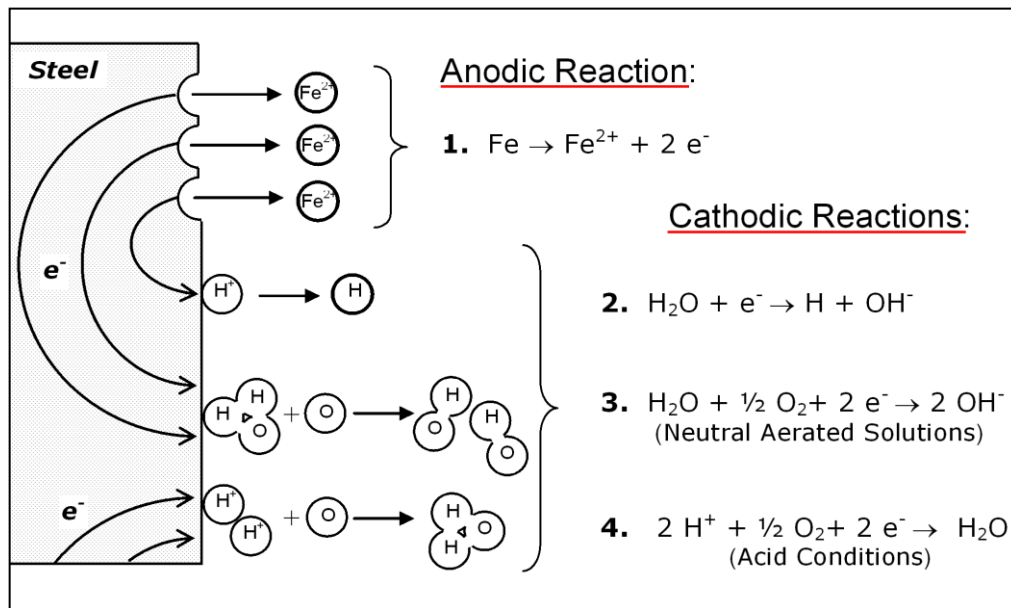


Figure 3.1 Basic electrochemical corrosion cell between anodic and cathodic region on the steel surface ⁵⁶

The mechanism of corrosion resistance of stainless steels differs from that of carbon steels and alloy steels. For the carbon and alloy steels, the formation of a barrier of a true oxide separates the metal from the surrounding atmosphere. The degree of protection afforded by the oxide is a function of the thickness of the oxide layer, the continuity of the oxide layer, the coherence and adhesion of the oxide layer to the metal, and the diffusivities of oxygen in the oxide. At normal temperatures, stainless steels do not form a layer of a relatively thick oxide, but instead a passive film is formed. This film is generally considered to be some form of a hydrated oxide. The exact nature of the film is not known. However, it is known that the film must be continuous, nonporous, insoluble, and self-healing if broken in the presence of oxygen. When conditions are favourable for maintaining passivity, stainless steels exhibit very high corrosion resistance. The passive oxide must be free of pores up to the activated potential. Because of the absence of pores for the oxides, it may be concluded that the oxide layer grows directly on the metal. The excellent corrosion protection results because the metal phase can react only negligibly with

constituents of the solution, as metal ions or species of the oxidant migrate through the passive film. If passivity is destroyed under conditions that do not permit restoration of the passive film, then surface of a metal becomes exposed to the solution, positively charged metal ions tend to pass from the metal into the solution, leaving electrons behind on the metal.

Generally, it is well known that the corrosion properties of all stainless steels are defined by the ability to passivate and remain in the passive state in service. However, the scope of this study will be focused on the localized corrosion and susceptibility to hydrogen embrittlement, where the corrosion behaviour of the individual phases is a key factor for understanding the corrosion properties of the whole material.

3.1 Types of Damage Due to Hydrogen

The effect of hydrogen damage has long been recognized in many metals and alloys. Hydrogen embrittlement is a result of hydrogen concentration builds up in the metal that with time will form blisters and cracks at internal interphases such as grain boundaries, inclusions and second phase particles eventually lead to failure. Johnson ⁵⁷ in 1875 observed loss of ductility of iron after immersion in acids. Since this observation, hydrogen effect on metals has become one of the most investigated problems in the metallurgical engineering field.

3.2 Hydrogen Embrittlement

Two forms of the manifestations of hydrogen damage are hydrogen-induced cracking and hydrogen induced stress corrosion cracking (hydrogen embrittlement). Macroscopically speaking, hydrogen embrittlement is similar to stress-corrosion in that a normally ductile metal experiences brittle fracture when exposed to both a tensile stress and hydrogen resulting from metal dissolution in a corrosive atmosphere. Hydrogen-induced cracks are most often transgranular, although intergranular fracture is observed for some alloy systems. Hydrogen in its atomic form diffuses interstitially through the crystal

lattice, and concentrations as low as a few parts per million can lead to cracking⁸⁸. Hydrogen embrittlement is another case of delayed failure, in that there is a time dependency for the process to occur. This is often due to the fact that it is both stress and hydrogen dependent. Failure will not initiate until both conditions are met. It may take some time before the hydrogen is in sufficient quantities in the correct location to initiate failure. As no significant metal consumption is associated with the failure mode no corrosion products should be found on the fracture surface, provided the material is removed immediately from the environment after failure.

3.2.1 Mechanisms of Hydrogen Embrittlement

There are several different mechanisms of hydrogen embrittlement, some of which are specific to particular materials and others which are more general in application. In all cases, the time dependency has to be accounted for along with the transgranular nature of some failures and intergranular nature of others. A brief description of several proposed models for hydrogen embrittlement mechanisms are presented as the following:

3.2.1.1 The Internal Pressure

The internal pressure theory was originally advanced by Zapffe and Sims⁸⁹ which proposes that the effect of hydrogen is to create very high pressures of hydrogen gas in voids and other defects within the metal. This high pressure which is generated by the accumulation of the hydrogen gas, can act as an applied stress necessary for crack propagation that can lead to steel fracture. This situation occurs for instance in blister formation. Alternatively, the observation of the crack growth in dry gas at low pressure and chloride shows that this theory is not general⁹⁰.

3.2.1.2 Surface Energy

This theory was first proposed by Petch and Stables⁹¹. By lowering the surface energy of the newly-formed crack, the hydrogen reduces the stress intensity required for brittle fracture. As with the decohesion models, surface energy

models only seem reasonable for the case of hydrogen derived from surface layers or grain boundaries, since the hydrogen adsorption must occur at the same time as the fracture event in order for the reduction in surface energy to be effective in lowering the energy required for fracture, as figure 3.2 depicts.

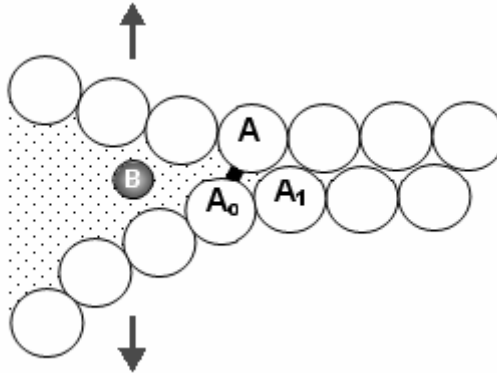


Figure 3.2 Schematic illustration of the adsorption model. The model requires that a specific ion from the environment, B , interacts and reduces the cohesive strength of the strained bond $A-A_0$ at the tip of the brittle crack ⁹²

3.2.1.3 Decohesion Theories

The decohesion models proposed by Troiano, and Oriani ⁹³ suggest that the role of hydrogen is to weaken the interatomic bonds in the steel, thereby facilitating grain boundary separation or cleavage crack growth (figure 3.3). In view of the very low hydrogen concentration in the matrix it is necessary for some method to exist by which the hydrogen can be concentrated at the site of the fracture. For cracking along phase or grain boundaries this can be explained in terms of the trapping of hydrogen at the phase boundary. It is a little more difficult to see how transgranular cracking can be explained; processes which have been invoked include the concentration of hydrogen at the region of triaxial tensile stress at the crack tip and local high concentrations of hydrogen being generated by reaction or adsorption at the crack tip.

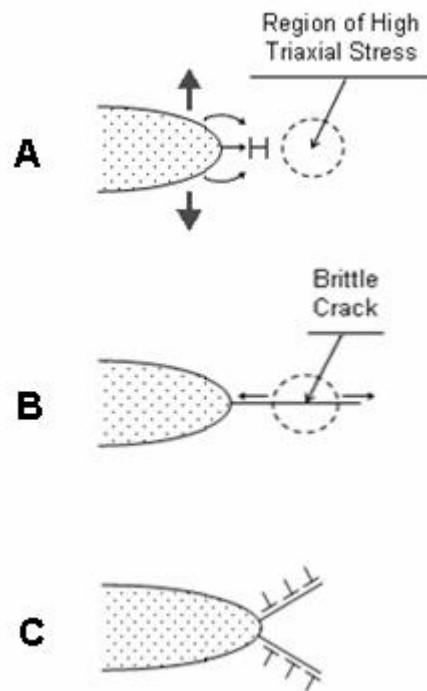


Figure 3.3: Schematic illustration of the decohesion model for hydrogen embrittlement⁹³

3.2.2 Methods for Hydrogen to Enter Metals

The source of hydrogen can be from different ways such as corrosive environment, electroplating and welding processes. The focus of this investigation was the electrochemical hydrogen evolution and diffusion that can be a result of the cathodic reaction. As hydrogen enters the material, it tends to accumulate at a wide range of locations within the microstructures such as on grain boundaries, inclusions, voids, dislocation and dislocation arrays, solute atoms, as well as in solid solution. Any of those locations is the most sensitive to fracture will control the magnitude of hydrogen effects. In general all of them will accumulate hydrogen albeit to different extents.

3.2.2.1 Pickling and Chemical metal Removal

Cleaning the surface oxide on the metal surface is called pickling process by using a strong acid which can produce a large amount of hydrogen. The hydrogen then can be diffuse in to the metal during this chemical dissolution process. Another similar way to clean or remove material from the surface is the chemical polishing process.

3.2.2.2 Plating Operations (another cathodic Process)

Electroplating is another electrochemical process. As the current efficiency of metal deposition is less than 100%, a significant amount of hydrogen is often produced in the cathodic reaction and absorbed by the substrate.

3.2.2.3 Crevice Corrosion Conditions

In this condition, hydrogen can be produced by the environmental changes. Failures of hydrogen embrittlement were found in some cases such as thread-root dues to stress concentration and local environmental conditions.

3.2.2.4 Service Condition

Some of the service conditions contain hydrogen sulphide gas or acid making plant in the petrochemical and gas industries can produce a significant amount of hydrogen.

3.2.3 Comparison of SCC and HE

The main feature to distinguish hydrogen embrittlement from stress corrosion cracking is generally by the influence of applied current or applied potential. Unlike stress corrosion cracking (a dissolution process) which is increased by applied anodic current, cracking by hydrogen embrittlement is accentuated by cathodic protection or impressed current. If an anodic current is applied and cracking is accelerated, then the attack might be attributed to stress corrosion cracking, whereas if cracking is accelerated by cathodic current and hydrogen evolution is observed, then the attack is hydrogen embrittlement. Another

simple difference is that stress corrosion cracking begins at the surface where corrosion can occur whereas the hydrogen embrittlement can begin internally as another source of hydrogen can be sufficient. In addition, the magnitude of corrosion is higher at the origin of stress corrosion cracking than observed with hydrogen embrittlement ⁹⁵ . Figure 3.5 differentiates between anodic stress corrosion cracking and cathodic hydrogen embrittlement. Hydrogen embrittlement can be grouped under some proposed mechanisms such as pressure theories, adsorption theory and decohesion theory.

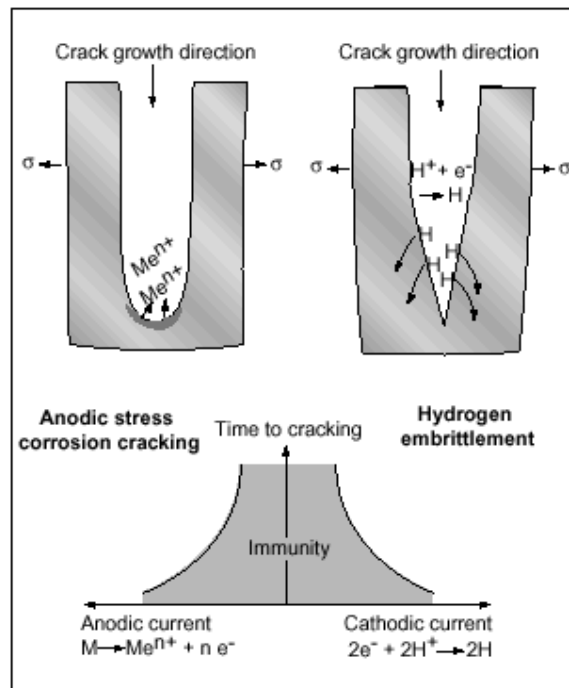


Figure 3.4: Schematic differentiation of anodic stress corrosion cracking and cathodically sensitive hydrogen embrittlement ¹⁸

However, there is evidence to show that under some circumstances hydrogen uptake can occur even at anodic applied potentials. Figure 3.4 shows the results of Taqi and Cottis ⁹⁴ for hydrogen permeation at a range of potentials

applied to the outside of carbon steel crevices in NaCl solution. Due to an IR drop induced within the crevice, the potential can remain below that required for hydrogen evolution.

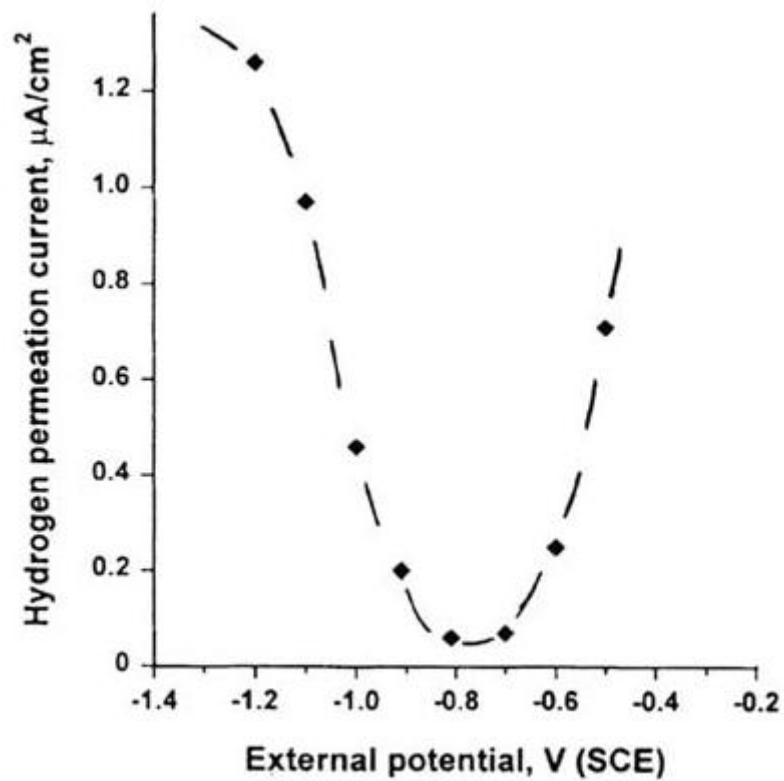


Figure 3.5: Hydrogen permeation rate, as a function of potential for carbon steel crevices in NaCl solution ⁹⁴

3.2.4 Diffusion of Hydrogen in Duplex Stainless Steels

The entrance of hydrogen atoms into the steel is the first step in the process resulting hydrogen embrittlement. Hydrogen atom can diffuse and occupy the interstitial sites inside the metal due to its small volume. Hydrogen may enter metals by dissolution of hydrogen gas phase or by adsorption by hydrogen produced by electrochemical reaction in solution. In duplex stainless steels the diffusion of hydrogen is more complicated due to the existence of the two phases. Austenite behaves differently in terms of hydrogen diffusion due to its high solubility and low diffusion coefficient. Hydrogen diffuses quickly in the ferrite and has a relatively low solubility. However, diffusion time is proportional to the square root of the thickness of the specimen.

3.2.4.1 Diffusion

In 1855, Adolf Fick developed equations governing diffusion that are now known as Fick's first and second laws of diffusion. Fick's first law describes the movement of hydrogen from a region of high concentration to a region of low concentration. Fick's second law defines the change in concentration with time at a given point. Both equations show the relationship between diffusion and concentration gradients as the following:

$$J = -D \frac{dc}{dx} \quad 1$$

$$\frac{\partial c}{\partial t} = \frac{\partial}{\partial x} \left(D \frac{\partial c}{\partial x} \right) \quad 2$$

Where:

J = diffusion flux (the number of particles diffusing down the concentration gradient per second per unit area.

D = the diffusion coefficient with typical units cm^2/s

c = concentration of the diffusing species.

The diffusion coefficient is generally assumed to be constant at a given temperature. The diffusion rate is sensitive not only to the concentration gradient but also to defects in materials such as grain boundaries, dislocations, and vacancies. Therefore, the diffusion coefficient varies with defect concentration and temperature. Surface and grain boundaries are more open structures, and the resistance to atom migration is expected to be less than inside the lattice. Vacancies play an important role when considering substitutional diffusion. In order to diffuse one lattice point to another, vacancies must be moving in the direction opposite to that of atomic diffusion.

3.3 Pitting Corrosion

Pitting corrosion is a form of localized corrosion as it does not spread laterally across an exposed surface rapidly but penetrates into the metal, usually at an angle of 90° to the surface. Pits may be initiated at localised surface defects such as scratches or slight variations in composition. They ordinarily appear inside the line-pipes and penetrate towards the outer surface. The mechanism for pitting is probably due to oxidation within the pit itself, with complementary reduction at the surface. The solution at the pit becomes more concentrated, acidic and dense as pit growth progresses.

3.3.1 Effect of Alloying Elements on E_{pit}

The alloying elements, chromium, molybdenum and nitrogen, play a major role in governing the pitting resistance of stainless steels in chloride environments the relation of these essential elements are expressed in the resistance equivalent number (PRE) which was introduced in the previous section.

The tendency to pitting corrosion of stainless steels decreases as the contents of Cr, Mo and N increases. The addition of Cr to steel changes the nature of the passive film to be an amorphous, more homogeneous one with less defects which can not be easily broken down ⁹⁶. E_{pit} of duplex stainless steels increases in the noble direction with the PRE number.

Bernhardsson⁹⁷ showed theoretical calculation results that, by adjusting the ferrite/austenite balance via adjusting Ni and the heat treatment temperature, it is possible to achieve an equal PREN for both ferrite and austenite as shown in figure 3.6. The best pitting corrosion resistance can be achieved by understanding the metallurgy of duplex stainless steel since pitting performance is a reflection of the microstructure. Higher ferrite ratio can cause the formation of Cr₂N or other intermetallic phases and higher austenite can reduce the nitrogen concentration and result in greater segregation of Cr and Mo in the austenite. Higher nickel content will result in higher austenite ratio which can stabilize sigma phase while lower Ni will increase the ferrite ratio. Proper heat treatment has a significant effect on the austenite/ferrite ratio. The higher the solution annealing temperature, for given nitrogen content, the higher ferrite ratio will become.

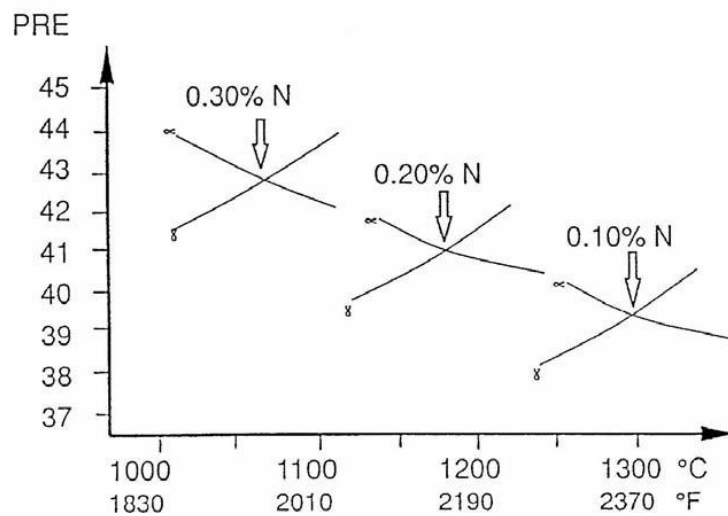


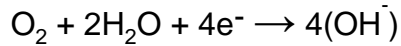
Figure 3.6: Theoretical calculations based on alloys with 25% Cr and 4% Mo. Ni was varied to keep constant ferrite content⁹⁷

3.3.2 Pitting Mechanism

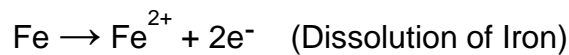
Pitting can be separated into two different regions, namely pit initiation and pit growth.

3.3.3 Pit Growth

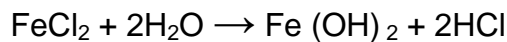
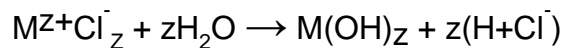
The exposed surface outside the growing pit may be partially cathodically protected by supporting the reduction of oxygen to hydroxyl ion reaction:-



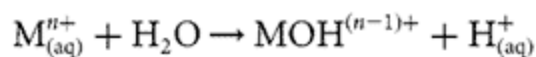
As this cathodically protects the region outside the pit, the metal dissolution region cannot spread laterally across the surface. In addition, the large cathodic surface can maintain this reaction and form a large cathode to small anode ratio which will accelerate the anodic reaction. Generally, the rate of corrosion is dependant on the cathode/anode area ratio⁹⁸. Within the pit, which is regarded as a small hemisphere at this stage, the metal dissolution reaction is taking place. This is the general anodic reaction inside the pit for stainless steel:



However, it is the only reaction within the pit and results in an electrical imbalance again which attracts negatively charge ions, usually chloride ions. The autocatalytic reaction to form hydrochloric acid in the pit is initiated and continues:-



The dissolution of chromium also occurs and chromium hydrolysis Cr^{3+} can lead to a very low pH value (from 0 to 1)⁹⁹. Acidification by hydrolysis can have a large effect on the pitting corrosion of stainless steels. The local environment is acidified by the hydrolysis of the dissolving metal cations according to the following reaction:



As a result of these reactions the electrolyte enclosed in the pit gains positive electrical charge in contrast to the electrolyte surrounding the pit, which becomes negatively charged. The positively charged pit attracts negative ions of chloride (Cl^-) increasing acidity of the electrolyte which causes further acceleration of the corrosion process. Once it is started, pits can propagate deeper into the alloy and the pH decreases while chloride ion concentration increases inside the pit.

Figure 3.7 shows a cross section of pit propagation in stainless steel. Pitting corrosion occurs by the breakdown of the passive film by a sufficient amount of Cl^- with a built up of low pH. The external surface can act as a large cathode area and the pit acts as a small anode area which can accelerate the pit growth. Generally, the external surface is passivated due to high oxygen plus high pH. A rapid metal dissolution (anodic dissolution) within the pit with an increase in the Cl^- is leading to acidification of the solution. In addition to O_2 reduction on the external surface, hydrogen reduction also takes place on the adjacent surface and hydrogen bubbles is formed at the pit wall, which increase the IR drop and could results in hydrogen embrittlement under loading. IR drop through the film and along electrolyte path between occluded region (pit) and external surface maintains potential difference (driving force) to keep the pit actively corroding. Pitting corrosion is stopped when pit internal and external solutions are mixed; pits are repassivated. Once pits are formed, they propagate at an increasing rate in an autocatalytic nature.

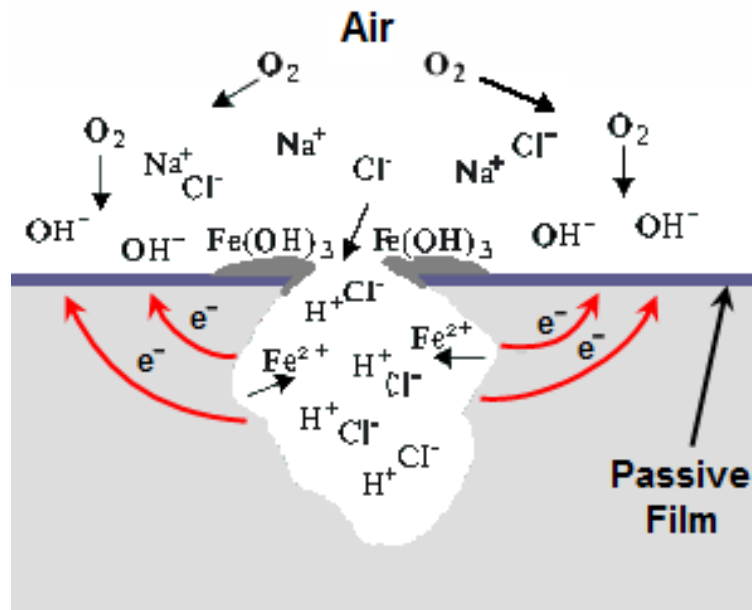


Figure 3.7 A generalized picture of pit propagation in stainless steel in containing chloride ions ¹⁰⁰

3.3.4 Pit Initiation

Pit initiation is still not well understood. The initiation time of pits can vary from short, days, to very long times, many years. Some changes in the passive layer of stainless steel can effect the pit initiation. Most of the pit initiation mechanisms are associated with the breakdown of the passive film on the metal. Stainless steels has a complicated passive layer thought to be 20 to 30 Angstroms thick (1 Angstrom is 10^{-8} cm), but the thickness can range between 10 and 100 Å depending on the condition in which the film was formed and also on the composition of the alloy ¹⁰¹. As an atom is only about 2 Angstroms in diameter, then a passive layer is only about 15 to 50 atoms thick. In pitting corrosion investigations, this passive layer is difficult to examine because experimentalist does not know which site is going to pit. The passive layer is thought to be a two phase type of structure with the side nearest the metal a crystalline phase while the layer nearest the solution side is thought to be an amorphous mixture of metal ions and hydroxyl ions ^{102, 103}.

3.3.5 Initiation Mechanism

The mechanism of pit initiation has been investigated by many researchers and it is known that it is associated with the presence of certain aggressive ions such as chloride (Cl^-) in solution which is the most common one to induce the film breakdown. Most of the initiation theories associated with the properties of the passive film.

3.3.5.1 Defect Theory

Some early investigators suspected that defects in the film broke down were related to metal defects such as grain boundaries or slip steps due to dislocations emerging from the surfaces. Breakdown initiation and local anodes could be one of the sites that the film probably was not fully formed over these local anomalies. Regrettably, a relationship between pits and defects can be found in some materials but it is not a general rule ^{104, 105}.

3.3.5.2 Chloride Ion Dissolutions

The fact that many metal chlorides are soluble in water has been used to suggest that the adsorption of hydroxyl ions results in passivity, whereas that of chloride ions does not. The pit can be developed on spots where the hydroxyl ions adsorbed on the solution/passive layer interface is replaced by chloride ions. Additional chloride ion dissolution would then form a pit into the metal surface. This mechanism predicts that once a pit forms it will continue to grow. According to this theory, some pits cease to grow when the chloride ions that had replaced the passivating oxygen from film are then desorbed and the surface repassivates ¹⁰⁶.

3.3.5.3 Peptisation

A small number of chloride ions jointly adsorb through the passive layer to the metal surface and then caused dissolution of the metal by forming complex ion, MCl^{n-} . Further chloride ions would then diffuse leading to thinning of the film. This auto accelerated dissolution will eventually result in film break down and pit

growing. This theory predicts that once a pit starts it continues and it is not always the case ¹⁰⁷.

3.3.5.4 Local Cells

In some alloys second phases are present and will behave differently electrochemically. One phase will be anodic to the matrix and other will be cathodic to the matrix. A good example is age hardening aluminium alloys, 2000 series, where the copper rich particles are cathodic to the matrix. These second phases can act like a local cells and could break down passive layers and initiate pits. Once again, this is not a generalized theory as pits can be formed in very pure single crystals ¹⁰⁸.

3.3.5.5 Stress Theory

As the passive films grow stresses are induced as they do not have the same crystal dimensions as the metal on which they are growing. Film break down occurs by reducing the surface tension, and then chloride ions can get to the surface and promote dissolution of the metal ¹⁰⁹.

3.3.5.6 Vacancy Theory

For a passive film to form, metal ions or cations must diffuse from the metal/passive film interface to the passive film/solution interface. The cation diffusion can be thought of as a cation vacancy diffusing to the metal/film interface. If enough of these can be brought together at the metal/film interface then a void would be created along with a stress concentration. The stress concentration in combination with the film stress may be sufficient to rupture the film and initiate pitting. The usefulness of this model is that by application of standard electrochemical theory, pit initiation rates can be determined. It works well for many systems ¹¹⁰.

3.3.5.7 Breakdown and Repair

One drawback of many of the above theories is that they rely on a static film prior to breakdown. One of the most recent and widely accepted theories is that

the passive film is a dynamic system. At any time portions of it are well established while others are breaking down by any of the above mechanisms. The film has the ability to repair and in many cases will do. However, a combination of film thickness and chloride ion concentration will be present when the film cannot repair and at this time a pit will initiate. Other areas of the film will also initiate a pit and some will grow while others will repair. This model fits with the dynamics of a corrosion reaction and also with the observation that some pits initiate but do not grow while others are initiated later and grow. It also takes into account the different breakdown theories which may be alloy specific ¹¹¹.

3.3.5.8 Inclusions

Pits can also initiate at some chemical or physical heterogeneity at the surface, such as inclusions, second-phase particles, solute-segregated grain boundaries, flaws, mechanical damage, or dislocations ¹¹². Most engineering alloys have many or all such defects, and pits will tend to form at the most susceptible sites first. In stainless steels, pits are often associated with MnS inclusions, which are found in most commercial steels. The role of MnS inclusions in promoting the breakdown and localized corrosion of stainless steels has been recognized for some time ^{113 114}. Recent improvements in alloy production have led to steels with lower sulfur content to improve pitting resistance.

4 Experimental Methods

4.1 Materials

The materials used in these experiments were super duplex stainless steels, specifically FERRALIUM 255-SD50 (S32550), SAF 2507 (S32750) and Zeron 100 (S32760) supplied by BÖHLER and Langley Alloys, which had the following manufacturer compositions as shown in Tables 4.1, The mechanical properties are shown in Tables 4.2 (after the manufacturer). The manufacturer test certificate stated that the three alloys are free from harmful intermetallic phases and precipitates.

Element Weight %	Ferrallium 255	SAF 2507	Zeron 100
Fe	Bal	Bal	Bal
Cr	24.5-26.5	25.7	25.3
Ni	5.5-6.5	6.9	7
Mo	3.1-3.8	3.4	3.6
Cu	1.5-2.0	0.3	0.6
N	0.2-0.25	0.27	0.23
C	0.03 Max	0.02	0.016
Si	0.2-0.7	0.3	-
Mn	0.8-1.2	-	0.5
P	0.025 Max	0.02	0.02
S	0.005 Max	0.0006	0.0005

Table 4.1: Chemical composition of test materials super DSS (Ferrallium 255, SAF 2507 and Zeron 100) investigated (after manufacturer's test certificate)

Material	Ultimate Tensile Strength (N/mm ²)	0.2% Proof Stress (N/mm ²)	Hardness (HBN)	Elongation (%)
Ferralium 255	793	607	247	35
SAF 2507	800-827	550-590	266-286	25-44
Zeron 100	800-827	550-551	257-286	25-37

Table 4.2: The mechanical properties of test materials super DSS (Ferralium 255, SAF 2507 and Zeron 100) investigated (after manufacturer's test certificate)

4.2 Specimen Preparation

The specimens were cut and mounted using epoxy resin to give better and easier handling for polishing and grinding, as shown in Figure 4.1. Two sections were cut to reveal the transverse and the longitudinal microstructure of duplex stainless steel specimens after etching. The specimen cross-section that was to be observed was ground and polished using a series of abrasive papers with successively finer grit sizes. The well-prepared cross-section specimen had a smooth mirror-like finish (1 μm) suitable for microscopic observation. Specimens were washed by isopropyl alcohol (IPA) to remove any grit or loose particles from the surface.

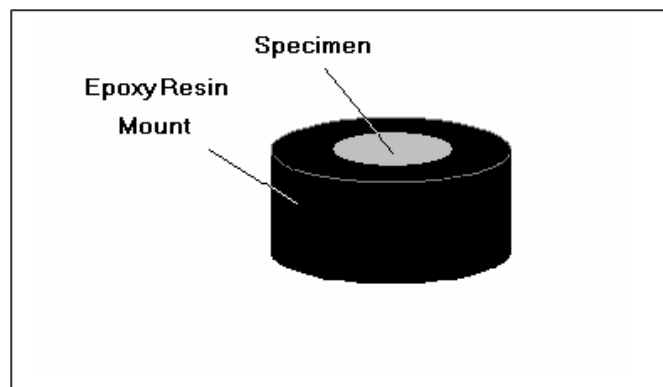


Figure 4.1: Specimen mounted in epoxy resin

4.3 Etching

Etching was used to reveal the microstructure of the super DSSs through selective chemical attack. These alloys contain several phases, and etching creates contrast between different regions through differences in topography or the reflectivity of the different phases. The specimens were electrochemically etched with 10M sodium hydroxide (NaOH) for approximately 10 seconds at a voltage of 5 V DC and rinsed thoroughly in water and then washed with acetone, followed by air drying. This etchant reveals inter-metallic phases, in addition to the ferrite and austenite phases. Optical examination was carried out using a Nikon optical metallurgical microscope. In all the cases, the austenite (γ) is shown as light grains in a dark matrix of ferrite (α).

4.4 Metallography

This technique was used to observe and verify the detailed features of the three duplex stainless steel alloys. The optical microscopic images were used to analyse the proportion of the two phases in the alloys by image analysis software that can distinguish the differences between the dark region (ferrite) and the bright region (austenite). The percentage volume of each phase was estimated for each material 5 times, based on the measured area of each phase. Fractured tensile specimens were also sectioned and viewed under the optical microscopy.

4.5 SEM

Detailed microstructural evaluation can be conducted by using Scanning Electron Microscopy (SEM) on metallographically prepared samples. A higher magnification of the microstructure can also be observed by using SEM. Furthermore, it is easier to identify the type of intermetallic phases present using SEM with regard to location and shape. Determination of the chemical composition of the phases can also be analysed for the identification of the intermetallic phase type on the specimens.

4.6 Hardness

Hardness is a measure of the ability of a material to resist indentation. It is a common non-destructive test that can be performed to evaluate the local hardness of the material and to give an indication of its expected tensile strength. Hardness tests are based on measuring the size of an indentation formed by a hard indenter under load. Hardness number can be consulted by a table of pre-calculated values. One of the standard methods for measuring the hardness of metals is the Vickers hardness test. The surface is subjected to a standard load for a standard length of time by means of a pyramid-shaped diamond. The diagonals of the resulting indentation are measured under a microscope and was converted to Vickers hardness (HV) using an index table for the applied load.

4.7 Electrochemical Measurements

Electrochemical methods have become more and more attractive for the study of corrosion phenomena because they can probe the mechanism of the corrosion process. Not only do electrochemical techniques offer a way to accelerate the corrosion process, but also they can be used to measure corrosion rates without removing the specimen from the environment or even significantly disturbing it. Most forms of metallic corrosion, including uniform, localized, galvanic, stress corrosion, and hydrogen-induced failure can be investigated through electrochemical approaches. In addition, electrochemical techniques have been applied to high-temperature and high-pressure aqueous applications. In this work, conventional potentiodynamic and potentiostatic techniques were employed to evaluate the pitting corrosion behaviour of the Ferralium 255, SAF 2507 and Zeron 100 in the 3.5 %(wt) NaCl solution. The experiments were carried out under atmospheric conditions (i. e., the cell was not deaerated) at room temperature.

4.7.1 Polarization Behaviour

Potentiodynamic measurements show the behaviour of the specimen over a range of potentials by providing information on the characteristics of the passive film on the super duplex stainless steels. It can assess the passivating behaviour by evaluating the pitting potential of the ferrite and the austenite phases in the duplex materials. In this case, the potential is swept at a fixed sweep rate, while the resulting current is measured continuously. The sweep was started at cathodic potentials (i.e., negative to the open-circuit potential) and increased until a preset limit was reached. The sweep rate is an important parameter in potentiodynamic polarization measurements, because it influences the resulting current, especially in the passive region.

4.7.2 Potentiostatic Measurement

On the other hand, potentiostatic experiments were used for assessing the pitting corrosion behaviour of the specimen at a given potential. In this type of measurement, a potential is applied to the specimen and scanned at a controlled rate, while the resulting current is measured and recorded. The instrument controls the electrical potential between the working electrode and reference electrodes of the three electrode cell at a value which is chosen to be around the pitting potential for each phase of the super duplex stainless steel. It forces whatever current is necessary to flow between the working and counter electrodes to keep the desired potential. The start potential of -300 mV and scan rates of 10 mV/min and 1 mV/min were used in a positive direction to the transpassive region and the plot of the log current density and time were recorded. The effect of applied potential on the corrosion of each phase in the microstructure of these tests was investigated by the SEM analysis.

4.7.3 Electrochemical Cell

The electrochemical cell used in this work represented a standard three-electrode configuration, with a platinum (Pt) electrode, saturated calomel electrode (SCE) as a reference electrode (RE) and the working electrode (WE).

The cylindrical working electrode, Ferralium 255, SAF 2507 and Zeron 100 was placed in an ordinary three electrode glass cell. The base of the polished cylindrical specimen, with an exposed surface area of 11.82 cm², was immersed in the 3.5 % (wt) NaCl solution while the rest of the specimen surface was freshly coated with Lacomit and held above the solution surface level. The test was started after placing the specimen in the cell. Crevice corrosion can be difficult to control in stainless steel specimens but it is believed that this approach was successful in avoiding it. This was supported by the appearance of polarisation scans described in a later section (pages 83 and 84). The cell contained 800 ml of 3.5% (wt) NaCl solution. Potentiodynamic measurement tests were conducted from the free corrosion potentials up to 1300 mV (SCE) and above. Potentiostatic tests were performed on the specimens for 2 weeks and then removed for SEM analysis. All experiments were performed at room temperature and all potentials are referred to the saturated calomel electrode (SCE). A typical set up for the computer controlled potentiodynamic test is shown in Figure 4.2 while for the potentiostatic is shown in Figure 4.3.

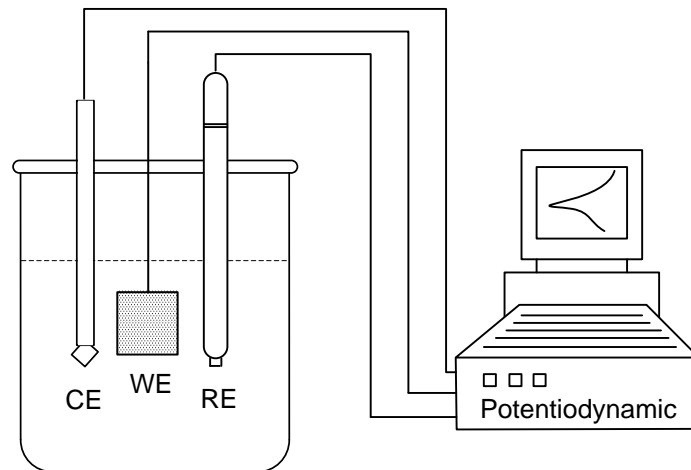


Figure 4.2: A typical set up for potentiodynamic measurements

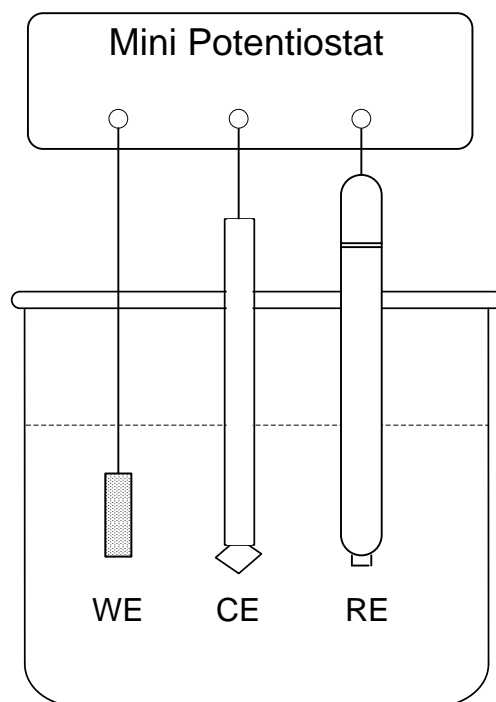


Figure 4.3: Detail of the cell arrangements showing the ministat used potentiostatic test

4.8 Scan Rate

The scan or sweep rate refers to the rate with which the potential is changed while the potentiodynamic scan is being performed (typically expressed in mV/s). The sweep rate is an important parameter in potentiodynamic polarization measurements, because it influences the resulting current. Slower sweep rates yield typically give lower current values at all potentials of the polarization curve, especially in the passive region ¹¹⁵.

The speed of the scan will largely influence the type of information obtained. In general, higher scan rates do not allow sufficient time for the system to stabilize at each potential. As a result, parameters such as the location and size of the active to the passive transition, the passivation potential, and the pitting potential are often shifted to more positive values. In this work, potentiodynamic measurements were carried out with a sweep rate of 0.1667 mV/s (10 mV/min), which is the ASTM standard scan rate.

A Few more tests were performed with a lower scan rate (1 mV/min) to reveal some of the characteristics of both phases in super duplex stainless steels. This scan rate could show the pitting potentials clearly for the two phases.

4.9 Hydrogen Precharging Cell

The gauge length of the specimens of super duplex stainless steels Ferralium 255, SAF 2507 and Zeron 100 were cleaned using IPA (Iso-propanol) solution just before starting any test to ensure that the surface would not be contaminated from the machining process which could affect the hydrogen uptake. Each tensile specimen was potentiostatically precharged in a small cell at range of potentials for two and four weeks periods in 3.5 % (wt) NaCl solution allowing the hydrogen to diffuse into the specimens as shown in figure 4.4. A platinum electrode was used as an anode and the specimen of super DSS was used as a cathode. The reduction reaction of hydrogen ions in the solution, $2\text{H}^+ + 2\text{e} \rightarrow \text{H}_2$, happened over the surface of the specimen. A proportion of the hydrogen escaped into the atmosphere, and part of it diffused into the specimen in atomic form. One test specimen was pre-charged at a time in a separate cell. The cathodic potentials were varied from -800 mV to -1250 mV against SCE. Temperature of the precharging cell was maintained using a thermostatically controlled heater at a temperature of 50° C. After the precharging, the specimen was moved immediately to a separate environmental cell applying the same potential and temperature for SSRT. On the SSR environment cell test, the temperature was controlled using a heating tape at a temperature of 50° C in a 3.5% NaCl solution.

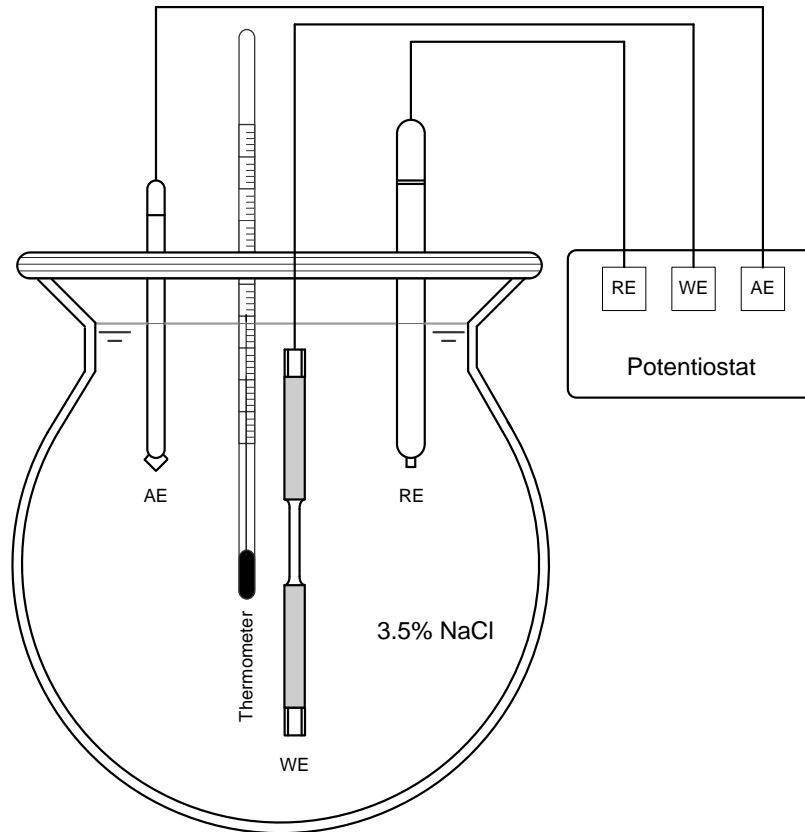


Figure 4.4: Precharging cell to promote hydrogen uptake of SSRT specimens

4.10 Environmental Corrosion Cell

The environmental cell was designed to be fitted within the SRRT machine spaces. The main consideration of this design was to allow the specimen to be installed into the cell containing the environmental electrolyte solution. The cell arrangement allows the gauge length to be sealed and exposed to the aggressive condition throughout the SSRT. The environmental cell was made of glass and perspex which was constructed by a specialist glassware manufacturer; the detailed dimensions are shown in figure 4.5 and 4.6. The top and bottom portions were made out of perspex while the middle portion was made out of glass for better heat transfer. The cell contained an electrolyte of approximately 400 cm³ of 3.5 % NaCl. As a precaution, the environmental cell was kept under a hood fitted with an extractor fan during the slow strain rate testing to remove any gases generated on the specimen or auxiliary electrode.

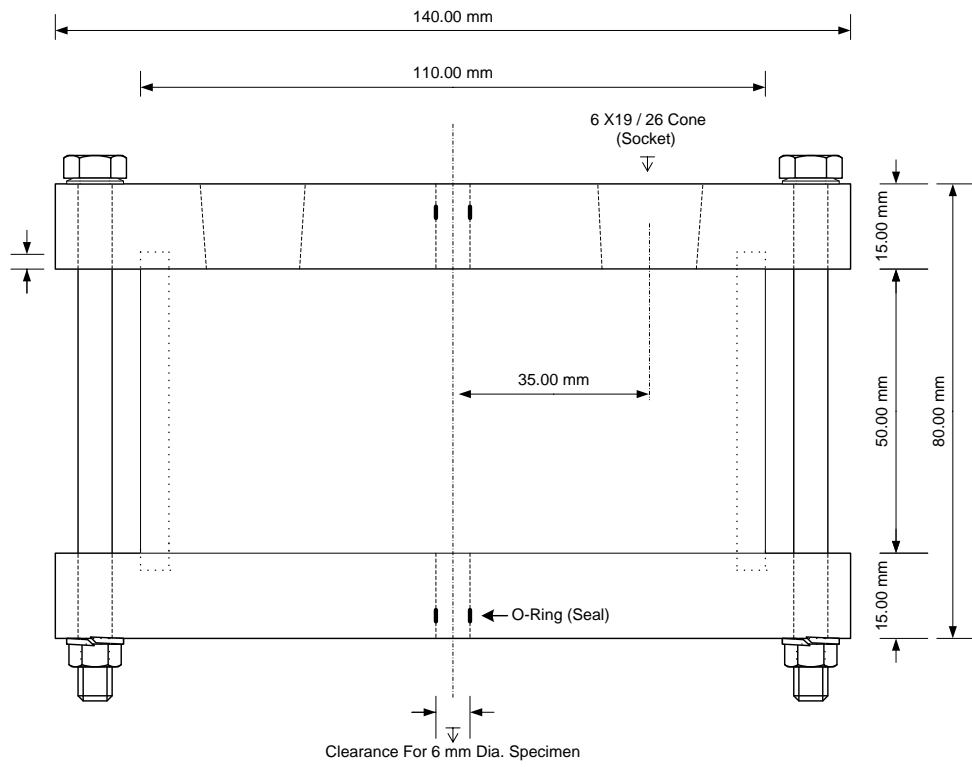


Figure 4.5: Glass-Perspex environmental cell for SSRT

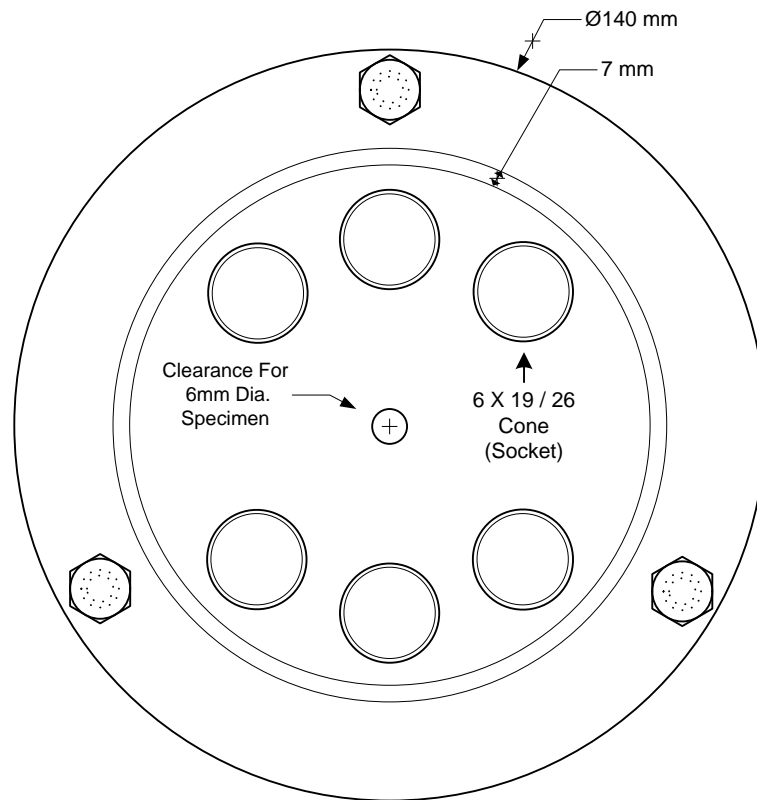


Figure 4.6: Glass-Perspex environmental cell for SSRT

The set up of the environmental cell with specimen and electrodes for SSR testing is shown in figure 4.7.

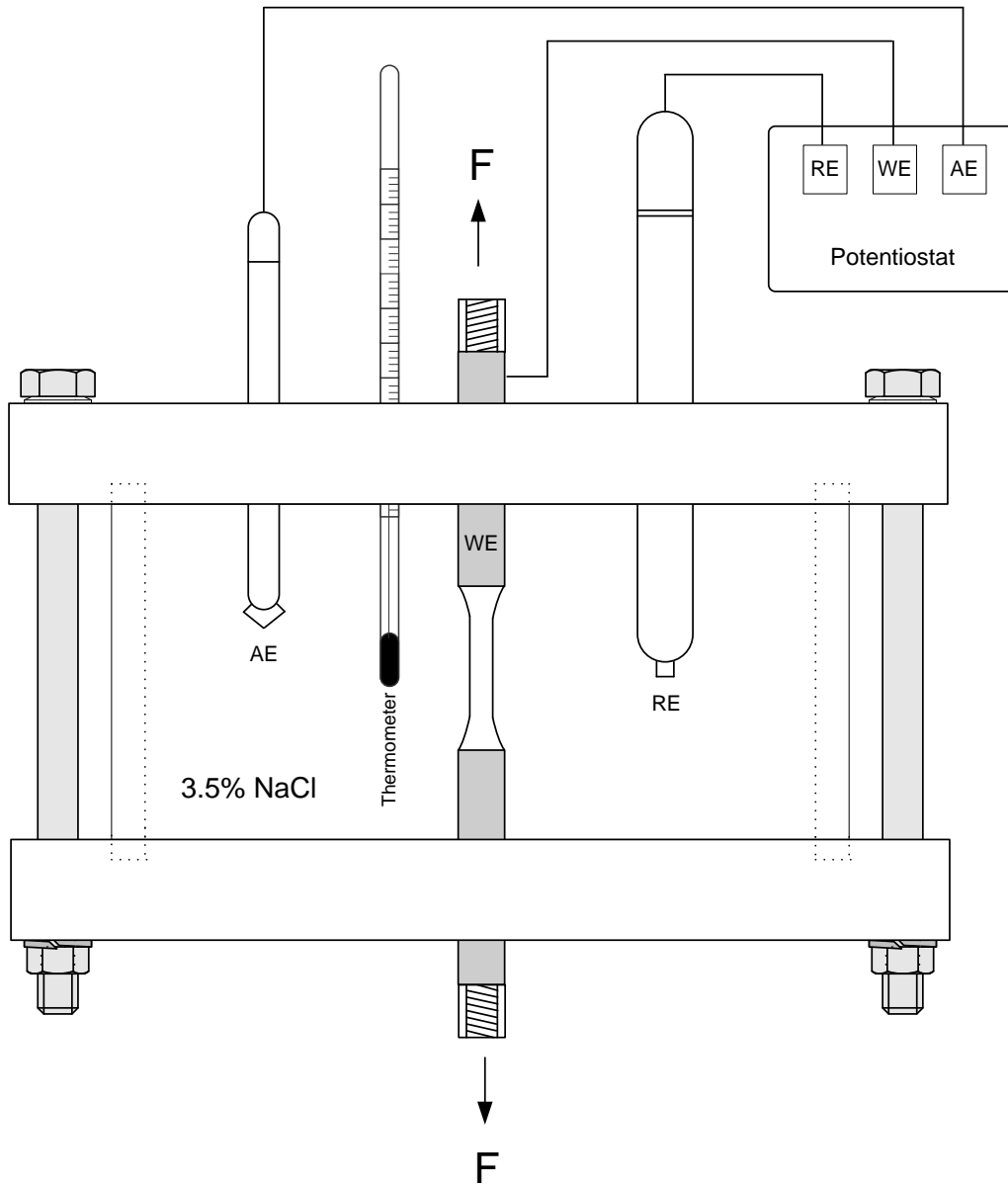


Figure 4.7: Experimental set – up for slow strain rate testing (SSRT) in a Glass-Perspex environmental cell

4.11 Slow Strain Rate Testing

The slow strain rate test (SSRT) has been used extensively over the last three decades to closely examine the effect of stress corrosion cracking and hydrogen embrittlement of high strength steels as compared to unaffected samples of the same steels with the same metallurgical characteristics. It can be used as a quick comparative technique based on time to failure alone but it is more useful as a quantitative measure of the extent of hydrogen embrittlement. A standard tensile specimen design was machined and threaded at the end from a 22 mm bar in order to test super duplex stainless steels Ferralium 255, SAF 2507 and Zeron 100 in a tensile test. These specimens were produced using a computer numerically controlled (CNC) lathe for maximum accuracy. The gauge length of the tensile specimen was ground using 1200 grit silicon carbide paper and washed in distilled water prior to test. The shape and dimensions of the specimen that was used in this work is presented in Figure 4.8. The specimen was a bar with reduced section, where the gauge length was 25 mm long and 3 mm in diameter with M6 thread at the ends.

The diameter of the gauge length was measured prior to SSRT testing at three different points along the gauge length (end 1, centre, end 2) of the specimens. It was observed that the diameter at one end was slightly greater than the diameter at the centre and the other end as shown in table 5.3 for one of the specimens that was measured. These measurements indicated a maximum tolerance of ± 0.006 mm for all of the specimens that were measured.

Material	Mean Gauge Length Diameter (mm)		
	End 1	Centre	End 2
Ferralium 255	3.049	3.049	3.044
SAF 2507	3.012	3.01	3.012
Zeron 100	3.022	3.022	3.023

Table 4.3: Average Diameters of the gauge length sections for a random specimen

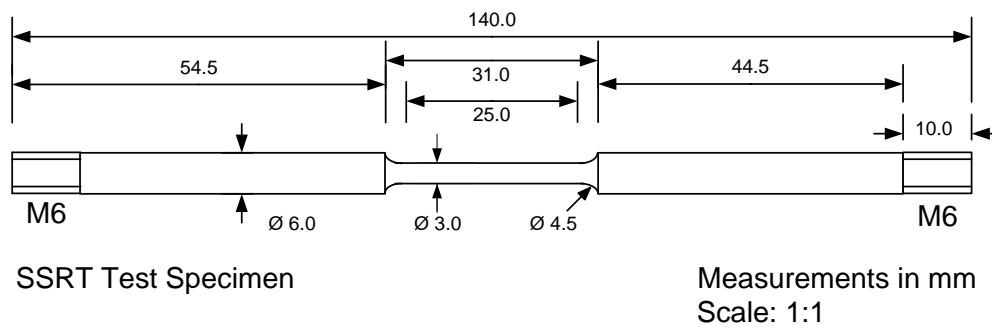


Figure 4.8: Dimensions of slow strain rate testing specimen

The crosshead velocity of the test machine and the strain rate of the specimens were measured over a period of several hours by using the following equations:

- $$v = \frac{\Delta l}{t}$$

where,

Δl = the distance travelled by the crosshead (mm)

v = the crosshead velocity (mm/sec)

t = time (sec)

- $$\dot{\varepsilon} = \frac{v}{l_o}$$

where,

$\dot{\varepsilon}$ = the strain rate (sec^{-1})

v = the crosshead velocity (mm/sec)

l_o = initial or original gauge length section (mm)

A strain rate of $1 \times 10^{-6} \text{ sec}^{-1}$ was established for testing.

4.12 Hydrogen Diffusion Measurements

The transport of hydrogen in steel occurs by the process of diffusion, i.e the migration of atoms through the lattice. The driving force for this movement is a concentration gradient and hydrogen will diffuse from a region of high activity to a region of low activity. Two electrochemical techniques were used to analyse the transfer of hydrogen through steel membranes.

4.12.1 Potentiostatic Hydrogen Charging

Devanathan and Stachurski¹¹⁸ described a simple double cell arrangement by which hydrogen can enter and permeate a metal. A thin membrane electrode, made of test steel, was the material isolating the two different electrochemical cells. One surface of this membrane act as the cathode in charging cell, and the other surface act as the anode in the opposite cell where current can be measured. Schematic of permeation cell can be shown in figure 4.9. This test was concerned with determination of diffusion parameters for the hydrogen movement into steel membrane which determine the extent of hydrogen embrittlement resulting from cathodic protection. In this technique the potential between specimen and the reference electrode was controlled by a potentiostat while the dependent variable current was measured as a function of time. The charging side of the cell was held at a potential of -1200 mV (SCE) to promote the generation and uptake of the hydrogen on the surface of the specimens. Consequently, the hydrogen diffused through the membrane and was oxidised and detected on the depletion side which was held at a potential of - 94 mV (SCE) [+150 mV (NHE)] which is sufficient to oxidise hydrogen ($H_2 \rightarrow 2H^+ + 2e$), without producing too high background current. The electrolyte used in both sides of the cell was 0.2M NaOH solution.

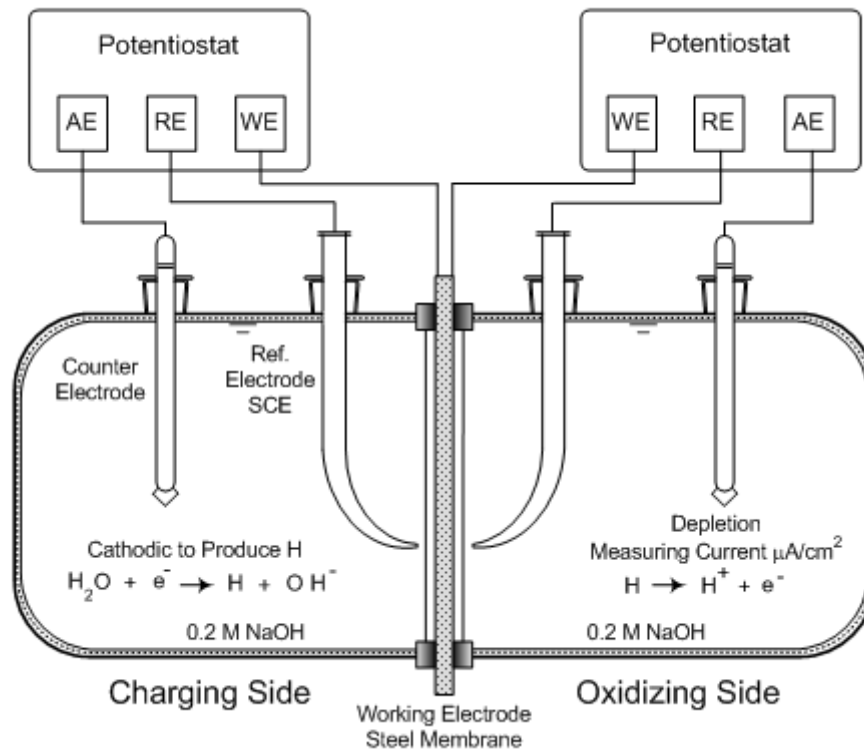


Figure 4.9: Modified Devanathan and Stachurski¹¹⁸ permeation cell

4.12.1.1 Steel Membranes

The permeation experiments were conducted to determine the diffusion coefficient based on two equations (as described in the literature review) at room temperature for cold-rolled carbon steel and at 50° C for super duplex stainless steels. The cold-rolled carbon steel shim with a thickness of 50 μm contain 0.04 % carbon [C], 0.24% manganese [Mn], 0.012% sulphur [S], < 0.01% chromium [Cr], 0.02% nickel [Ni], and 0.04% copper [Cu] in wt% with a microstructure of ferrite and pearlite. The membranes of the super duplex stainless steels were cut to a thickness of 1.2 mm using a wire cut technique and then grounded to a final thickness of 1mm. The surfaces of both sides of the cell were polished to 1μm then washed by isopropyl alcohol (IPA solution) and rinsed with distilled water followed by air drying. An electrical connection was spot welded to the membrane's edge (WE) for an electrical contact. The reference electrode was effectively positioned 8 mm away from the working

electrode by using a Lugin capillary tube, while the counter (platinum) electrode was 80 mm away from the working electrode. The effective area used in these tests was 63 cm², as shown in figure 4.10.

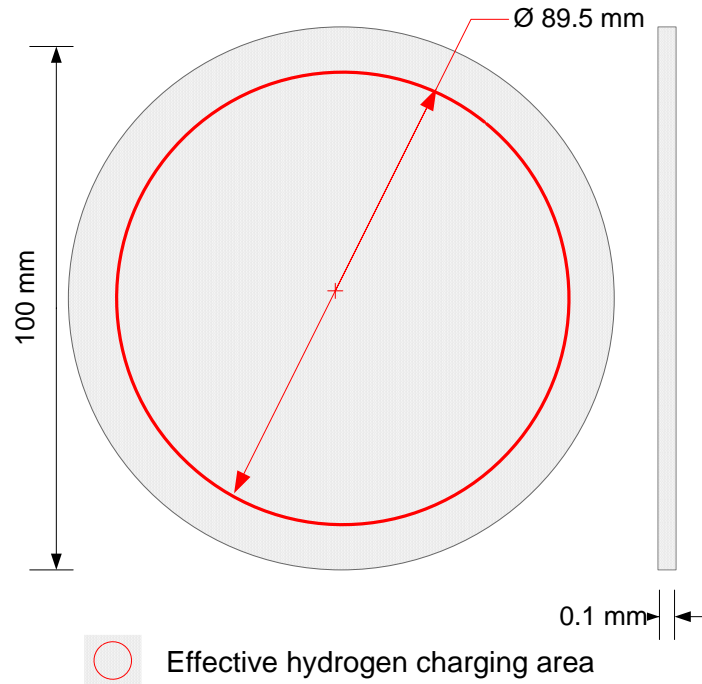


Figure 4.10: Effective area of the membrane for the hydrogen permeation cell

4.12.2 Galvanostatic Hydrogen Charging

The galvanostatic technique has been used in many studies to measure the hydrogen diffusion coefficient (D)^{119 - 121}. This electrochemical method can be used by applying a small constant current passed through the cell for a time interval t . The voltage is monitored as a function of time during this current flow. The increasing voltage provides a direct measure of the activity of the diffusing hydrogen. Thus, a constant flux of diffusing hydrogen is maintained at the electrode/electrolyte interface, $x=0$. The boundary conditions for a charged specimen from both sides with a thickness $2L$ are:

$$C = C_0 \quad 0 \leq x \leq L, \quad t = 0$$

$$-D \frac{dC}{dx} = \frac{I}{zFS} \quad x = 0, \quad t > 0$$

$$\frac{dC}{dx} = 0 \quad x = L, \quad t \geq 0$$

Where:

C = molar hydrogen concentration

t = diffusion time

D = hydrogen diffusion coefficient

x = distance from the metal surface

I = charging current

S = specimen area

z = charge number of the ion reduced in the electrolyte (ie H^+)

F = Faraday's constant

The hydrogen diffusion coefficient of the specimen can be determined by solving the second Fick's law with the appropriate boundary conditions.

$$\frac{\partial C}{\partial t} = \frac{\partial}{\partial x} \left(D \frac{\partial C}{\partial x} \right)$$

The concentration of the hydrogen at the interface can be approximated by the measured cell potential for the very short time ($t \ll L^2/D$). In this case the difference of the potential, E , can be linearly related to $t^{1/2}$, as shown in equation (6). The gradient $dE/dt^{1/2}$ can be obtained from the gradient of the graph of E vs $t^{1/2}$.

The amount of the hydrogen at the electrode/electrolyte interface can be constant when assuming a steady state is reached

$$\frac{dE}{dt^{1/2}} = \frac{2 I Vm}{z F S (\pi D)^{1/2}} \left(\frac{dE}{d\delta} \right) \quad \text{if } t \ll \frac{L^2}{D}$$

Where

Vm = The molar volume of the steel sample

$dE/d\delta$ = The change in cell voltage with change in hydrogen concentration

At longer times, ($t > L^2/D$), the surface hydrogen concentration is approximated by the first two terms of the infinite trigonometric series and dE/dt is linearly related to the diffusion time, as given in the following equation:

$$\left(\frac{dE}{dt} \right) = \frac{I Vm}{F S L} \left(\frac{dE}{d\delta} \right) \quad \text{if } t > \frac{L^2}{D}$$

Combining the two equations above can eliminate $dE/d\delta$ and the diffusion coefficient can be calculated from the gradients $dE/dt^{1/2}$ and dE/dt at short and long times, respectively.

$$D = \left(\frac{2L \frac{dE}{dt}}{\pi^{1/2} \frac{dE}{dt^{1/2}}} \right)^2$$

The galvanostatic method was also used to determine the diffusion coefficients of the super duplex stainless steel alloys. Hydrogen uptake by thin membranes was charged by a galvanostatic technique in electrolyte of 0.2 M NaOH with 1g/l of thiourea to act as a hydrogen recombination poison. The current between the specimen and the counter (auxiliary) electrodes was held constant while the potential between the specimen and the reference electrode was measured as a function of time. Membranes of 100 mm in diameter were precisely wire cut to a thickness of 0.12 mm and then grounded to a final thickness of 0.1 mm to

perform this test. The hydrogen effective charging area of the two opposite faces of the specimen was measured to be 18 cm^2 in this test. The galvanostatic hydrogen charging cell was submerged in a water bath that was thermostatically controlled at a temperature of 50° C . A charging current density of 1 mA/cm^2 was applied to promote hydrogen evolution and uptake on the two sides of the specimen. A plot of the measured electrode potential and time at the desired temperature were performed and analysed to determine the diffusion coefficient of hydrogen. Figure 4.11 shows a schematic illustration of the electrochemical cell used for the technique.

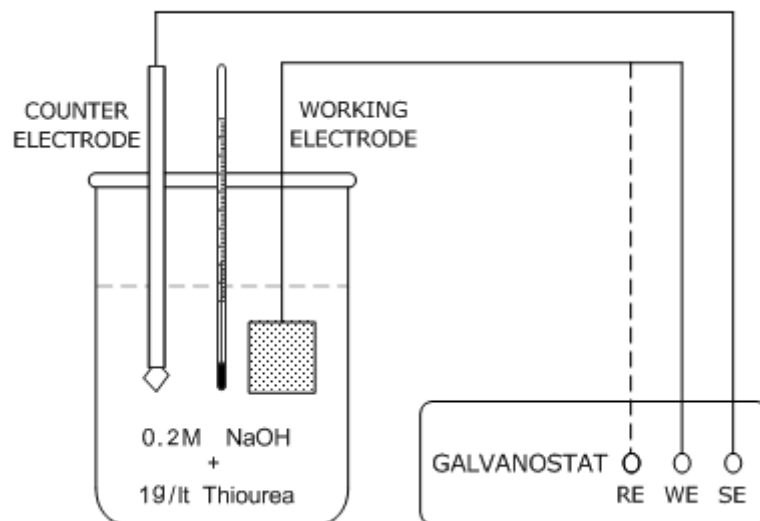


Figure 4.11 Galvanostatic Hydrogen charging cell

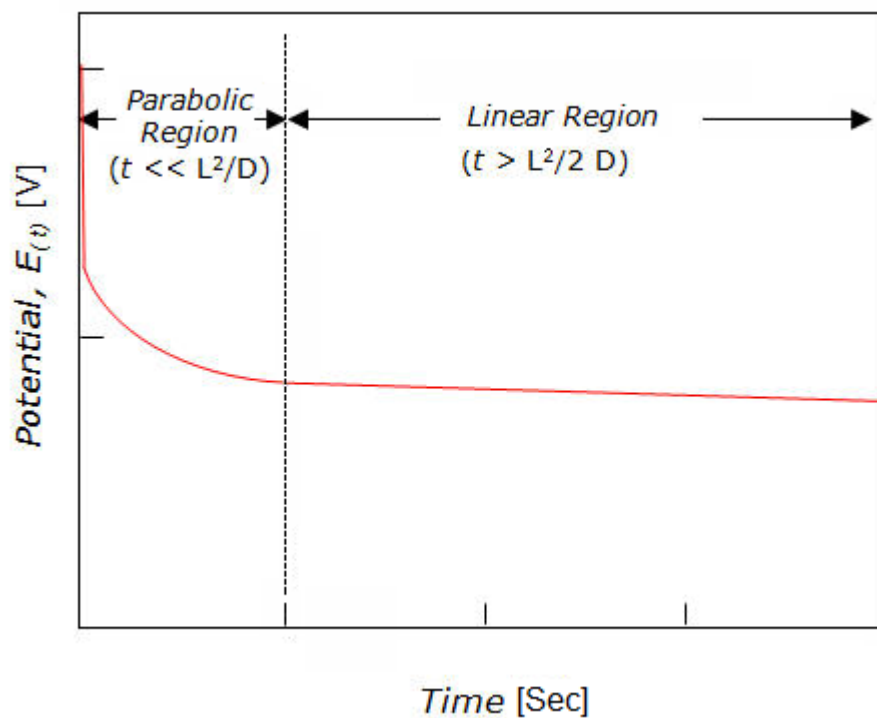


Figure 4.12: Typical potential as a function of time trend from galvanostatic charging method ¹¹⁹

A typical galvanostatic method result showing the potential as a function of time trend is shown in figure 4.12 where the *short time* and *long time* segments are described.

5 Results and Discussion

5.1 Characterizing SDSS

Metallographic images of super duplex stainless steels, FERRALIUM 255, SAF 2507, and Zeron 100, are shown in the following sections.

5.2 Optical Metallography

The micrograph of the etched specimen was observed under an Olympus Vanox-T metallographical microscope. The micrographs as shown in figures 5.1 to 5.6 reveal the microstructure of the super duplex stainless steels (Ferralium 255, SAF 2507, and Zeron 100) for the transverse and longitudinal sections respectively.

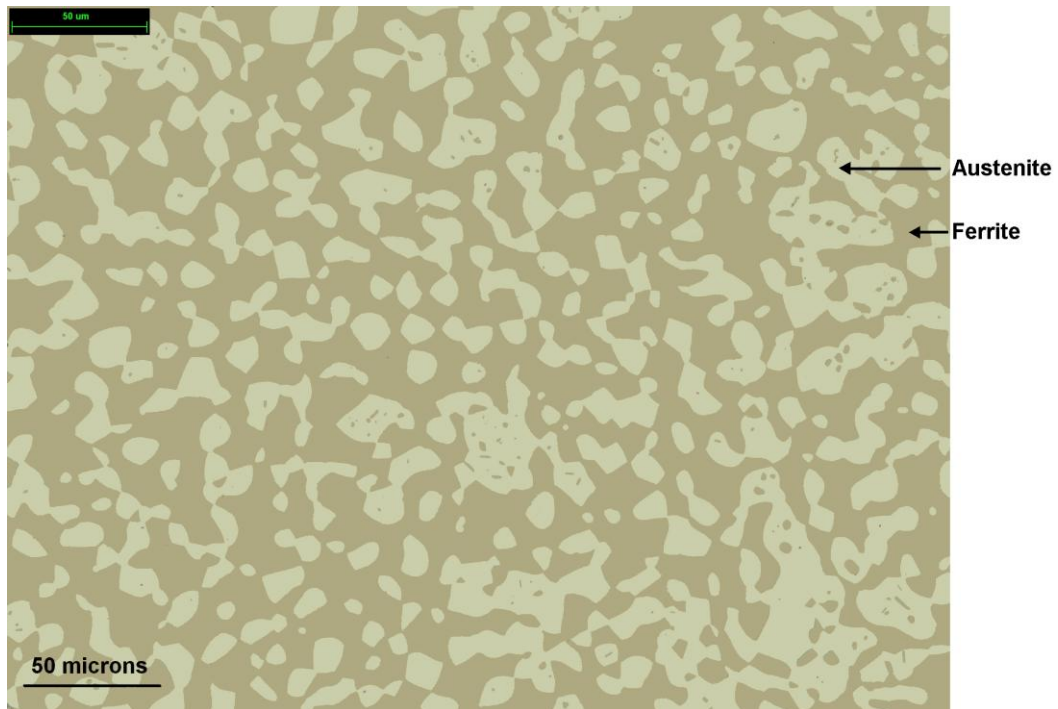


Figure 5.1 Optical micrograph of the transverse section of SDSS Ferralium 255 etched by 10M of NaOH solution



Figure 5.2: Optical micrograph of the longitudinal section of SDSS Ferralium 255 etched by 10M NaOH solution

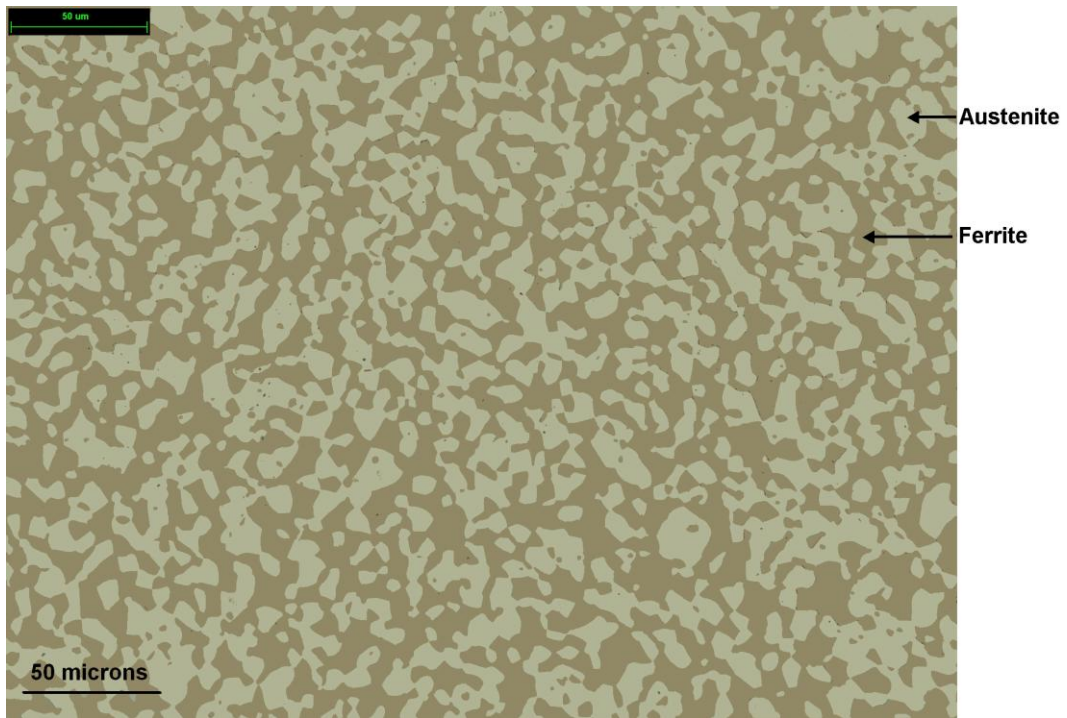


Figure 5.3: Optical micrograph of the transverse section of SDSS SAF 2507 etched by 10M of NaOH solution



Figure 5.4 Optical micrograph of the longitudinal section of SDSS SAF 2507 etched by 10M NaOH solution

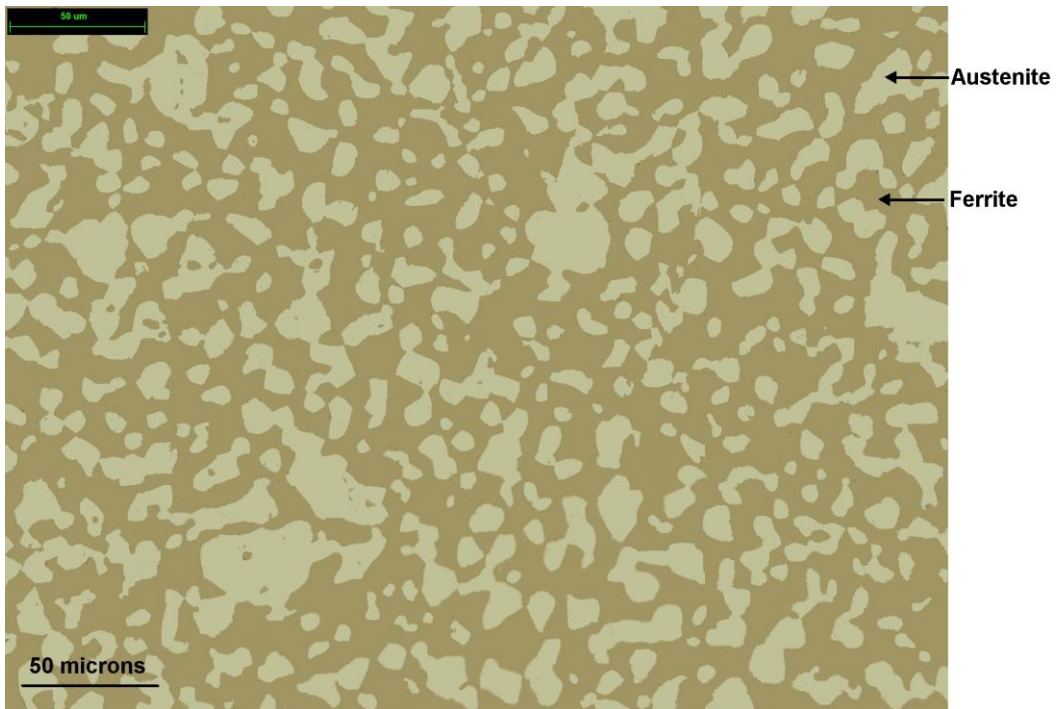


Figure 5.5: Optical micrograph of the transverse section of SDSS Zeron 100 etched by 10M of NaOH solution



Figure 5.6: Optical micrograph of the longitudinal section of SDSS Zeron 100 etched by 10M NaOH solution

The longitudinal sections show the extensive elongated light austenite phase while it is more rounded in the transverse section. It can be observed that the austenite phase (light area) is embedded in the semi-continuous ferrite matrix (dark area) banded due to rolling.

Duplex stainless steels solidify 100% ferrite above 1200 °C. The two phase microstructure is formed during slow cooling. Upon cooling from the melting temperature the ferrite starts to partially transform into austenite that nucleates and grows first at the grain boundaries of ferrite, following favorable crystallographic orientations inside of the grains. As the temperature lowers down to 700 °C, the ferrite content decreases as austenite increases (figure 5.7). Therefore the austenite appears with rounded shape within the ferrite matrix. The alloy composition and the annealing temperature can control the ratio of the austenite and ferrite phases. The desired phase balance in duplex stainless steel is around 50/50 (austenite/ferrite).

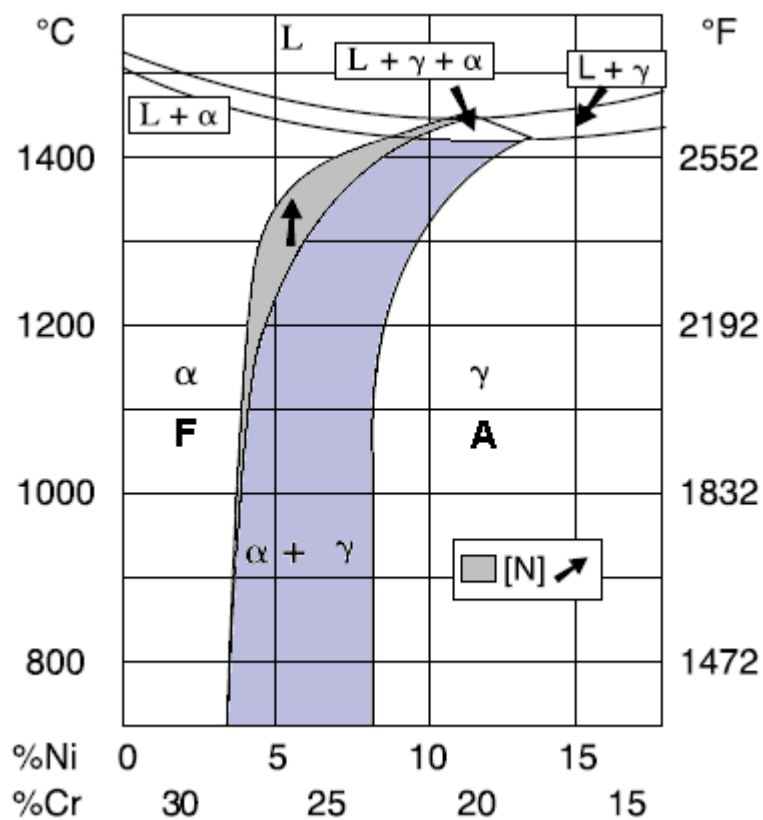


Figure 5.7: Phase forming of super duplex stainless steel ¹²²

The metallurgical structure of DSS can also be linked to its composition by means of Schaeffler diagram, which is shown in Figure 5.8. The figure exhibits a wide composition range in which the stainless steels exhibit a duplex structure and varying the concentration of different alloying elements in this range, a variety of commercial DSS grades can be obtained with different austenite and ferrite ratio. Alloying elements are grouped as austenite stabilizers such as Ni, N, C, and Cu) and ferrite stabilizers such Cr, Mo, and Si which are expressed in terms of chromium equivalence and nickel equivalence respectively and form the two axis of the Schaeffler diagram. The chromium and nickel equivalence formulas are as the following:

$$Ni_{eq} = Ni + 0.5 Mn + 0.3 Cu + 25 N + 30 C$$

$$Cr_{eq} = Cr + 1.5 Mo + 0.75 W$$

These elements can give rise to the dual microstructure of DSS with the correct proportions. The desired phase balance in duplex stainless steel is around 50/50 (austenite/ferrite) this requires approximately $Ni_{eq} = 0.5 Cr_{eq} - 2$. The formula for Nickel equivalent shows nitrogen is a strong austenite stabiliser

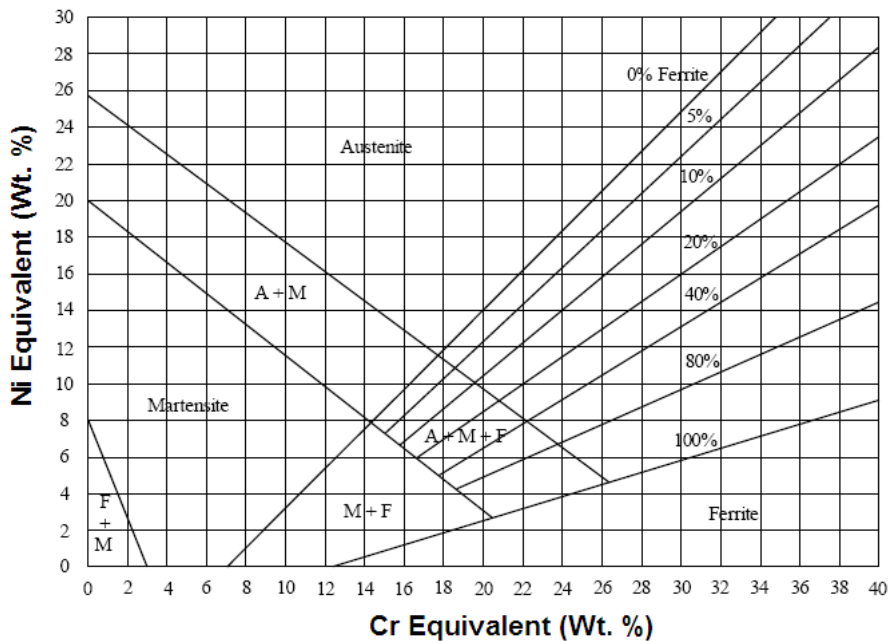


Figure 5.8: Schaeffler diagram showing composition range in which stainless steels exhibit a duplex structure

The Images of ferrite-austenite microstructure of super duplex stainless steels analyzed in order to determine relative content of ferrite and austenite ratio. Measurement like phase ratio, length and area of grains, can be calculated by phase selecting according to the colour on the optical image when using image analyser programme. Results of the phase (ferrite and austenite) ratio were calculated based on 50 point counts for the longitudinal and transverse sections are shown in table 5.1.

Material	Mean phase ratio of longitudinal and transverse sections	
	% Ferrite (Dark phase)	% Austenite (Light phase)
Ferralium 255	52	48
SAF 2507	51	49
Zeron 100	52	48

Table 5.1: Phase ratio (Ferrite and Austenite) of super DSSs

The results of the grain colonies size and the phase ratio were calculated using an image analysing programme called Image J developed by the National Institute of Health (USA). Grain size is one of the important microstructural properties, which controls mechanical properties like strength and fracture toughness. Measurements of the colonies grain size are shown in table 6.2. Super DSS SAF 2507 had the smallest mean area, length and standard deviation of the austenite grains than the three materials in the longitudinal and transverse sections. Note: colonies of austenite grains were found at boundaries of the elongated ferrite grains rather than single grains (see figure 5:10, for example). The boundaries of these austenite grains were not resolved by etching, giving the impression of elongated austenite grains and it is these features that were measured in the image analyser.

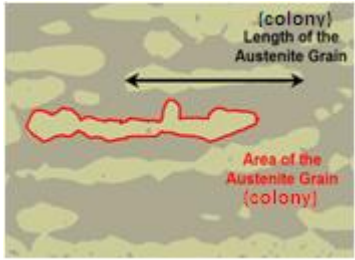
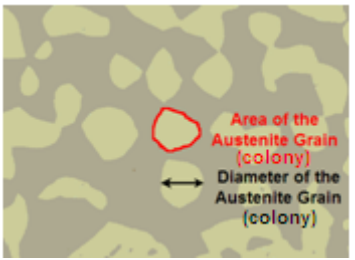
Material					
		Longitudinal section	Transverse Section	Area μm^2	Length μm
Ferralium 255	Mean	489.9	53.8	139.3	16.2
	SD	807.2	55.5	234.6	10.6
	Min	0.4	2	0.03	3
	Max	4123.5	235.5	1759.5	51.1
SAF 2507	Mean	305.6	39.1	99.4	20.5
	SD	635.1	64.2	121.5	10.7
	Min	1.7	1	0.1	2.5
	Max	3878.7	338.5	664.8	54.9
Zeron 100	Mean	469.1	46.5	100.5	12.5
	SD	1113.5	50.7	154	11.4
	Min	0.4	1	0.5	1
	Max	7491.7	223.3	940.4	68

Table 5.2: The area and length of the colonies of austenite grains of all three super DSS alloys

5.3 SEM

SEM composition analysis of the three alloys was used to confirm that the dark phase was ferrite and the light phase was austenite. The ferrite phase contained more Cr and Mo and less Ni than the austenite phase as shown in Figures 5.7 to 6.19. The results obtained from SEM composition analysis are in the range of the manufacturer chemical specification (see tables 6.1).

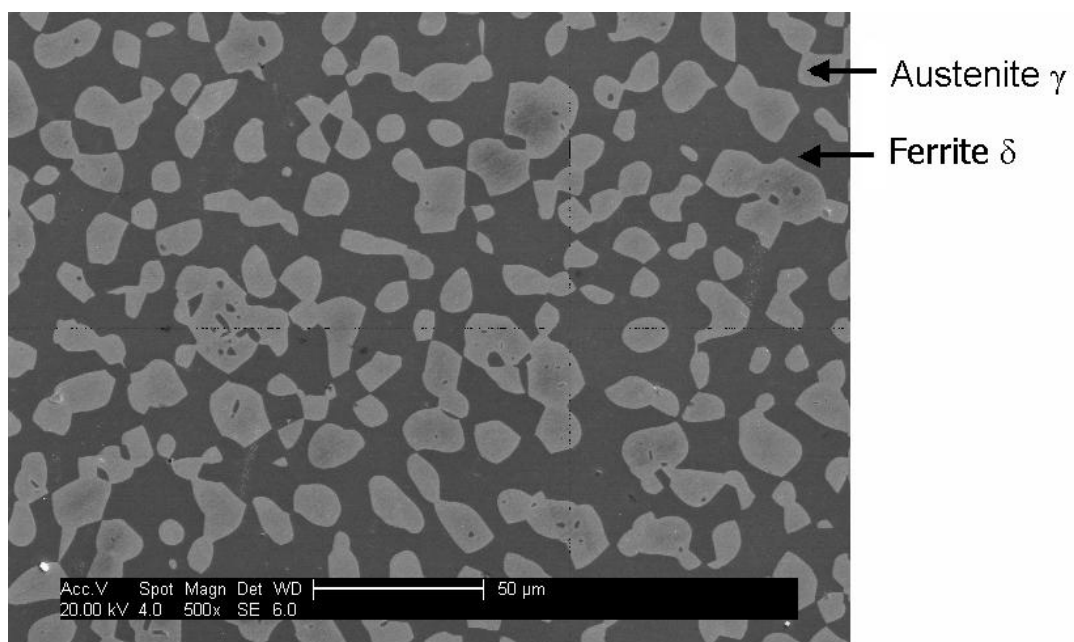


Figure 5.9 SEM image of the transverse section of DSS Ferralium 255 etched by 10M NaOH solution

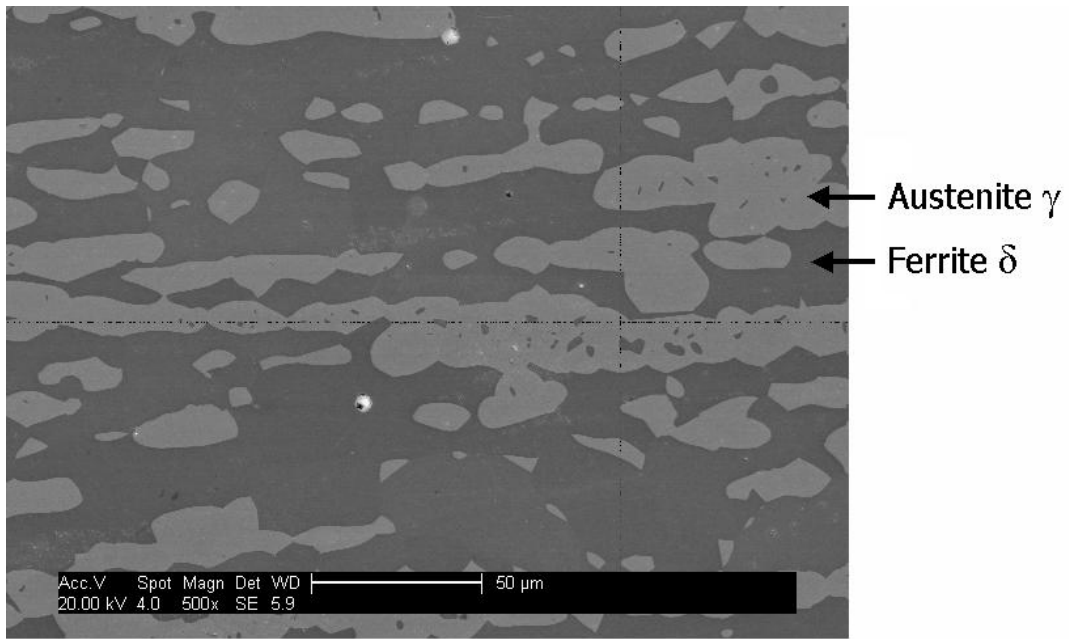


Figure 5.10 SEM image of the longitudinal section of DSS Ferralium 255 etched by 10M NaOH solution

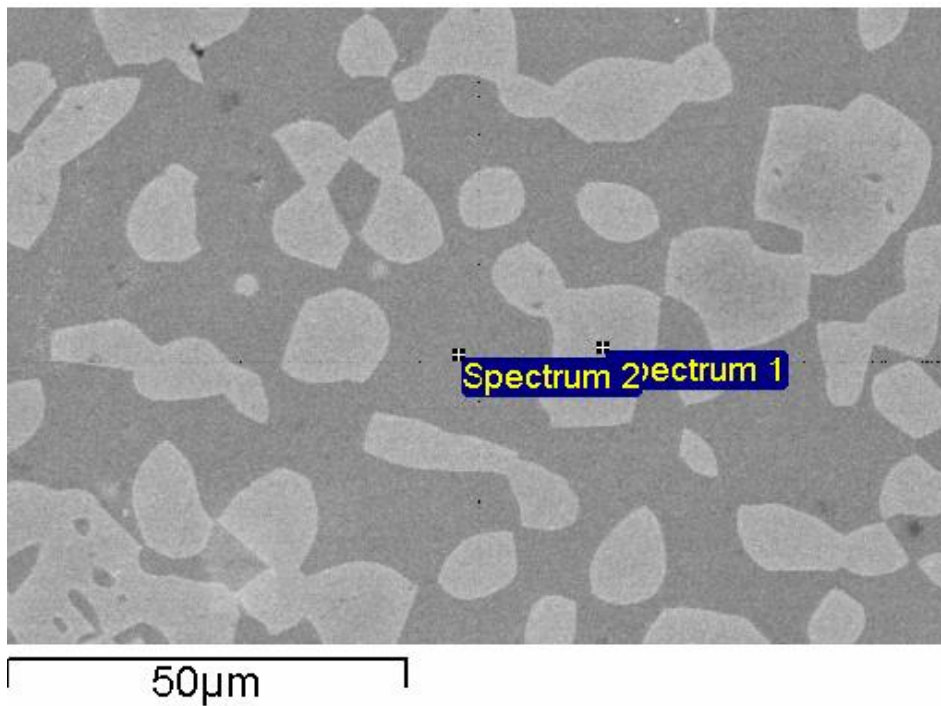


Figure 5.11 SEM Image for phase analysis Transverse Section of super DSS Ferralium 255 etched by 10M NaOH solution

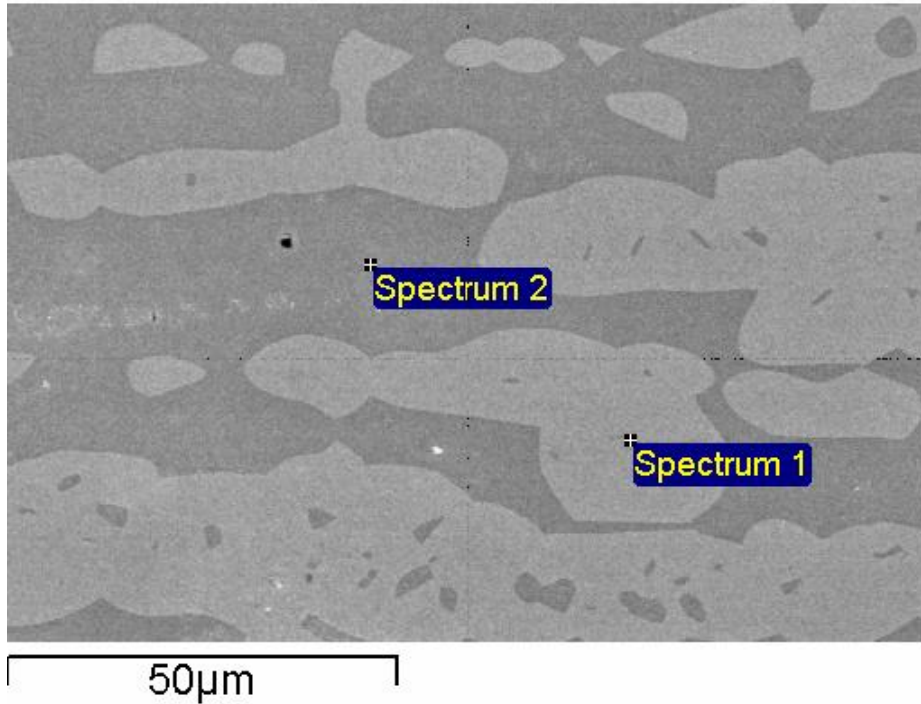


Figure 5.12 SEM Image for phase analysis Longitudinal Section of super DSS Ferralium 255 etched by 10M NaOH solution

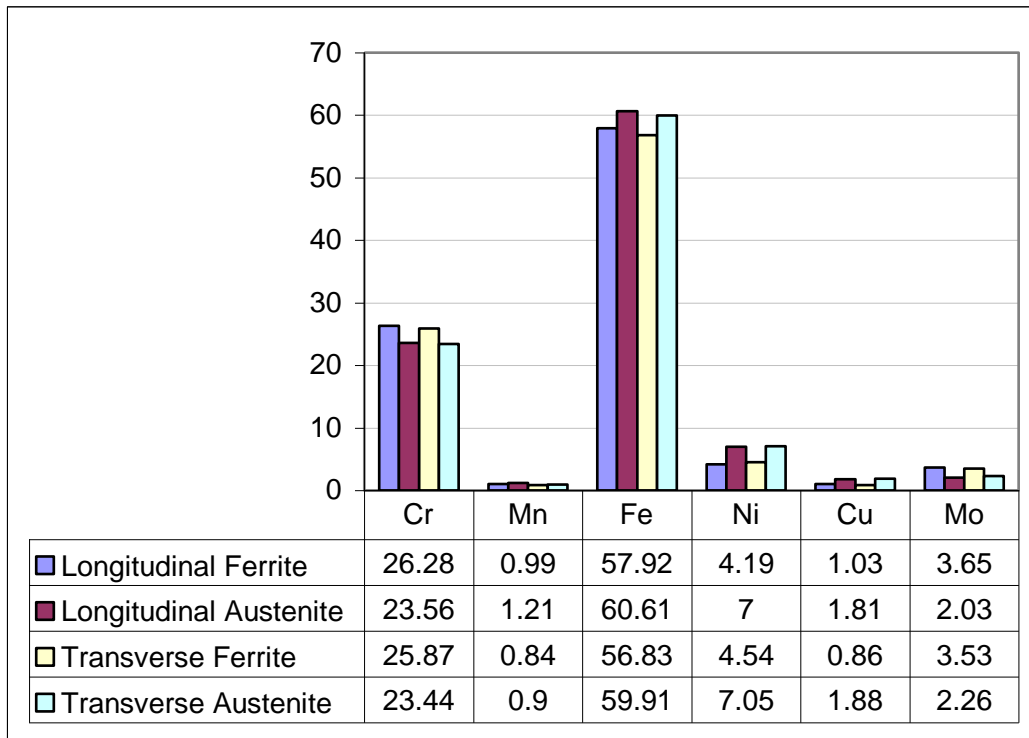


Figure 5.13: Analysis by SEM for the austenite and ferrite phase of the transverse and longitudinal sections for Ferralium 255 showing the range of composition for each phase

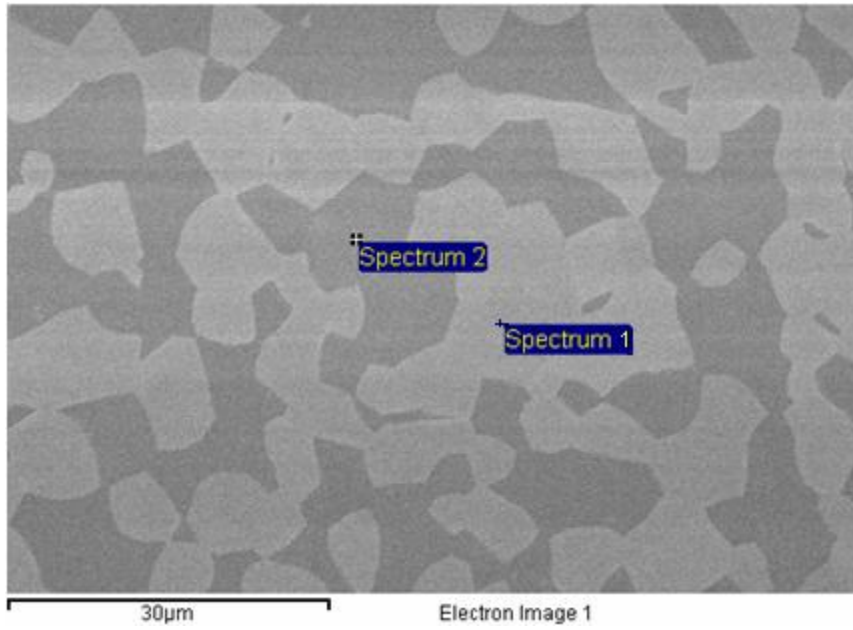


Figure 5.14 SEM image of the transverse section of DSS SAF 2507 etched by 10M NaOH solution

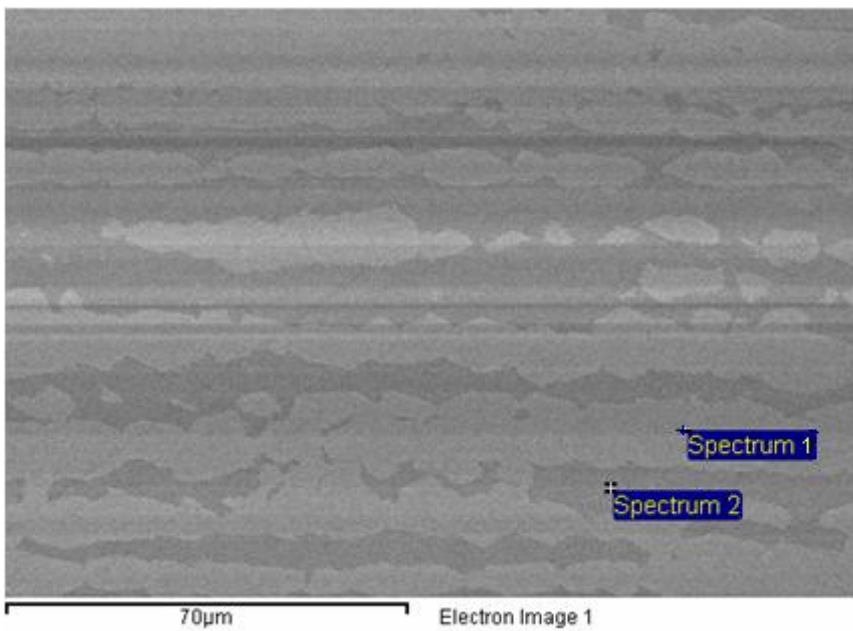


Figure 5.15 SEM image of the longitudinal section of DSS SAF2507 etched by 10M NaOH solution

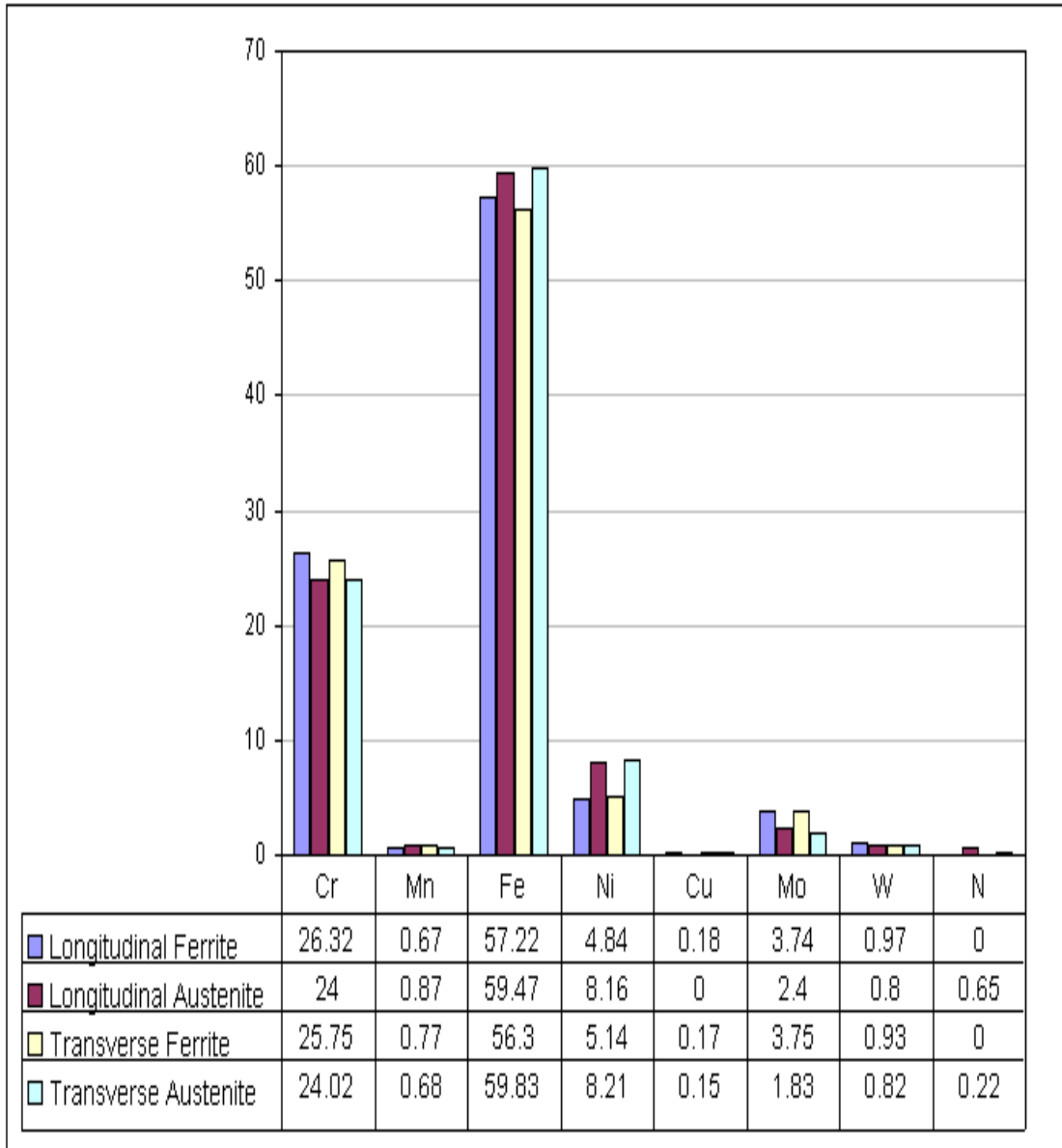


Figure 5.16: Analysis by SEM for the austenite and ferrite phase of the transverse and longitudinal sections for SAF 2507 showing the range of composition for each phase

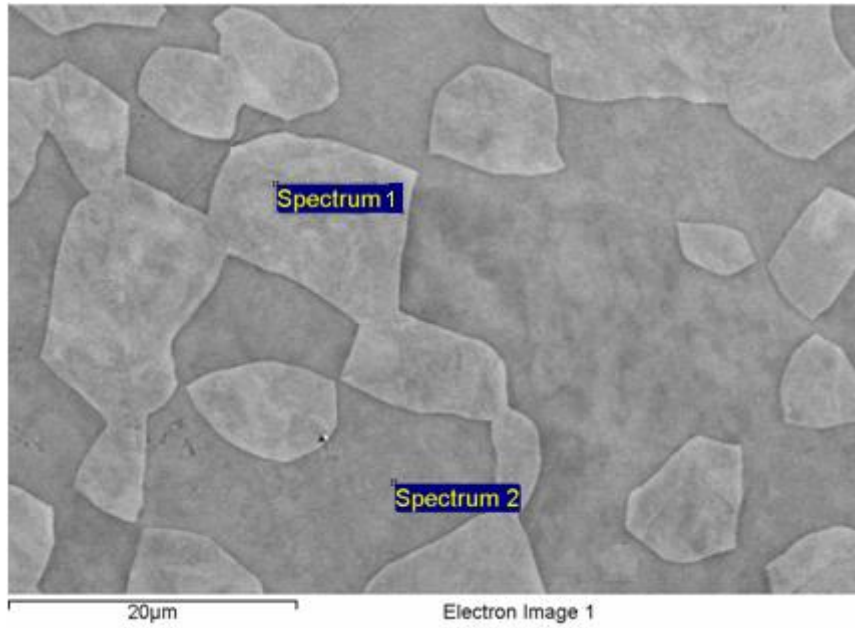


Figure 5.17 SEM image of the transverse section of super DSS SAF 2507 etched by 10M NaOH solution

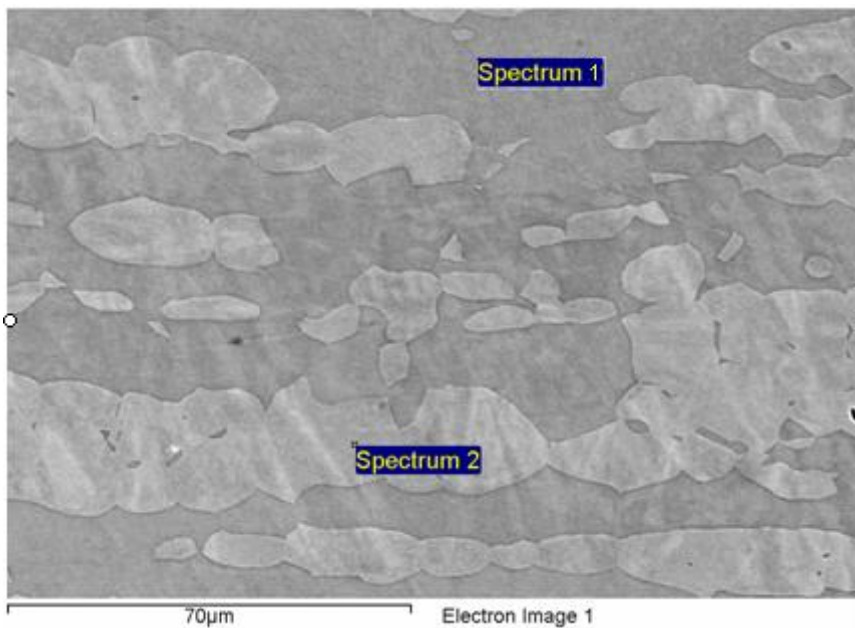


Figure 5.18 SEM image of the longitudinal section of super DSS Zeron etched by 10M NaOH solution

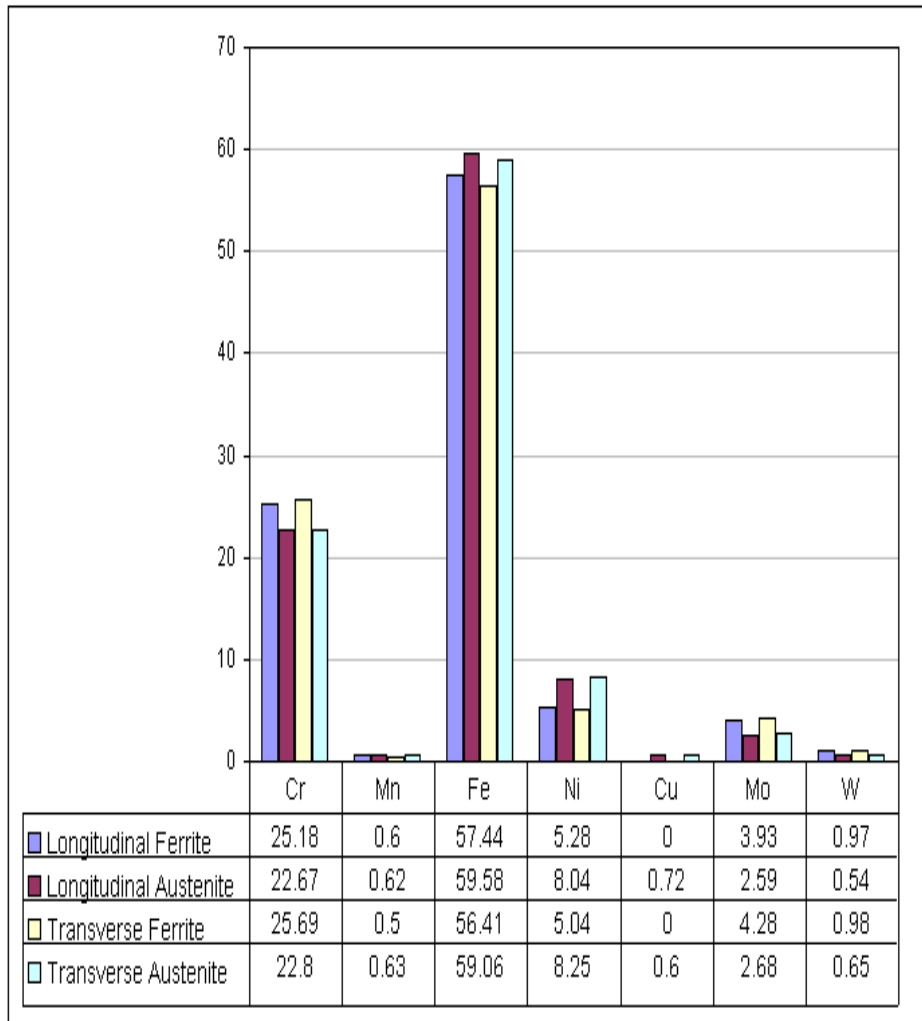


Figure 5.19: Analysis by SEM for the austenite and ferrite phase of the transverse and longitudinal sections for super DSS Zeron 100 showing the range of composition for each phase

The weight percentage of chromium in the ferrite phase is higher than in the austenite phase, while the nickel content in the ferrite phase is less than in the austenite phase. In addition, the amount of the molybdenum in the ferrite phase is also greater than the austenite phase. These observations confirm that chromium and molybdenum segregate in the ferrite phase and act as a ferrite formers and nickel as austenite phase stabilizer. The weight percentage of the chromium on the longitudinal of austenite phase, which should be less than the ferrite phase, was a little lower than was expected. This error is thought to be due to the noise recorded by the SEM. The error expected in the percentage

of the chromium and other elements led to an expected error in the calculations of the PREN as will be presented in the General Discussion. Microanalysis using a scanning electron microscope showed that partitioning of Cr and Mo in the ferrite and Ni and Mn in the austenite. The chemical composition for a fresh specimen of each phase was analysed five times for all the three alloys. The average composition of both phases was taken and the error shown by the standard deviation. Nitrogen in the ferrite was taken as fixed at the saturation value $\approx 0.05\%$, the rest partitions to the austenite. The results of these data for the ferrite and the austenite phase are presented in the general discussion section (table 7.2).

Saki ¹²⁶ has shown that the nickel content in duplex stainless steels should be maintained between 4 and 8 wt% for super DSS alloys (25 wt % Cr) and 4 to 7 wt% for DSS alloys (22 wt% Cr) to obtain optimum pitting resistance. When nickel concentration is considerably in excess of that required for optimum pitting resistance, then the austenite ratio increases noticeably above 50%. The resulting residual, more highly alloyed ferrite (as a result of alloying element partitioning) will more readily transform to the brittle sigma phase at temperatures in the range 650-950°C ¹²⁷. This will adversely affect the hot working characteristics of wrought steels, impact toughness, ductility and weldability of cast duplex stainless steels ¹²⁸.

On the other hand, if the nickel concentration is reduced lower than the optimum level for pitting resistance, it will result in too high ferrite contents and low toughness. This is because the ferrite formed immediately on solidification tends to have low ductility associated with larger grain size ¹²⁸. Since nickel is known as an austenite stabilizer, it partitions into the austenite. Therefore its content in the ferrite phase is lower than in the austenite phase. This inconsistency in the changes of nickel content in the ferrite and austenite phases is accounted for by changes in the relative volume fraction of the two phases.

5.4 Hardness

The measured hardness test was carried out using a micro Vickers diamond pyramid indenter with loads 30 kg and 50 kg for 15 seconds. The average of results for the two loads were recorded and converted into a Vickers hardness number, which, for carbon steels, would correspond to an expected hardness numbers as shown in table 5.3.

Material	Mean Hardness (HV)
Ferralium 255	255 ± 8
SAF 2507	265 ± 4
Zeron 100	262 ± 7

Table 5.3: Measured Vickers hardness for super DSSs

5.5 Polarization behaviour

At the completion of the potentiodynamic measurements, graphs of potential vs. log current density were produced and the pitting potential was noted from the graph for each experimental condition. Usually, initiation of pitting occurs at a critical potential known as E_{pit} obtained during the forward potential scan, due to the localized breakdown of protective surface film beyond the (anodic) passive region. This phenomenon is associated with a change in slope as the current density is increased.

From the anodic polarisation curves of the super duplex stainless steels Ferralium 255, SAF 2507 and Zeron 100 we can observe two pitting potentials present on the graphs. These pitting potentials are related to the two phases in the microstructure of the super duplex stainless steels. For Ferralium 255 the ferritic phase, which has the more active potential, around 800 mV (SCE), and the austenitic phase a more noble at around 900 mV (SCE). The passive film

starts to break down when the pitting potential is reached which leads to pit initiation at the surface of the metal. The potential vs. log current density plots obtained from potentiodynamic measurements for Ferralium 255, SAF2507 and Zeron 100 alloys in 3.5 % NaCl solution are presented in Figures 5.21 to 5.25. The pitting potentials for both phases were measured from the graphs by the intersections of the two red lines in the anodic curve (see figure 5.21) The difference in the pitting potential of the two phases was confirmed by metallography, as will be described in later section. The scattering in the measured pitting potential depends on the stability of the surface film, effect of microstructure, temperature and time dependants. Figure 5.23 shows the mean values for pitting potentials for the austenite and the ferrite phase obtained from the potentiodynamic test for super DSS Ferralium 255.

Evans ¹²⁹ introduced a graphical method for representing the polarisation behaviour in the relationship between log current and potential E. Figure 5:20 illustrates the example of a theoretical Evans diagram for material exhibiting active/passive behaviour. The polarisation curve can have two cases, A and B as shown in figure 5:21. Case A occurs when the cathodic curve intersects the anodic curve in the active range and results in a measured polarisation curve in which the active loop is visible. This behaviour corresponds to the case of crevice corrosion, where access of dissolved oxygen is limited and the cathodic curve is strongly polarised.

Case B shows the cathodic curve intersecting the anodic curve in the passive range. As a result, the material exhibits stable passivity up to the pitting potential. Each of the polarisation scans recorded in this project corresponded to case B. For this reason it is not thought that crevice corrosion had led to active conditions on the specimens tested in this work. The polarisation behaviour appears to have been the result of distinct differences in the pitting behaviour of the ferrite and austenite phases, as shown by the micrograph in the following section.

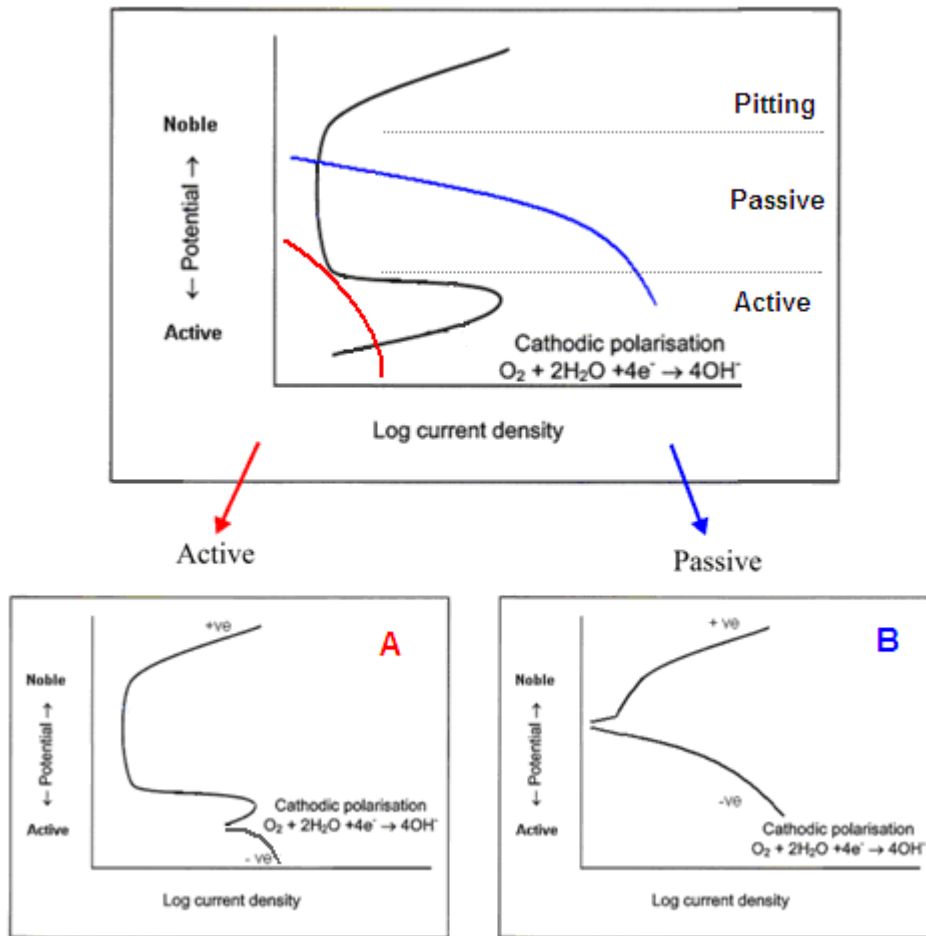


Figure 5.20: Illustrated polarisation behaviour on the cathodic reaction for stainless steels

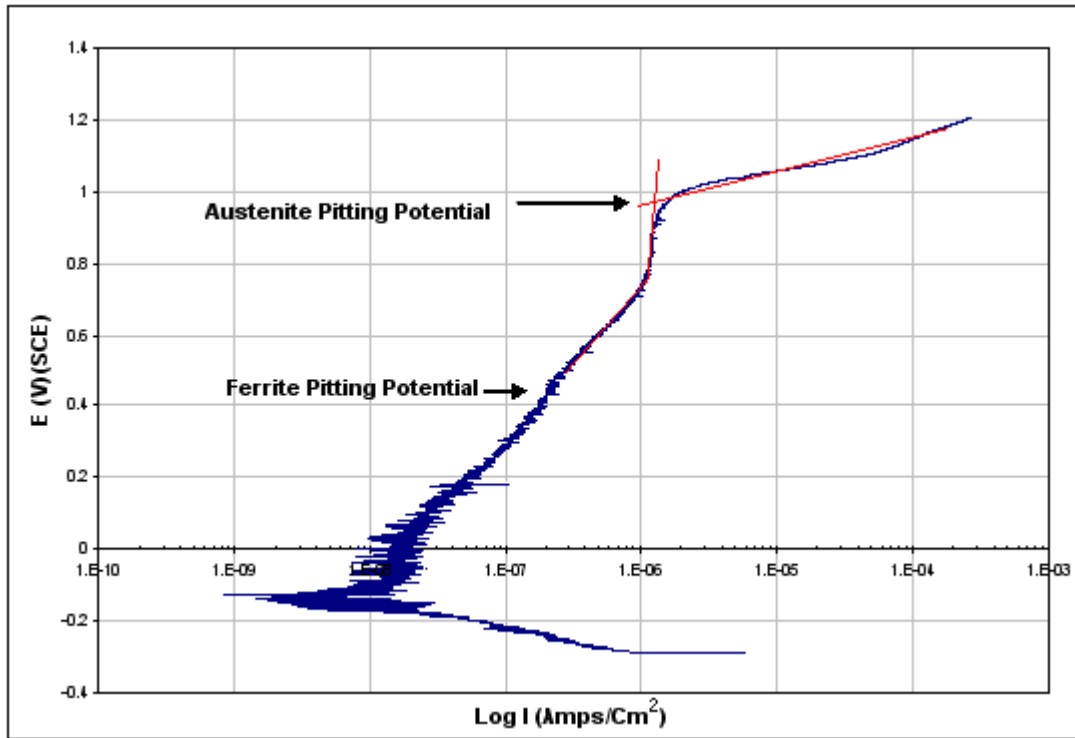


Figure 5.21: Potentiodynamic scan test for Ferralium 255 with a scan rate of 10 mV/min.

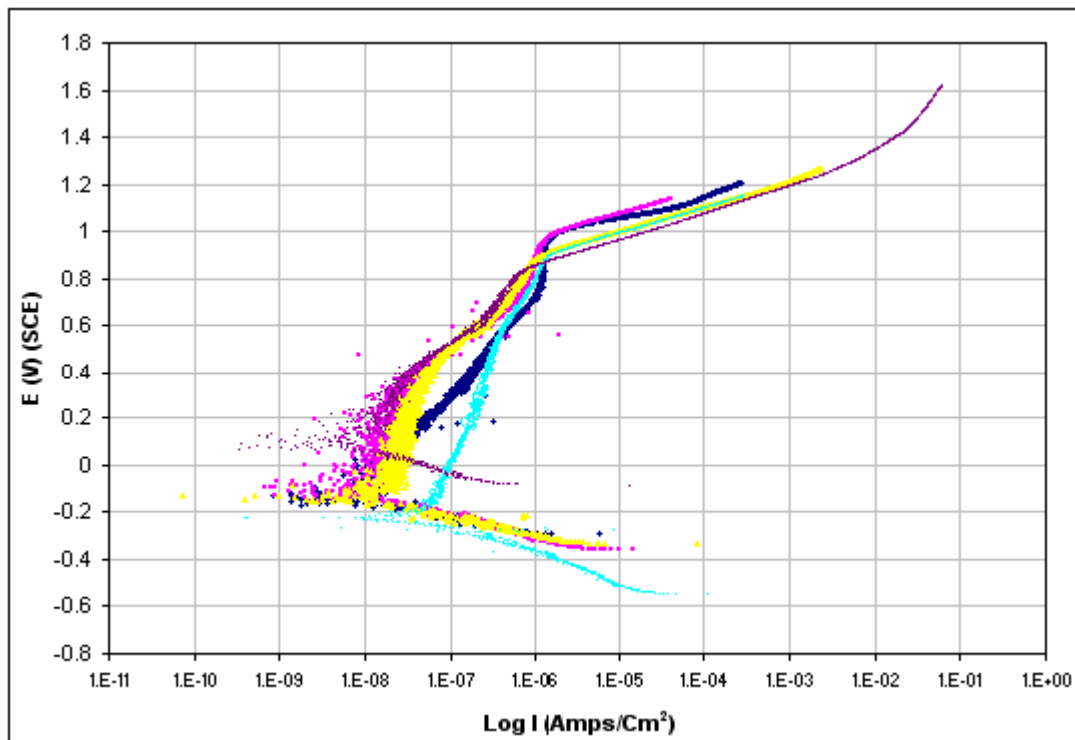


Figure 5.22 Comparison of the 5 potentiodynamic scan tests for super DSS Ferralium 255 with a scan rate of 10 mV/min

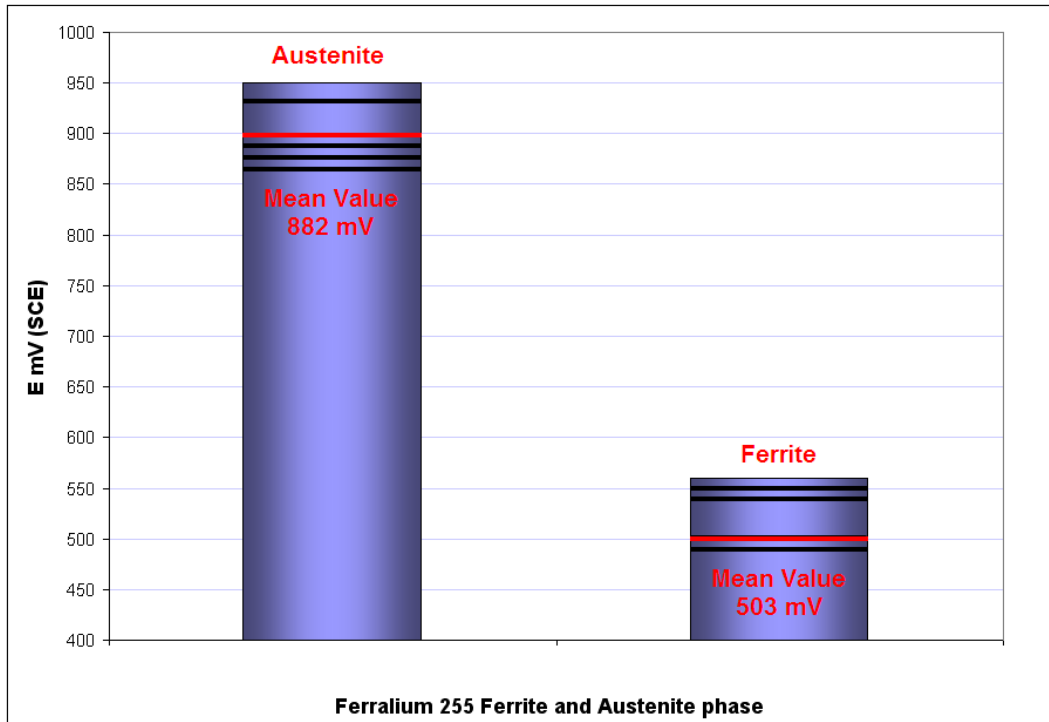


Figure 5.23 Values of the pitting potentials of the austenite and ferrite phase for super DSS Ferralium 255 with a scan rate of 10 mV/min

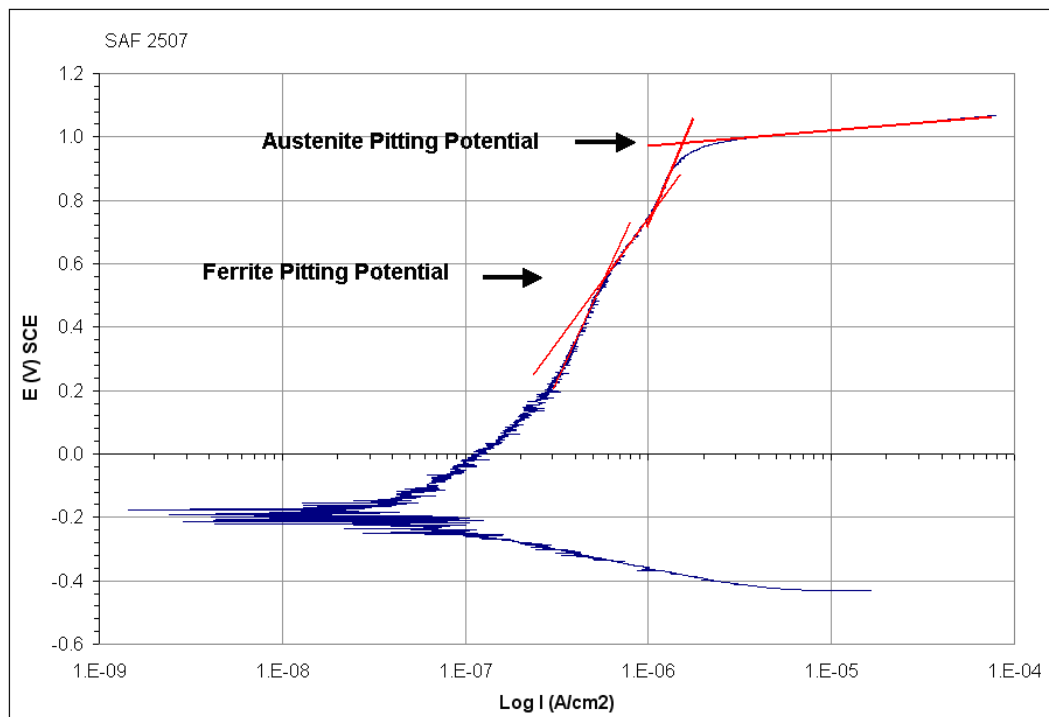


Figure 5.24 Potentiodynamic scan test for super DSS SAF 2507 with a scan rate of 10 mV/min.

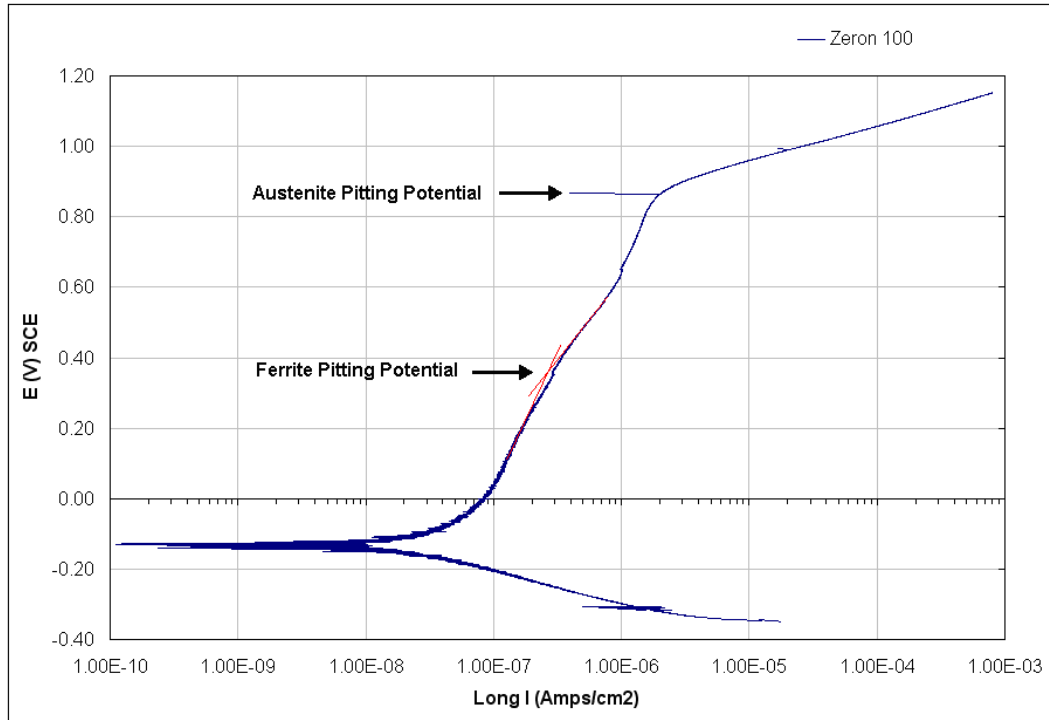


Figure 5.25: Potentiodynamic scan test for super DSS Zeron 100 with a scan rate of 10 mV/min.

Figure 5.25 shows the mean value of the austenite and ferrite pitting potential measurements for the three super DSSs obtained from the polarization results. These results are based on five tests conducted in 3.5% NaCl at room temperature. From 5.25, Ferralium 255 had the highest austenite pitting potential (882 mV SCE) while SAF 2507 had the lowest value (862 mV SCE). On the hand, SAF 2507 had the highest Ferrite pitting potential (540 mV SCE) while Zeron 100 had the lowest value (503 mV SCE) of the three alloys.

These pitting values need more detailed investigation of the pitting resistance equivalent number (PREN) on each phase based on alloy partitioning. The austenite phase had more resistance to pit formation than the ferrite phase which is due to the different alloy composition. In addition, the effect of applying a potential corresponded to each ferrite and austenite pitting will be demonstrated in the next section.

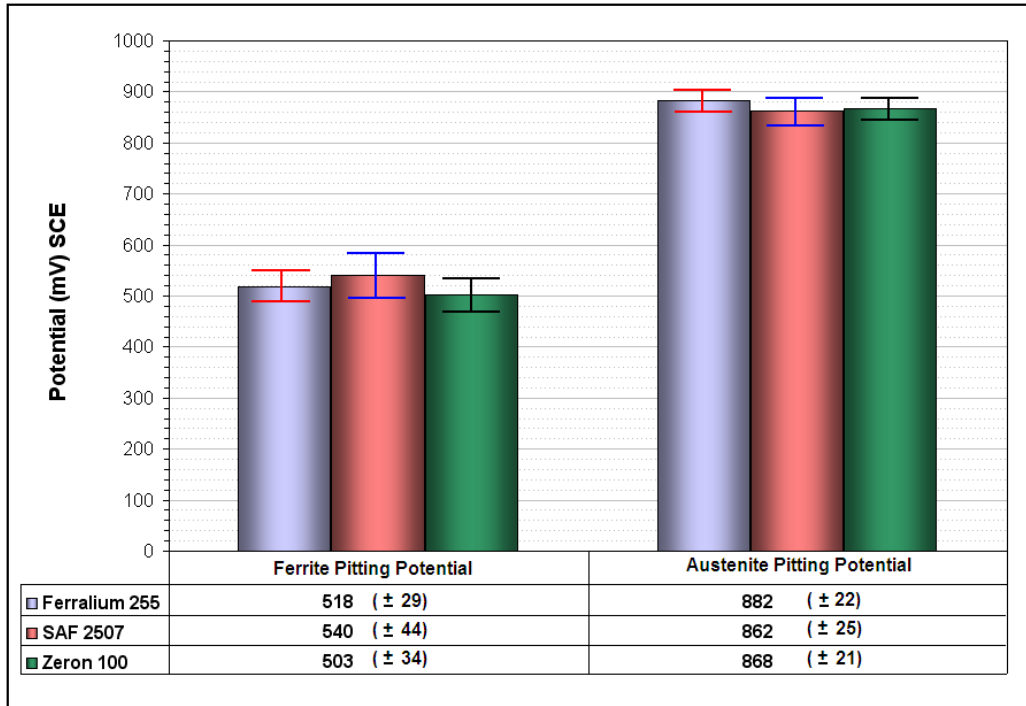


Figure 5.26: Mean values from five measurements of the pitting potentials of the austenite and ferrite phase for super DSS alloys

Potentiodynamic polarization was carried out to understand the role of composition and microstructure on the corrosion and passivation behaviour of super duplex stainless steels in 3.5% NaCl solution at room temperature. The difference in chemical composition between the two phases (ferrite and Austenite) can significantly affect the corrosion behavior of duplex stainless steel (DSS). Although the results clearly demonstrate the difference between austenite and ferrite phases in DSS, the specific electrochemical behavior of each of the constituent phases in DSSs is still of interest.

The two different anodic peaks appeared in the active to passive transition region of the potentiodynamic results were also reported by some other researchers^{130 - 132}. Ferrite phase contains higher amount of Cr and Mo, while austenite phase has higher concentrations of Ni and Mn. Some investigations also indicated that N is enriched in austenite phase^{133, 134}. Definitely, the partitioning of alloying elements in DSSs plays important role in affecting the mechanical properties as well as the electrochemical behavior in different solutions.

5.6 Potentiostatic Test

The aim of the potentiostatic tests was to hold the specimens within the ferrite pitting range, between the pitting potentials for ferrite and austenite and to observe the effects on the microstructure. Applying a breakdown pitting potential related to the ferrite or the austenite, pit initiation can occur, followed by pit propagation. The specimens of super DSS Ferralium 255 were held potentiostatically at potentials of 800mV, 850mV, and 950 mV against a saturated calomel electrode for 2 weeks. At the completion of each test, specimens were analysed by SEM for the composition of each phase as shown in figures 5.27 to 5.34.

When applying a pitting potential of 800 mV (SCE) analysis showed the unattacked phase was the austenite (spectrum 1 or 3) which has higher Ni and Mo content. This has been found in agreement with the metallographical observations of the specimens, which showed that pits mainly formed in the ferrite. The austenite was not attacked when applying a potential that corresponded to the ferrite pitting potential.

The ferrite (spectrum 2 or 4) shows heavy pitting at higher potentials than 800 mV (SCE). The ferrite has a BCC structure which has a lower corrosion resistance than the austenite which has a FCC structure.

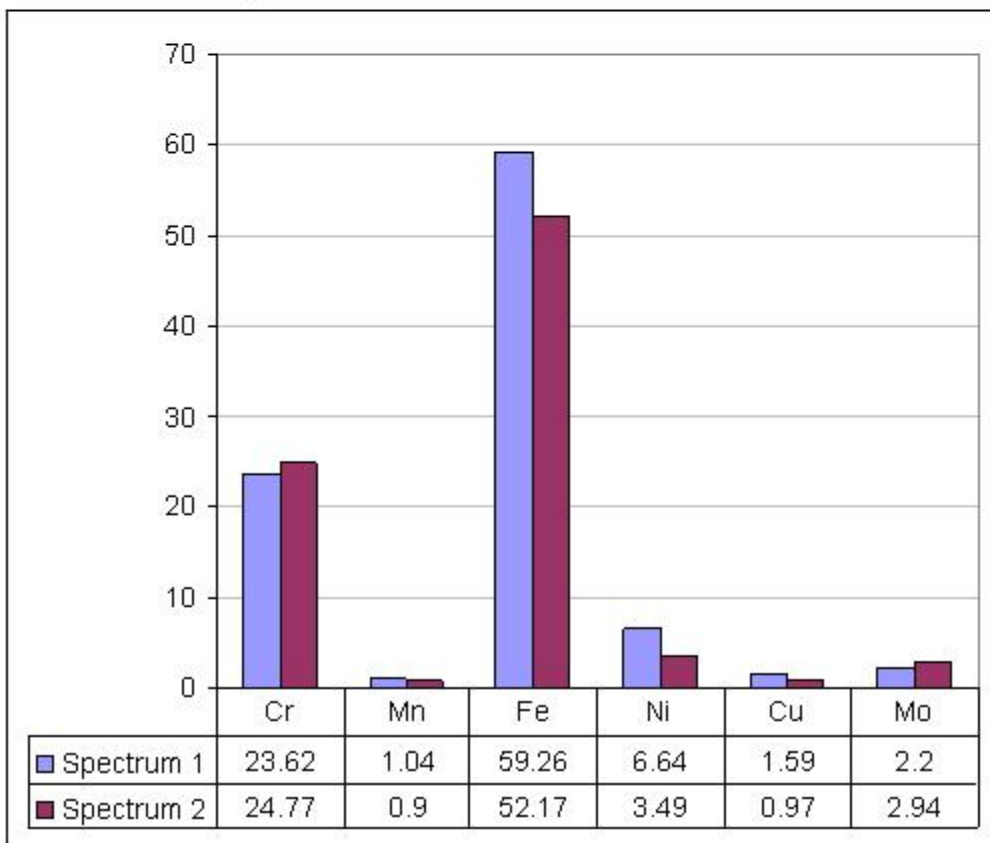
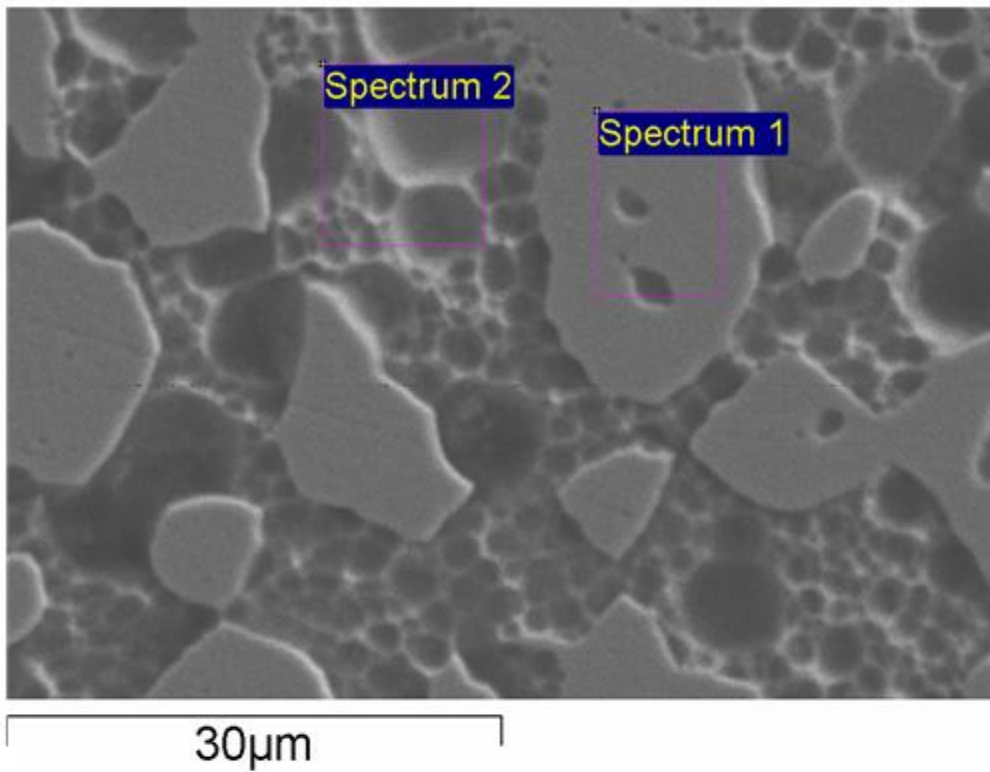


Figure 5.27: SEM image for potentiostatic test of super DSS Ferralium 255 specimen at 800 mV (SCE) for weeks

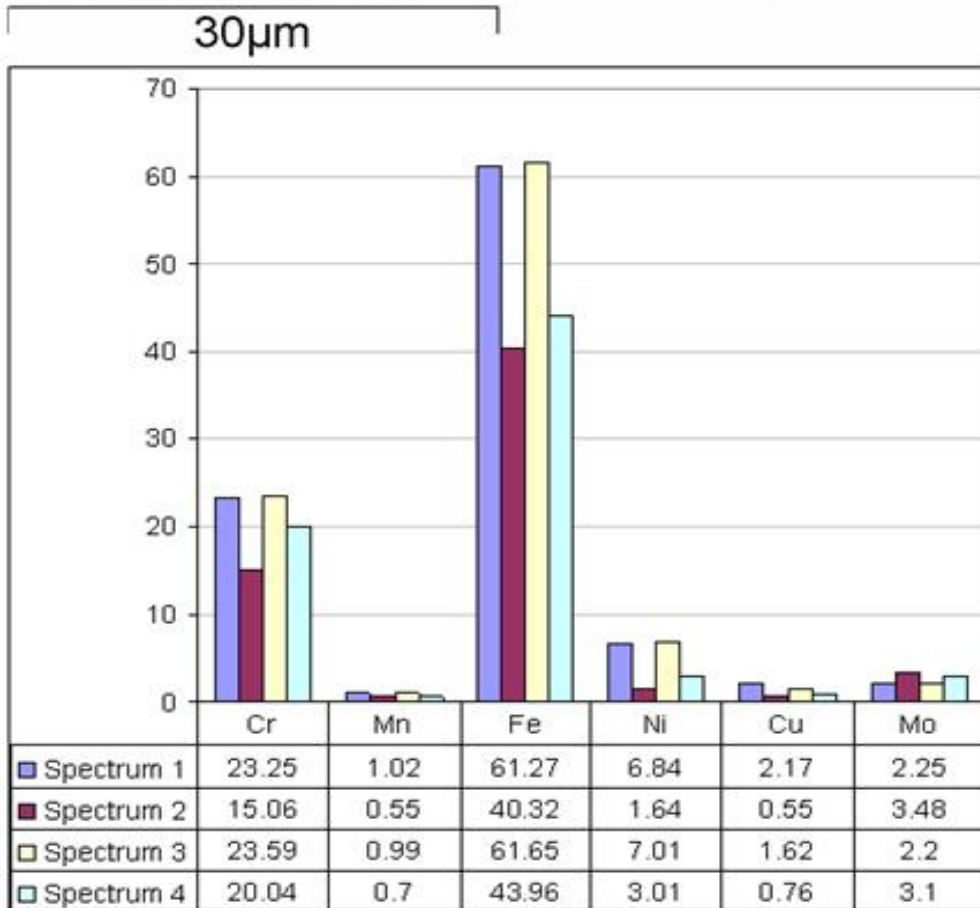
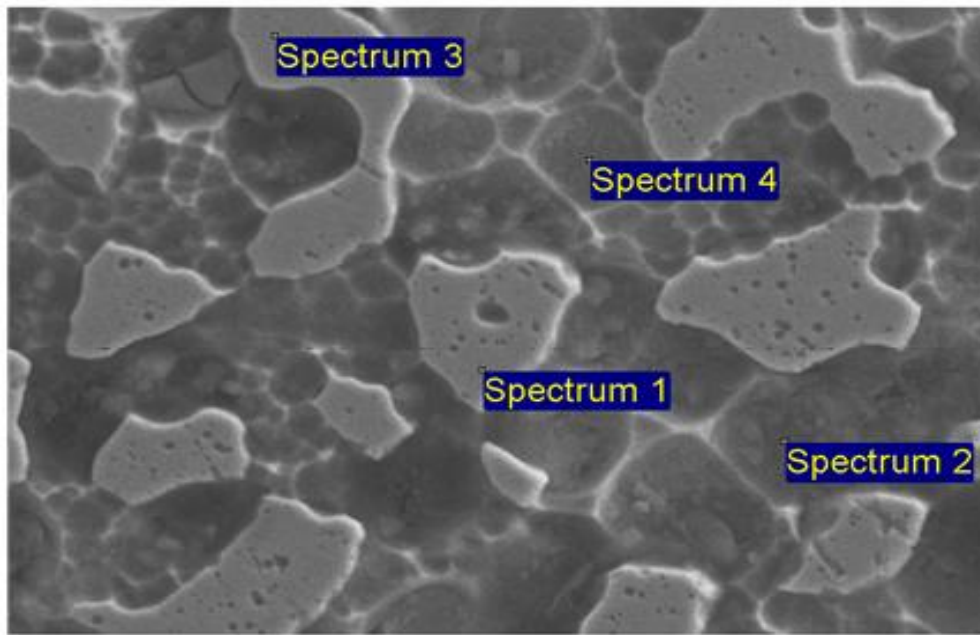


Figure 5.28: SEM image for potentiostatic test of super DSS Ferralium 255 specimen at 800 mV (SCE) for 2 weeks (Austenite and Ferrite Phase)

Optical microscopy was used to examine the surface characteristics and evaluate the effect of the applied pitting potential. Figure 5.29 shows localized pit initiation was produced at approximately 200 μm in diameter on the specimen of Ferralium 255 after applying a potential of 800 mV (SCE) for 2 weeks.

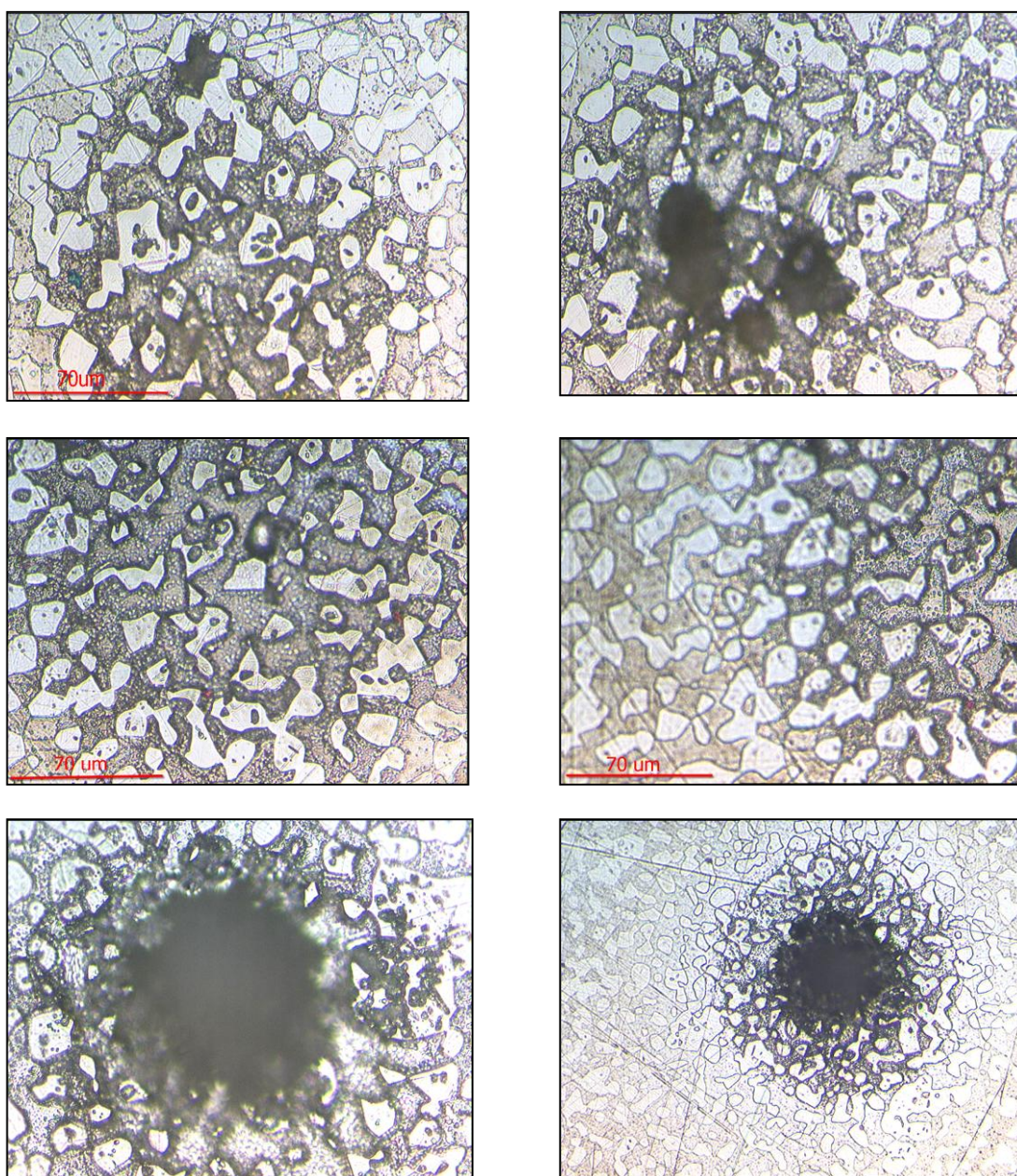


Figure 5.29: Optical images for potentiostatic test – pit initiation for super DSS Ferralium 255 specimen at 800 mV (SCE) for 2 weeks.

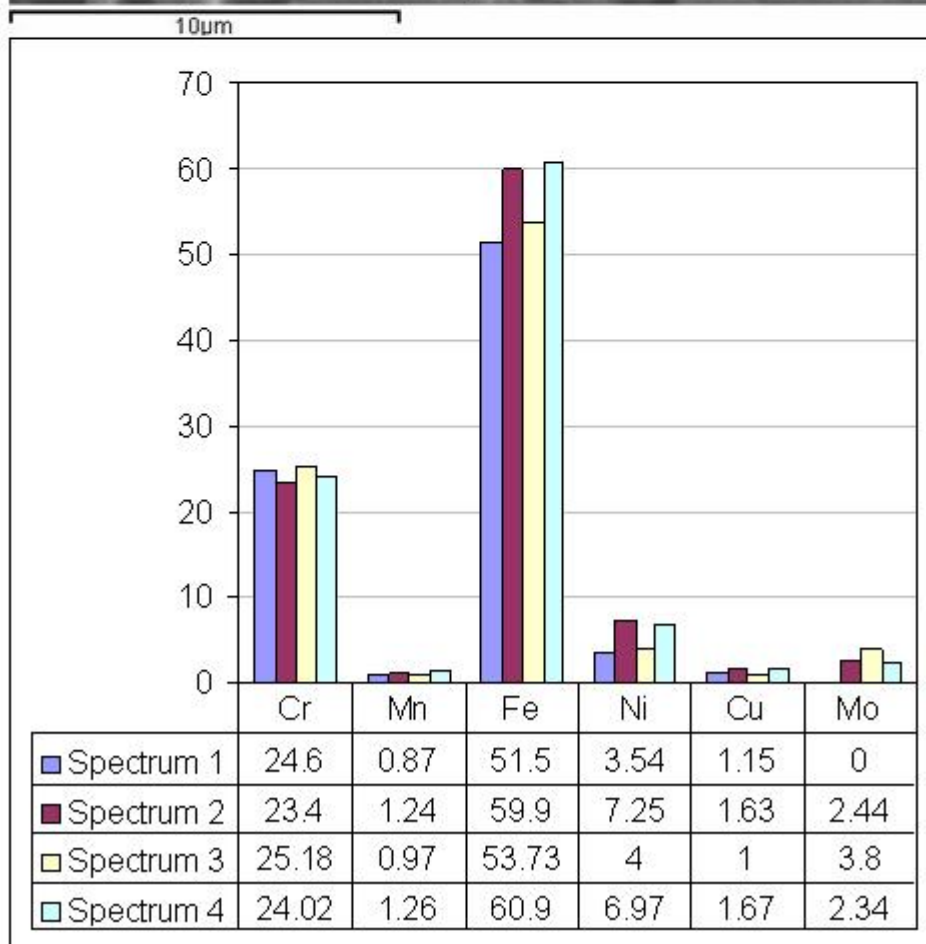
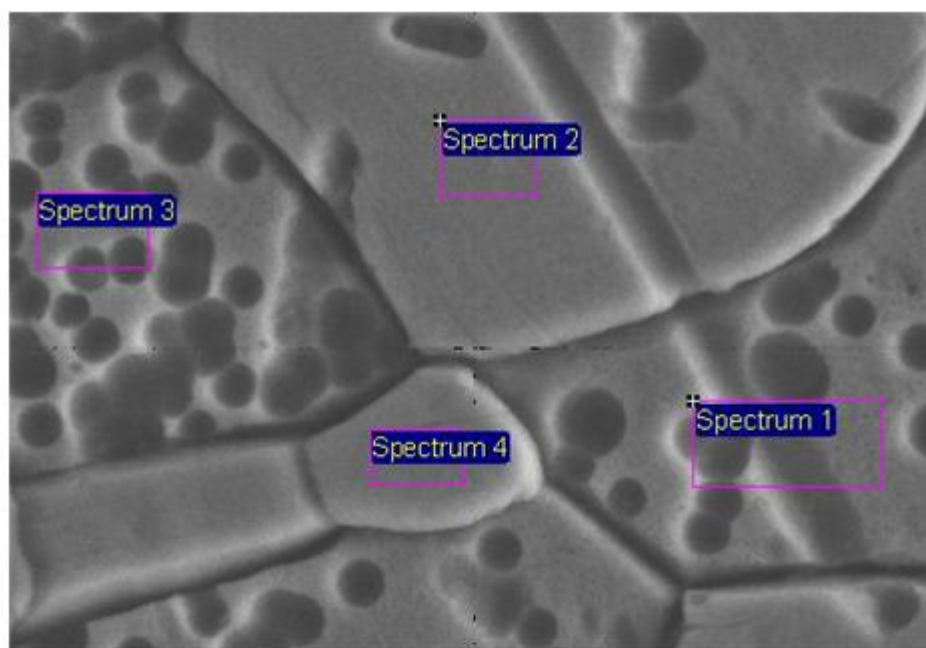


Figure 5.30: SEM image for potentiostatic test of super DSS Ferralium 255 specimen at 850 mV (SCE) for 2 weeks (Austenite and Ferrite Phase)

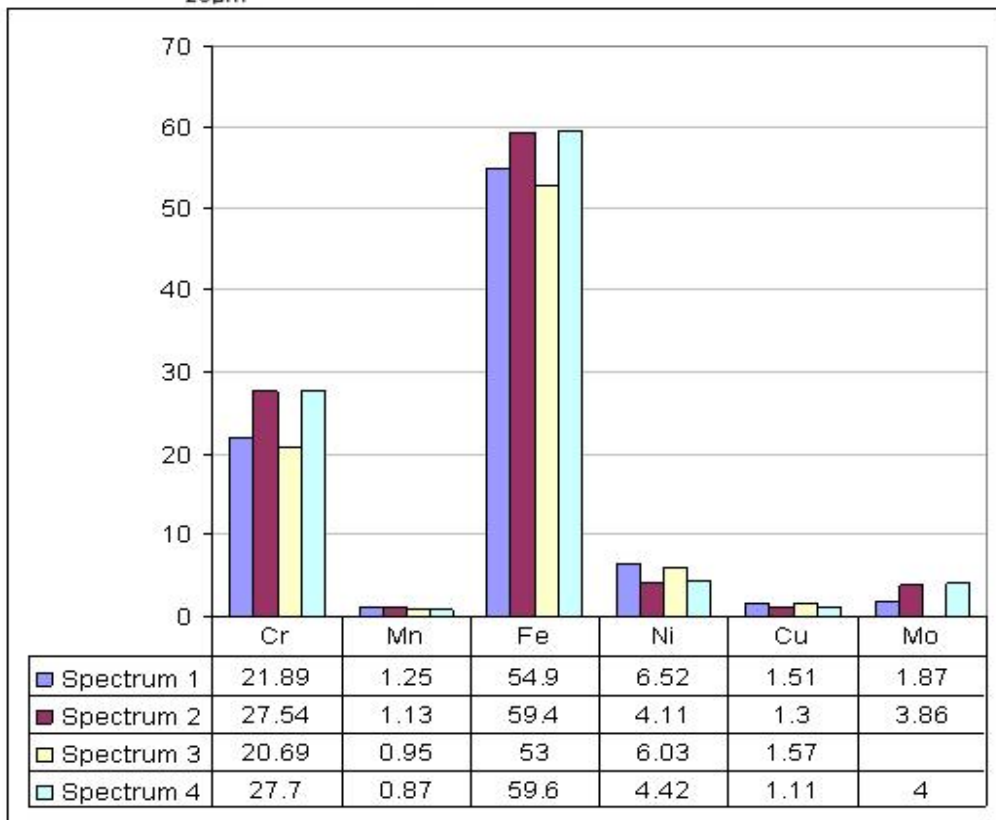
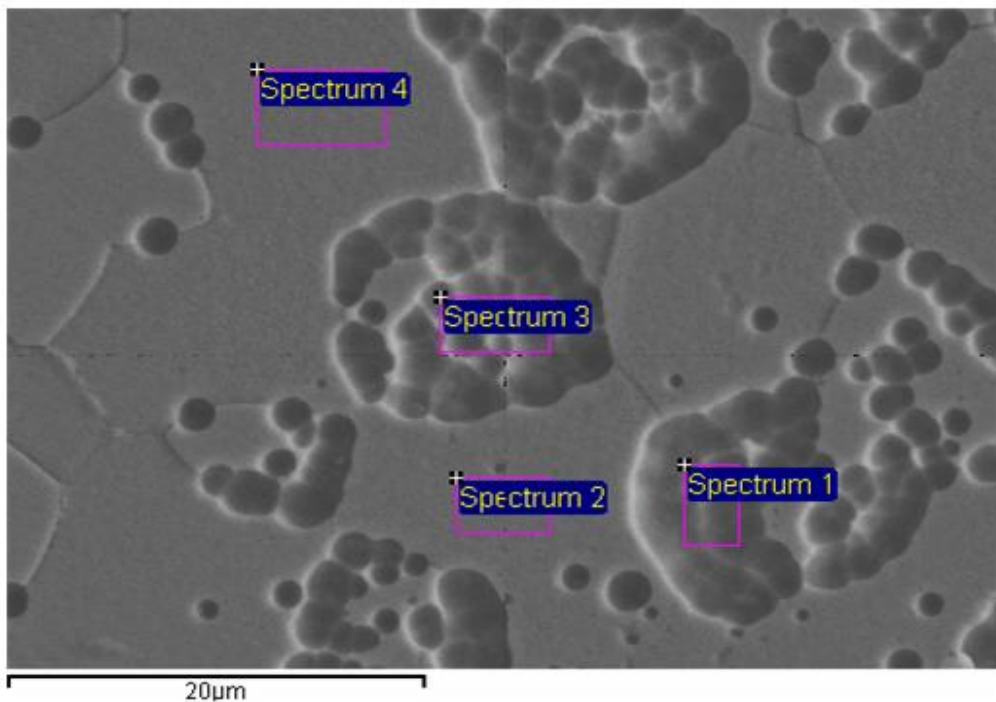


Figure 5.31: SEM image for potentiostatic test of super DSS Ferralium 255 specimen at 850 mV (SCE) for 2 weeks (Austenite and Ferrite Phase)

There was some pitting in the ferrite (γ) phase. However, this may have been isolated region of the austenite α within the ferrite γ (see Figure 5.1).

This is an unexpected result as the pitted region (spectrum 1 and 3) are shown to be the austenite phase or it might be the grain boundary where the pitting is originated in the adjacent ferrite as it can be seen in figure 5.1. Another possible reason is that the electron beam (SEM) penetrated into a subsurface ferrite grain which is below the detected grain as illustrated in figure 5.32.

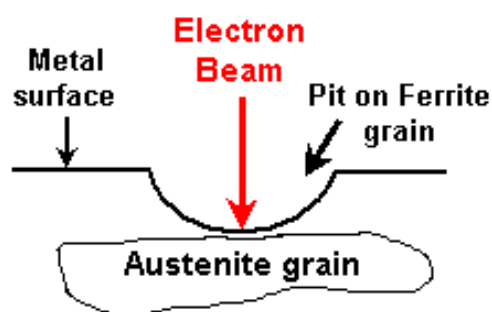


Figure 5.32: Electron beam penetration into the a subsurface of ferrite grain

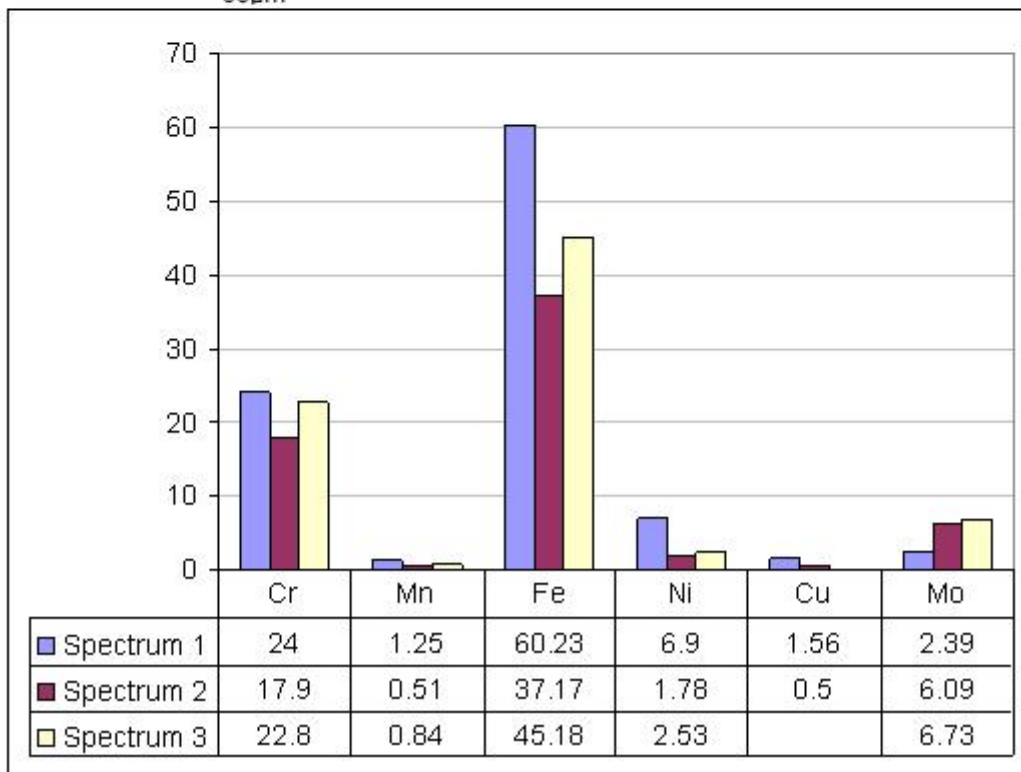
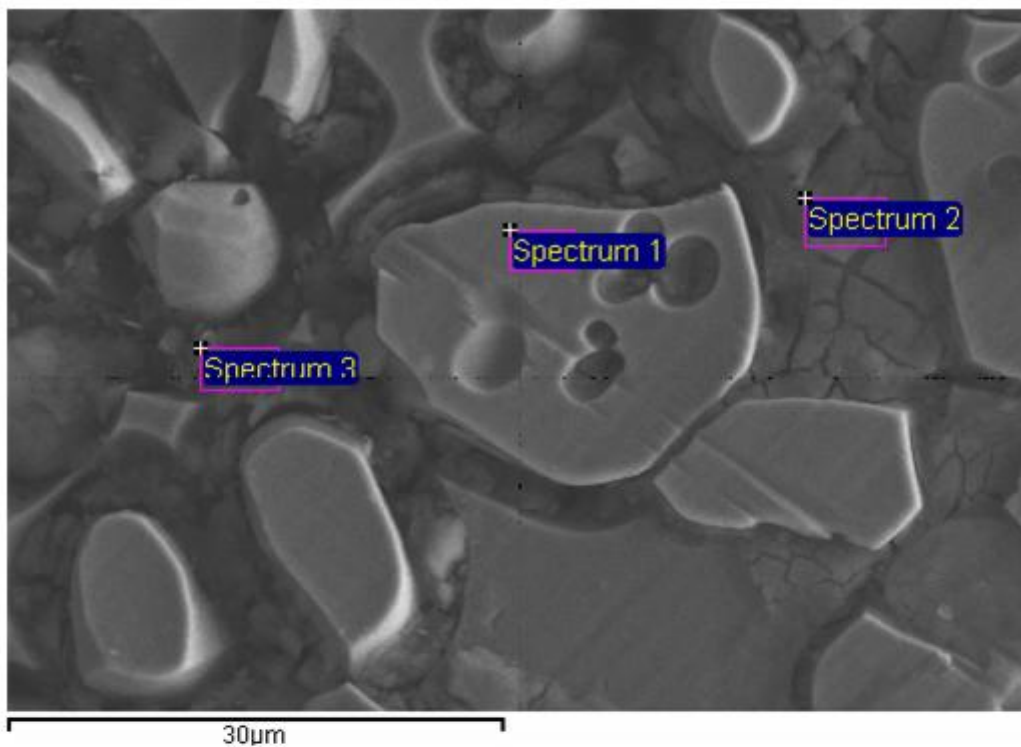


Figure 5.33: SEM image for potentiostatic test Super DSS Ferralium 255 specimen at 950 mV (SCE) for 2 weeks (Austenite and Ferrite Phase)

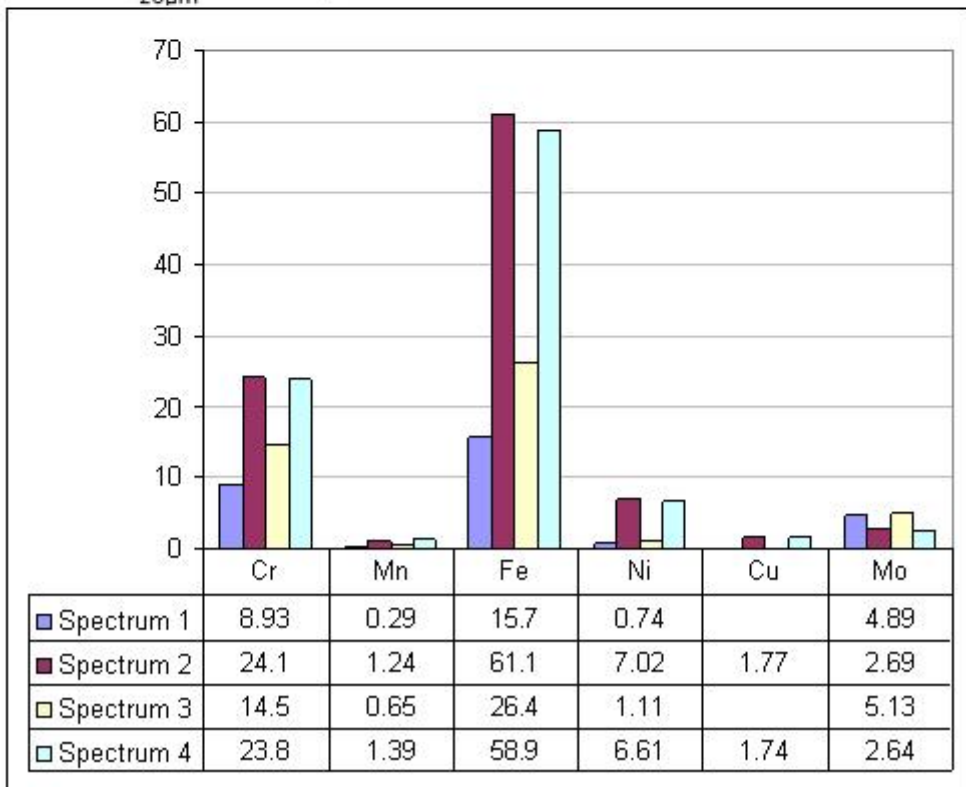
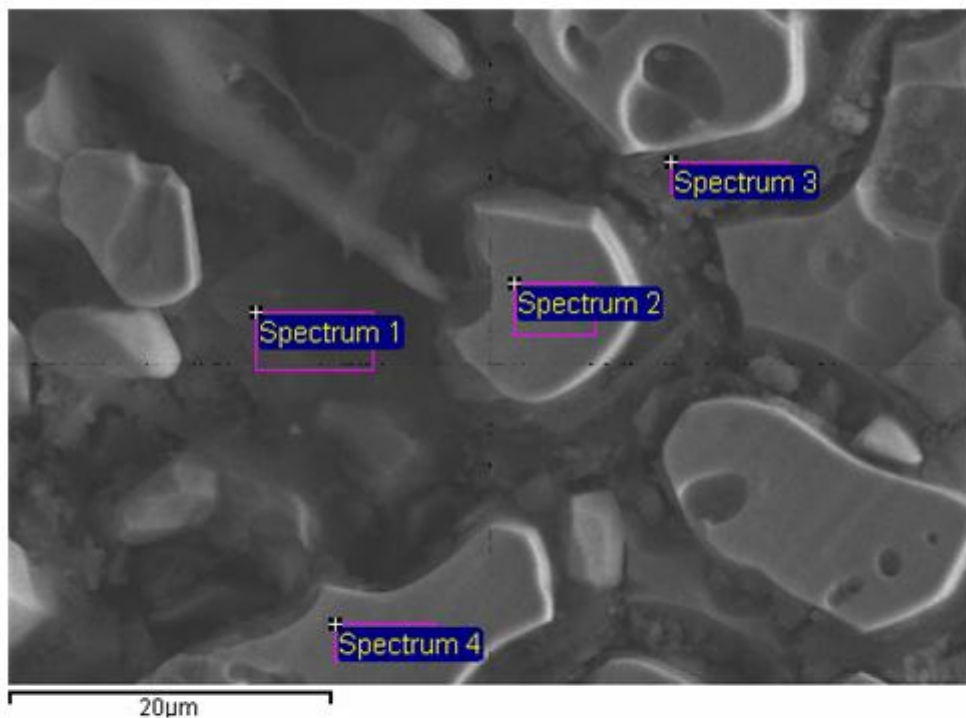


Figure 5.34: SEM image for potentiostatic test of super DSS Ferralium 255 specimen at 950 mV (SCE) for 2 weeks (Austenite and Ferrite Phase)

5.7 Slow Strain Rate Testing

The slow strain rate testing method was used for super DSSs Ferralium 255, SAF 2507 and Zeron 100 specimens at strain rates of $1 \times 10^{-6} \text{ sec}^{-1}$ in air at room temperature and also with a range of applied cathodic potentials at a temperature of 50° C to simulate the conditions on a cathodically protected subsea manifold or pipeline. It was loaded in a tensile machine subjected to a steady increasing stress in the desired environment. This procedure resulted in rupture of surface films and thus tended to eliminate initiation time required for surface crack to form. The test was continued till the fracture of the specimen occurred. The ductility and strength parameters coupled with surface morphology of the fracture provided information about the mode of failure.

Optical images of the 3mm gauge length cross sections for the three alloys polished and etched by 10M NaOH are show in the appendix (figure 10.1, 10.2 and 10.3). The microstructure of the gauge length shows the rolling orientation (longitudinal) of the austenite grains which are surrounded by the ferrite matrix.

The applied load data was plotted directly from the measured values. Figure 5.34 indicates that failure occurred at a load of 5.90 KN with time to failure of 92.8 hours for super duplex stainless steel Ferralium 255. The data was converted to engineering stress and strain, as shown in Figures 5.35 to 5.37.

The parameters, which are used to describe the stress-strain curve, are the tensile strength, yield strength or yield point, percent elongation, and reduction of area. The first two are strength parameters; the last two indicate ductility. For ductile fracture, the stress slowly decreases after the UTS while for brittle fracture there is a rapid decrease in stress. This can be determined from analysis of the stress vs. time graph (Figure 5.37).

Tensile or ultimate strength is that property of a material which determines how much load it can be withstand until failure. Yield strength is a measure of the resistance of a material to plastic deformation; that is, before assuming a

permanent set under load. For stainless steel, which does not have a well defined yield point, the proof stress is measured instead. It is a point at which a line drawn parallel to and offset 0.2 % from the straight line portion on the curve intersects the curve. It can be seen from the data that there is a considerable spread between the tensile and yield strength values, which is characteristic of stainless steels that strongly work harden. The yield strength is used for design calculations and is the stress above which the mechanical properties (tensile and yield strengths) can be increased by cold work or strain hardening.

The values obtained from SSR testing of super duplex stainless steels, Ferralium 255, SAF 2507 and Zeron 100, are listed in figures 5.35 through 5.72. The stated value of the reduction of cross sectional area has been calculated using two different methods: the average diameters of the fracture surface and selecting the fracture surface which can be calculated automatically by the SEM software as shown in figure 5.48 and 5.49.

The results obtained during the slow strain rate test on the super DSSs after hydrogen charged were compared with the same test performed in air. SEM images of the fracture surface of the SSRT in air and in charging conditions indicates clearly that the two failures occurred by a ductile mode in air testing, and either brittle mode in charged specimens or a combination of the two.

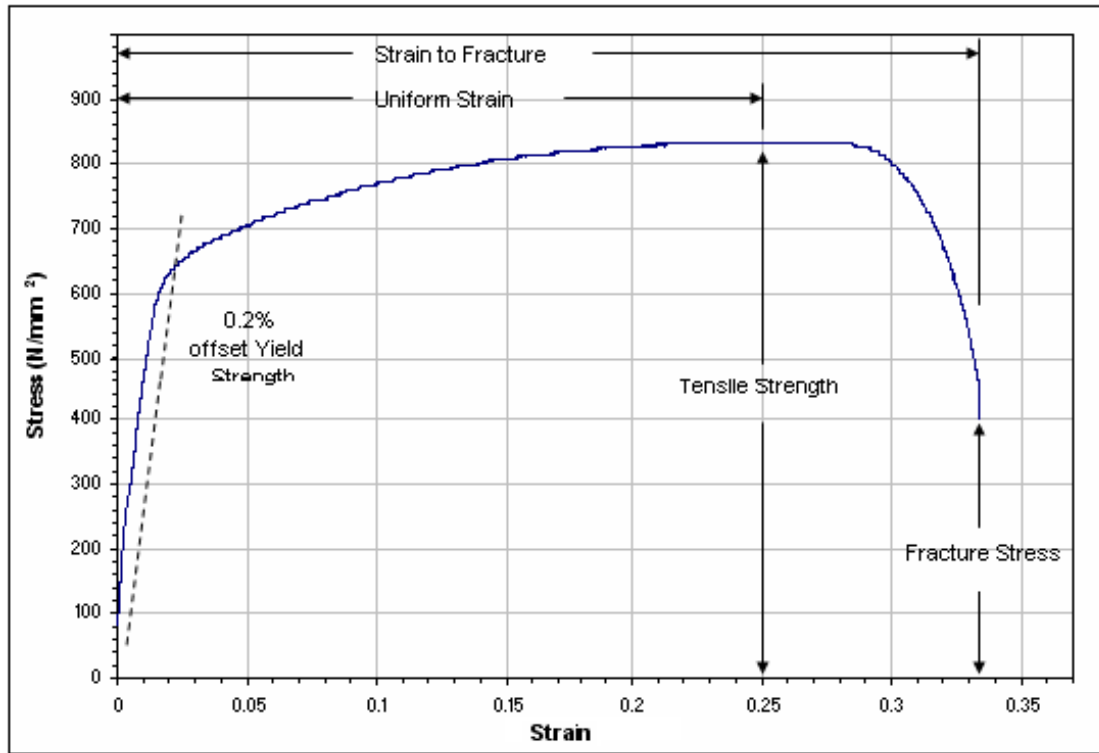


Figure 5.35: Stress / Strain curve for Ferralium 255 in air test condition showing the mechanical properties.

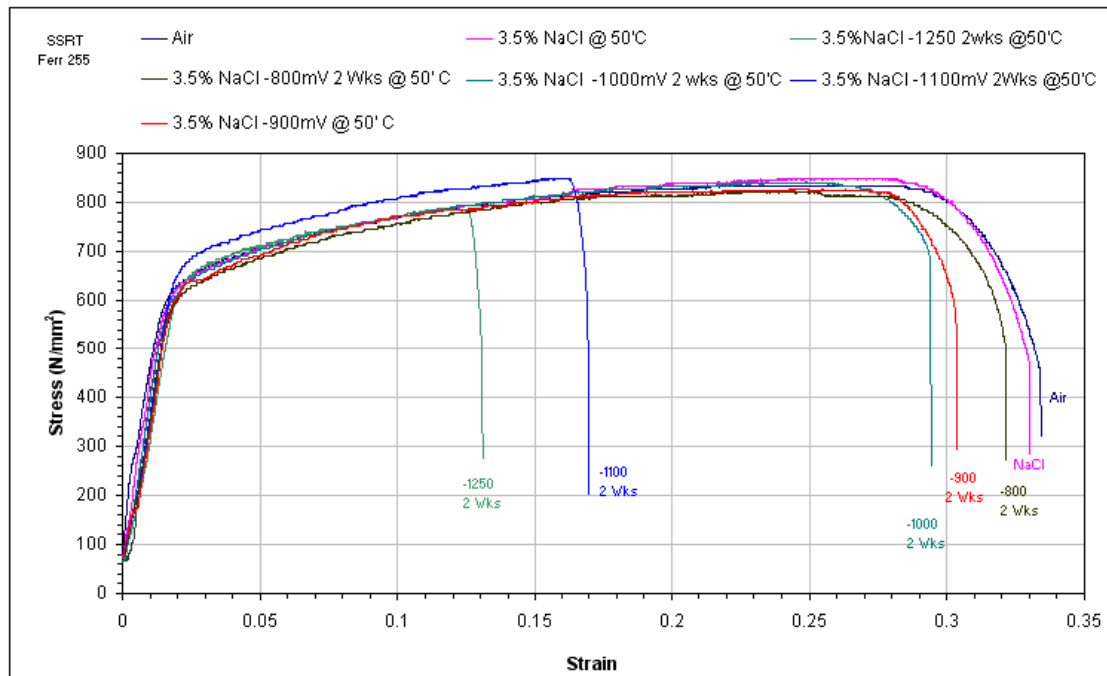


Figure 5.36: SSR Testing stress vs. strain for Ferralium 255

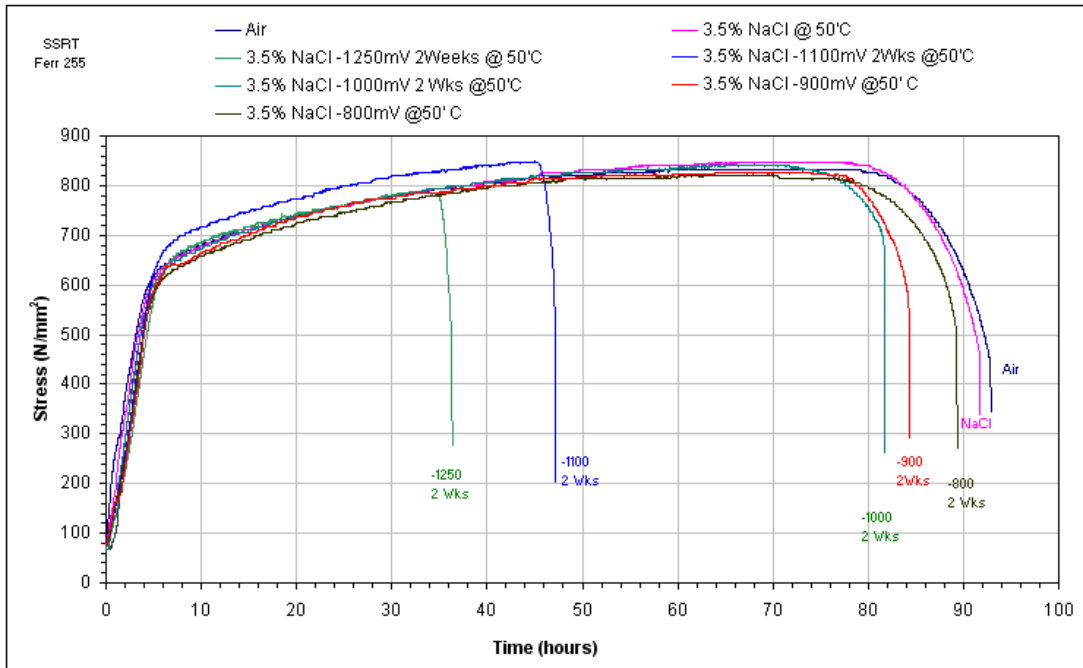


Figure 5.37: SSR Testing stress vs. time for Ferralium 255

The result in figure 5.38 shows that the baking treatment was effective in restoring the ductility and removing the absorbed hydrogen for specimens that were precharged for four weeks. Baking for 24 hours gave incomplete recovery and the time to failure was about 65% of the air test. On the other hand, when the baking time increased to 72 hours, the recovery was about 88 % of the air test. It is worth to mention that some pits were observed on the gauge length of the specimen which reduced the diameter to less than 3 mm.

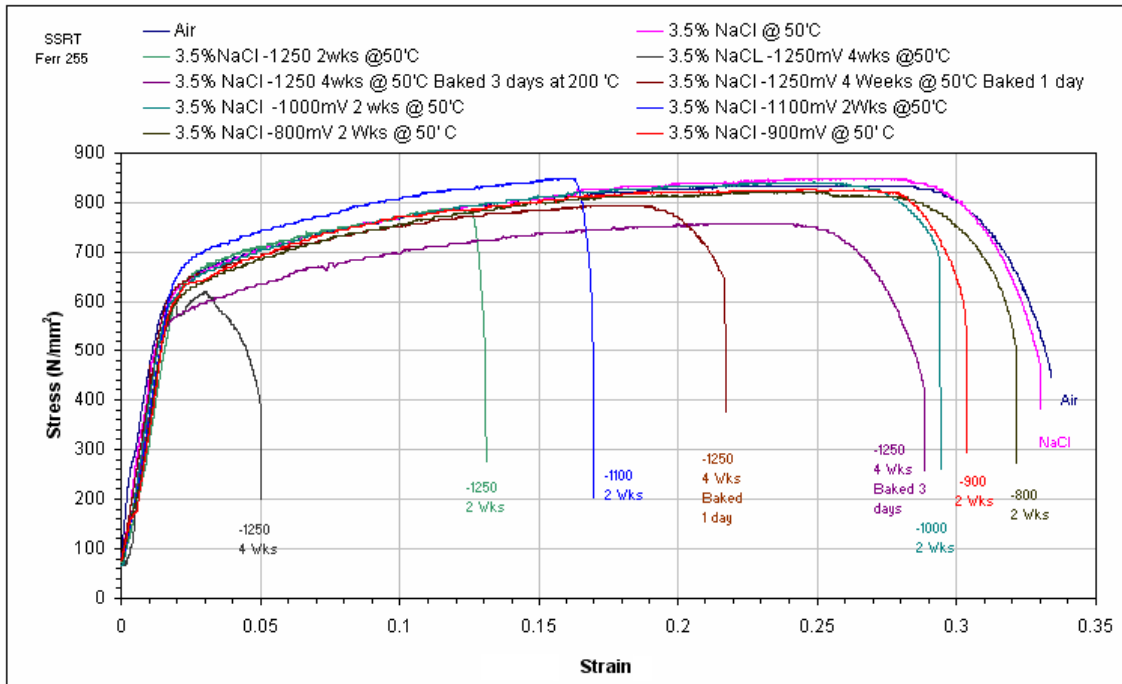


Figure 5.38: SSR Testing - Ferralium 255 Effect of Baking

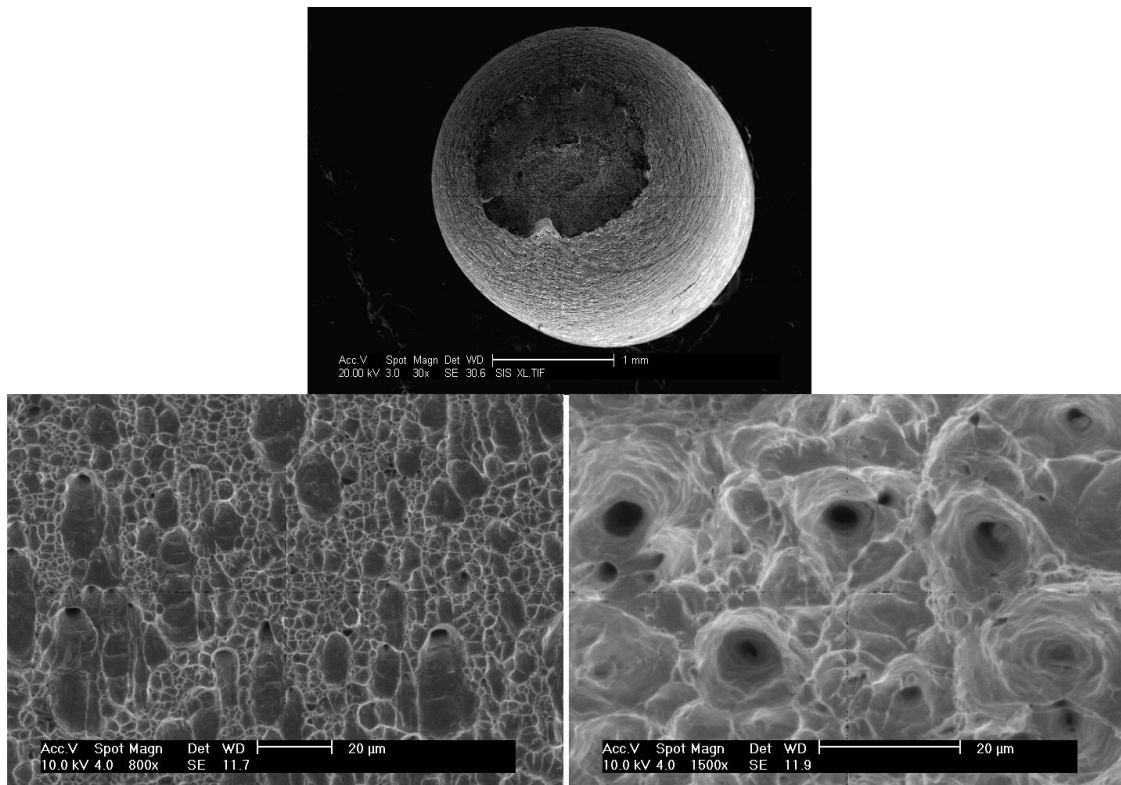


Figure 5.39: Macrographs at of the fracture surface of super DSS Ferralium 255 specimen showing the necking and microvoid coalescence resulting from the air test

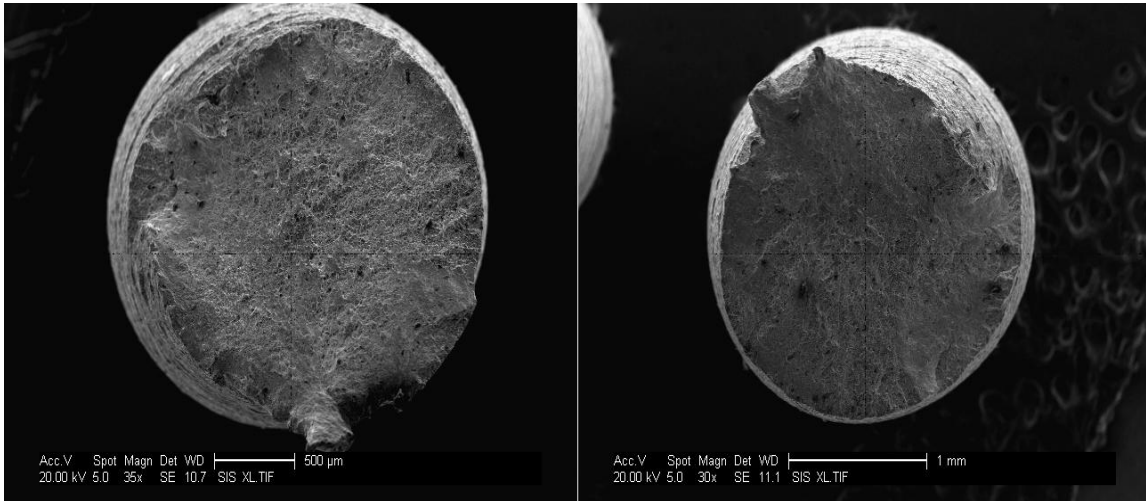


Figure 5.40: The macrograph showing brittle nature of the fractured surface of super DSS Ferralium 255 specimen – 3.5% NaCl at 50 °C, -1000 mV (SCE) for 2 weeks Test

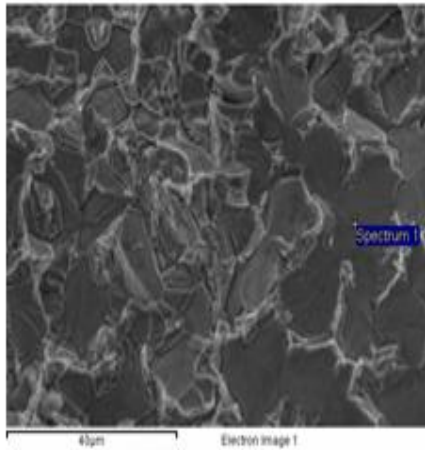
The SEM was used to examine the surface characteristics and evaluate the metallurgical information including the analysis of the phase microstructure. Figure 5.41 shows that the ferrite is the embrittled region and the austenite is the ductile region.

Element	Weight%
Cr	25.80
Ni	3.62
Mo	4.15

-1250 mV
(SCE) for 4
Weeks Test

Element	Weight%
Cr	23.88
Ni	6.58
Mo	1.01

Ferrite



Austenite

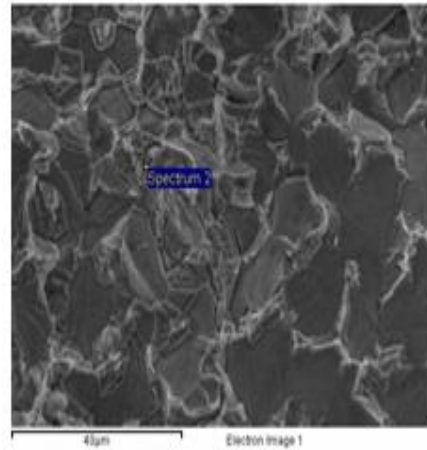


Figure 5.41: Composition analysis by SEM for the austenite and ferrite phase of the fracture surface specimen for Ferralium 255

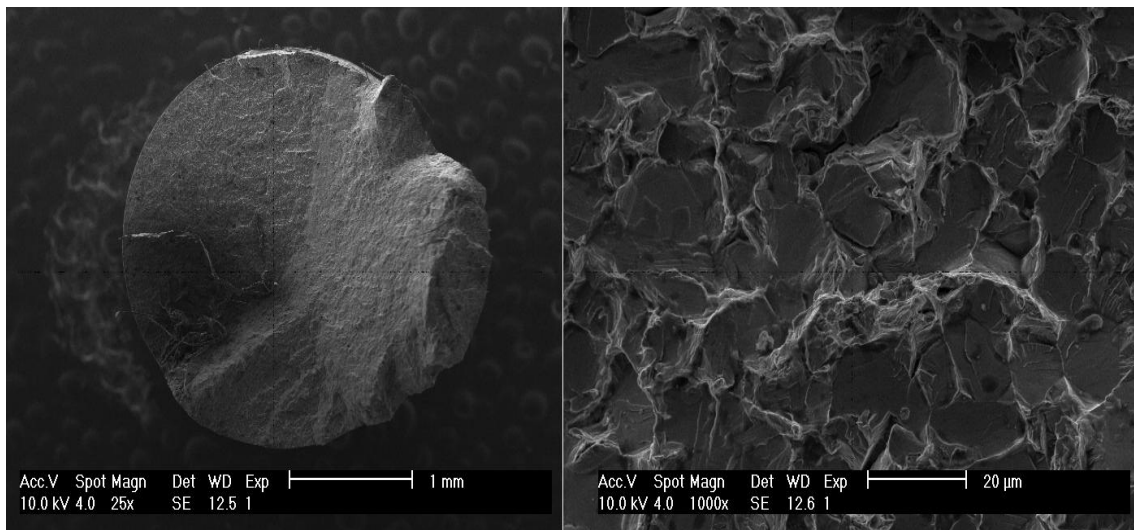


Figure 5.42: The macrograph showing brittle nature of the fractured surface of super DSS Ferralium 255 specimen – 3.5% NaCl at 50 °C -1250mV (SCE) for 2 weeks Test

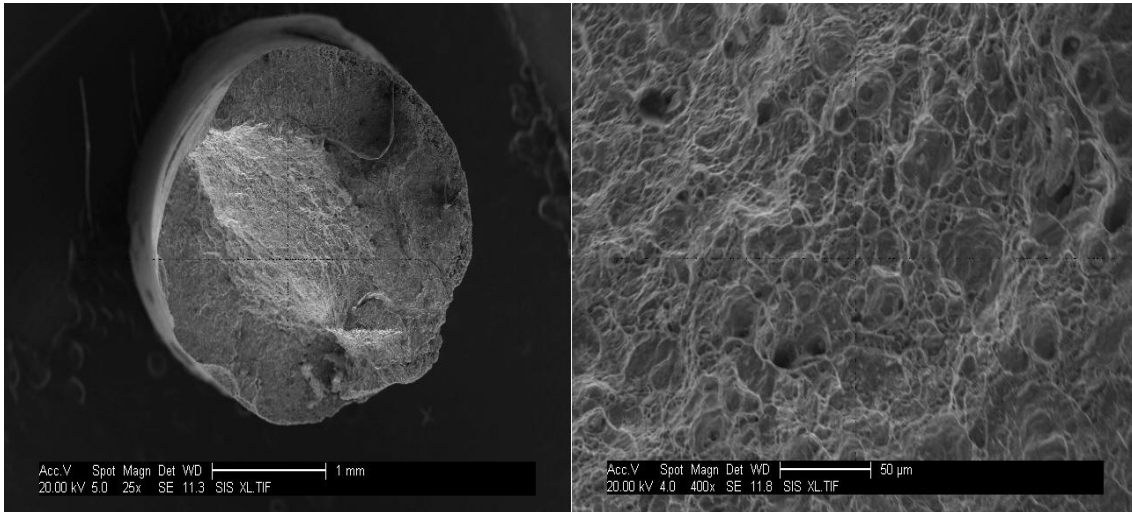


Figure 5.43: The macrograph showing brittle nature of the fractured surface of super DSS Ferralium 255 specimen – 3.5% NaCl at 50 °C -1250mV (SCE) for 4 weeks Test

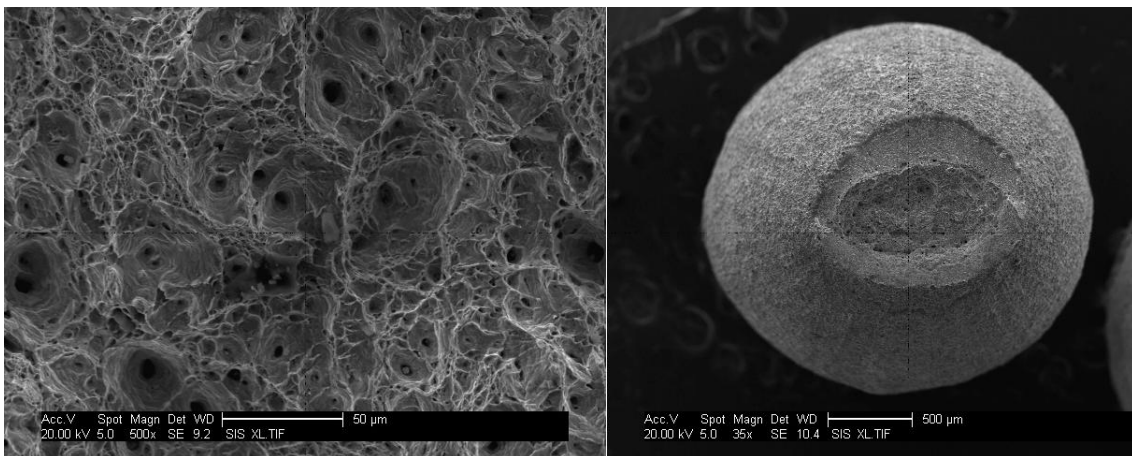


Figure 5.44: The macrograph showing ductile nature of the fractured surface of super DSS Ferralium 255 specimen precharged at -1250mV (SCE) in – 3.5% NaCl at 50 °C, for 4 weeks Baked for 3 day at 200 °C after SSRT

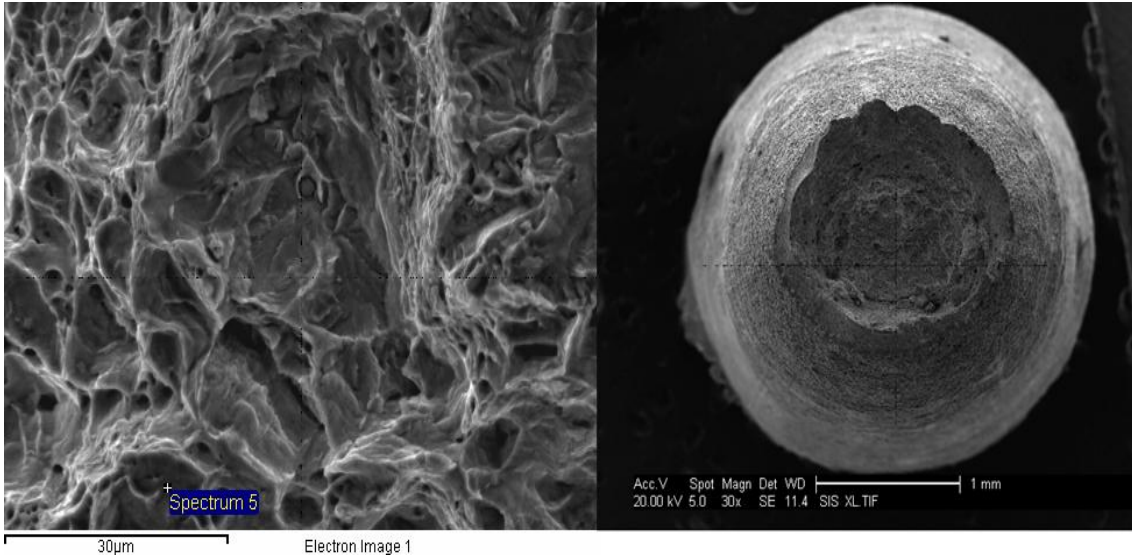


Figure 5.45: The macrograph showing ductile nature of the fractured surface of super DSS Ferralium 255 specimen precharged in 3.5% NaCl at -1250mV (SCE) at 50 °C for 4 weeks – Baked for one day at 200 °C after SSRT

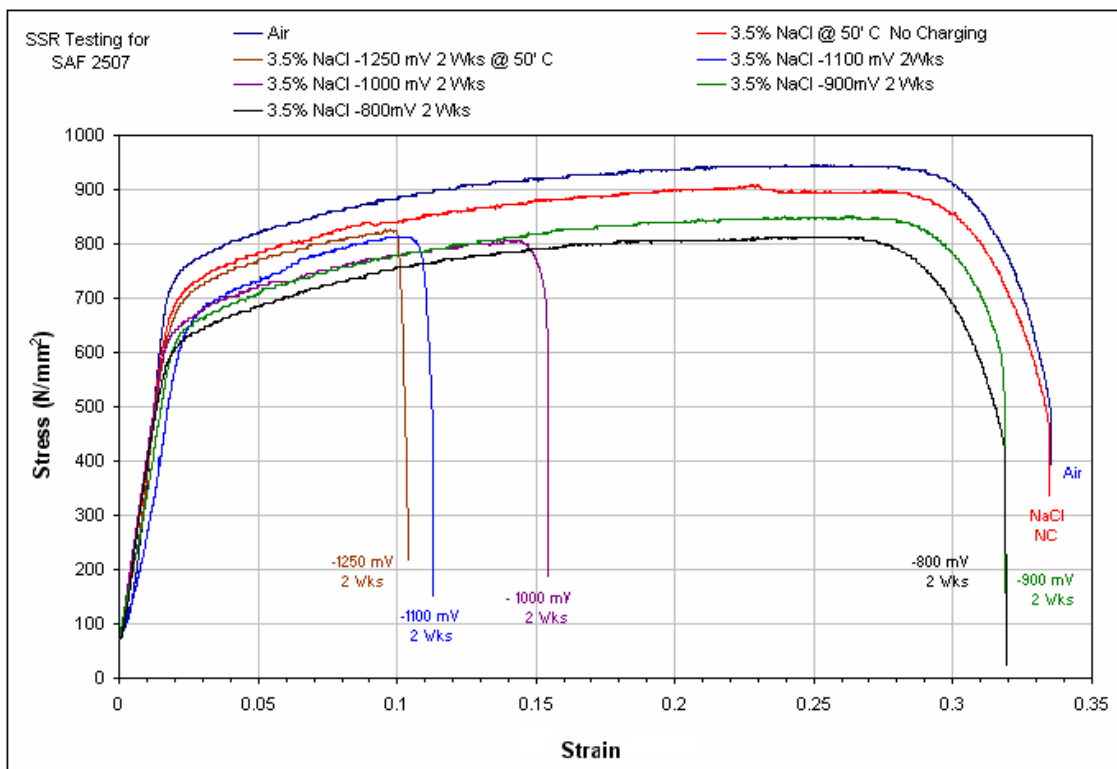


Figure 5.46: SSR Testing Stress vs. Strain for SAF 2507

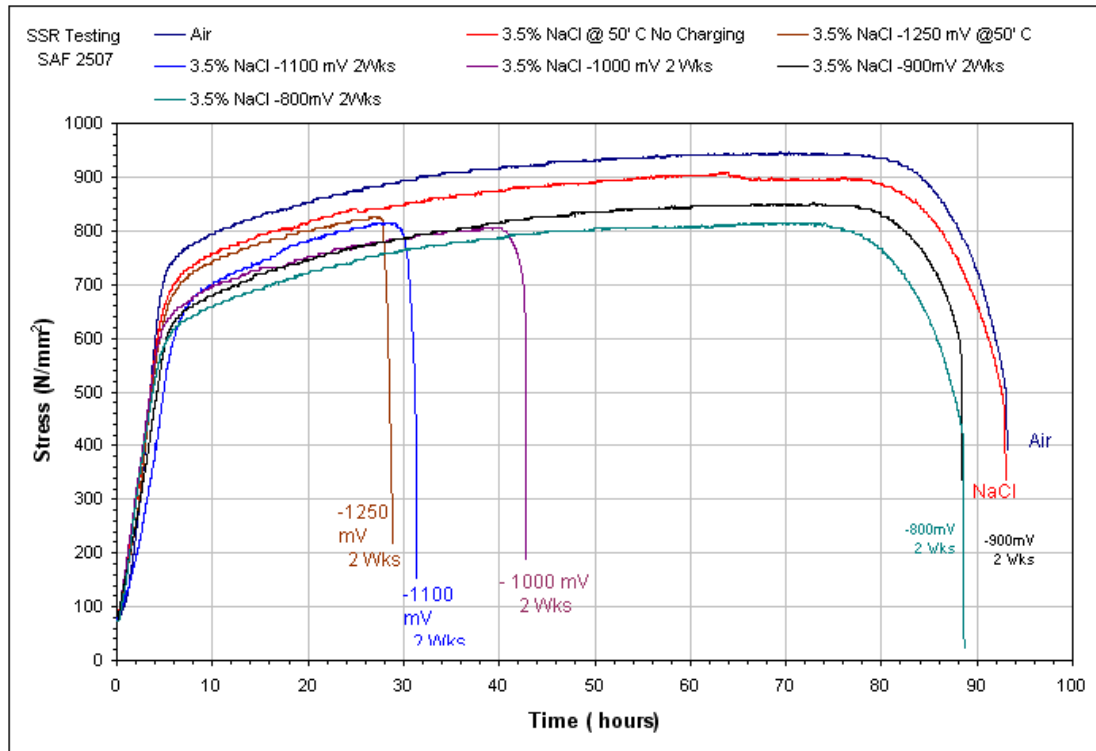


Figure 5.47: SSR Testing Stress vs. time for SAF 2507

Once total fracture had occurred, the fractured specimen was removed from the test cell, rinsed with distilled water and acetone then ultrasonically cleaned to produce a clean fracture surfaces. The reduced gauge diameter at the point of fracture was computed for each specimen. Due to the non-uniform nature of the fracture surface, measurements were recorded by using the SEM by taking the average of 4 diameters measured across the fracture surface for each specimen and by selecting the fracture surface area while the program computed this area as shown in figures 5.48 and 5.49. In both methods, the area calculations appeared to be close in measurements.

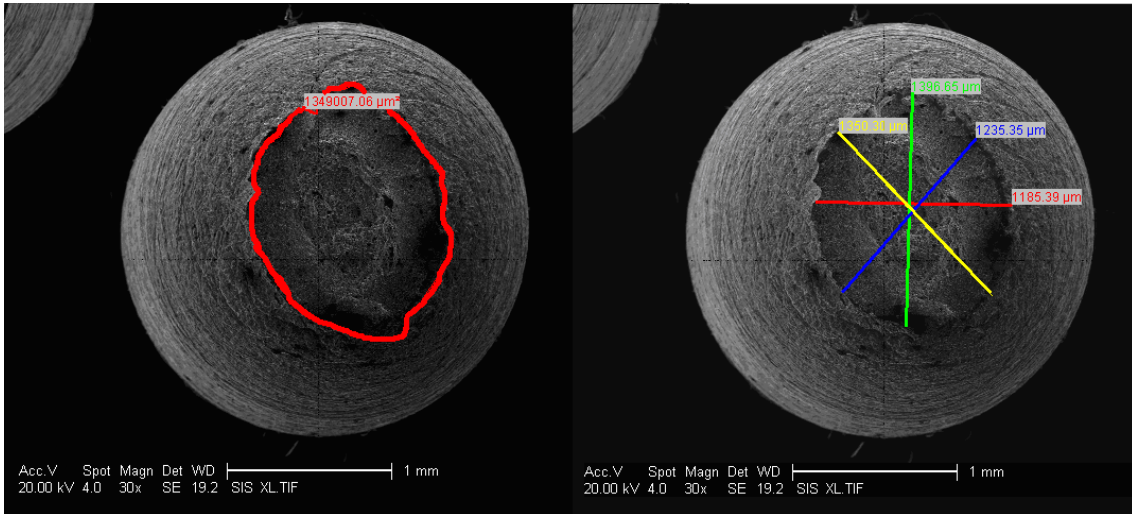


Figure 5.48: Measuring the fracture surface area of SDSS SAF 2507 after SSR testing in 3.5% NaCl without charging at 50° C temperature

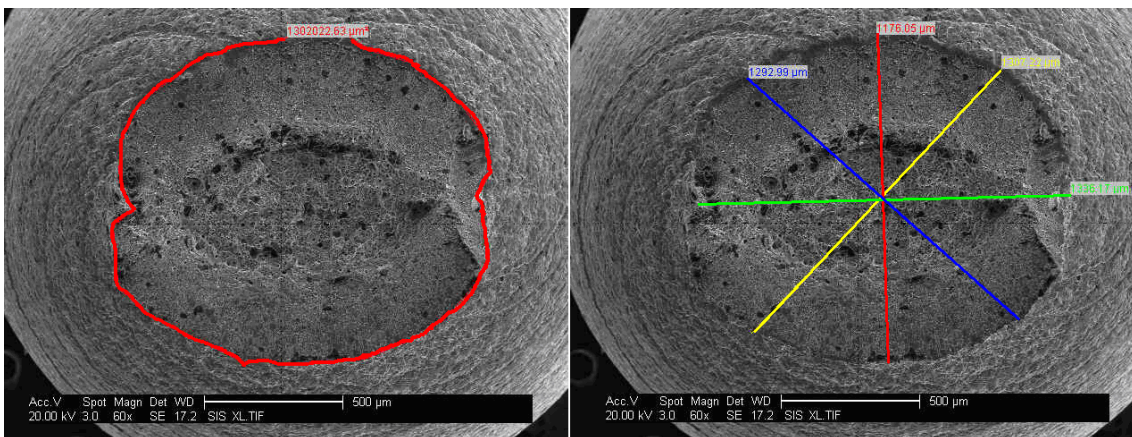


Figure 5.49: Measuring the fracture surface area of SDSS SAF2507 after SSR testing in 3.5% NaCl without charging at 50° C temperature

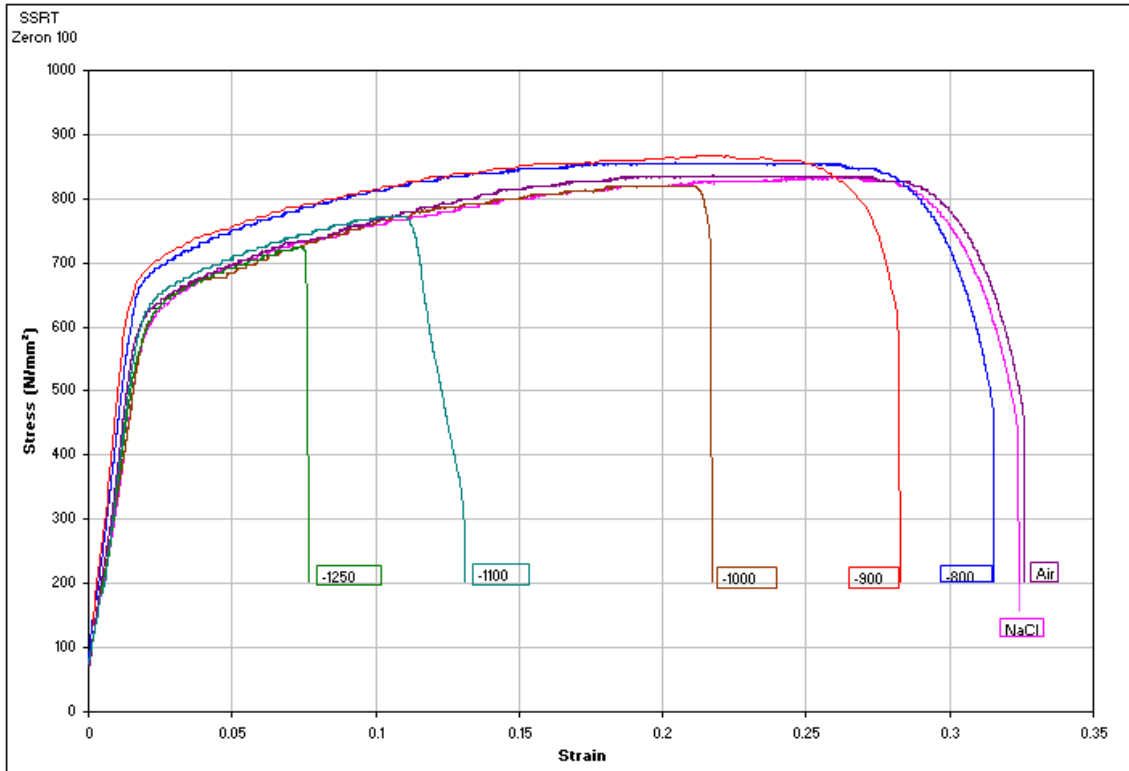


Figure 5.50 SSR Testing Stress vs. Strain for Zeron 100

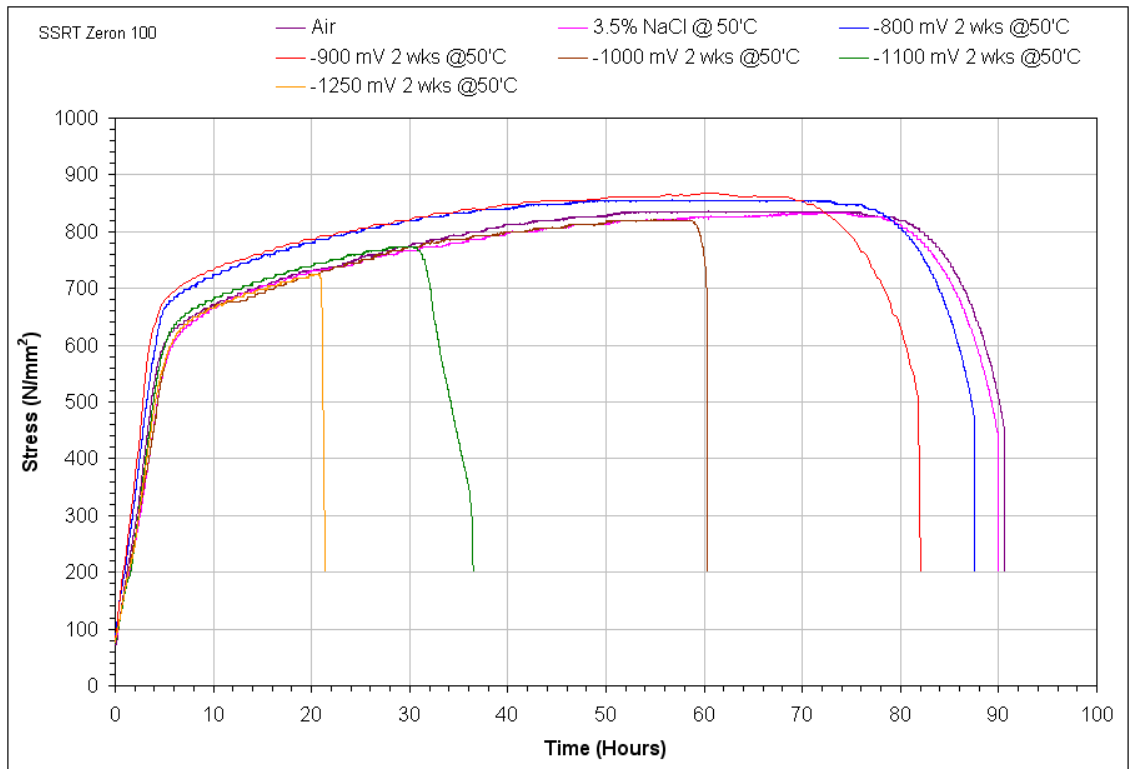


Figure 5.51: SSR Testing Stress vs. time for Zeron 100

5.8 Analysis of SSRT Results

The embrittlement indices, EI , were based on two parameters; time to failure (TTF) and percentage of reduction of area (% RA) that can be obtained from the slow strain rate test for air and precharged specimens. This relation is described by the following equations:

$$EI = 1 - \left(\frac{TTF_{Env}}{TTF_{Air}} \right) \qquad EI = 1 - \left(\frac{\% RA_{Env}}{\% RA_{Air}} \right)$$

Logically, when the embrittlement index (EI) is a number close to zero, it indicates a ductile behaviour. If the value of EI was greater or equal than 0.6¹⁴⁰ ($EI \geq 0.6$) the specimen was considered to be highly susceptible to hydrogen embrittlement. In the present work, the hydrogen embrittlement susceptibilities of super DSS Ferralium 255, SAF 2507 and Zeron 100 were evaluated by comparing EI values, based on the criteria described above.

Attention was paid to errors in order to be able to determine whether variations in material behaviour can make significant differences with the same experimental factors. Two specimens were tested for each condition for super DSS Ferralium 255 and SAF 2507 and the mean value was plotted together with the range of variation of each individual condition in each graph. Only one test was performed on super DSS Zeron 100 for each charging condition.

In terms of the ultimate tensile strength (UTS) and 0.2% proof stress, the slow strain rate tests did not show a significant difference between the specimens tested in air and those that were precharged (figure 5.70 and 5.71). However, it is possible to see clear differences when trying to compare the time to failure (TTF) percentage of reduction of area (% RA), and percentage of elongation (% Elong) with respect to the environments considering the effect of the hydrogen charging.

An examination of these results indicated that all the parameters were reduced due to the precharging of external electrochemical cathodic potentials to the test

specimen during straining comparing to the air test. SSRT in air indicated that all super DSS specimens were having a ductile fracture by with necking and cup and cone.

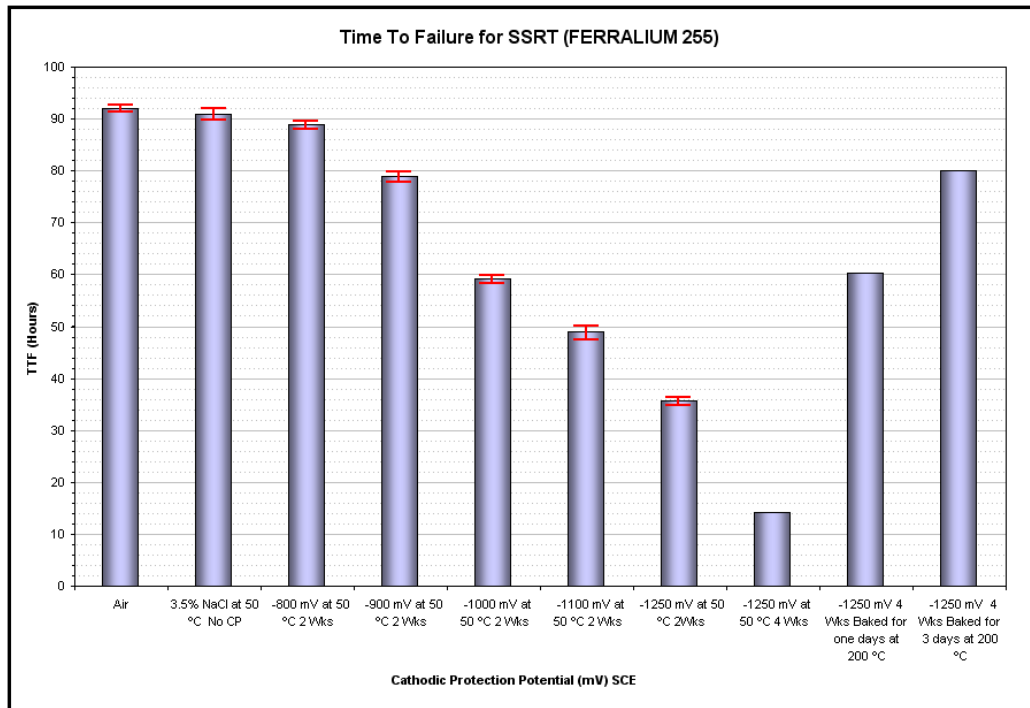


Figure 5.52: Time to failure (TTF) of all SSR testing for SDSS Ferralium 255

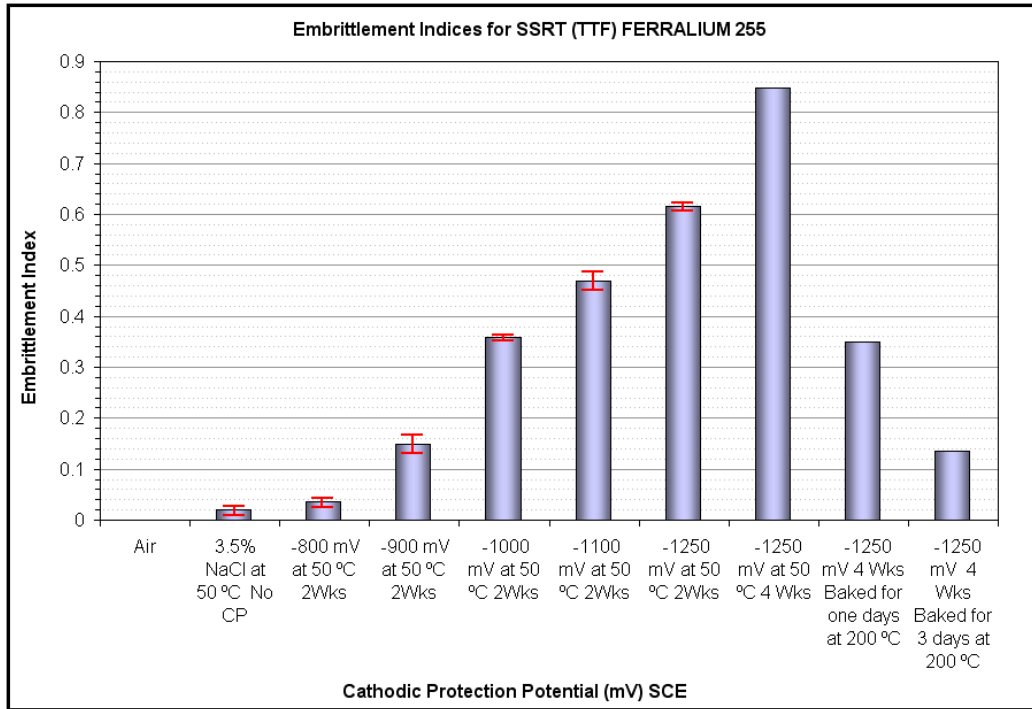


Figure 5.53: Embrittlement index after SSR testing for SDSS Ferralium 255, calculated from time to failure (TTF)

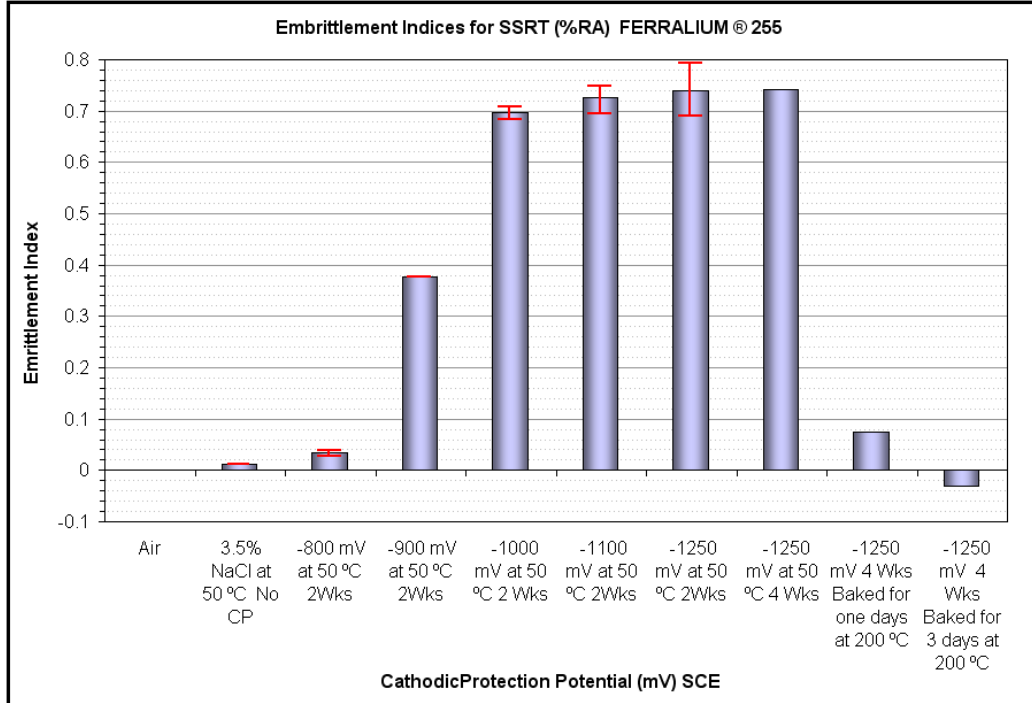


Figure 5.54: Embrittlement index after SSR testing for SDSS Ferralium 255, calculated from the percentage of reduction of area (%RA)

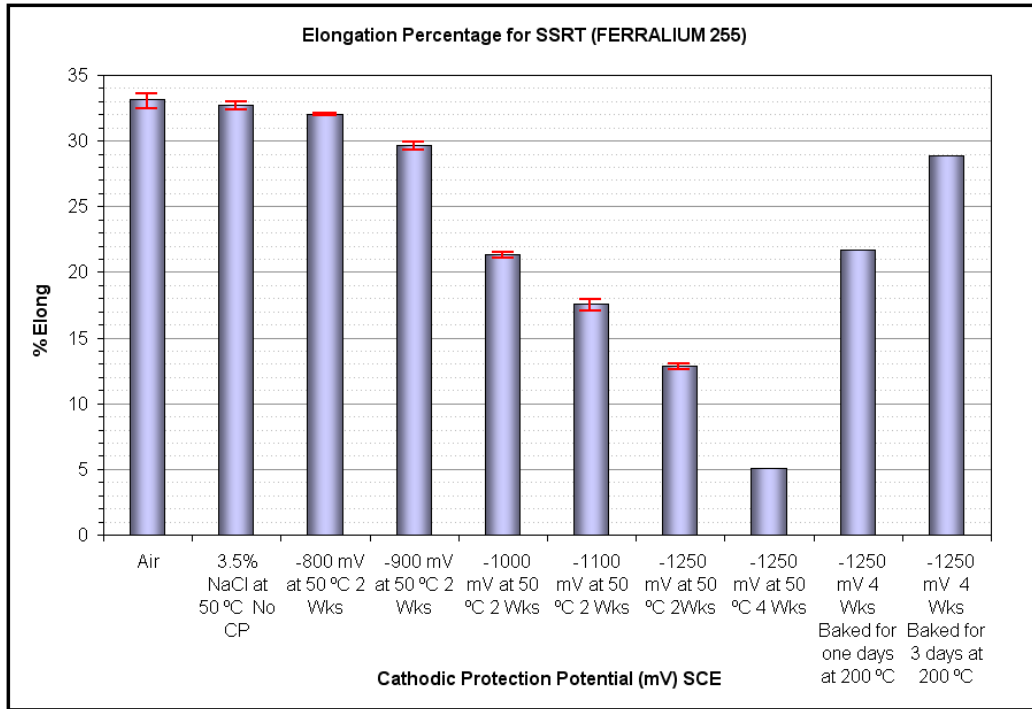


Figure 5.55: Percentage of the elongation (% Elong) of all SSR testing for SDSS Ferralium 255

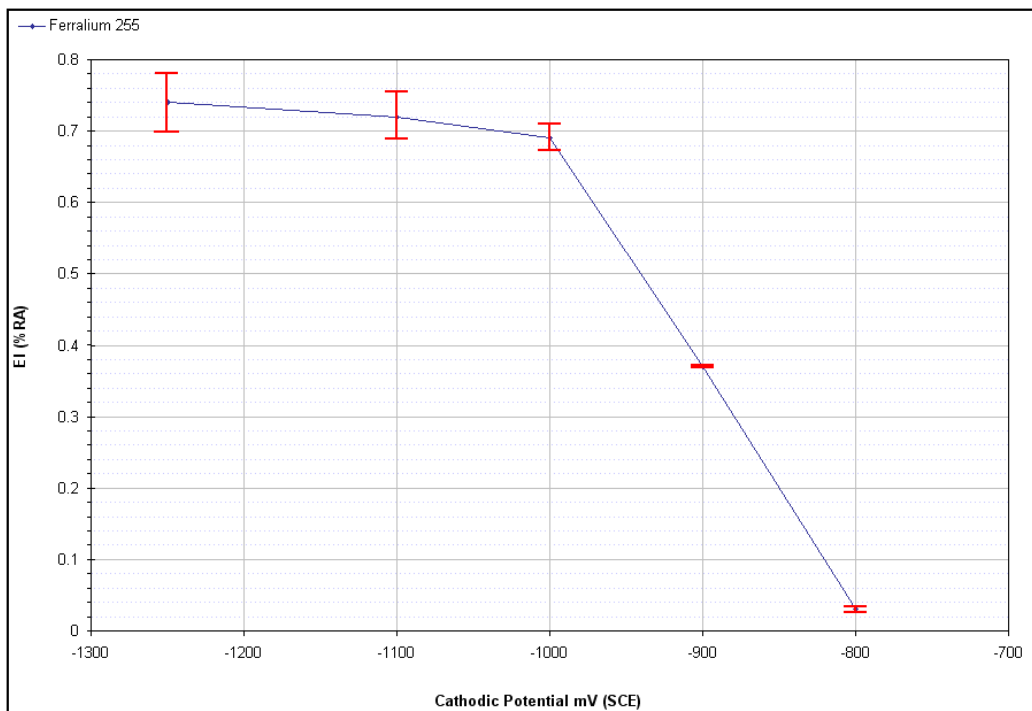


Figure 5.56: Embrittlement index Vs. cathodic potentials after SSR testing for SDSS Ferralium 255

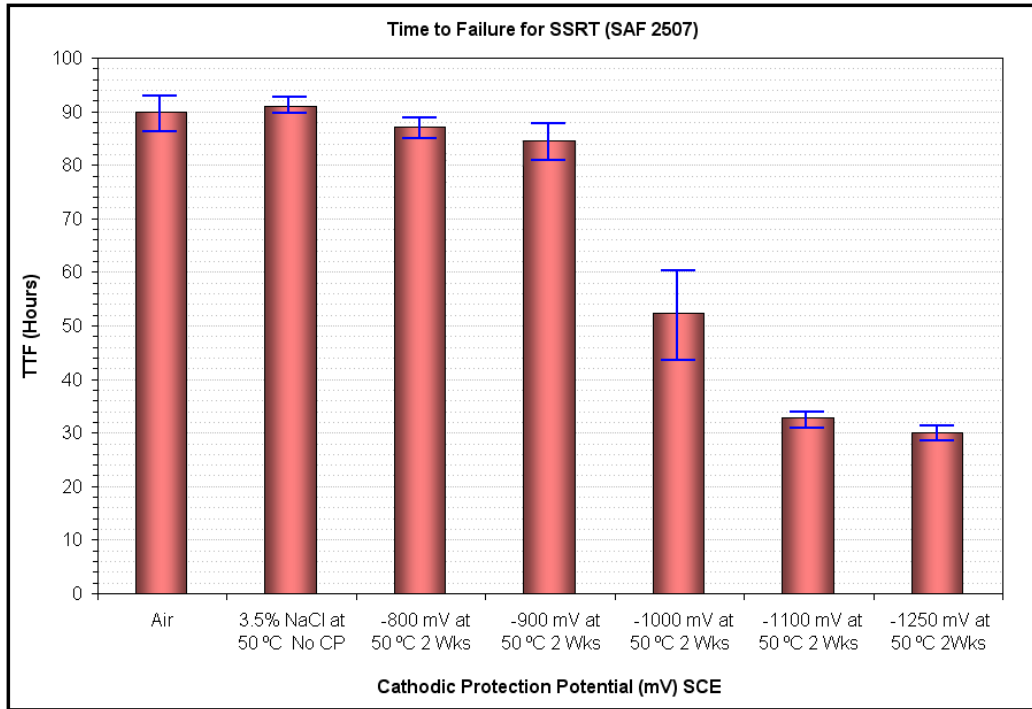


Figure 5.57: Time to failure (TTF) of all SSR testing for SDSS SAF 2507

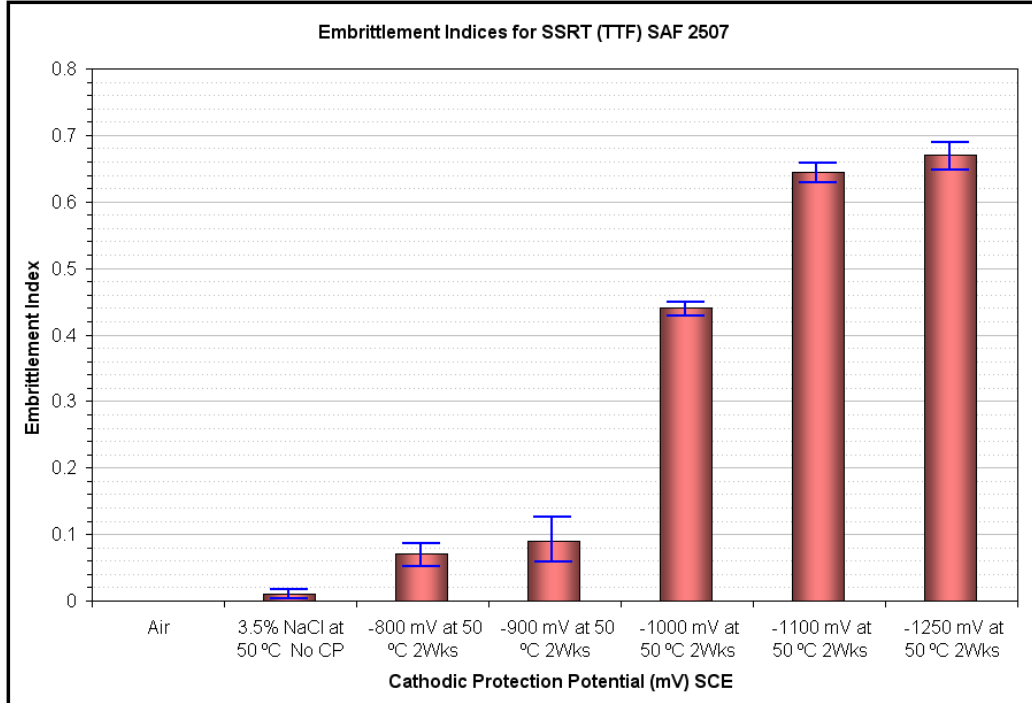


Figure 5.58: Embrittlement index after SSR testing for SDSS SAF 2507, calculated from the time for failure (TTF)

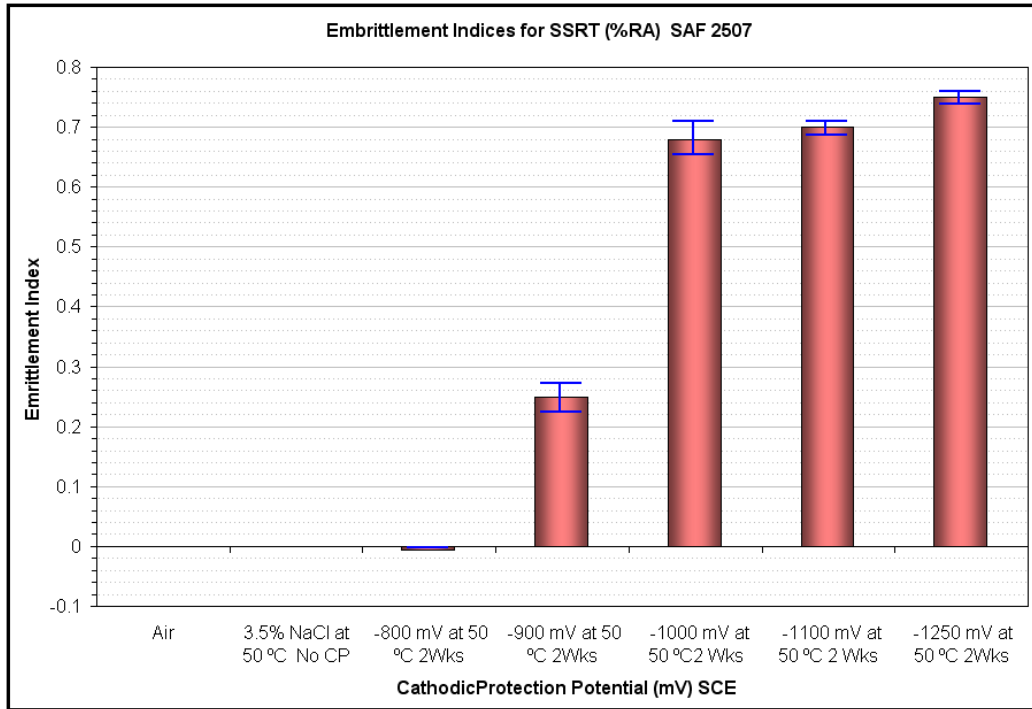


Figure 5.59: Embrittlement index after SSR testing for SDSS SAF 2507 calculated from the percentage of reduction of area (%RA)

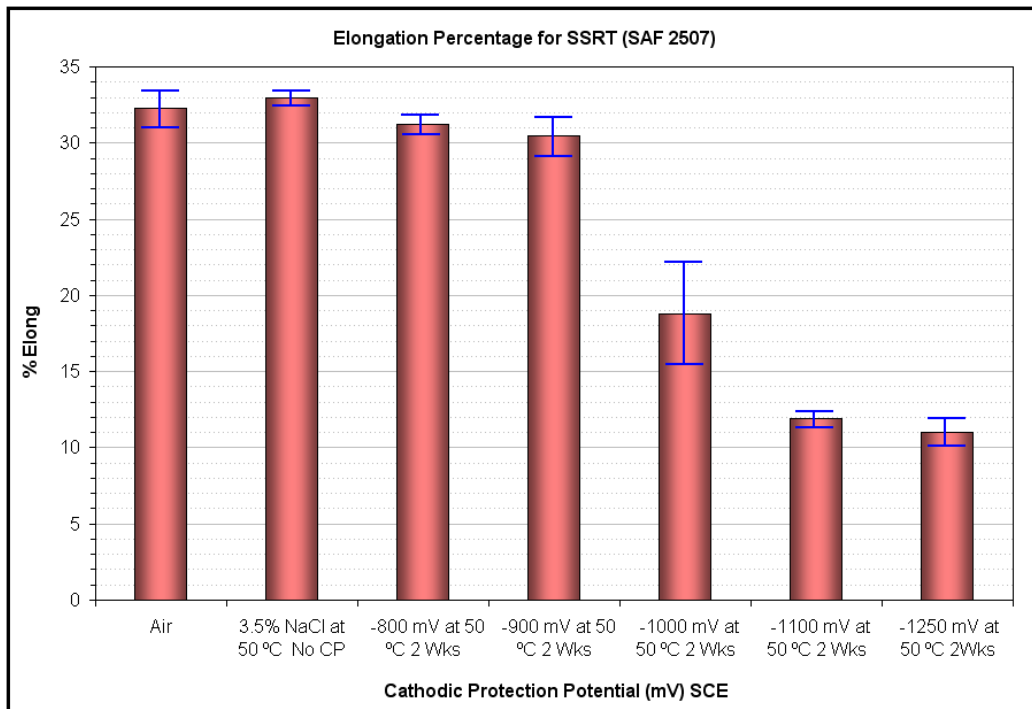


Figure 5.60: Percentage of the elongation (% Elong) of all SSR testing for SDSS SAF 2507

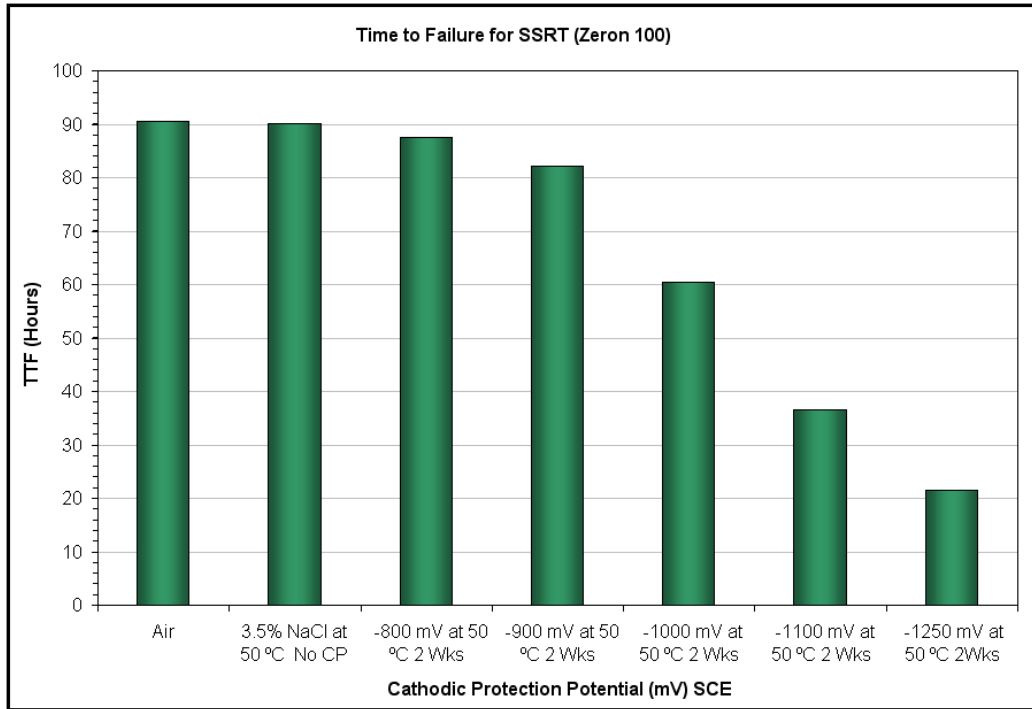


Figure 5.61: Time to failure (TTF) of all SSR testing for SDSS Zeron 100

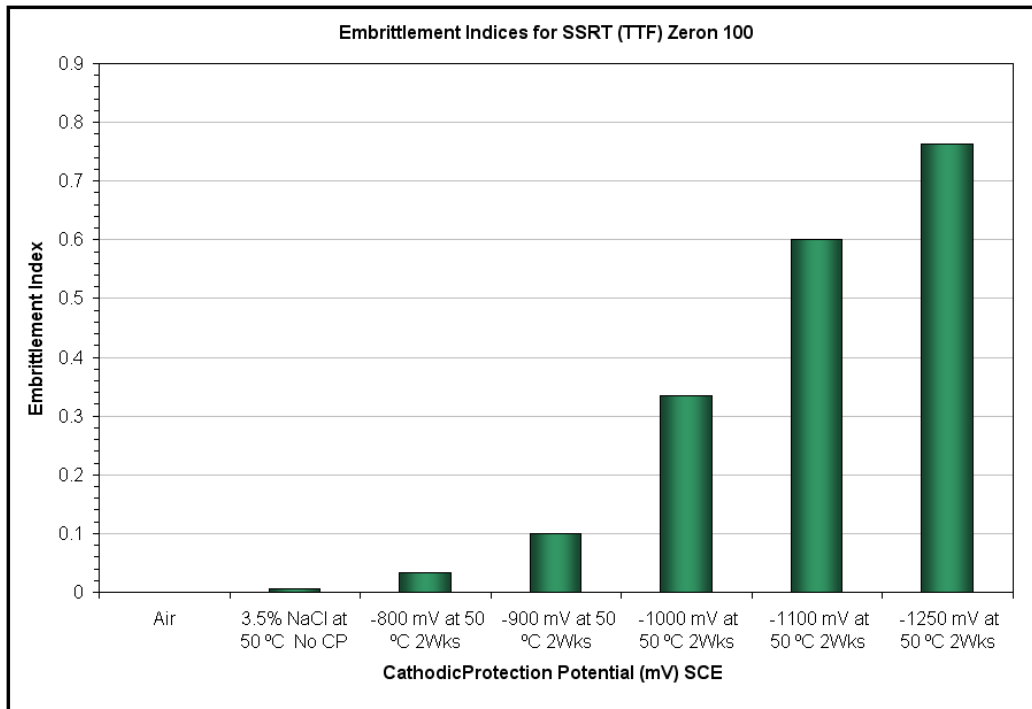


Figure 5.62: Embrittlement index after SSR testing for SDSS Zeron 100, calculated from the time for failure (TTF)

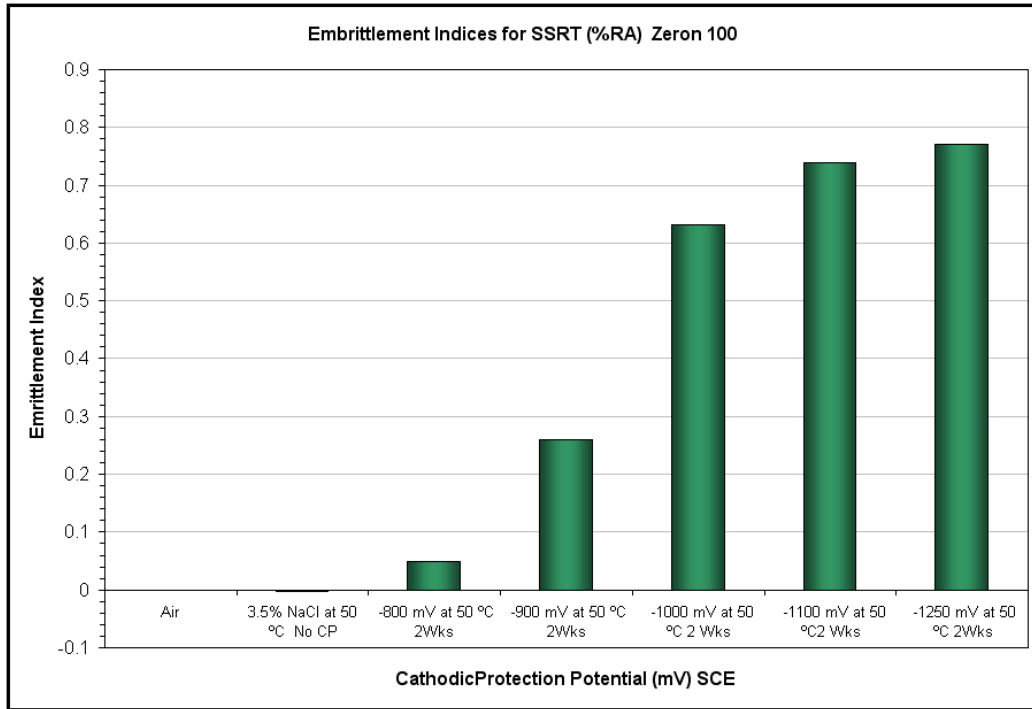


Figure 5.63: Embrittlement index after SSR testing for SDSS Zeron 100 calculated from the percentage of reduction of area (%RA)

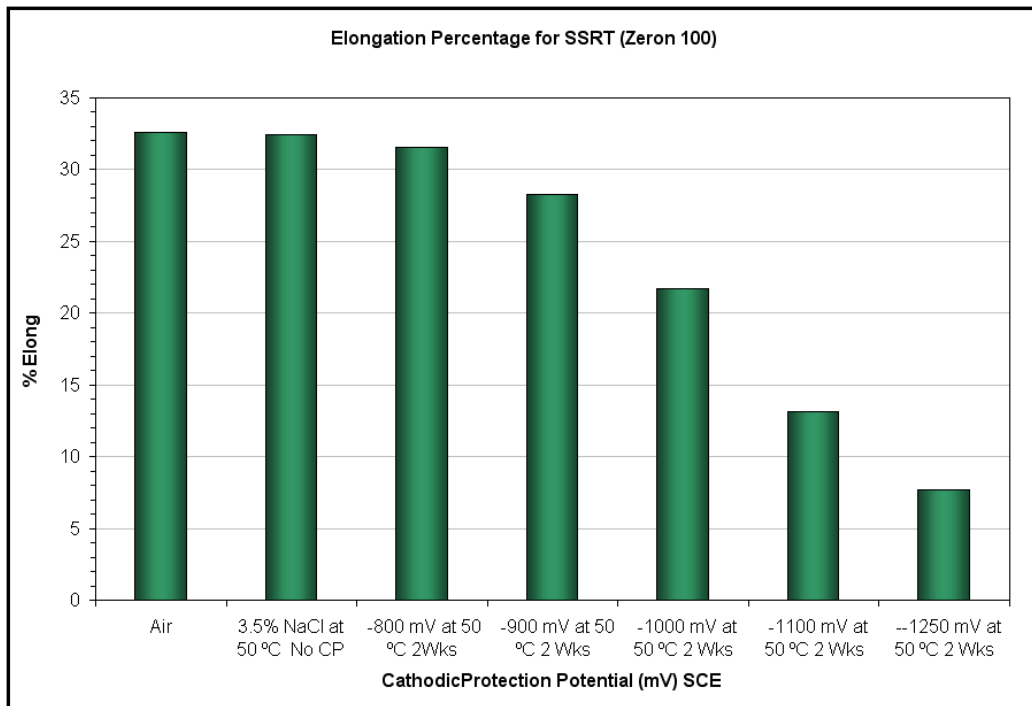


Figure 5.64: Percentage of the elongation (% Elong) of all SSR testing for SDSS Zeron 100

5.9 Comparison of SSRT

The slow strain test is a very aggressive method of testing due to the requirement of the specimen's failure. The results attained from this test for super DSS show signs of increased susceptibility to hydrogen embrittlement. By comparing the time to failure (TTF) after SSR test in air and in 3.5% NaCl at 50 °C, it can be seen that all the three super DSSs had a similar behaviour. The time to failure for all three alloys in air was in the range of 91 ± 1 hour as it can be seen in figure 5.65. Stress vs. strain plots behaviour for the three super DSSs in air also were similar where the percentage of the elongations was within the range of 33% as shown in figure 5.68.

When comparing results of the precharged specimens (-800 to -1250 mV SCE) in term of time to failure (TTF) and the percentage of elongation (% Elong), Ferralium had a better performance in the embrittling environment (figure 5.70). On the other hand, comparing the three alloys based on the embrittlement index calculated from the percentage of reduction, SAF 2507 had a better performance than the other two alloys. The evaluation of this performance is valid when comparing the potentials of -900, -1000, and -1100 mV (SCE). These potentials can simulate the cathodic protection that is used as a protection in the service field.

A comparison of the mechanical properties after the slow strain rate test of super DSSs, Ferralium 255, SAF 2507 and Zeron 100, specimens are shown in figures 5.72 and 5.73. It can be seen that there was no significant loss in the strength level. The ultimate tensile strength and the 0.2% proof strength for all three materials were similar and within the design safety. Usually the design safety factor set to a maximum level of load at approximately $\frac{2}{3}$ proof strength for structural engineering components. However, the load that was applied in the slow strain rate test has exceeded the load that represents the design condition. It should be assumed that the applied cathodic potential is a determining factor in the field only under conditions where the load is close to the yield strength^{141, 142}. The ductility has been greatly reduced by the

application of the embrittling environment (more negative potential) but the cracking occurred after reaching the proof strength.

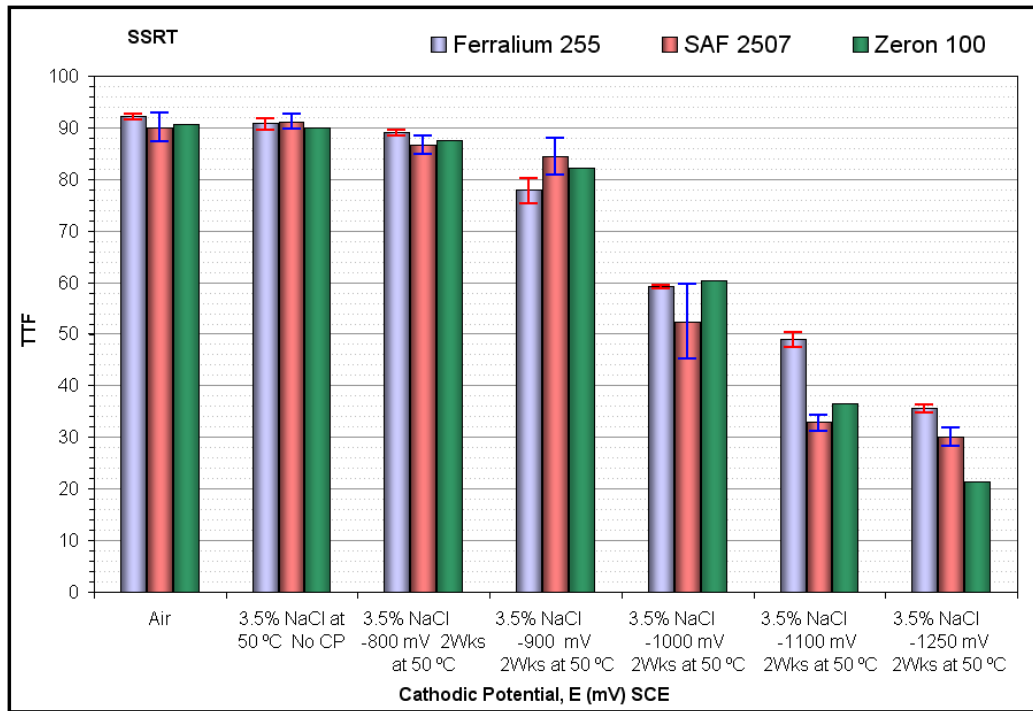


Figure 5.65: Comparison of Time to failure (TTF) for all three super DSSs after SSR testing

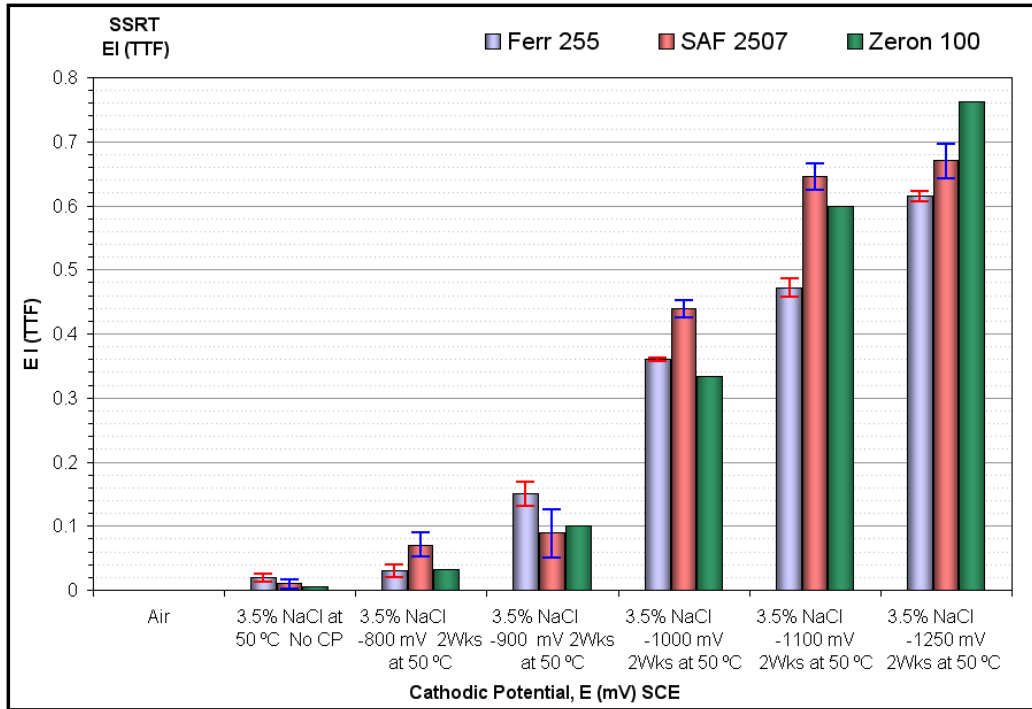


Figure 5.66: Comparison of embrittlement indices of all three super DSSs after SSR testing, calculated from time for failure (TTF)

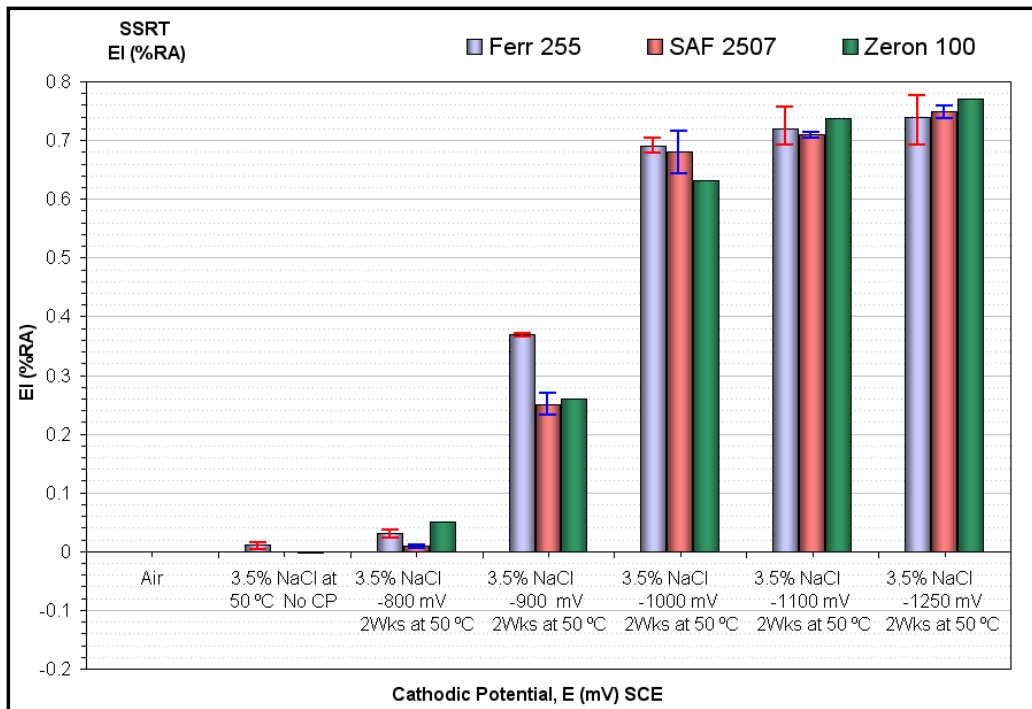


Figure 5.67: Comparison of embrittlement indices of all three super DSSs after SSR testing calculated from the percentage of reduction of area (%RA)

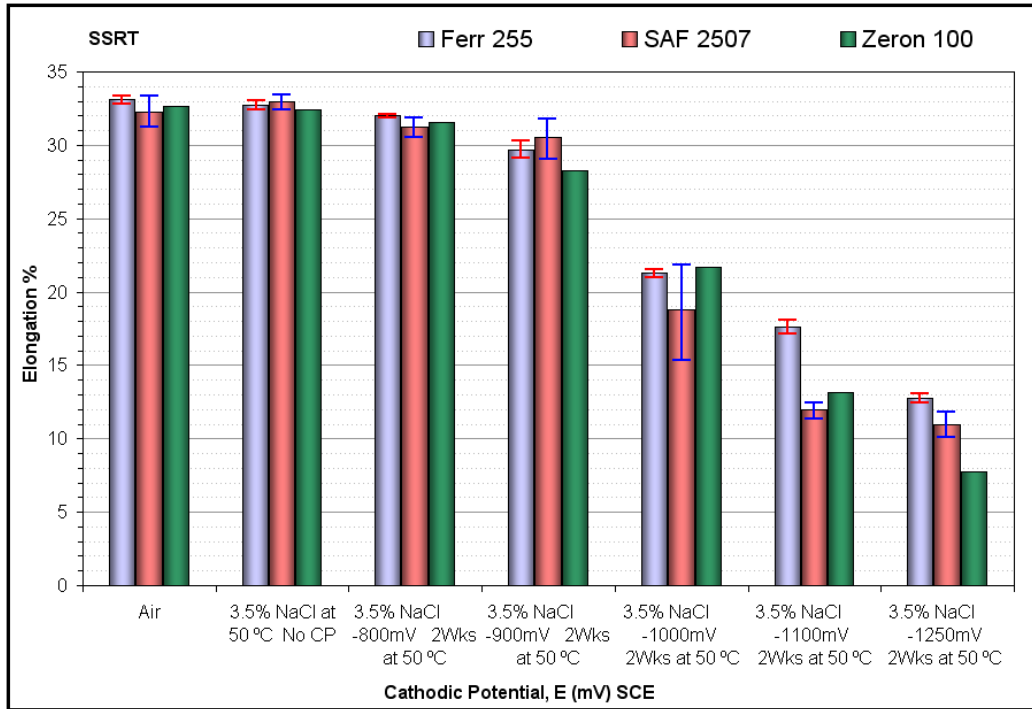


Figure 5.68: Comparison of percentage of elongation (% Elong) of all three super DSSs after SSR testing

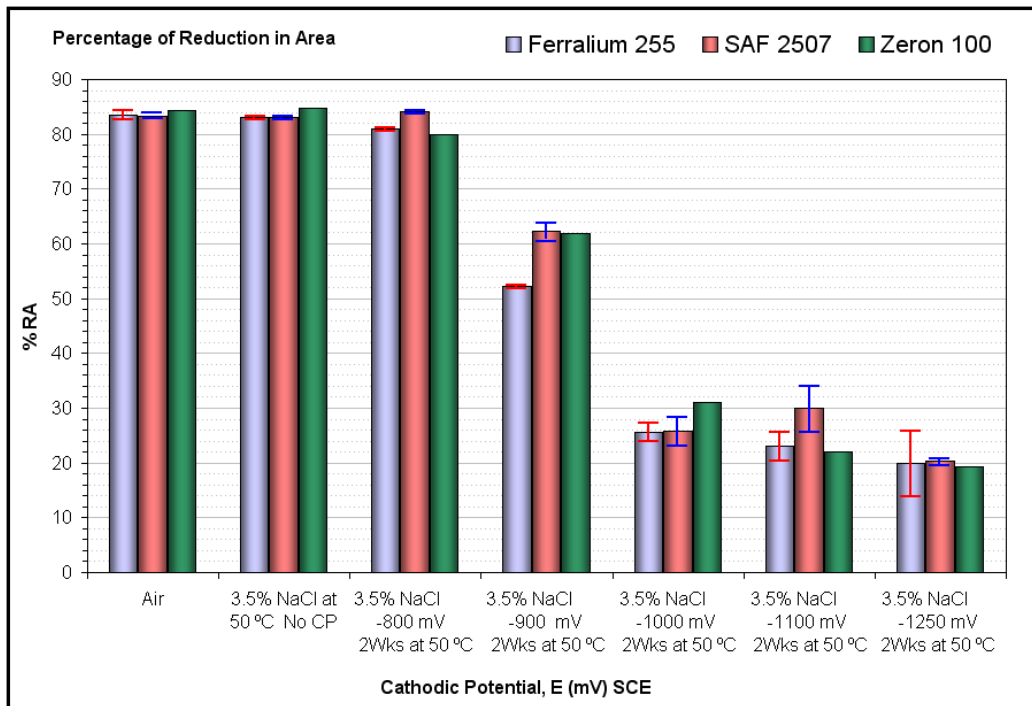


Figure 5.69: Comparison of Percentage of reduction in area (%RA) of all three super DSSs after SSR testing

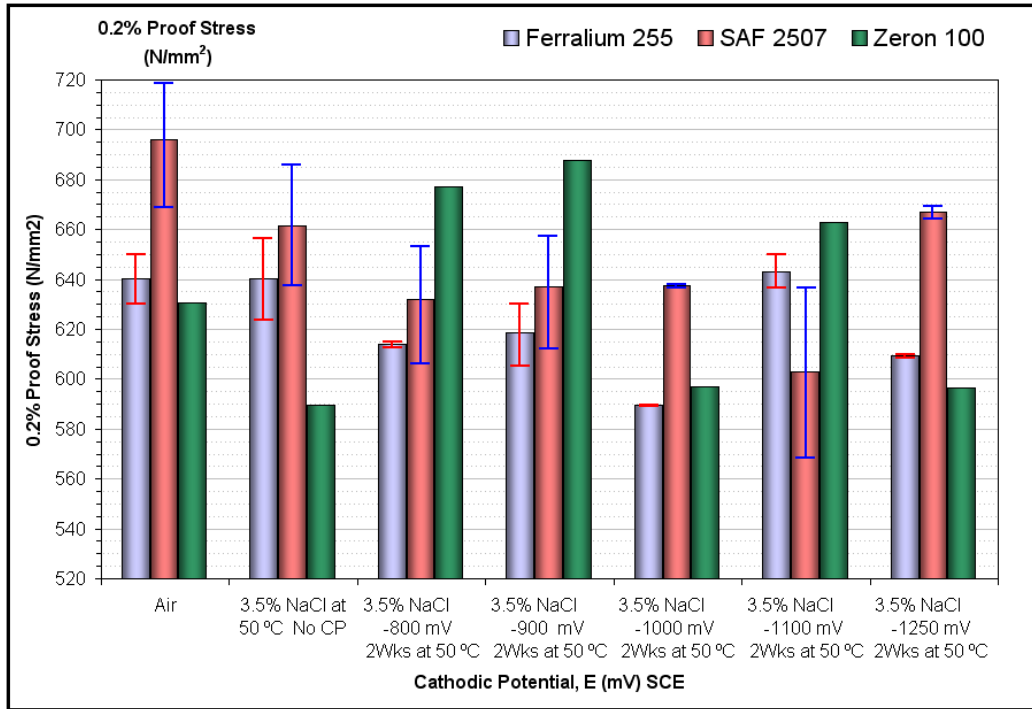


Figure 5.70: Comparison of 0.2% proof stress of all three super DSSs after SSR testing

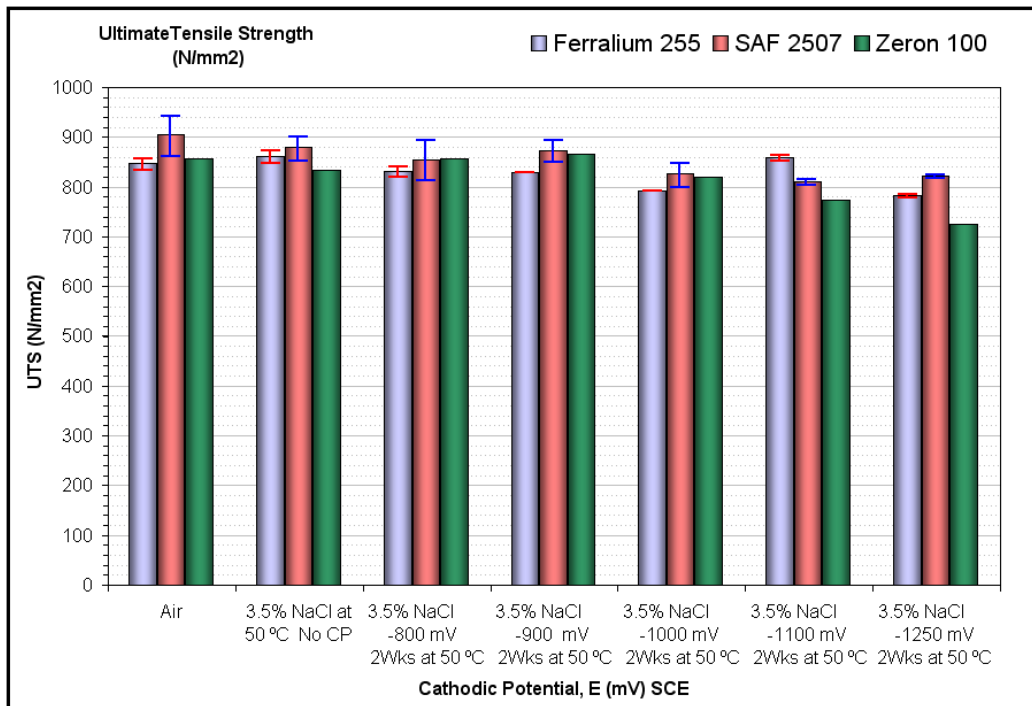


Figure 5.71: Comparison of ultimate tensile strength (UTS) of all three super DSSs after SSR testing

5.10 Fractography Analysis

By observing the SEM images of the fracture surface of the specimens tested in air and at different potentials, a noticeable change in the brittle and ductile failure mode can be observed as shown in figures 5.67 to 5.71. The brittle mode of the fracture surface increased at more negative potentials. The proportion of ductile and brittle fracture modes on the fracture surface can be related to the amount of hydrogen that diffused into the specimens and how far it penetrated toward the centre.

SSR testing in air at room temperature and 3.5% NaCl at a temperature of 50 °C indicated that all super DSS specimens undergo ductile fracture by elastic-plastic deformation. In ductile fracture by elastic plastic deformation voids were developed within the necked region of the specimens and coalescence of voids occurred to produce an internal crack by normal shear rupture. Development of voids in ductile fracture surface can be seen in the form of dimples in the microstructure.

At a potential of -800 mV (SCE) there is no marked loss in ductility for all three super DSSs as seen in figure 5.66, 5.67 and 5.68. This indicates that the amount of hydrogen absorbed at the metal surface was not sufficient to cause embrittlement. The fractographic analysis of the specimen at a precharged potential of – 800 mV (SCE) shows that the failure was by microvoid coalescence and no clear brittle fracture had occurred.

At a potential of – 900 mV (SCE) a loss in ductility was observed indicating that the hydrogen concentration had reached a level capable of causing embrittlement. The embrittlement was observed at the fracture surface edge while it was ductile dimple in the centre of the specimen.

At a potential of – 900 mV (SCE) and below a greater loss of ductility was observed as a result of more hydrogen entering the tensile specimens. These precharged specimens subjected to SSRT indicated failure by brittle fracture without necking or cup and cone. The fracture surface shows features

resembling those of hydrogen embrittlement indicating thereby the possibility of hydrogen damage during cathodic precharging.

A larger area of embrittlement was seen on the edges of the fracture surface indicating that more hydrogen was entering the specimen. The centre region of all fracture surface specimens was identified as a ductile fracture indicating that the hydrogen precharging time was not enough for sufficient hydrogen to reach the centre of the specimen.

5.11 Cracking Profile

Metallographic observations of the prepared cross sections of the precharged specimens were done for studying morphology and propagation of the cracks upon completion of SSR testing. These graphs exhibited secondary cracks with branches along the gauge length of the tested specimens as shown in figures 5.72 and 5.73. Cracks propagated perpendicularly to the applied load, passing through the ferrite phase and stopped their propagation at the boundary of the austenite phase for precharged specimens during the SSR testing, as shown in figure 5.75. An internal micro crack was observed and stopped in its travel through the ferrite by an austenite grain as shows in figure 5.75 and 5.76. The general observation for most of the metallographic cross section concerning the crack profile is that propagation of the cracks was preferentially in the ferrite microstructure and where austenite grains were poorly distributed in comparison to the bulk austenite distributions. The crack propagation must encounter austenite grains several times before fracture failure indicating that the austenite phase presents a blocking resistance to crack propagation. This argument led us to consider the austenite grain size and distribution as the key microstructural parameter of super DSS to impact fracture resistance to hydrogen embrittlement.



Figure 5.72: Optical micrograph of crack profile on failed cross section of super DSS SAF 2507 precharged at -1250 mV for 2 weeks



Figure 5.73: Optical micrograph of crack profile on failed cross section of super DSS Ferralium 255 precharged at -1250 mV for 2 weeks

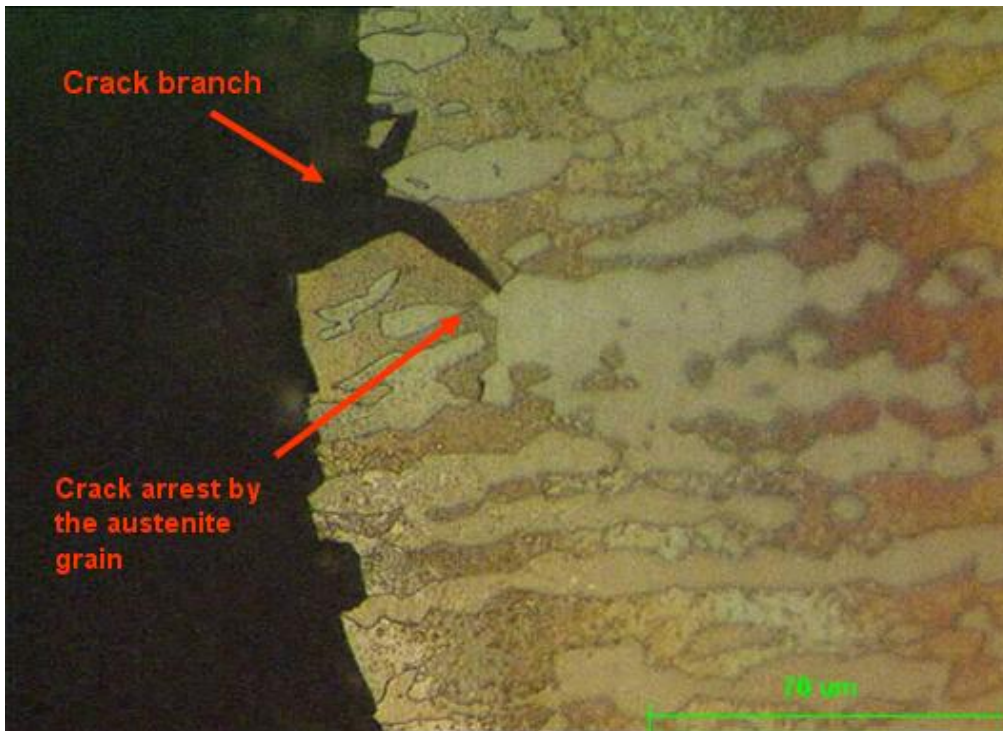


Figure 5.74: Optical micrograph of sectioned fracture surface of SDSS specimen of Ferralium 255 precharged at -1250 mV (SCE) for 4 weeks in 3.5% NaCl at 50° C, the crack occurred in the ferrite phase and was blocked by the austenite phase.



Figure 5.75: Optical micrograph of internal microcrack on failed cross section of super DSS SAF 2507 precharged at -1250 mV for 2 weeks



Figure 5.76: Optical micrograph of internal microcrack on failed cross section of super DSS SAF 2507 precharged at -1250 mV for 2 weeks

5.12 Hydrogen Diffusion Coefficient

This section shows results of hydrogen diffusion coefficients for low carbon steel and three super DSS alloys membranes. Potentiostatic hydrogen permeation and galvanostatic measurements methods were used to calculate the hydrogen diffusion coefficient for low carbon steel and super DSSs Ferralium 255, SAF 2507 and Zeron 100.

5.12.1 Hydrogen Permeation Measurements

5.12.1.1 Cold Rolled Carbon Steel Shim

Hydrogen transport in the carbon steel was measured using the hydrogen permeation cell which was explained previously. The aim of this test was to measure hydrogen diffusion coefficient by using two different equations. Hydrogen atoms generated on the charging side of the membrane by cathodic polarization can diffuse into the metal. On the exit side of the membrane,

hydrogen atoms are oxidized (oxidation reaction) producing a current which is a measurement of hydrogen permeation rate. The transient curves for the hydrogen permeation current on the oxidation cell (exit side) for different applied potentials in room temperature are shown in figure 5.77.

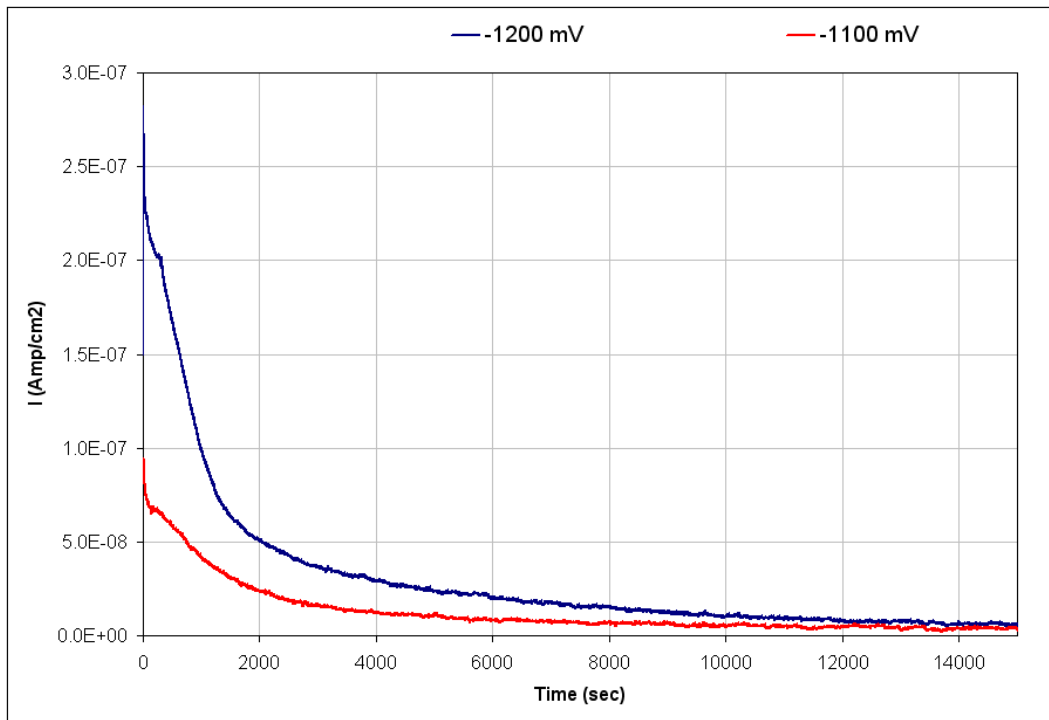


Figure 5.77: Hydrogen Depletion Transient for cold-rolled Low Carbon Steel Shim in 0.2 M NaOH Solution with different charging potentials vs. (SCE)

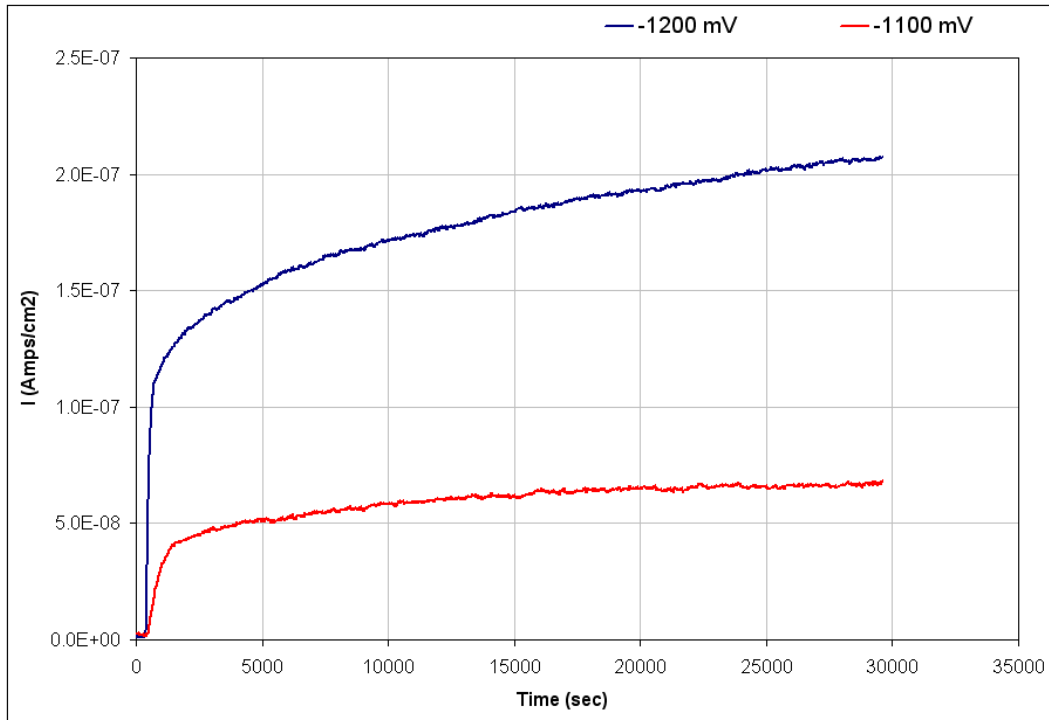


Figure 5.78: Hydrogen Permeation Transient for cold-rolled Low Carbon Steel Shim in 0.2 M NaOH Solution with different charging potentials vs. (SCE)

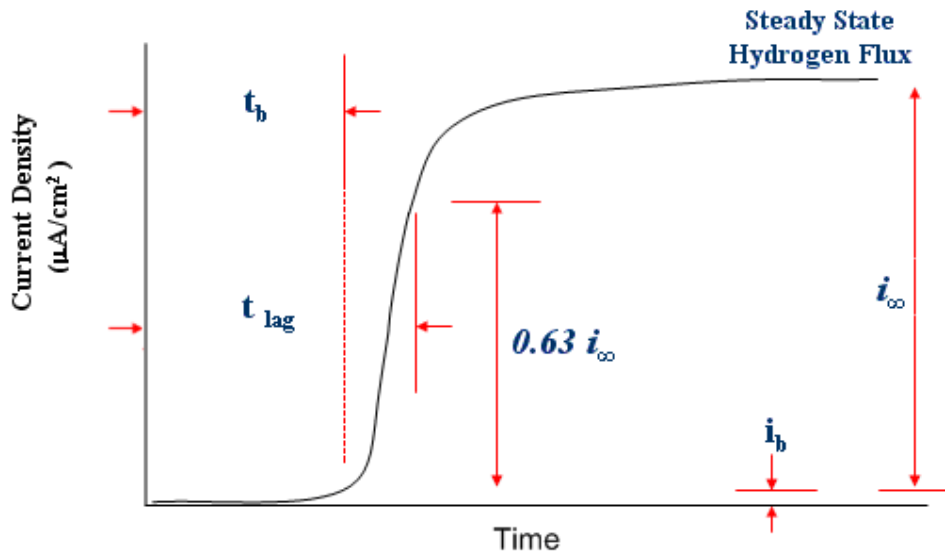


Figure 5.79: graphical illustration of the permeation curve at a potential of -1250 mV (SCE)

From the illustrated graph (figure 5.79), it can be seen that the breakthrough time, t_b , is the time for the first hydrogen to penetrate or exit through the

thickness (L) of the metal test membrane. The "breakthrough time" can be thought of as the point on the permeation curve in which the anodic current first begins to increase¹²³. The t_{lag} refers to the time lag which defined as the time at which the anodic current density is 0.63 of the steady state current density i_{∞} ¹²⁴.

From the permeation curve in figure 5.78, the break through time was 144 seconds while the time lag was 460 seconds. The hydrogen diffusion coefficient (D) for carbon steel is calculated by using the following formula:

$$D = \frac{L^2}{6 t_{lag}} = \frac{(0.0055)^2}{6 (460)} = 1.1 \times 10^{-8} \text{ cm}^2 \text{ s}^{-1}$$

$$D = \frac{L^2}{15.3 t_b} = \frac{(0.0055)^2}{15.3 (154)} = 1.3 \times 10^{-8} \text{ cm}^2 \text{ s}^{-1}$$

As observed, the hydrogen diffusion coefficients calculated from t_{lag} and t_b methods were found to be consistence with each other. The mean value for both methods is $1.2 \times 10^{-8} \text{ cm}^2/\text{s}$.

The cold rolled carbon steel shim has a lower diffusion coefficient value than carbon steel because of the microstructure. The microstructure had a very important consideration in the development of hydrogen charging and permeation process. The effect of the cold work was resulting in grains being elongated along the rolling direction texture. This difference in the grain shape and dimension increases the dislocation density which acts as low energy traps sites. This process makes the amount of hydrogen permeating through it is low, thus a lower hydrogen diffusion coefficient value than carbon steel.

5.12.1.2 Carbon Steel 1 mm

The hydrogen permeation result with the measured current against time of low carbon steel 1 mm thick sheet as a result of the cathodically applied potential in 0.2 M NaOH is shown in figure 5.80. The potentiostatically applied potential was -1200 mV (SCE). The current is seen to be increased slowly attaining a steady state value of 0.3415 Amps/cm² after about 26 hours.

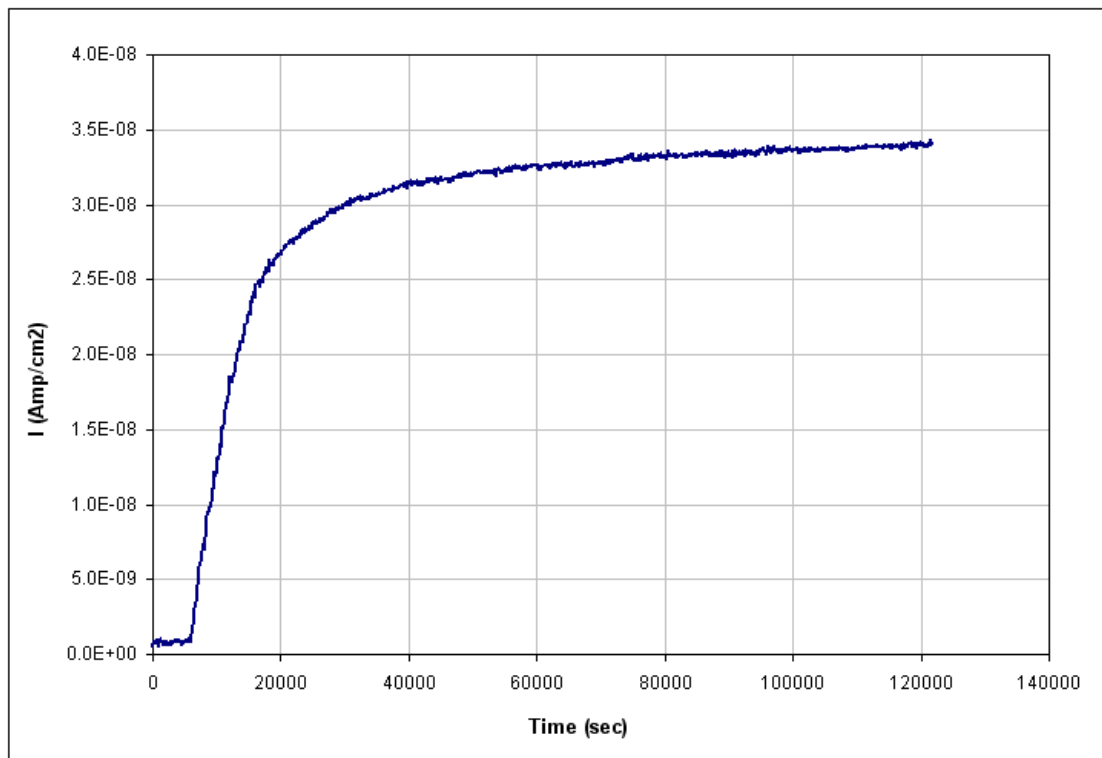


Figure 5.80: Permeation transient for 1 mm thick of low carbon steel membrane cathodically charged at -1200 mV (SCE)

The time lag t_{lag} was calculated to be as followed:

$$\begin{aligned}t_{lag} &= 0.63 i_{\infty} \\ &= 0.63 (0.3325) \\ &= 0.209 \text{ amps/cm}^2\end{aligned}$$

These values have been used for the evaluation of the diffusion coefficient (D) of 1 mm carbon steel membrane at room temperature based on the following relationship:

$$D = \frac{L^2}{6 t_{lag}} = \frac{(0.1)^2}{6 (14200)} = 1.1 \times 10^{-7} \text{ cm}^2 \text{ s}^{-1}$$

$$D = \frac{L^2}{15.3 t_b} = \frac{(0.1)^2}{15.3 (6175)} = 1.06 \times 10^{-7} \text{ cm}^2 \text{ s}^{-1}$$

As observed, the hydrogen diffusion coefficients calculated from t_{lag} and t_b methods were found to be consistent with each other. The mean value for both methods is $1.08 \times 10^{-7} \text{ cm}^2/\text{s}$.

5.12.1.3 Super DSS Ferralium 255

The hydrogen permeation transient for the 1mm thick membrane of Ferralium 255 is shown in figure 5.81. The hydrogen permeation test was run over a period of 3 months at a cathodic potential of -1200 mV (SCE) and a temperature of 50 °C in 0.2M NaOH solution. The breakthrough time, t_b , value obtained from the graph was $4.7 \times 10^6 \text{ sec}$ (54.6 days).

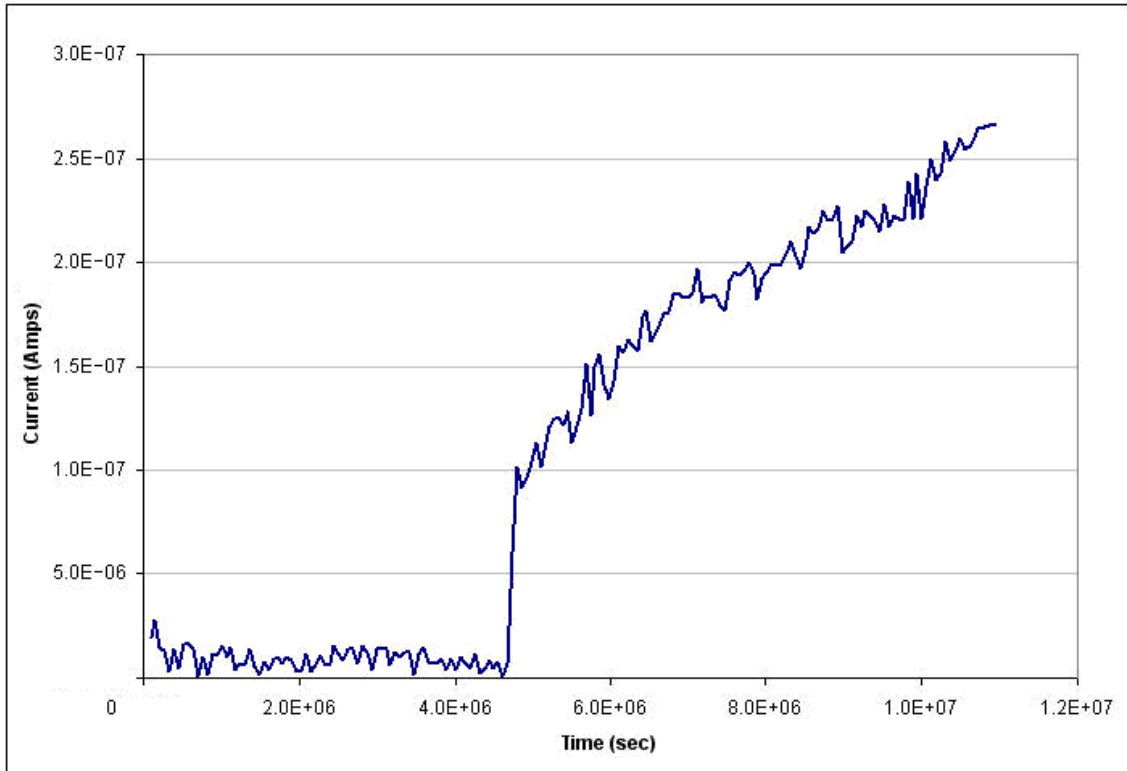


Figure 5.81: Hydrogen Permeation Transient for SDSS Ferralium 255 in 0.2 M NaOH Solution at 50° C with charging potential of -1200 mV vs. (SCE)

From the permeation curve, the hydrogen diffusion coefficient (D) for the duplex stainless steel Ferralium 255 was calculated by using the following formula:

$$D = \frac{L^2}{15.3 t_p} = \frac{(0.1)^2}{15.3 (4.72 \times 10^6)} = 1.38 \times 10^{-10} \text{ cm}^2 \text{ s}^{-1}$$

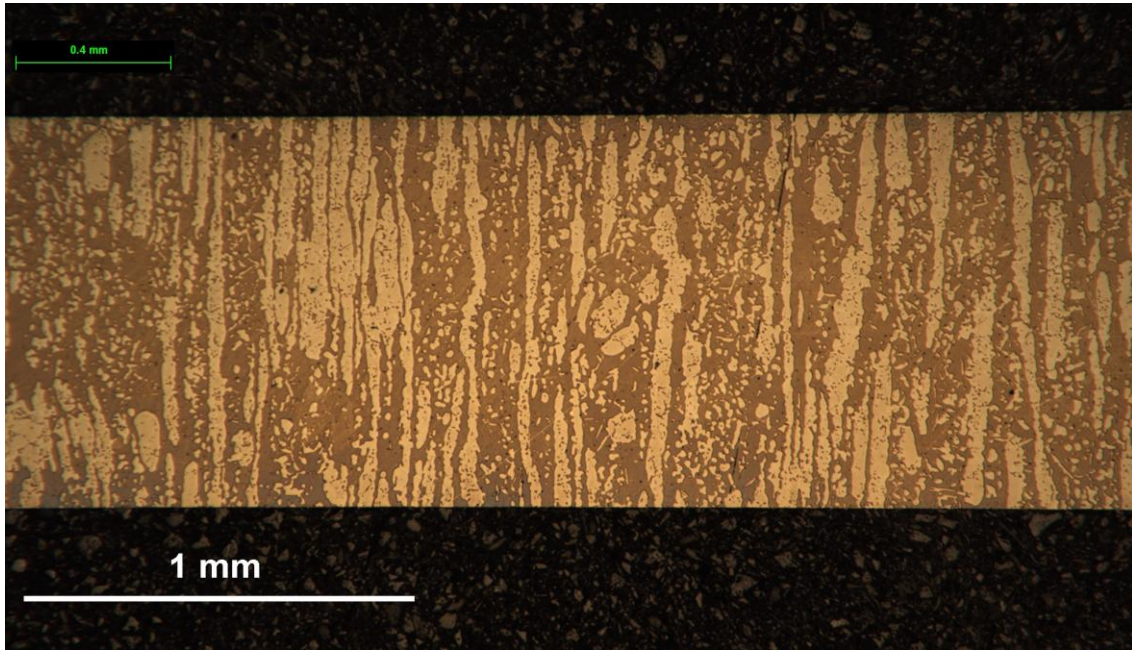


Figure 5.82: Cross section of 1 mm thick membrane used in the permeation test for super DSS Ferralium 255 showing the direction of the austenite grains

5.12.1.4 Super DSS SAF 2507

The transient curve for the hydrogen permeation current on the oxidation cell (exit side) is shown in figure 5.83. The breakthrough time, t_b , value obtained from the graph was 4.6×10^6 sec (53.3 days).

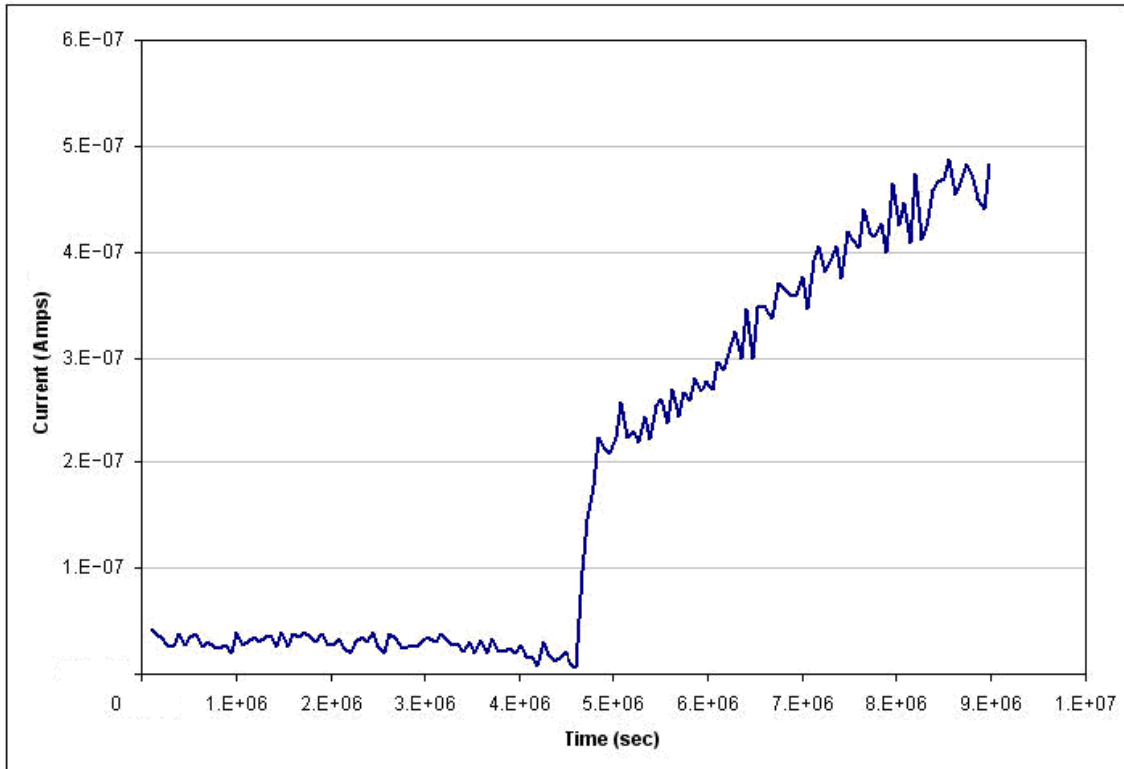


Figure 5.83: Hydrogen Permeation Transient for SDSS SAF 2507 in 0.2 M NaOH Solution at 50° C with charging potential of -1200 mV vs. (SCE)

From the permeation curve, the hydrogen diffusion coefficient (D) for the duplex stainless steel SAF 2507 was calculated by using the following formula:

$$D = \frac{L^2}{15.3 t_b} = \frac{(0.1)^2}{15.3 (4.61 \times 10^6)} = 1.42 \times 10^{-10} \text{ cm}^2 \text{ s}^{-1}$$

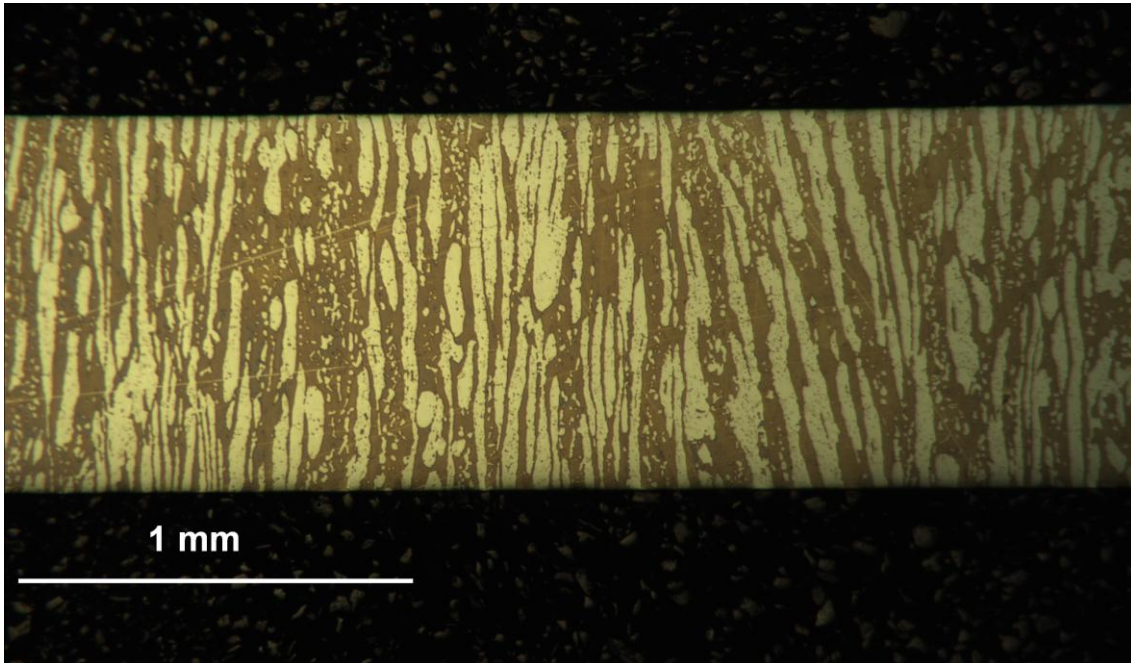


Figure 5.84: Cross section of 1 mm thick membrane used in the permeation test for super DSS SAF 2507 showing the direction of the colonies of the austenite grains

The error in the hydrogen diffusion coefficients were assessed from the equation on page 134. Considering the variation of each membrane thickness, a standard deviation value was calculated after measuring four different areas of the membranes with a Multimoyo micrometer (0.001 mm precision). Similarly, standard deviations of diffusion coefficient were calculated as shown in table 5.4. Similarly, standard deviations were calculated for the breakthrough times, obtained from the permeation measurements. The combined errors from thickness measurements and breakthrough times resulted in standard deviation in D values as shown in table 5.4.

Alloy	Membrane Thickness (cm)	SD (L) (cm)	SD (t_b) (sec)	D (cm²/s)
Cold rolled carbon steel shim	0.0055	1.25×10^{-4}	4	$1.1 \pm 0.05 \times 10^{-8}$
Carbon steel	0.1	5×10^{-3}	33	$1.1 \pm 0.1 \times 10^{-7}$
Ferralium 255	0.1	4×10^{-4}	30000	$1.38 \pm 0.01 \times 10^{-10}$
SAF 2507	0.1	4×10^{-3}	30000	$1.42 \pm 0.12 \times 10^{-10}$

Table 5.4: Comparison of hydrogen diffusion coefficient using the permeation technique

The permeation tests for super duplex stainless steels were technically more difficult, particularly because of the long term test, usually several weeks. The calculations were based on only the time break through method since the time to reach the steady state current will take much longer than several weeks. It was confirmed from the carbon steel permeation test that this method is reliable as well as the steady state and time lag methods.

The diffusion coefficient is a measure of ease of hydrogen movement or transport in a material. If the material has high density of dislocations as a consequence of cold work, these sites will reduce the diffusivity of hydrogen by the effect of irreversible trapping as mentioned earlier. The effect of the grain size is another parameter that impacts the hydrogen transport in metals. The specimens of super DSSs, Ferralium 255 and SAF 2507, obtained for the hydrogen permeation measurements were having the same thickness with particular microstructure. The microstructure is a feature that affects the

hydrogen diffusion and consequently its permeability and solubility. The microstructure of Ferralium 255 and SAF 2507 are shown in figures 5.1 and 5.3 for the longitudinal sections respectively. The grains of the austenite for super DSS SAF 2507 are more elongated and narrower comparing to super DSS Ferralium 255 and Zeron 100. Table 5.4 shows the list of the three alloys with corresponding grain size and length. The area and length of grains were calculated based on 50 points counts for the longitudinal and transverse sections. The results obtained from the hydrogen permeation measurement showed that the diffusion coefficient for super DSS SAF 2507 is slightly lower than Ferralium 255. This is thought to be due to the smaller grains size of the austenite phase. Table 5.4 shows a summary of the austenite grain size and area of the super DSS Ferralium 255 and SAF 2507. Austenite behaves differently in term of hydrogen diffusion and it has a higher solubility and much lower diffusion coefficient. The diffusion coefficient for the austenite is much less than that of the ferrite. Also the solubility is estimated to be 30 times higher³⁹.

Hydrogen atoms diffuse within the unit cell and after reaching the grain boundaries they are retained, thereby spending more time than in the initial case, and consequently suffer low diffusivity and permeation. Since grain boundaries act as irreversible trapping sites, then hydrogen tend to recombine and form molecules within the grain boundaries, as will be discussed in the General Discussion section. Therefore, if the specimen has a small grain size, the grain boundary length (the grain boundary area) increases, then the trap density sites increase and hence a decrease in the diffusion coefficient. The grain size is inversely proportional to grain boundary length as the grain boundary is a potential trapping sites.

As a consequence of increasing trapping sites (dislocation and grain boundary), the trap binding energy is increased. The binding energy for material that having a small grain size is higher than materials with large grain size. It is important to know that with increasing thickness of materials, there is also increase of trapping sites.

The hydrogen diffusion coefficient of super duplex stainless steels, Ferralium 255 and SAF 2507, is lower than the carbon steel. This is mainly due to the mixed microstructure of duplex steel practically the presence of austenite phase ($\approx 50\%$). It is likely that a significant amount of hydrogen remained trapped in the austenite microstructure or in the ferrite-austenite interface. It is known that the diffusion coefficient of hydrogen is lower in the austenite phase, but the solubility is very high. Modelling of hydrogen diffusion in the two phase microstructure of duplex stainless steel has been carried out by Turnbull and his co-workers ¹²⁴ .

Material		Longitudinal Section		Transverse Section		Measured D (cm ² /s)
		Area μ m ²	Length μ m	Area μ m ²	Length μ m	
Ferralium 255	Mean	490	53.8	139.3	16.2	1.38 x 10 ⁻¹⁰
	SD	807.2	55.6	234.6	10.6	
	Min	0.4	2	0.03	3	
	Max	4123.5	235.5	1759.5	51.1	
SAF 2507	Mean	305.6	39.1	99.4	20.5	1.42 x 10 ⁻¹⁰
	SD	635.1	64.2	121.5	10.7	
	Min	1.72	1	0.11	2.5	
	Max	3878.7	338.5	664.8	54.9	
Zeron 100	Mean	469.1	46.5	100.5	12.5	No Measurement
	SD	1113.5	50.73	153.99	11.4	
	Min	0.42	1	0.47	1	
	Max	7491.7	223	940.4	68	

Table 5.5: Summary of the effect of the austenite grain size on the hydrogen diffusion coefficient

5.13 Galvanostatic Method

A galvanostatic method was proposed for the determination of the hydrogen diffusion coefficients of two of the super duplex stainless steel alloys. The method was shown to give diffusion coefficients that correlate well with tests assessed by the permeation methods. The method was successfully used to determine the diffusion coefficients of carbon steel, super DSS Ferralium 255 and SAF 2507 membranes and proved to be reliable and shorter in terms of the test time. A very thin square-shaped membrane of 1 mm thick carbon steel membrane at room temperature was used in this test. While 0.1 mm thickness for the super DSSs with a total effective area of 18 cm² (charged from both side) in 0.2 M NaOH with an addition of 1g/L of Thiourea at a temperature of 50° C was used to in order to carry out the hydrogen charging. A charging current density of 1 mA/ cm² was applied to the specimens for a period of approximately 10 days.

5.13.1 Carbon Steel

The result from the galvanostatic hydrogen charging methods for 1 mm thick low carbon steel is shown in figure 5.85. The plot of decreasing potential against time is produced for approximately 17 hours. Assuming a diffusion coefficient of 1×10^{-7} which is a value for typical carbon steel, then L^2/D can be calculated to estimate the short and long time. From this value $t > 25000$ sec for the long time and $t \ll 25000$ sec for the short time. The first 166 minutes of the plot represent a decreasing potential in a parabolic rate during the hydrogen charging which can correspond to the short time period. The slope of the linear fit was extrapolated to define the long time when $t > L^2/D$. Figure 5.86 shows the linear fit as a function of the short time ($t^{1/2}$). The value of the slope ($\partial E / \partial t^{1/2}$) for the linear short time ($t^{1/2}$) was calculated to be 1.03×10^{-3} V/s^{1/2}, while the slope of the linear fit for the long time ($\partial E / \partial t$) was 3.1×10^{-6} V/s.

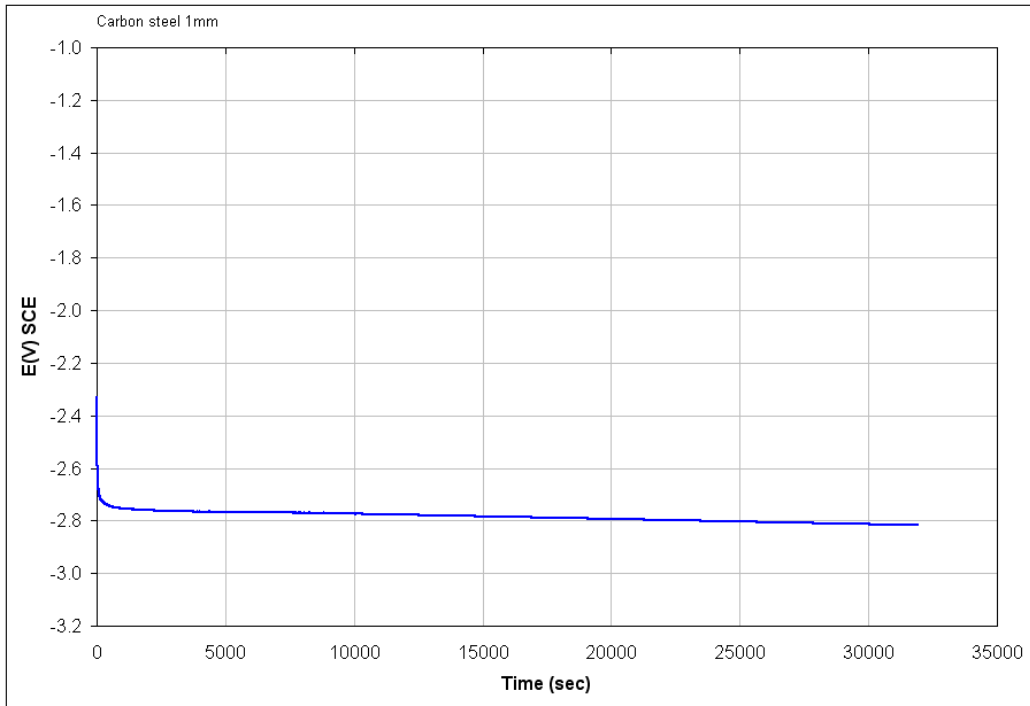


Figure 5.85: Galvanostatic hydrogen charging method for low carbon steel membrane in 0.2M NaOH solution

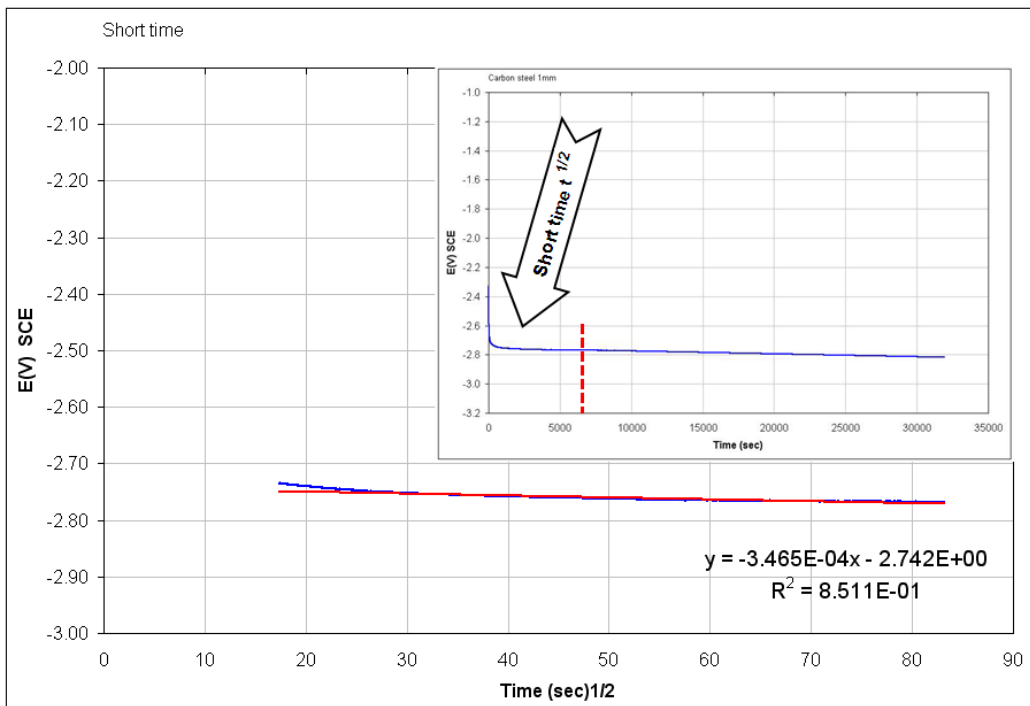


Figure 5.86: Linear plot of potential (E) as a function of $t^{1/2}$ at the short time period ($t \ll L^2/D$) for low carbon steel specimen in 0.2M NaOH solution

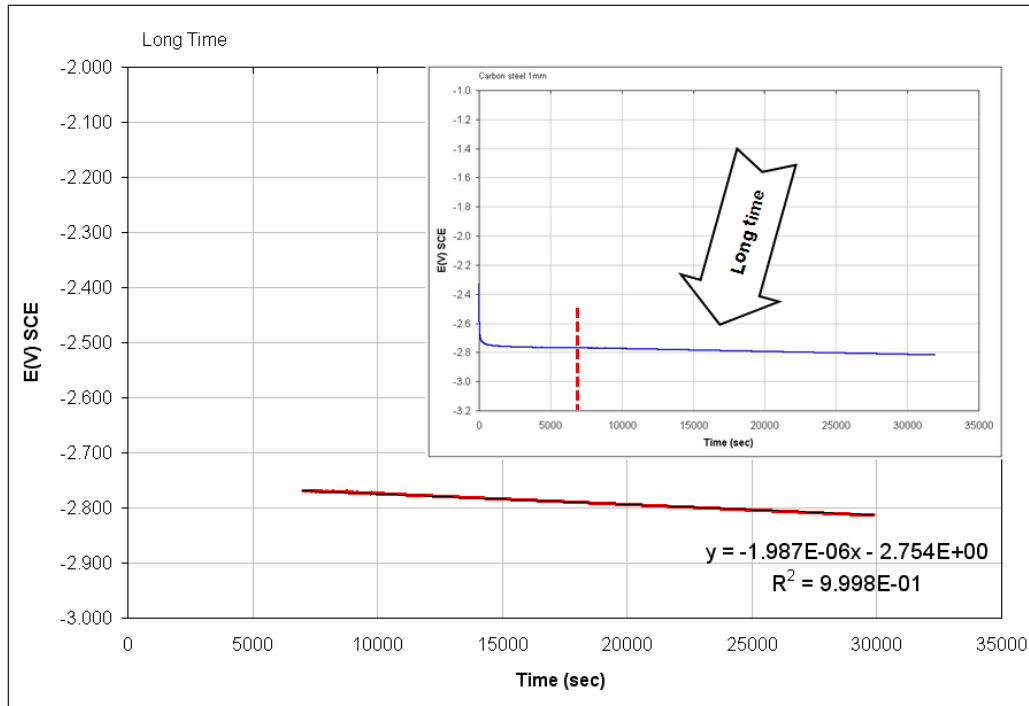


Figure 5.87: Linear plot of potential (E) as a function of time at the long time period ($t > L^2/D$) for low carbon steel specimen in 0.2M NaOH solution

The hydrogen diffusion coefficient for the galvanostatic hydrogen charging method was calculated using the following formula:

$$D = \left(\frac{2 L (\partial E / \partial t)}{\pi^{1/2} (\partial E / \partial t^{1/2})} \right)^2$$

$$D = \left(\frac{2 (0.1) (2 \times 10^{-6})}{\pi^{1/2} (3.5 \times 10^{-4})} \right)^2$$

$$D = 1. \times 10^{-7} \text{ cm}^2 \cdot \text{sec}^{-1}$$

5.13.2 Super DSS Ferralium 255

The results from the galvanostatic method for super DSS Ferralium are shown in figure 5.88, 5.89 and 5.90. The value of the slope ($\partial E / \partial t^{1/2}$) for the linear short time ($t^{1/2}$) was calculated to be $3.95 \times 10^{-4} \text{ V/s}^{1/2}$, while the slope of the linear fit for the long time ($\partial E / \partial t$) was $7.5 \times 10^{-7} \text{ V/s}$. The hydrogen diffusion coefficients for the galvanostatic hydrogen charging method were calculated by using the following equation (see section 4.12.2):

$$D = \left(\frac{2 (0.005) (7.5 \times 10^{-7})}{\pi^{1/2} (0.000395)} \right)^2$$

$$D = 1.15 \times 10^{-10} \text{ cm}^2 \cdot \text{sec}^{-1}$$

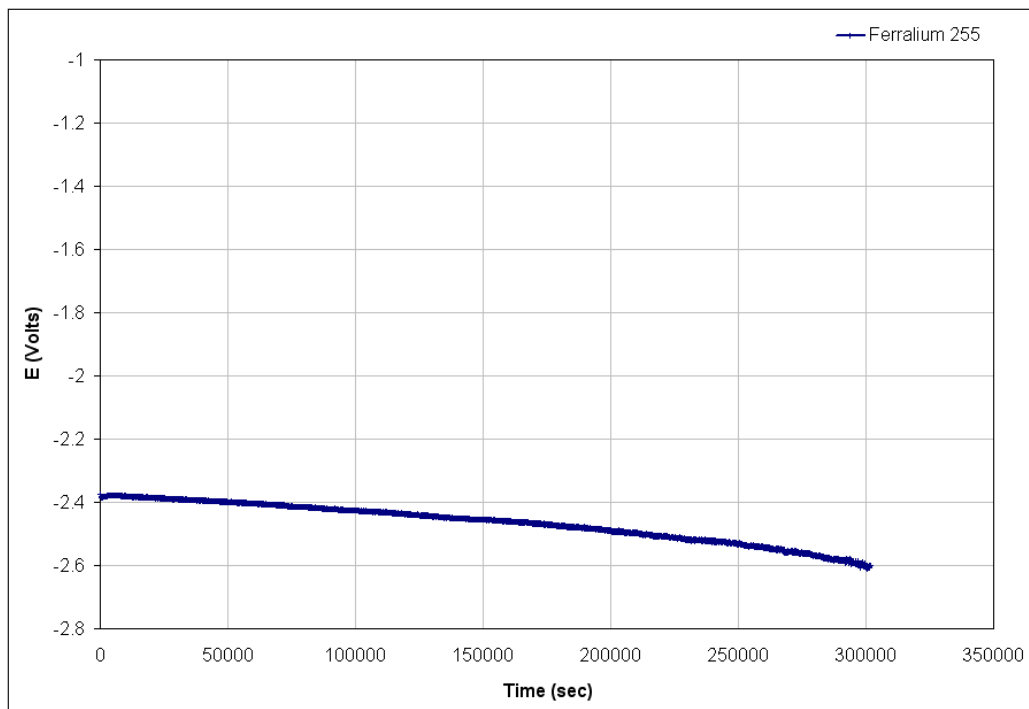


Figure 5.88: Galvanostatic hydrogen charging plot for super DSS Ferralium 255 specimen

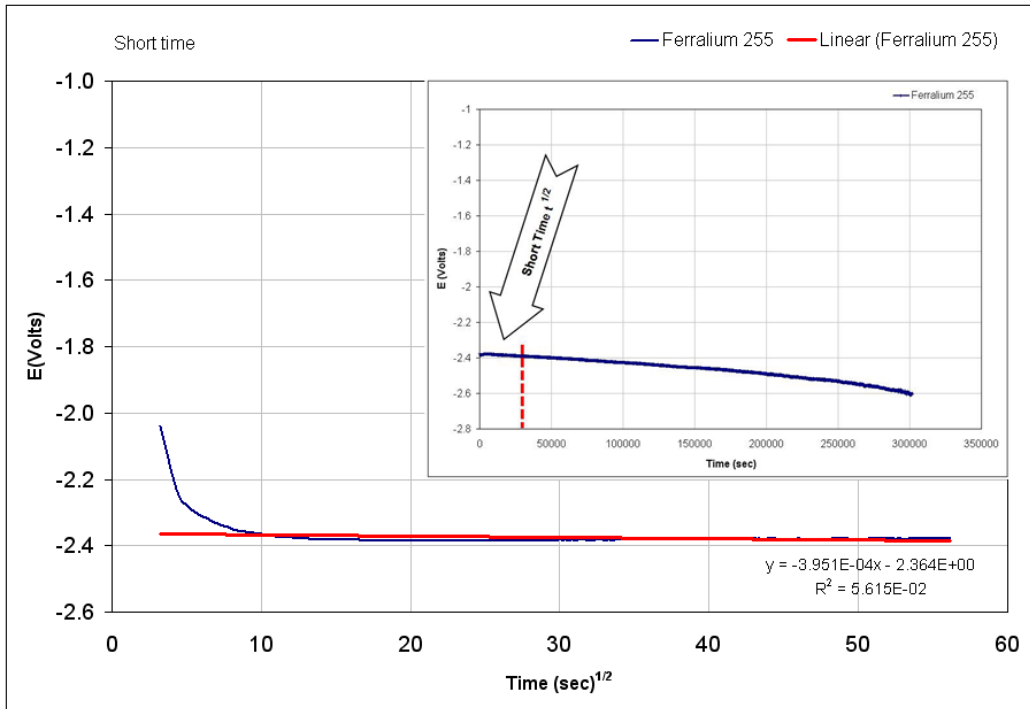


Figure 5.89: Linear plot of potential (E) as a function of $t^{1/2}$ at the short time period for super DSS Ferralium 255 specimen in 0.2M NaOH solution

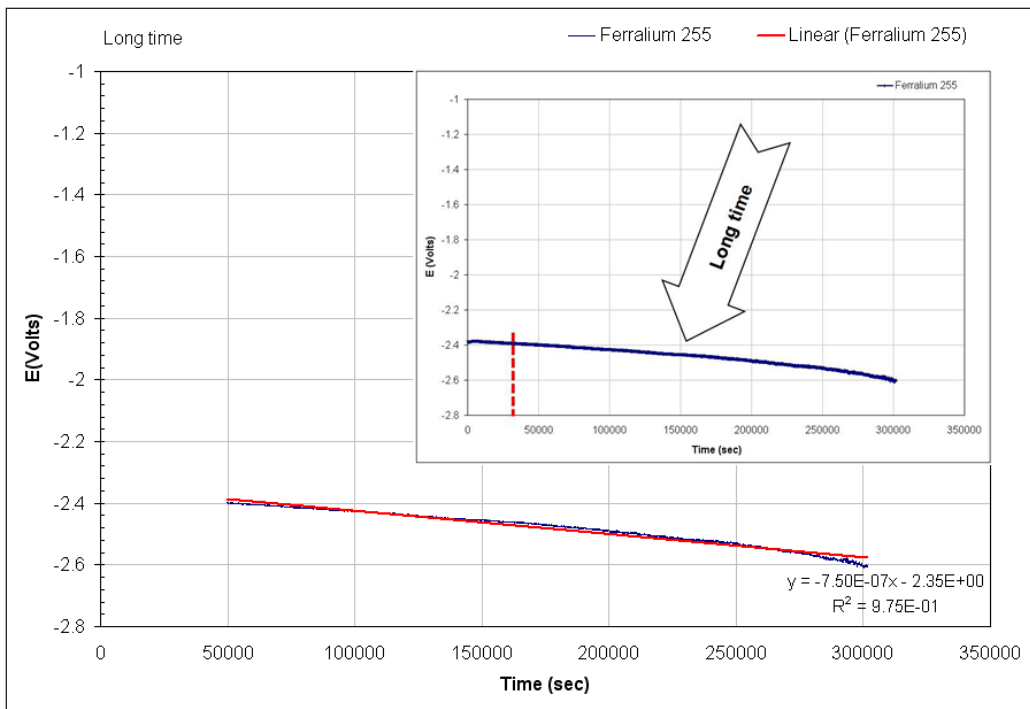


Figure 5.90: Linear plot of potential (E) as a function of time at the long time period for super DSS Ferralium 255 specimen in 0.2M NaOH solution



Figure 5.91: Cross section of 100 μm thick membrane used in the galvanostatic test for super DSS Ferralium 255 showing the orientation of the colonies of the austenite grains

Figure 5.91 shows a cross section of 0.1 mm thick membrane used in the galvanostatic method to determine the diffusion coefficient for super DSS Ferralium 255. The dark and light colours correspond to the ferrite and austenite phases respectively.

5.13.3 Super DSS SAF 2507

The results from the galvanostatic method for super DSS SAF 2507 are shown in figure 5.92, 5.93 and 5.94 respectively. The value of the slope ($\partial E / \partial t^{1/2}$) for the linear short time ($t^{1/2}$) was calculated to be $5.63 \times 10^{-4} \text{ V/s}^{1/2}$, while the slope of the linear fit for the long time ($\partial E / \partial t$) was $1.08 \times 10^{-6} \text{ V/s}$. The hydrogen diffusion coefficients for the galvanostatic hydrogen charging method were calculated by using the following equation:

$$D = \left(\frac{2 (0.005) (1.08 \times 10^{-6})}{\pi^{1/2} (0.000563)} \right)^2$$

$$D = 1.17 \times 10^{-10} \text{ cm}^2 \cdot \text{sec}^{-1}$$

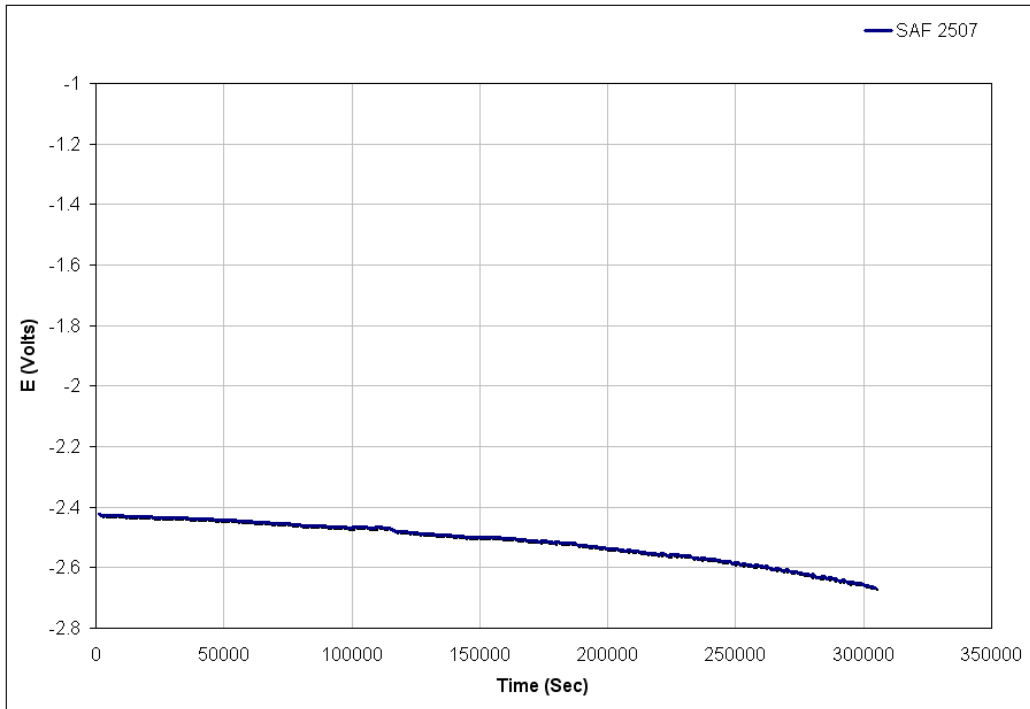


Figure 5.92: Galvanostatic hydrogen charging plot for super DSS SAF 2507 specimen

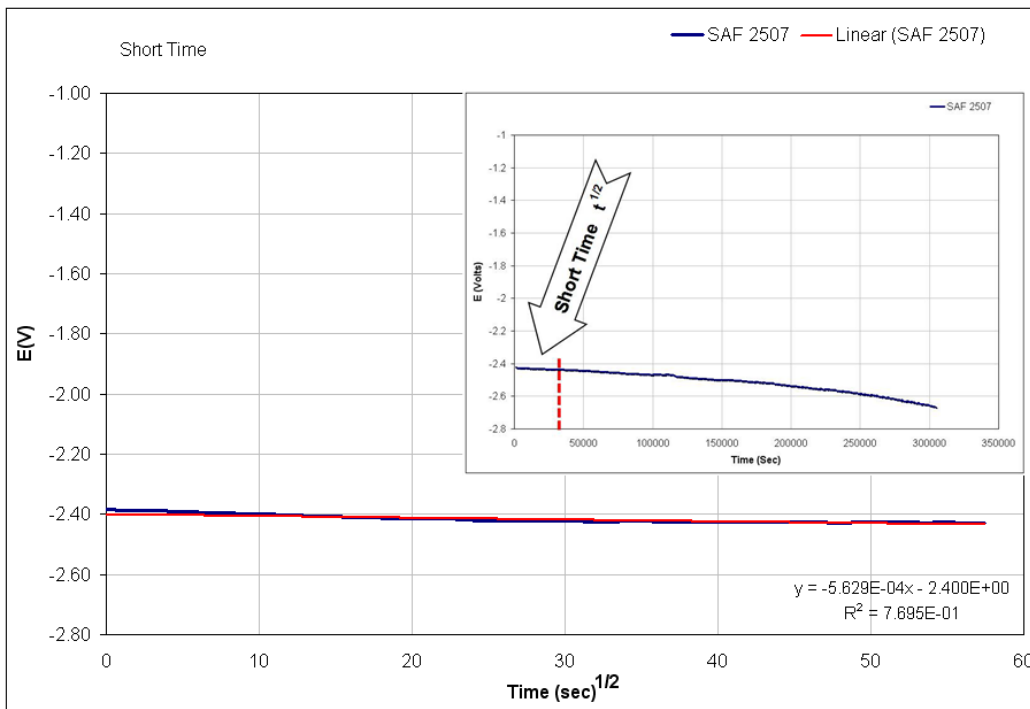


Figure 5.93: Linear plot of potential (E) as a function of $t^{1/2}$ at the short time period for super DSS SAF 2507 specimen in 0.2M NaOH solution

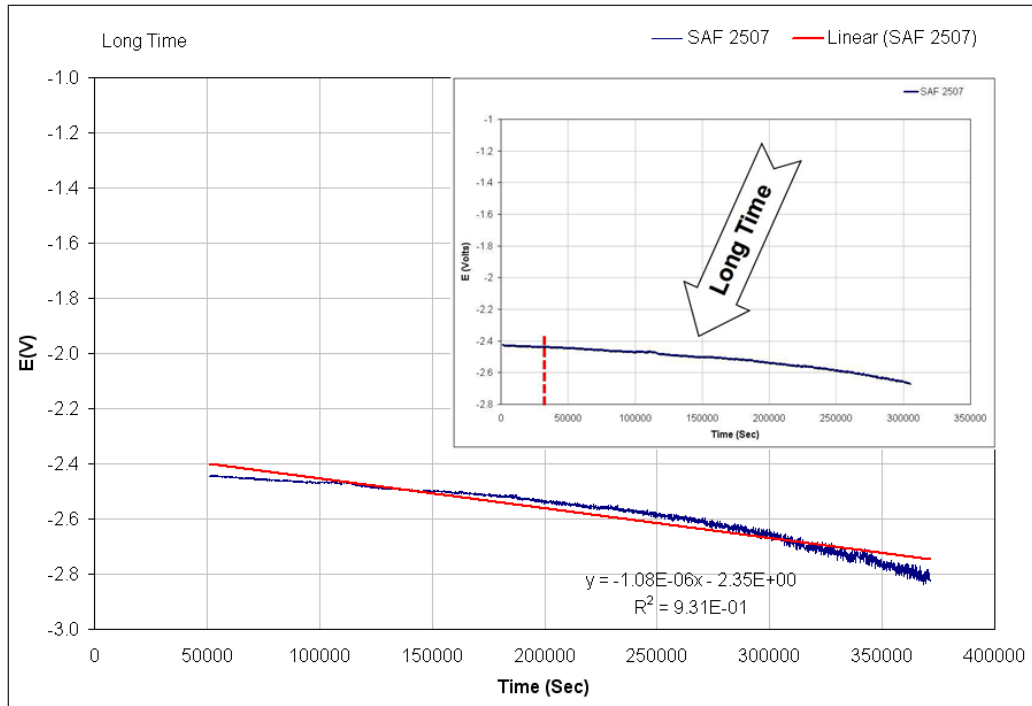


Figure 5.94: Linear plot of potential (E) as a function of time at the long time period for super DSS SAF 2507 specimen in 0.2M NaOH solution

Figure 5.95 shows a cross section of 0.1 mm thick membrane used in the galvanostatic method to determine the diffusion coefficient for super DSS SAF 2507. The dark and light colours correspond to the ferrite and austenite phases respectively



Figure 5.95: Cross section of 100 μm thick membrane used in the galvanostatic test for super DSS SAF 2507 showing the direction of the colonies of the austenite grains

By considering the variation of the membrane thickness, the standard deviation value was calculated after measuring the 4 different areas of the membranes with a Multimoyo micrometer (0.001 mm precision). The standard deviation of the diffusion coefficient values were calculated as shown in table 5.4.

Alloy	Membrane thickness (cm)	Standard deviation (cm)	D (cm^2/s)
Ferrallium 255	0.01	3.75×10^{-6}	$1.15 \pm 2.5 \times 10^{-10}$
SAF 2507	0.01	7.5×10^{-6}	$1.17 \pm 2.6 \times 10^{-10}$

Table 5.6: Comparison of hydrogen diffusion coefficient using the galvanostatic charging technique

The galvanostatic technique for measuring the hydrogen diffusion coefficient is less familiar than the permeation method, but the validity of its results was compared with the permeation technique. Although, the charging conditions were different and hence the boundary conditions at the electrolyte specimen

interface, a good agreement in the hydrogen diffusion coefficient values was found. The hydrogen diffusion coefficient values for super duplex stainless steel Ferralium 255 and SAF 2507 using the permeation technique were 1.38×10^{-10} and 1.42×10^{-10} cm²/sec respectively. On the other hand, the hydrogen diffusion coefficient values for super duplex stainless steels Ferralium 255 and SAF 2507 by using the galvanostatic technique were 1.15×10^{-10} and 1.17×10^{-10} cm²/sec respectively. Therefore the result from both techniques proved to be consistent with each other.

It should be noted that the results obtained from the galvanostatic test to measure the hydrogen diffusion coefficient used promoters for hydrogen entry, while the hydrogen permeation test was carried out without those promoters. In addition, the real service conditions have no indication of the presence of such promoters.

Comparing the diffusion coefficient results of the carbon steel and super DSS, it can be seen that there should be some obstruction in the microstructure that can slow down the hydrogen movement through the metal. The cause of hydrogen diffusion reduction can be due to the microstructure of both austenite and ferrite phases.

Looking at figures 5.91 and 5.95, it can be seen that the hydrogen enters from the transverse direction which gives the hydrogen atoms less chance of encountering an austenite band because the ferrite is rolled in the longitudinal direction considerably elongating the grains of both phases. On the other hand, if the hydrogen enters from the longitudinal direction it would not penetrate deeply due to much higher probability of encountering an austenite band. These findings are substantiated by the research carried out by ¹²⁵.

The grain size is inversely proportional to grain boundary length. As the grain boundary is a potential trapping site, and act as reversible trapping sites. In specimens with small grain size the diffusivity coefficient is higher in comparison to the large grain sized ones. Small austenite grains will result in an increase boundary surface area and hence in a more active surface.

Table 5.5 shows the values obtained for hydrogen diffusion coefficient with the two methods of hydrogen permeation and galvanostatic technique. Table 5.6 shows the austenite and ferrite grain size.

Material	Measured diffusion coefficient by using two methods (cm ² /sec)			
	Permeation method	Thickness (mm)	Galvanostatic method	Thickness (mm)
Low Carbon Steel	$1.1 \pm 0.1 \times 10^{-7}$	1	$1.04 \pm 0.1 \times 10^{-7}$	1
Ferralium 255	$1.38 \pm 0.01 \times 10^{-10}$	1	$1.15 \pm 2.5 \times 10^{-10}$	0.1
SAF 2507	$1.42 \pm 0.12 \times 10^{-10}$	1	$1.17 \pm 2.6 \times 10^{-10}$	0.1

Table 5.7: Hydrogen diffusion coefficient values (D) obtained from the hydrogen permeation and galvanostatic techniques

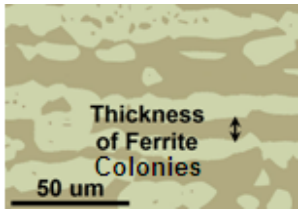
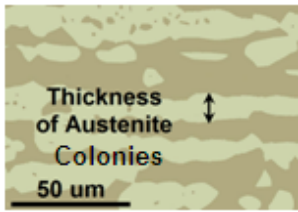
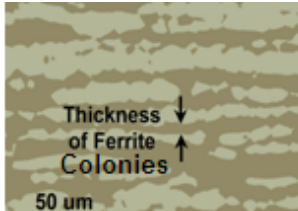
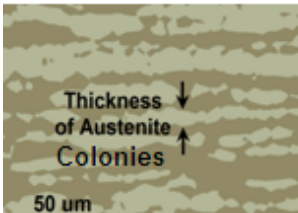
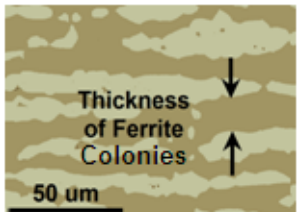
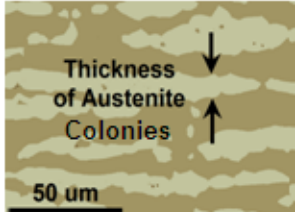
Material		Mean μm	SD μm	Min μm	Max μm	Measured D (cm^2/s)
Ferralium 255		16.7	11.4	2.6	45.6	1.38×10^{-10}
		10.6	5.3	2.1	29.2	
SAF 2507		8.1	6.3	1.5	37.4	1.42×10^{-10}
		7.4	5	1	23.6	
Zeron 100		12.7	7.5	1.6	44.2	No Measurement
		9.2	5.6	1.6	31.6	

Table 5.8: Summary of the effect of the size of ferrite and austenite grain colonies thickness on the hydrogen diffusion coefficient measured by permeation method

6 Modelling of Hydrogen Transport

6.1 Introduction

The hydrogen atoms are produced at the cathode, which is the surface of the specimen and diffuse toward the centre of the specimen. These hydrogen atoms diffuse by migration through the lattice and can be trapped at flaws in the steel, such as dislocations, grain boundaries and carbide interfaces. Only the smaller atomic form of hydrogen can effectively penetrate through it. The hydrogen will diffuse away from a region of high hydrogen concentration to a region of low hydrogen concentration till reaching the uniform concentration in the structure¹²³.

A diffusion model was used to describe the hydrogen transport and determine the distance to which the hydrogen penetrates toward the centre of the specimen in a given time. The depth of the embrittled region on the fracture surface of the cylindrical specimen of SDSS is related to the hydrogen penetration, which can be calculated from a mass transport equation.

The hydrogen distribution can then be calculated by solving this equation and using a diffusion coefficient D value from the previous permeation experiments. The technique of monitoring and prediction is very important to provide answers to the hydrogen effect which is a major source of cracking problems and inspection costs in the oil and gas industry

6.2 The Model

The aim of this work was to apply the model using the hydrogen precharging time for the three super DSSs, charged with a range of cathodic potentials used in the slow strain rate tests causing failure by hydrogen embrittlement. The precharging time was correlated with the hydrogen transport into the super DSSs specimens. A sufficient hydrogen concentration initiated a crack which propagated towards the centre to the depth that hydrogen had penetrated during the precharging period (14 days). Also a prediction of the time for

hydrogen embrittlement to occur in super DSSs samples with different dimensions can be estimated.

The model is based on application of Fick's first law of diffusion ¹⁴³ which defines the flow of hydrogen atoms in terms of the diffusion coefficient and the concentration gradient.

$$F = -D \frac{\delta C}{\delta x}$$

Where D is the diffusion coefficient, C is the concentration of hydrogen and x is the distance. It was assumed that the initial hydrogen concentration C_1 in the gauge section of the specimen is zero and the surface concentration C_0 took a value and remained constant when the hydrogen charging began. The boundary conditions are defined as the following where r is the distance from the centreline of a tensile specimen of radius a .

$$C = C_0 = 0, \quad 0 < r < a, \quad t = 0$$

$$C = C_0, \quad r = a, \quad t \geq 0$$

The hydrogen distribution and concentration profiles were calculated by an equation for two dimensional mass transport, derived by Crank ¹⁴³ and represented as follows:

$$\frac{C - C_1}{C_0 - C_1} = 1 - \frac{2}{a} \sum_{n=1}^{\infty} \frac{\exp(-D \alpha_n^2 t) J_0(r \alpha_n)}{\alpha_n J_1(a \alpha_n)}$$

C : Concentration

C_0 : Concentration at the surface

n : Integer

D : Coefficient of diffusion

a : Radius (half length of the cylindrical specimen)

t : Charging time

J_0 : Bessel function of the first kind of order zero

J_1 : Bessel function of the first order

This equation can describe the diffusion of hydrogen into a cylindrical specimen from the surface and the progressive increase in concentration across the specimen section. The expression was evaluated in a spread sheet by calculating the first 50 terms, which was shown to be sufficient for the series to converge.

By varying the values of this non-dimensional term, different hydrogen concentration profiles can be obtained, as shown in figure 6.1. The value of $\frac{Dt}{a^2}$ determines a family of curves showing the concentration of hydrogen inside the specimen. In a cylindrical specimen, the hydrogen just reaches the centre when $\frac{Dt}{a^2} = 0.04$, which is the breakthrough case.

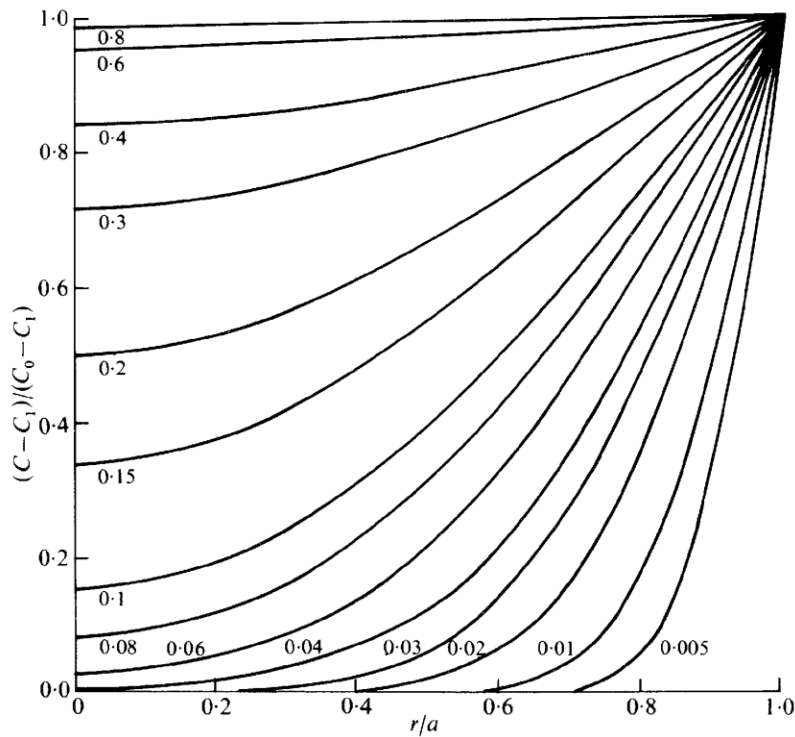


Figure 6.1: Different profiles of hydrogen concentration for cylinders obtained with different values of Dt/a^2 ¹⁴³

6.3 Consider an Example

Supposing $D = 5 \times 10^{-10} \text{ cm}^2/\text{s}$ and $a = 1.5 \text{ mm}$ which is the radius of the SSRT specimen and $t = 14 \text{ day}$ which is the hydrogen precharging time, then $\frac{Dt}{a^2} = 0.027$. Therefore from figure 6.1 the concentration of diffused hydrogen in the specimen is zero over 0.9 of the radius (ie. Hydrogen has diffused 0.1 of the radius). When $t = 28 \text{ days}$ then $\frac{Dt}{a^2} = 0.054$ and the hydrogen diffused 0.3 of the radius of the SSRT specimen. The time needed for the hydrogen to just reach the centre of the SSRT specimen can be calculated from $\frac{Dt}{a^2}$ is a value of 0.04. This corresponds to a time of 20.8 days.

Figure 6.2 shows the profile of the hydrogen concentration modelling in a 3mm diameter gauge length for the tensile specimen of super DSS with different time using a diffusion coefficient value of $1.38 \times 10^{-10} \text{ cm}^2/\text{sec}$. This D value was

measured previously in this research by using the permeation method for Ferralium 255 alloy. The time needed for the hydrogen to reach the centre of the specimen is calculated to be approximately 75 days. For the super DSS SAF 2507, the time needed the hydrogen to just reach the centre is 73 days when using a measured diffusion coefficient value of $1.42 \times 10^{-10} \text{ cm}^2/\text{sec}$.

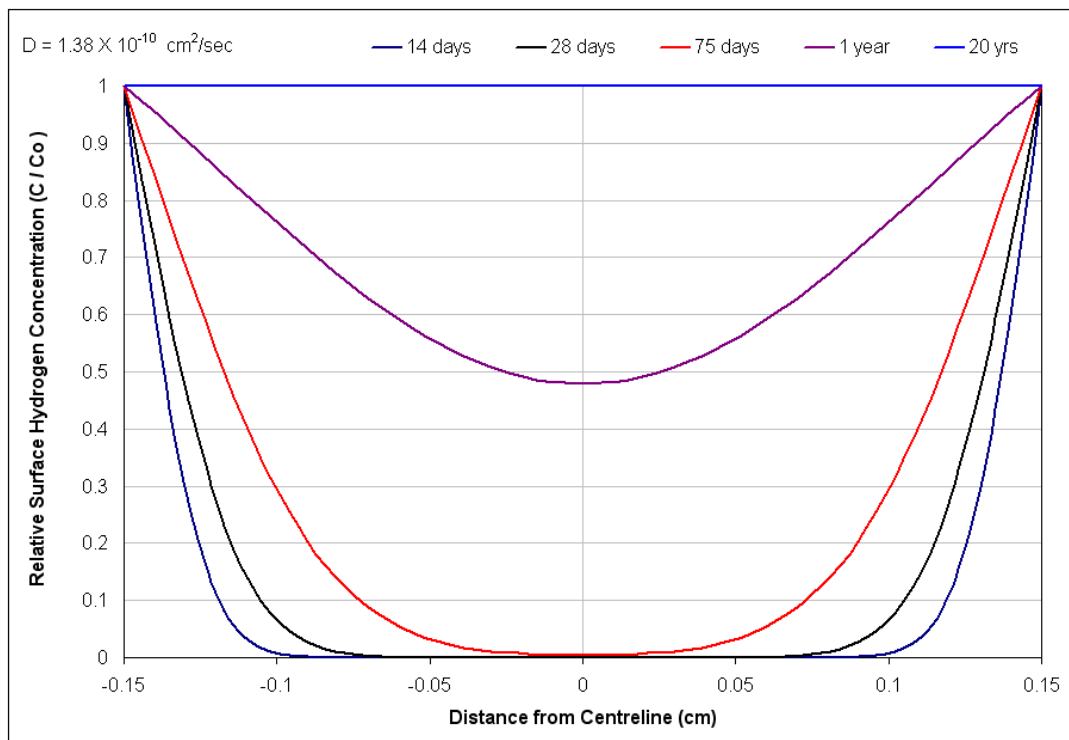


Figure 6.2: Profile of hydrogen concentration modelling in a 3 mm diameter gauge length for the tensile specimen of super DDS Ferralium 255 with different charging times using a measured D value of $1.38 \times 10^{-10} \text{ cm}^2/\text{sec}$

6.4 Applications of the Model

6.4.1 Estimation of the Diffusion Coefficient

Using this model, the diffusion coefficient value for each alloy was estimated from the profile of hydrogen concentration that corresponds to the depth of the embrittled area of the fracture surface of the slow strain rate specimen. This diffusion coefficient was then compared with values obtained from the permeation technique previously described in this research for two alloys, Ferralium 255 and SAF 2507. In addition, the model enabled the critical hydrogen concentration for embrittlement to be estimated.

The x axis of all plots of the hydrogen concentration profiles corresponds to the position along the radial axis of the specimen (i.e. $\frac{x}{L} = 0$ at the centreline and

$\frac{x}{L} = 1$ in the surface, where L equals the specimen radius). The y axis is the ratio of C/C_0 , the concentration of hydrogen over the hydrogen concentration at the surface.

6.5 Depth of the Embrittlement Measured on the Fractured Surface

SEM images show that the brittle crack propagated a distance toward the centre of the SSRT specimen and that distance can be related to the hydrogen concentration and the applied cathodic potential. Figures 6.3 and 6.4 show the depth of the embrittled region and the boundary of the brittle and ductile regions on the fracture surface of the SSRT specimen of super DSS Zeron 100 charged at a potential of -1250 mV (SCE) in 3.5% NaCl solution at 50 °C for 2 weeks. Figure 6.5 shows the ductile fracture which is close to the centre while the brittle fracture is close to or near the surface of the specimen.

The maximum value of the crack length was measured by the SEM as shown in Table 6.1. The brittle part, which corresponds to the crack length near the surface, increases when decreasing the pre-charging potential.

Cathodic precharged potential E (mV (SCE))	Maximum crack depth (mm) for SDSS		
	Ferralium 255	SAF 2507	Zeron 100
-1250	1.026±0.0012	1.25±0.001	1.035±0.001
-1100	0.698±0.0015	1.047±0.0014	0.731±0.001
-1000	0.698±0.001	0.918±0.0013	0.712±0.0012
-900	0.66±0.0011	0.462±0.0012	0.656±0.0011
-800	0.074±0.001	0.076±0.001	0.069±0.0015

Table 6.1: Values of maximum crack depth measured by SEM at a range of applied potentials in 3.5 % NaCl at 50 °C for 2 weeks.

This depth of the embrittled region was measured to be 1.035 mm and was related to the profile of hydrogen concentration modelling in a 3 mm diameter gauge length for the tensile specimen of super DDS Zeron 100 with different diffusion coefficient values for a period of 2 weeks, as shown in figure 6.3. The arrow in figure 6.3 shows the distance to which the hydrogen travelled causing the embrittled fracture. From this graph, the diffusion coefficient is estimated to be at least $1.4 \times 10^{-10} \text{ cm}^2/\text{s}$, at a temperature of 50°C. The diffusion coefficient for super DSS Ferralium 255 was estimated to be $1.4 \times 10^{-10} \text{ cm}^2/\text{s}$ while for super DSS SAF 2507 and Zeron 100 are $1.8 \times 10^{-10} \text{ cm}^2/\text{s}$ and $1.4 \times 10^{-10} \text{ cm}^2/\text{s}$ as show in figure 6.8 to 6.10 respectively.

Materials	D (cm ² /s)
Ferralium 255	1.4±0.1 x 10 ⁻¹⁰
SAF 2507	1.8±0.1 x 10 ⁻¹⁰
Zeron 100	1.4±0.1 x 10 ⁻¹⁰

Table 6.2: Estimated minimum diffusion coefficient D values from the hydrogen concentration graph for the three SDSSs materials

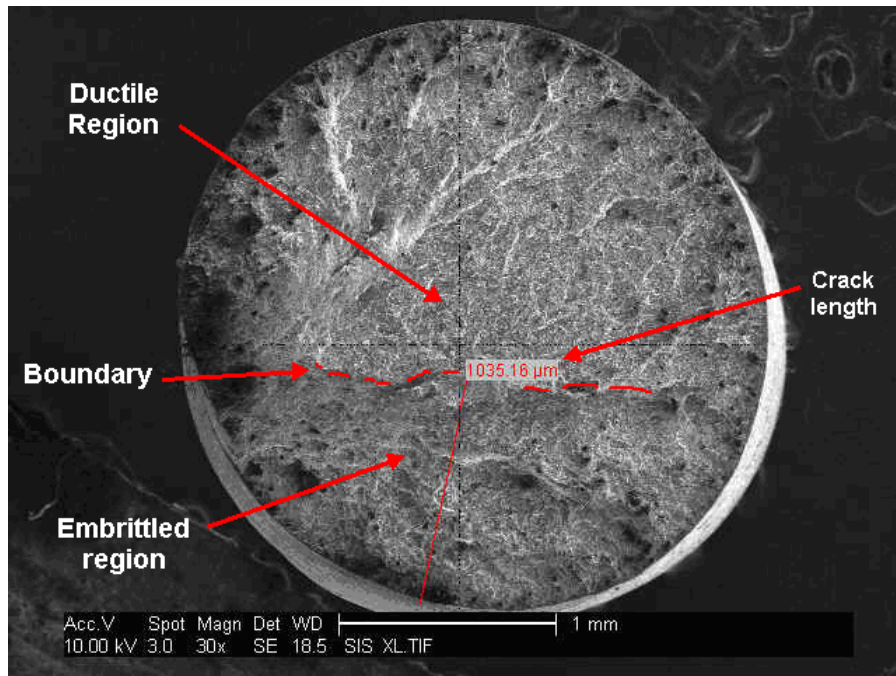


Figure 6.3: Fracture surface of super DSS Zeron 100 showing the depth of the embrittled region where the hydrogen travelled toward the centre precharged at a potential of -1250 mV (SCE) for 2 weeks at 50 °C

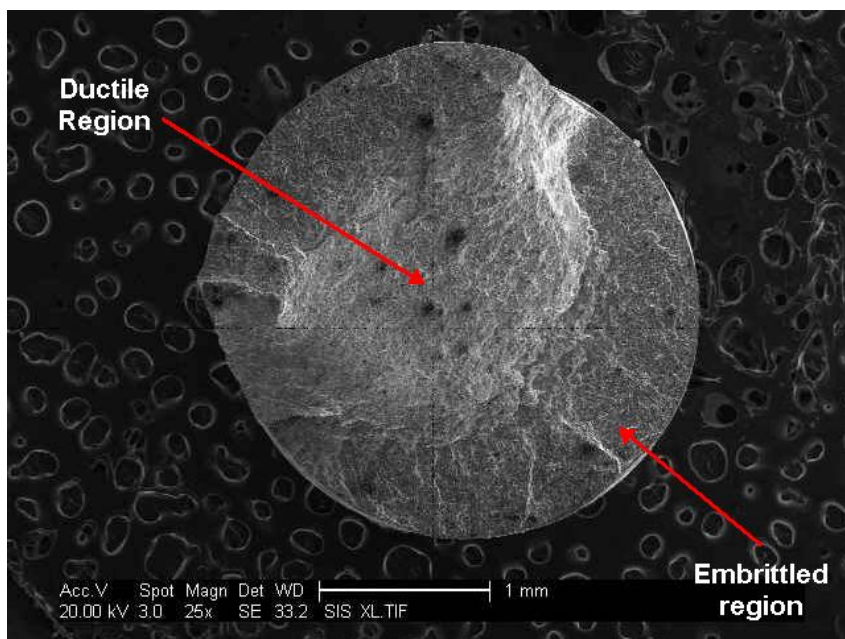


Figure 6.4: Fracture surface of super DSS Ferralium 255 showing the depth of the embrittled region where the hydrogen travel toward the centre and the boundary of ductile & brittle regions of SSR testing in 3.5% NaCl at 50 °C precharged at -1250mV (SCE) for 2 weeks

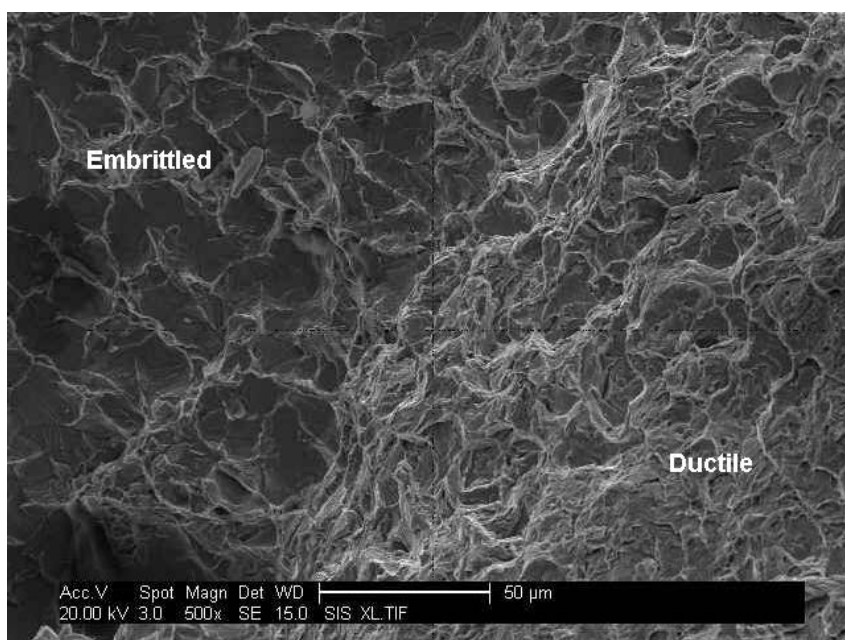


Figure 6.5 Fracture surface of super DSS Ferralium 255 Showing the boundary of ductile & brittle regions of SSR testing in 3.5% NaCl at 50 °C precharged at -1250mV (SCE) for 2 weeks (embrittled region is where the hydrogen travel toward the centre)

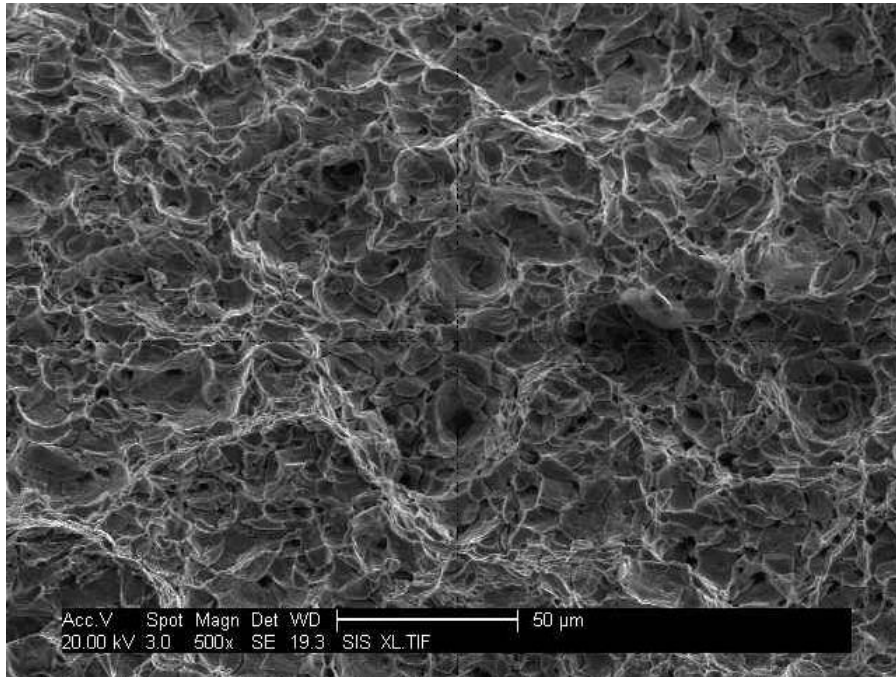


Figure 6.6: Fracture surface of super DSS Ferralium 255 showing ductile region in centre of the specimen precharged at -1250mV (SCE) for 2 weeks in 3.5% NaCl at 50 °C

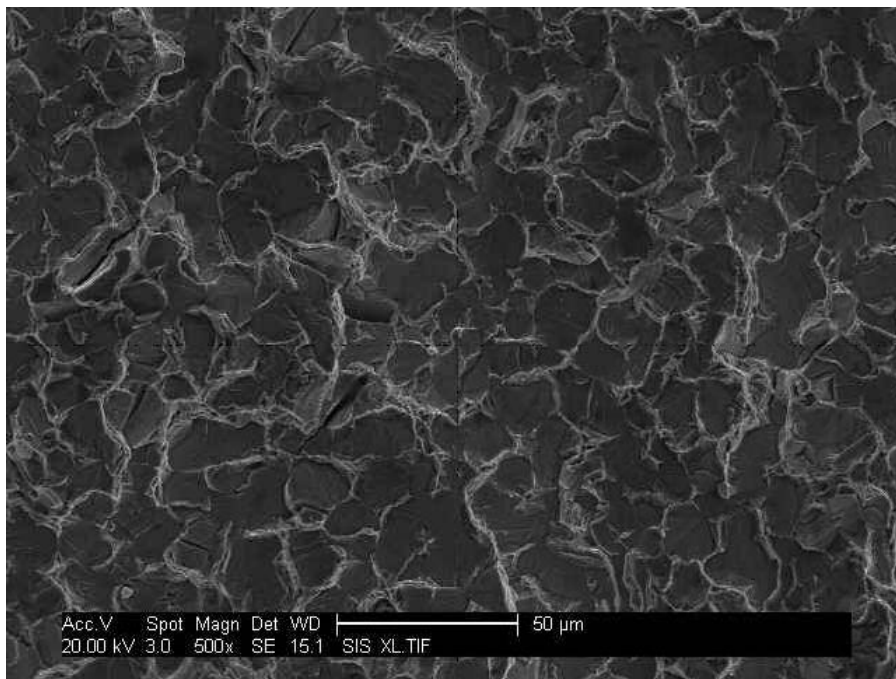


Figure 6.7 Fracture surface of super DSS Ferralium 255 after SSR test showing brittle region on the circumference of the specimen precharged at -1250mV (SCE) for 2 weeks in 3.5% NaCl at 50 °C

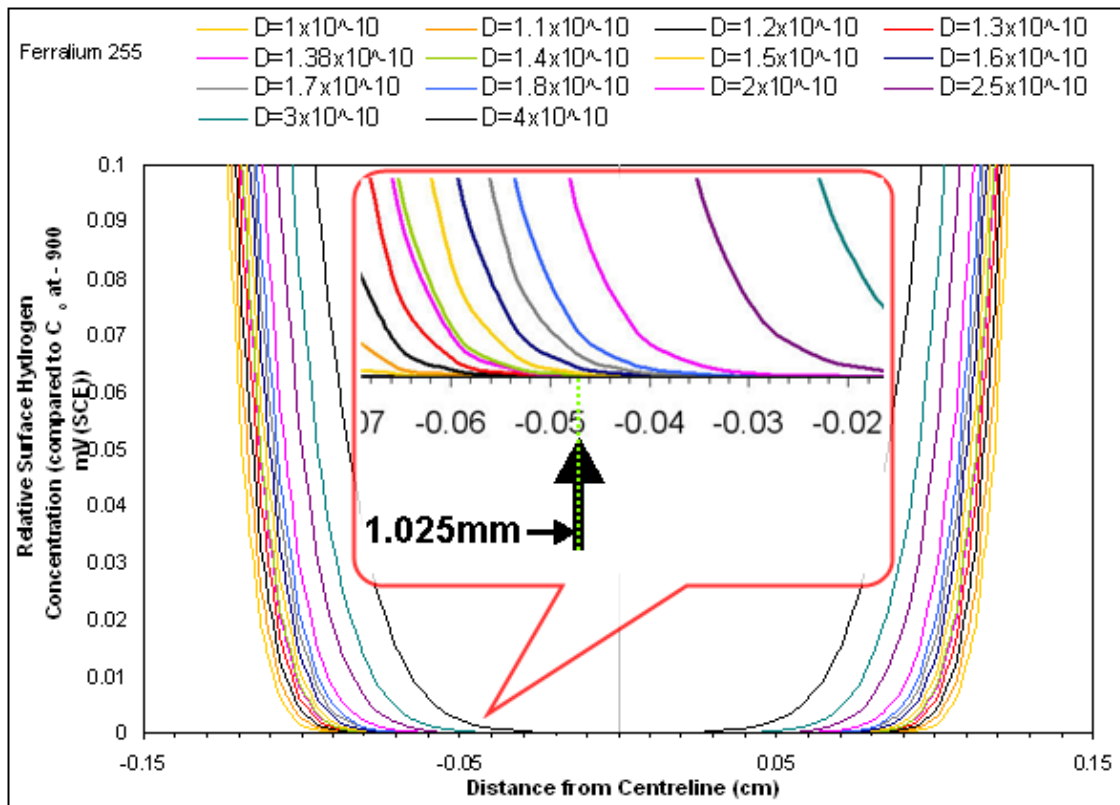


Figure 6.8 Profile of hydrogen concentration modelling in a 3 mm diameter gauge length for the tensile specimen of super DSS Ferralium 255 with different diffusion coefficient values for a period of 2 weeks (The area in the box shows the hydrogen distributions at higher magnification, for ease of comparison)

The estimated D value according to the crack depth for super DSS Ferralium 255 in this graph is $1.4 \pm 0.1 \times 10^{-10} \text{ cm}^2/\text{s}$.

All specimens were precharged for two weeks followed by slow strain rate testing until failure occurred. The time to failure of SSRT was relatively short and was found to make little difference when compared to the precharging time of two weeks. Therefore, all the profiles of hydrogen concentration graphs were based on the precharging time and the time to failure in the SSRT was not added to the hydrogen uptake period.

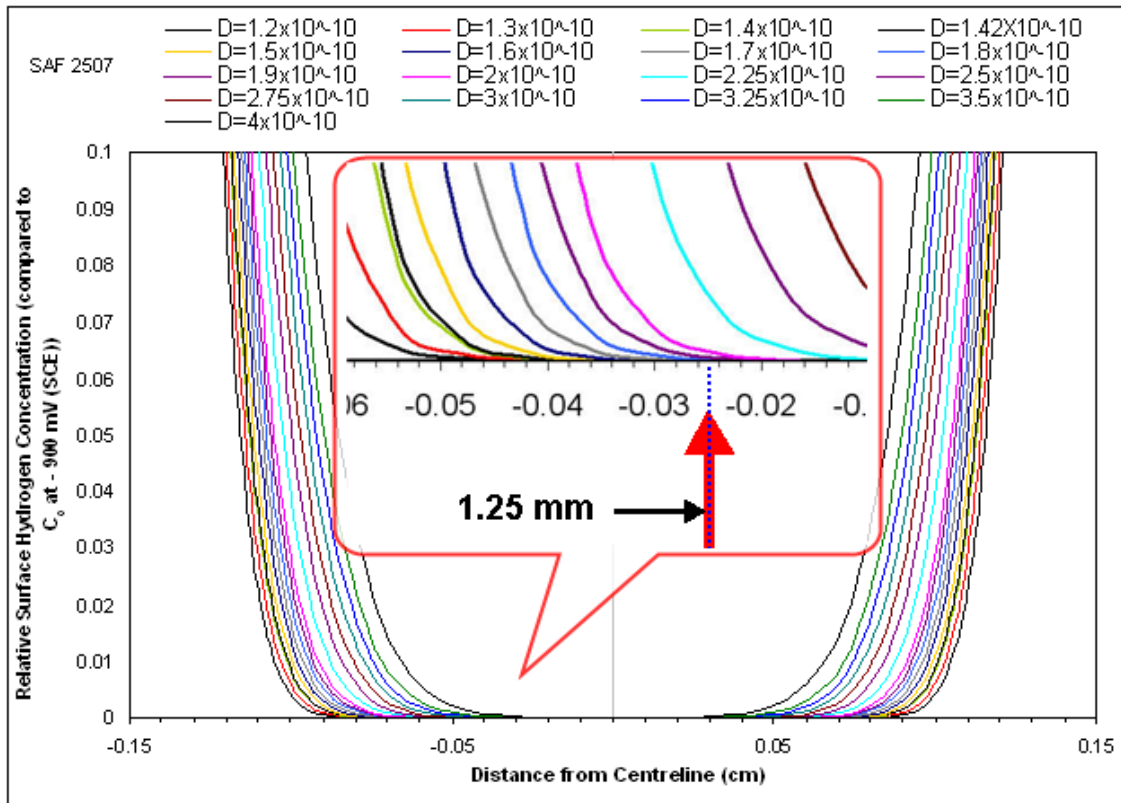


Figure 6.9 Profile of hydrogen concentration modelling in a 3 mm diameter gauge length for the tensile specimen of super DSS SAF 2507 with different diffusion coefficient values for a period of 2 weeks

The estimated D value according to the crack depth (1.25 mm) for super DSS SAF 2507 in this graph is $1.8 \pm 0.1 \times 10^{-10} \text{ cm}^2/\text{s}$.

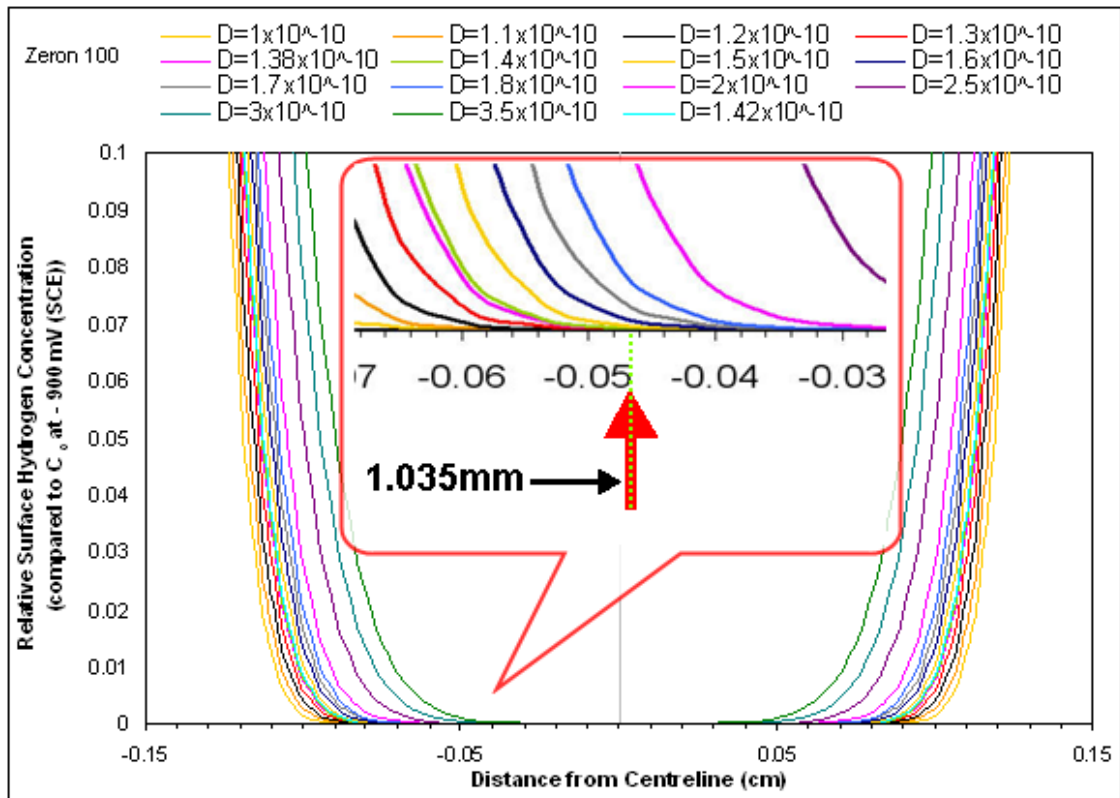


Figure 6.10 Profile of hydrogen concentration modelling in a 3 mm diameter gauge length for the tensile specimen of super DSS Zeron 100 with different diffusion coefficient values for a period of 2 weeks

The estimated D value according to the crack depth (1.035mm) for super DSS SAF 2507 in this graph is $1.4 \pm 0.1 \times 10^{-10} \text{ cm}^2/\text{s}$

Material	Potential E (mV) SCE	Maximum crack length (mm)	Minimum D Value (to give measured crack length)	Measured D value (permeation)
Ferralium 255	- 1250	1.026	$1.4 \pm 0.1 \times 10^{-10}$	$1.38 \pm 0.01 \times 10^{-10}$
SAF 2507	- 1250	1.25	$1.8 \pm 0.1 \times 10^{-10}$	$1.42 \pm 0.12 \times 10^{-10}$
Zeron 100	- 1250	1.035	$1.4 \pm 0.1 \times 10^{-10}$	No Measurement

Table 6.3 Comparison of the hydrogen diffusion coefficients for the three super DSS materials measured by the permeation method and modeling

In addition, it is important to underline that the diffusion coefficient values obtained from the crack lengths on the fracture surface of the precharged specimens after slow strain rate testing are within the range of those obtained by the other two methods (hydrogen permeation and galvanostatic). The estimated diffusion coefficient values from the depth of the embrittled region for super duplex stainless steels, Ferralium 255, SAF 2507 and Zeron 100 were $1.4 \pm 0.1 \times 10^{-10}$, $1.8 \pm 0.1 \times 10^{-10}$ and $1.4 \pm 0.1 \times 10^{-10}$ cm²/sec respectively.

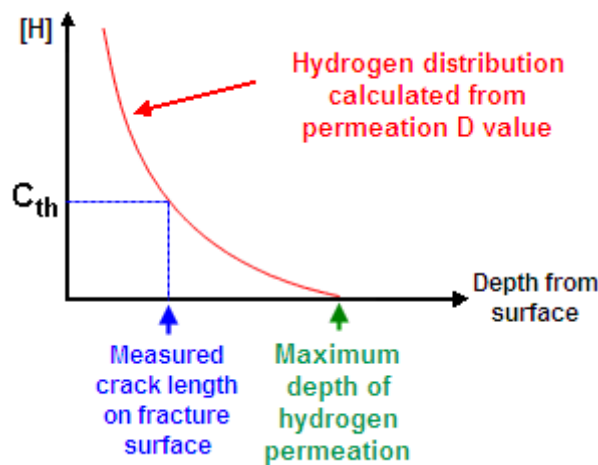


Figure 6.11: Illustration of measuring the threshold hydrogen concentration (C_{th}) for crack propagation

If the measured diffusion coefficient from the permeation method is greater than the minimum diffusion coefficient obtained from the crack length, then it implies that there is a threshold hydrogen concentration (C_{th}) greater than zero, for crack propagation to occur, as represented in figure 6.11.

Concerning the effect of stress, Beck et al.¹⁴⁴ suggested that tensile strain increases the concentration of absorbed hydrogen as a result of the dilation of the interstitial lattice sites where hydrogen accumulates, but it does not affect the diffusivity of hydrogen. The effect of straining on hydrogen transport in iron, nickel and stainless steel was also reported by Zakroczymski¹⁴⁵. In his study

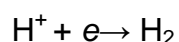
he observed two cases; elastic and plastic deformation. In the elastic region he noticed a slight increase in permeation rate with no change in diffusivity. For the plastic region, both diffusivity and permeability of hydrogen were substantially reduced irrespective of the strain rate, but depending on strain. Therefore, it was suggested that enhanced trapping of hydrogen was caused, which in turn was responsible for the behaviour in the plastic region.

6.6 Predicted Hydrogen for each precharging potential and Profile

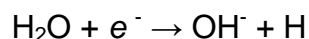
The aim of this modelling was to estimate the hydrogen threshold (C_H) concentration required to propagate a brittle crack in each alloy. Figures 6.12 to 6.13 show the hydrogen concentration profile inside the super duplex stainless steel after different charging time. These plots explain how hydrogen penetrates inside the alloys from the surface after a cathodic charging time of 2 weeks with a range of applied cathodic potential. In addition, the distributions of hydrogen plots estimate the concentration of the hydrogen which is a function of its position across the gauge section of 3 mm diameter specimen. The hydrogen concentration profiles for the three alloys corresponded to two weeks precharging with hydrogen. A value of $1.4 \times 10^{-10} \text{ cm}^2/\text{s}$ was used for the super DSS Ferralium 255 and Zeron 100, while a value of $1.8 \times 10^{-10} \text{ cm}^2/\text{s}$ was used for super DSS SAF 2507. The maximum length of brittle cracks for each charging condition was considered according to the assumption that some hydrogen has diffused to this distance.

The surface hydrogen concentration increased with increasing cathodic over-voltage (ie negative potential) and the appropriate values have been calculated from the cathodic Tafel equation; i.e. over voltage = $-b \log(I/I_0)$, where b is 100mV^{146} for each decade increase in cathodic current (and each decade increase in hydrogen generated). This value can be used to establish a relationship between the amounts of hydrogen evolving and taken up on the steel surface during the cathodic precharging process. The C_0 at -800 mV

(SCE) is taken as 0.1 while -900mV is taken as 1. Lowering the potential to -1000mV increases the C_o by a factor of 10. Similarly, lowering the potential to -1100mV increases C_o by 100 and lowering it to -1250mV increases C_o by 3162. This assumes that the hydrogen remains on the surface, and can therefore be absorbed by the metal lattice, rather than being evolved as bubbles. It is also assumed that the hydrogen entry was quantitatively related to the charging current, according to the following reactions:



Or



In the hydrogen charging experiments, gas bubbles (H_2) did not form on surface and a cathodic poison (thiourea) was used to promote hydrogen uptake.

By applying the diffusion coefficient values which were estimated from the figures 6.8, 6.9 and 6.10 for the three materials a profile of the hydrogen concentration for each applied potential with the appropriate values can be calculated for each of the three tested alloys as seen in figures 6.12, 6.13 and 6.14.

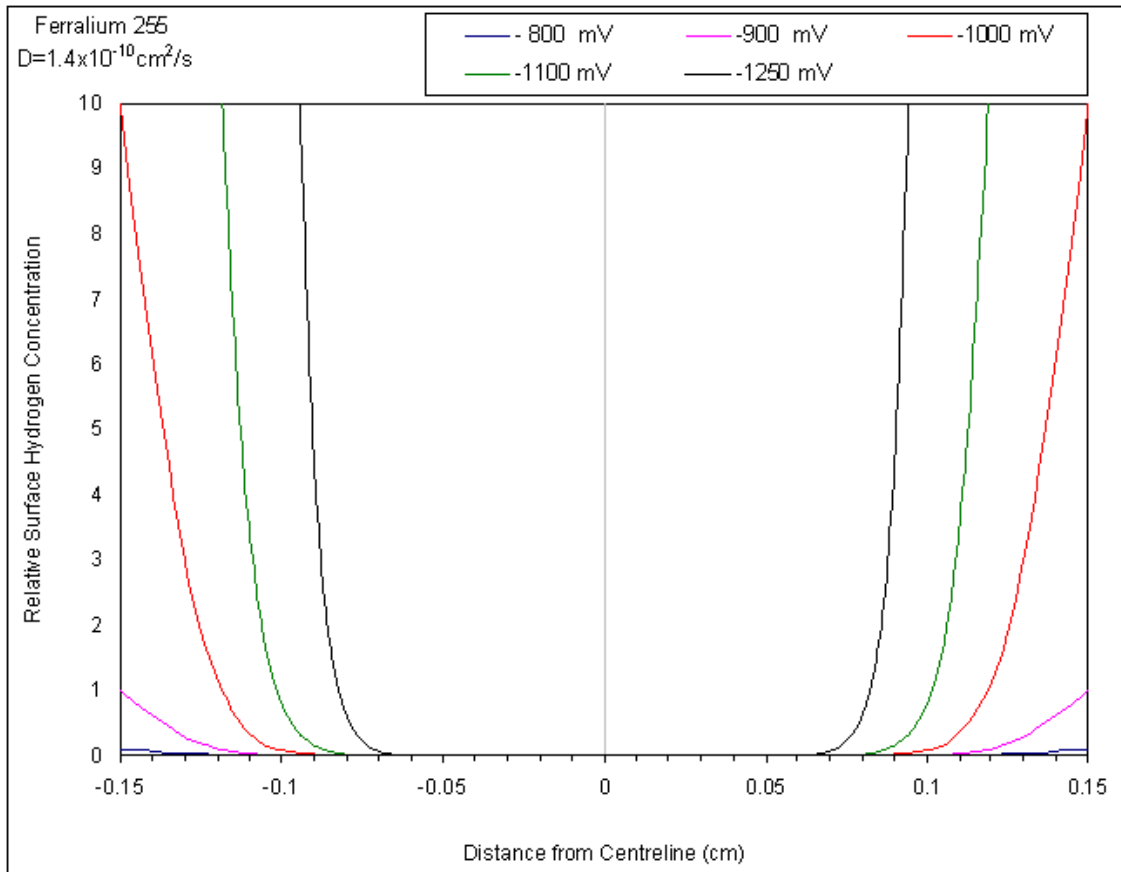


Figure 6.12: Profile of hydrogen concentration modelling in a 3 mm gauge length for the tensile specimen of super DSS Ferralium 255 at a range of applied cathodic potentials for a period of 2 weeks

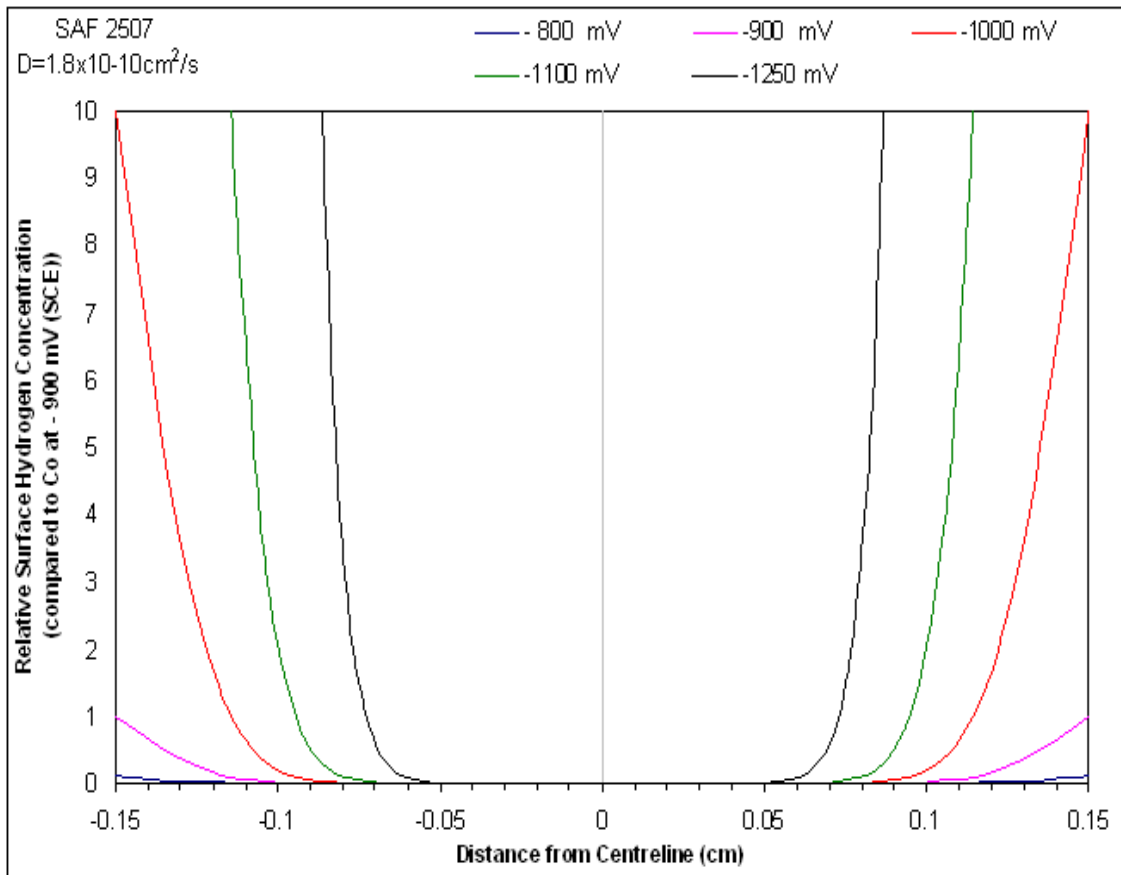


Figure 6.13: Profile of hydrogen concentration modelling in a 3 mm gauge length for the tensile specimen of super DSS SAF 2507 at a range of applied cathodic potentials for a period of 2 weeks

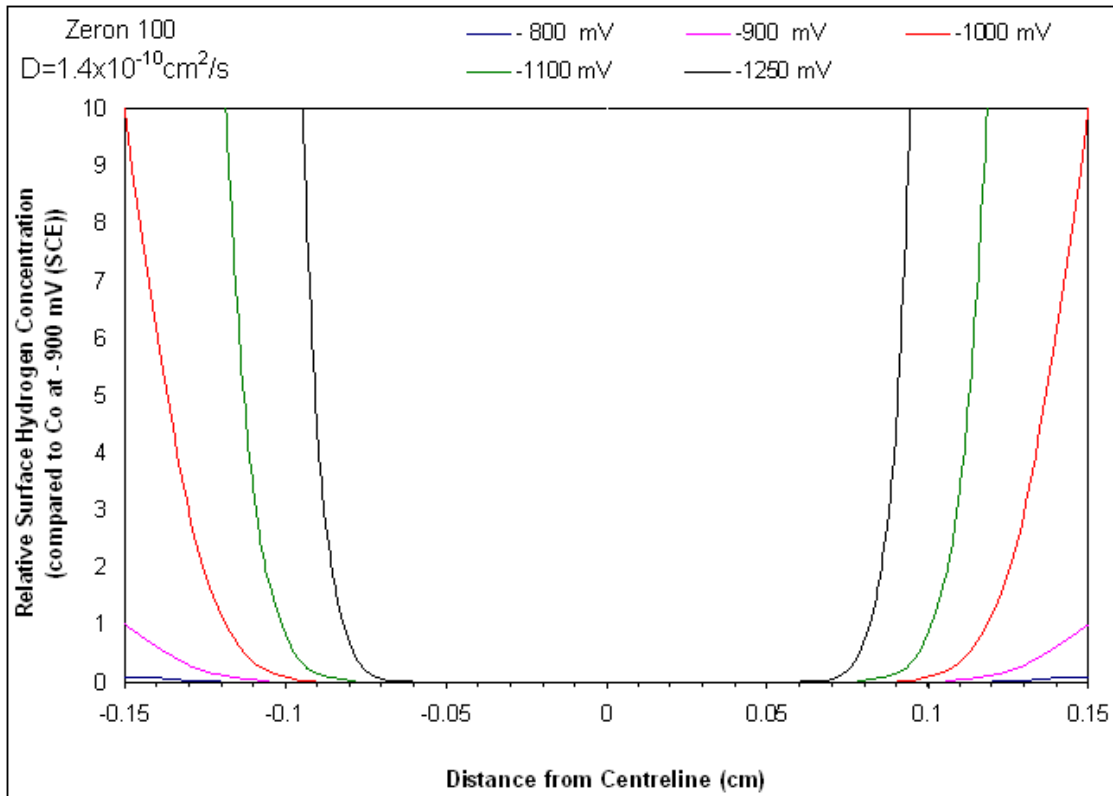


Figure 6.14: Profile of hydrogen concentration modelling in a 3 mm gauge length for the tensile specimen of super DDS Zeron 100 at a range of applied cathodic potentials for a period of 2 weeks

6.7 Crack Propagation Influence

When applied stress and the hydrogen concentration reach critical values, cracks propagate. The crack initiation is expected to occur near the surface where the hydrogen concentration is the highest. The surface hydrogen concentration increases with increasing cathodic over-voltage (i.e. more negative potential). This explains the increase of the brittle fracture area on the fracture surface when decreasing the applied potential (more negative value) as shown on the SEM Images. The production of hydrogen at the surface is higher when applying more negative potential; therefore the hydrogen concentration is higher which can be illustrated on the graph with different profiles.

By knowing the length of the on the fracture surface of the 3mm gauge section of the SSRT specimens from the SEM images, then the critical hydrogen concentration can be estimated from the hydrogen concentration plots for each case. Figures 6.15 to 6.17 have been used to estimate the hydrogen concentration C/C_0 where the hydrogen penetrated into the specimen causing failure.

If the initiation occurred below the surface then more time would be necessary to reach the required hydrogen concentration and therefore the initiation time would not be the same in all cases. However, when the crack initiated, it would grow rapidly into the specimen to the limiting depth where the concentration for the crack propagation had already been exceeded.

Surprisingly, the crack lengths did not increase very much when the severity of charging was increased. This is shown in the graphs in case of -1000mV and -1100 mV (SCE), which reached similar distances from the surface (0.698 mm).

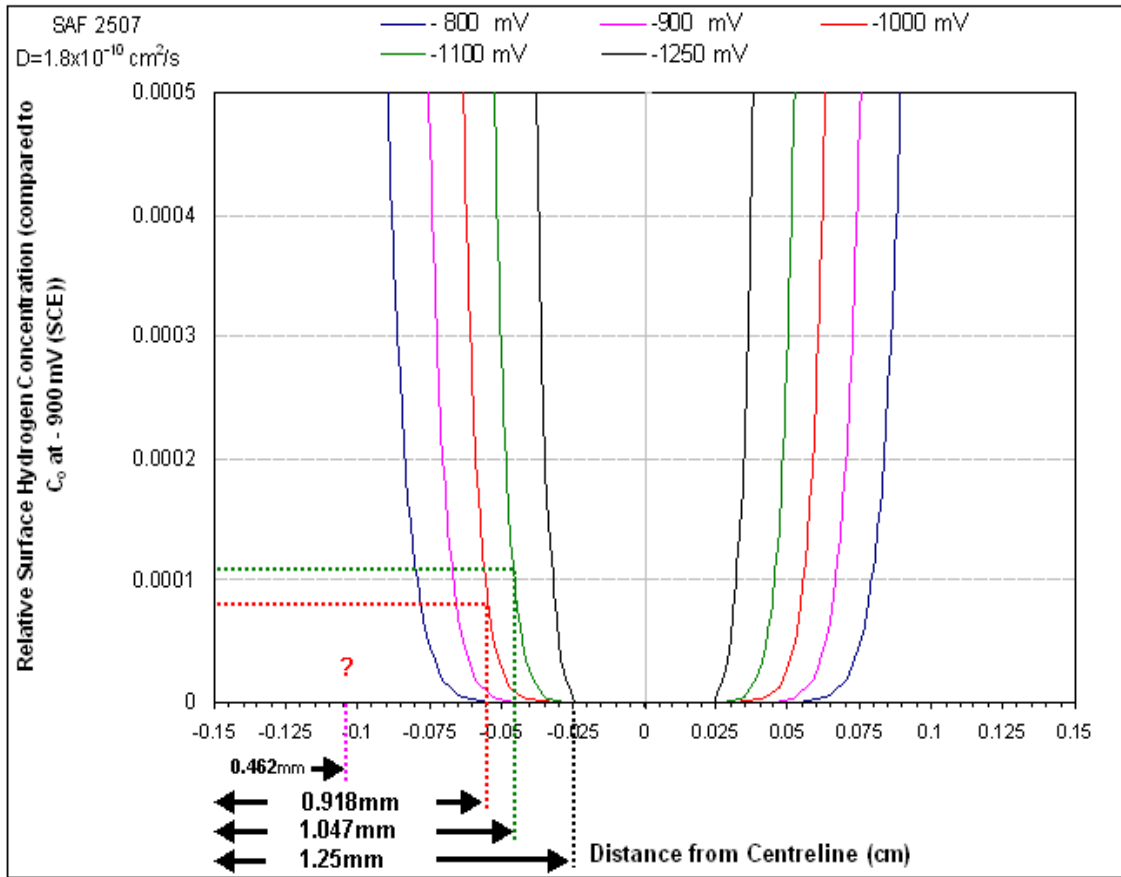


Figure 6.15: Profile of hydrogen concentration modelling in a 3 mm gauge length for the tensile specimen of super DDS SAF 2507 at a range of applied cathodic potentials for a period of 2 weeks

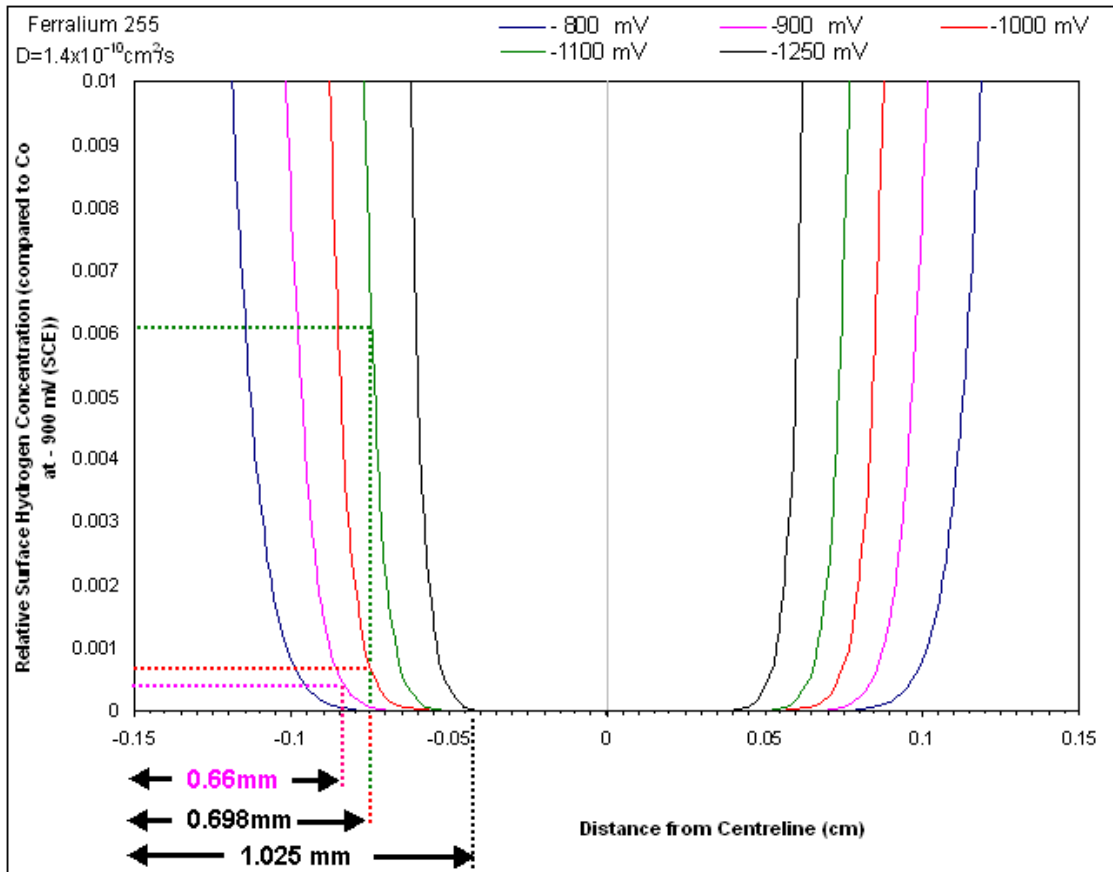


Figure 6.16: Profile of hydrogen concentration modelling in a 3 mm gauge length for the tensile specimen of super DSS Ferralium 255 at a range of applied cathodic potentials for a period of 2 weeks

If the threshold hydrogen concentration had been high, as shown in the red line and (?) mark as show in figure 6.15 then it can be seen that no cracking would have occurred at -900mV and the cracks would have been very different lengths at -1000 and -1100mV. The fact a low measurable crack lengths observed at -800mV suggests that the threshold concentration is above the C_0 for that potential but well below the value at -900mV.

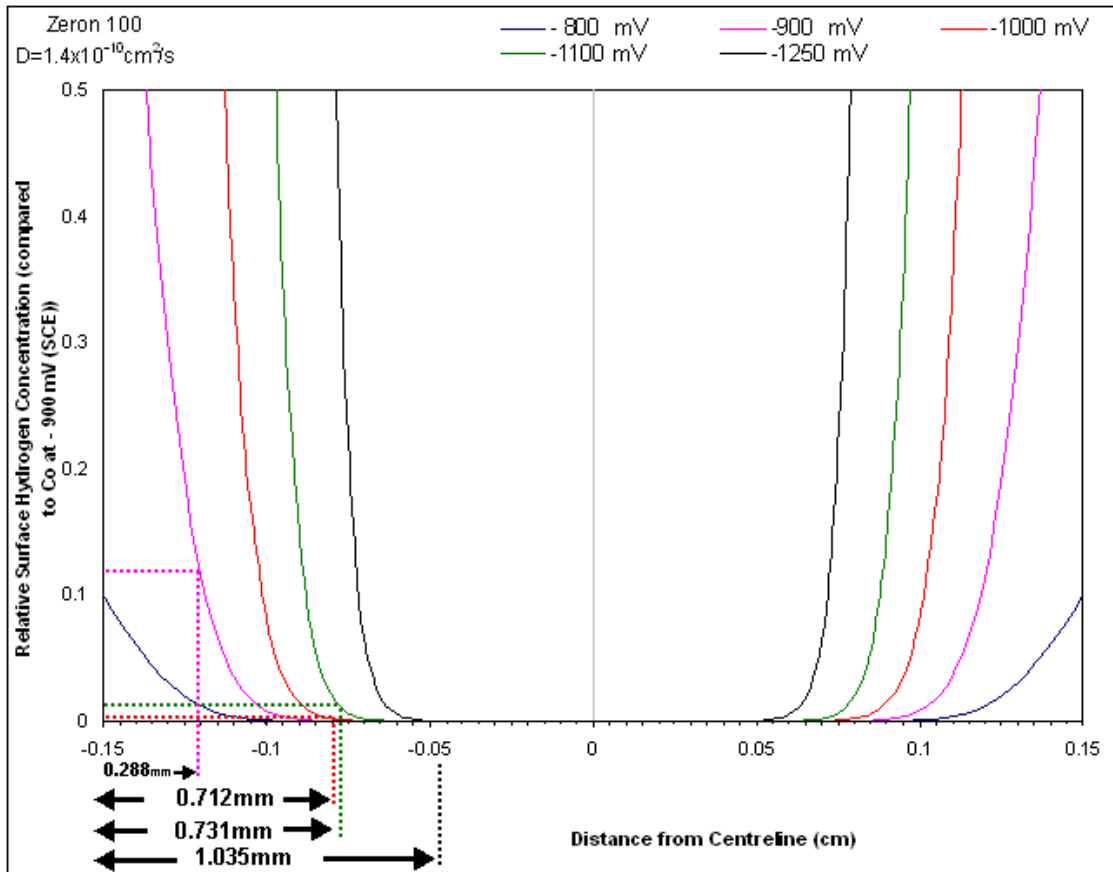


Figure 6.17: Profile of hydrogen concentration modelling in a 3 mm gauge length for the tensile specimen of super DDS Zeron 100 at a range of applied cathodic potentials for a period of 2 weeks

The model can be now applied to generate a hydrogen concentration graph to estimate the minimum diffusion coefficient (D) from each potential corresponded to its maximum crack length for the three alloys. A summary of the diffusion coefficient values are presented in table 6.4. Theoretically, the critical hydrogen concentration can also be read from the hydrogen profile by using the measured D from the permeation methods for Super DSS Ferralium 255 and SAF 2507. The value for each alloy represents the hydrogen threshold value (C_{th}) relative to the surface concentration (C_o) at -900 mV (SCE). A summary of those values are shown in table 6.5. It is worth noting that the diffusion coefficient does not change with the applied potential. However, one can

expect that a change in applied potential can change the surface concentration of hydrogen and therefore the depth to which hydrogen will diffuse to give a specific concentration (greater than zero) in a given time will also be effected.

Material	Potential E (mV)	Maximum crack length (mm)	Minimum D value (to give measured crack length)	Mean minimum D Value	D Value from permeation measurement
Ferralium 255	- 1250	1.026	1.4×10^{-10}	0.86×10^{-10}	$1.38 \pm 0.01 \times 10^{-10}$
	-1100	0.698	6.5×10^{-11}		
	-1000	0.698	6.5×10^{-11}		
	-900	0.66	7.5×10^{-11}		
SAF 2507	- 1250	1.25	1.8×10^{-10}	1.16×10^{-10}	$1.42 \pm 0.11 \times 10^{-10}$
	-1100	1.047	1.42×10^{-10}		
	-1000	0.918	1.15×10^{-10}		
	-900	0.462	3×10^{-11}		
Zeron 100	- 1250	1.035	1.4×10^{-10}	0.76×10^{-10}	No Measurement
	-1100	0.731	4×10^{-11}		
	-1000	0.712	5×10^{-11}		
	-900	0.656	7.5×10^{-11}		

Table 6.4: Estimated mean minimum diffusion coefficients (D) from each potential corresponded to the crack depth from the hydrogen concentration graph for the three super DSSs materials

Material	Potential E (mV)	Maximum crack length (mm)	C_{th} values relative to C_o at -900 mV (SCE) using measured D from permeation $(C/C_o)_{-900}$	Mean C_{th} value $(C/C_o)_{-900}$
Ferralium 255	- 1250	1.026	0	0.00135
	-1100	0.698	0.0048	
	-1000	0.698	0.0005	
	-900	0.66	0.0001	
SAF 2507	- 1250	1.25	0	0.00375
	-1100	1.047	0.00002	
	-1000	0.918	0.000011	
	-900	0.462	0.015	

Table 6.5: Values for the hydrogen concentration obtained from the hydrogen profiles

Some basic assumptions in a modified brittle fracture model intended in SSR testing have been presented. The model used the maximum crack length on the fractured surface where the hydrogen penetrated. This brittle region was found in all specimens that precharged from -900 mV to -1250 mV (SCE). The relation between the maximum detectable crack depth and the hydrogen diffusion coefficient was calculated based on the precharging potential. The results of these calculations are satisfactory when compared with the measured hydrogen diffusion coefficients.

The meaningful information regarding the brittle crack length on the fracture surface of the tensile specimen has added another advantage to SSR testing. The crack length can be used to estimate the value of the hydrogen diffusion coefficient. Therefore, it extended the use of the SSRT further than a ranking

method for different materials, microstructural and environmental conditions. In this project the method was used in ranking material in terms of their susceptibility to hydrogen embrittlement and comparing ductility loss in the same environment. In addition, the SSR test was effective in highlighting the embrittlement index for a range of applied cathodic potential.

7 General Discussion

7.1 Influence of Microstructure

Duplex stainless steel or ferritic austenitic stainless steel, have a long commercial existence history for almost 80 years. Due to an encouraging combination of corrosion resistance and mechanical properties, they attract interest in a very wide range of applications. During the past years, several duplex alloys have been developed to meet the design requirements of many applications. Mats et al ¹⁴⁸ has described some of the primary technical reasons for selecting a DSS, and some of the main reasons are given below:

- Raw material cost (steel price)
- Weight saving (also in combination with those below);
- Uniform or pitting corrosion resistance;
- Stress corrosion cracking;
- Resistance to intergranular corrosion;
- Combination corrosion resistance and high mechanical strength;
- Fatigue endurance
- Hardness wear resistance
- Physical properties, such as thermal expansion
- Super plastic behaviour

In some cases, more than one factor can be the reason for selecting a DSS. Many variables characterize the corrosive environment such as chemicals and their concentration, atmospheric conditions, temperature, load, life and maintenance type. Knowing the exact nature of the environment is very important in selecting the right alloy. In general a wide range of DSS alloys can meet many of those requirements in terms of corrosion performance. They can be utilized under many conditions and can replace many stainless steel grades with great benefits. Today DSS have gained their popularity because of their good corrosion resistance, excellent price / performance ratio.

However, DSSs components are subjected to cathodic protection as a result of being coupled to a cathodically protected steel structure by sacrificial anodes (typically -1000 to -1100 mV SCE)¹⁴⁹. Cathodic protection can generate hydrogen, which, if absorbed, may lead to embrittlement of metallic components with the resultant danger of failure. Failure occurs when the residual ductile core is reduced in area by an encroaching hydrogen embrittlement front to a cross-section which cannot carry the load placed upon it. This threat of damage caused by hydrogen embrittlement of metals has become a problem to the gas and oil industry where high concentrations of hydrogen are present.

Three combined factors must exist to embrittle the material. These factors are: source of sufficient hydrogen, residual or applied tensile stress (mechanical load) and a susceptible material. With DSSs, a large forging alloy with a coarser structure is more susceptible than a powder metallurgy material containing small grains¹⁵⁰.

7.2 Ranking of Alloys

Slow strain rate tests have proven to be a successful method to rank material for their hydrogen susceptibility. This technique is widely used to study the environmental cracking of materials. In this research, the results of slow strain rate tests showed that the ductility of duplex stainless steels is decreased when a sufficient hydrogen concentration is present (when precharged at a potential of -900 mV (SCE) and below).

The ranking of the hydrogen embrittlement susceptibility of the super DSSs was obtained from the SSR testing based on the embrittlement index calculated from the percentage of the reduction of area (%RA). Figure 7.1 shows the embrittlement index for the three tested alloys. The evaluation of this performance is valid when comparing the potentials of -900, -1000, and -1100 mV (SCE). These potentials can simulate the cathodic protection that is used in the service field. Moreover, the calculated values of the embrittlement index increased dramatically at precharged potentials from -800 to -1100 mV (SCE) and increased uniformly (plateau) with further potential decrease (to -1250 mV

(SCE)). This means that the reduction area of the brittle fracture surface reaches a uniform value at a potential of -1100 mV (SCE).

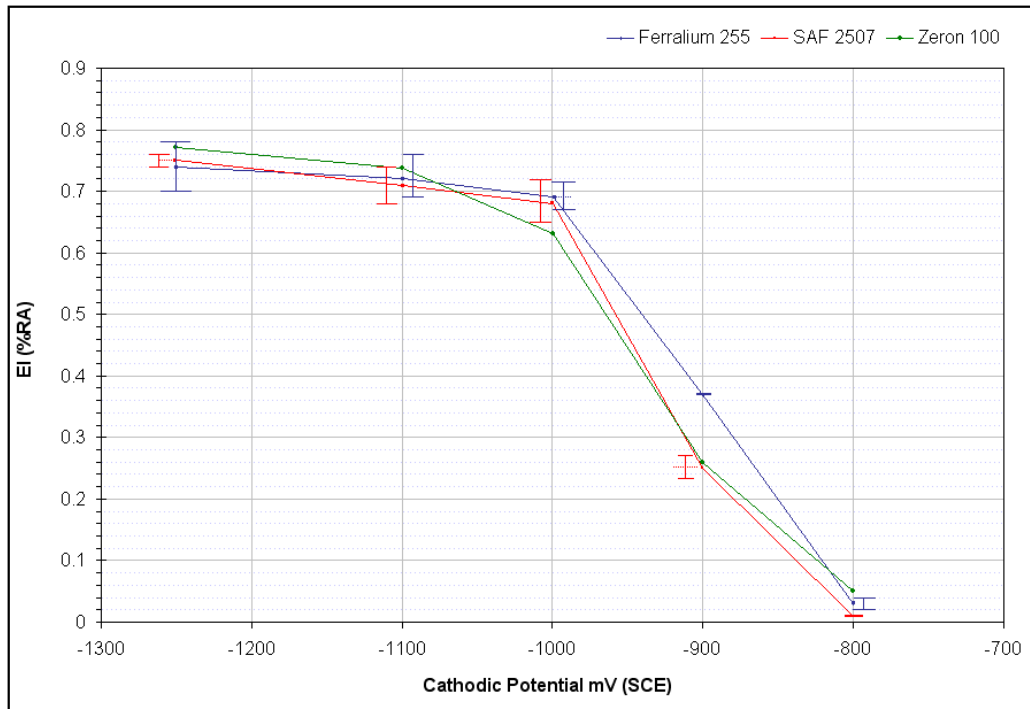


Figure 7.1: Comparison of Embrittlement Index (%RA) Vs. cathodic potentials from -1250 to -800 mV SCE after SSR testing for all three super DSSs

The results of slow strain rate tests showed that the ductility of duplex stainless steels is decreased when a sufficient hydrogen concentration is present (when precharged at a potential of -800 mV (SCE) and below). At this point, it is possible in this project to compare the hydrogen embrittlement susceptibilities for the three super DSS alloys, ranked in the order as shown in Table 7.1:

Material	Degree of Embrittlement				
	-800 mV	-900 mV	-1000 mV	-1100 mV	-1250 mV
SAF 2507	Least	Least	↓	Least	↓
Zeron 100	Most	↓	Least	Most	Most
Ferralium 255	↓	Most	Most	↓	Least

Table 7.1: Degree of Embrittlement susceptibilities based on the reduction of area after SSR testing for the tested alloys

It can be noticed that the super DSS SAF 2507 has the least embrittlement index (for precharging potentials of -800, -900 mV SCE) but the highest diffusion coefficient and crack length. It is very important to consider the actual cathodic protection potential that is used in the offshore structure. Over protection may lead to hydrogen damage while under protection may lead to corrosion. On the other hand, Ferralium 255 has the least embrittlement index when considering the precharging potential at -1250 mV (SCE). In this case the potential that resembles the actual cathodic protection in the service condition should be taken as a guide to choose what material is less susceptible to hydrogen embrittlement based on the %RA of SSR testing considering the crack length and the diffusion coefficient.

It should be noted that variation of the diffusion coefficients for all the three alloys is small when comparing the measured value obtained from the hydrogen permeation technique.

Although, the SSR test method can be successfully used for ranking materials in terms of their hydrogen susceptibility, it is a time consuming test and needs special costly laboratories. So, it would be interesting to consider a simple alternative method to evaluate these materials for industrial service under cathodic protection. Investigating the corrosion behaviour of the individual

phases might be a key factor to understand the corrosion properties for the whole alloy but there is always a risk in overestimating the importance of the imagined events. Using a combination of many techniques might be helpful especially when it has sufficient background data. A correlation between the results obtained in this research and some of the material properties could be used to gain more understanding and this can be presented in the following section.

It would be interesting if there is a hydrogen embrittlement resistance equivalent (HERN) number to rank alloys in terms of hydrogen embrittlement susceptibility, similar to the pitting resistance equivalent number (PREN). The PREN number of duplex stainless steel does not give any direct indication of hydrogen embrittlement (HE) susceptibility, but it does give an indication of the alloy microstructure, which can be related to the hydrogen effect in the alloy structure.

7.3 Consideration of Pitting

The variation of alloying elements in super DSSs is not systematic, which makes it difficult and more complicated to point out the positive effect for particular alloying element. The relationship between the corrosion behaviour and the partitioning of the alloying elements plays an important role between the two phases. It was possible to point toward the effect of various elements on the basic structure of the two phases by presenting the PREN number. The aim of these measurements was to evaluate the effect of the segregation of the alloying elements on the pitting corrosion for each phase and compare it with other measurements.

The pitting resistance of stainless steel is primarily determined by its composition. The three elements which have a significant beneficial effect are chromium, molybdenum and nitrogen. The most widely used formula¹³⁵ for DSS which gives their relative contribution is:

$$PRE_N = \% Cr + 3.3 (\% Mo) + (16 \%N)$$

Tungsten was also included in the molybdenum-rating factor to acknowledge its affect on pitting resistance (PER_W)³⁹. Later, copper was introduced as a beneficial effect in the PRE number with a modified extended formula¹³⁶.

$$PRE_W = \% Cr + 3.3 (\% Mo + 0.5 W) + (16 \%N)$$

$$PRE_{EXT} = \% Cr + 3.3 (\% Mo + 0.5 W) + 2 (\% Cu) + (16 \%N)$$

It is still possible to point towards certain tendencies in how the addition of certain alloying elements affects the corrosion behaviour of the steels. The Cr and Mo addition improves the pitting resistance and enhances the passivity. This improvement occurs due to producing a more resistant passive film by providing better coverage/connectivity of the protective layer, reducing the anodic peak making the change from active to passive behaviour easier, and reducing the dissolution rate for material at local corrosion sites making sustaining the local chemistry necessary for localized corrosion more difficult. Nitrogen has a complex synergistic effect in Fe-Cr-Mo alloys that produces a strong effect in practice, but its mechanism is not well understood.

The influence of the alloying elements on the corrosion properties of stainless steel is summarized in figure 7.2. Chromium has a beneficial effect on the stability of the passive file and increasing its content raises the pitting potential and the critical pitting temperature of duplex stainless steel¹³⁷. However higher content of chromium can promote the precipitation of undesirable carbides and sigma phase.

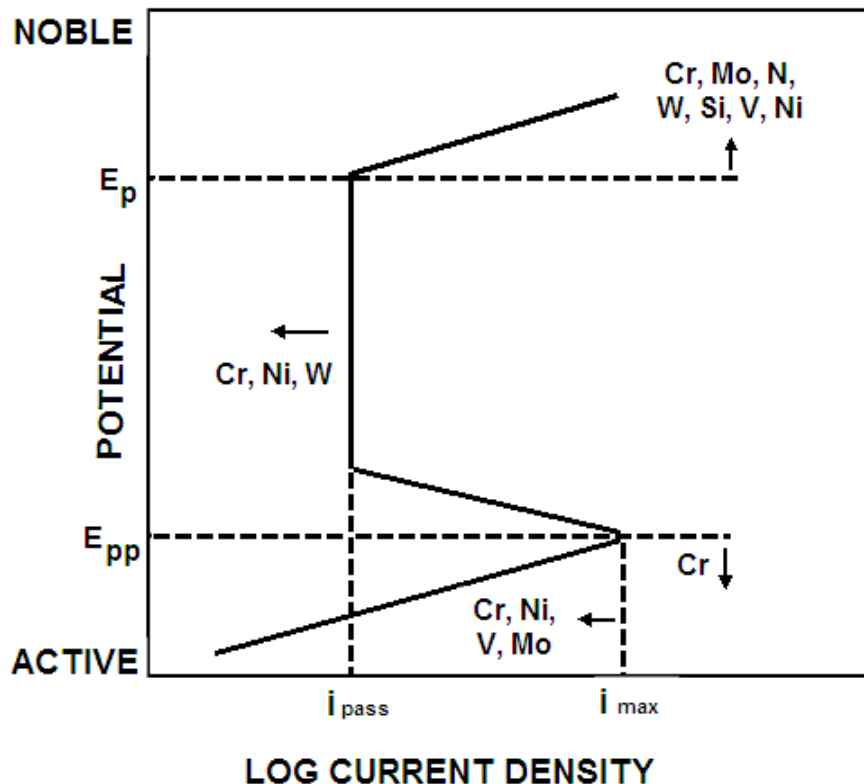


Figure 7.2: Schematic summary of the effect of alloying elements in stainless steels on the anodic polarization curve ¹³⁷ .

Since there are two phases in the super DSS, with unevenly elements partitioned between them, it is obvious that the PREN for each phase should have a different value which can be calculated separately according to its chemical composition. Therefore, it is worth considering the actual pitting resistance number by whichever phase gives the lower value.

The chemical composition of each phase in the microstructure was analysed five times for all the three alloys. The average composition of both phases was taken and the error shown by the standard deviation. The nitrogen content from the supplier test certificate was considered to be partitioned between the ferrite and the austenite in the ratio of 1:6 ¹³⁸ .

A summary of a range of calculated PREN values for the three super DSS alloys with the content of the important elements like Cr, Mo, N, W and Cu in both austenite and ferrite are shown in table 7.2.

Material	Phase	Chemical Composition (wt%) (Avg)					PRE _N (Avg)	PRE _W (Avg)	PRE _{EXT} (Avg)	E _{pit} (mV) SCE
		Cr	Mo	Cu	W	N				
Ferralium 255	Austenite	24	2.5	1.7	-	0.5	40.1	40.1	43.4	882
	SD	0.18	0.09	0.1	-	-	0.25	0.25	0.3	22
	Ferrite	25.3	3.4	1.1	-	0.07	37.6	37.6	40	518
	SD	0.3	0.23	0.08	-	-	0.6	0.6	0.7	29
SAF 2507	Austenite	24	2.4	0.24	0.7	0.52	40	41.5	42	862
	SD	0.09	0.04	0.03	0.07	-	0.12	0.44	0.35	25
	Ferrite	26.2	3.8	0.18	0.9	0.07	39.8	41.6	42	540
	SD	0.29	0.08	0.01	0.03	-	0.37	0.52	0.53	44
Zeron 100	Austenite	23.3	2.8	0.7	0.6	0.46	39.8	41.6	42.6	868
	SD	0.43	0.1	0.05	0.04	-	0.7	0.6	0.6	21
	Ferrite	25.6	3.3	0.48	0.9	0.07	37.8	39.4	40.4	503
	SD	0.36	0.1	0.02	0.07	-	0.47	0.38	0.38	34
$PRE_N = \%Cr + (3.3 \%Mo) + (16 \%N)$ $PRE_W = \%Cr + 3.3 (\%Mo + 0.5\% W) + 16 (\%N)$ $PRE_{EXT} = \%Cr + 3.3(\%Mo + 0.5 \% W) + 2(\%Cu) + 16 (\%N)$										

Table 7.2: Chemical composition and PRE of super DSSs

Even though the ferrite phase had higher chromium content than austenite phase, the dissolved nitrogen in the austenite was higher than in the ferrite, which may have increased the pitting resistance equivalent number (PREN) of austenite to be higher than that of ferrite.

The error in the composition analysis and calculating PRE numbers for the three tested material was assessed by the standard deviation and is thought to not have a very significant effect.

Ferralium had the highest mean austenite pitting potential (882 mV SCE) with an austenite PRE_{Ext} number of 43.4 but the lowest mean ferrite pitting potential (518 mV SCE) with a ferrite PRE_{Ext} number of 40 when comparing with the

other two alloys, as shown in figure 5.26. However, when the standard deviations in these values are considered the differences between the three alloys are smaller and may not be particularly significant. However, a possible explanation for slightly better properties of the Ferralium 255 is that it had the highest copper content of all three alloys and since copper segregates in the austenite phase it might gain its resistance due to the higher copper content. This can be supported by using the extended pitting equivalent (PRE_{Ext}) which takes in to account other positive alloys effect like copper.

Figure 7.3 shows a comparison of the extended PREN number in each phase (ferrite and austenite) for the three super DSS alloys. It is worth to consider the actual pitting resistance number by whichever phase gives the lowest value. Pitting corrosion primarily takes place in the ferrite phase due to the lower pitting potential than the austenite phase. This is because nitrogen and nickel are higher in the austenite phase. From Figure 7.3, SAF 2507 has a better pitting potential based on the assumption that the ferrite phase should be considered as the alloy pitting potential. The ferrite pitting potential should be considered the alloy pitting potential since it is more active than the austenite and it is the first phase to corrode in the alloy. Moreover, the development of duplex grades always optimises to have almost the same PREN number for both phases. A uniform distribution, when it is possible, can improve the pitting corrosion behaviour by eliminating the composition differences in the two phases.

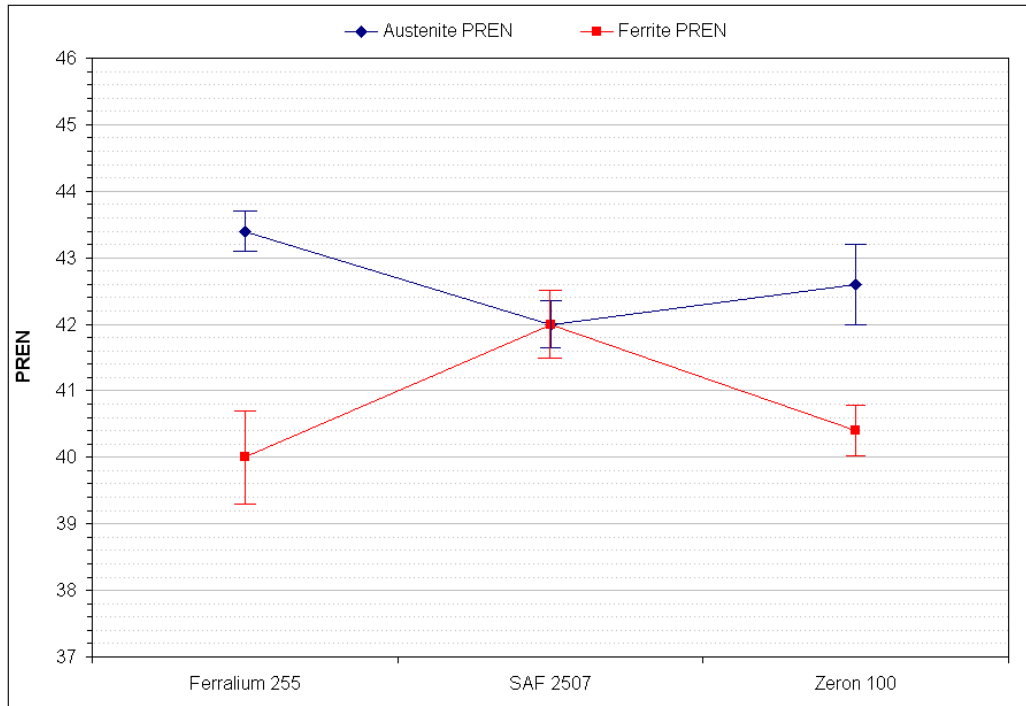


Figure 7.3: PREN of the ferrite and austenite phases for the three alloys based on extended PRE number calculations

7.4 Influence of Microstructure

Based on the chemical compositions, the ratios of nickel equivalent (Ni_{eq}) to chromium equivalent (Cr_{eq}) for the three alloys are also shown in Table 7.3. The Ni_{eq}/Cr_{eq} ratio can express the concentration behaviour of the essential elements. The following formulas¹⁴⁷ were used to determine both Ni_{eq} and Cr_{eq}

$$Ni_{eq} = \%Ni + 30 \%C + 0.5 \%Mn + 25 \%N + 0.3 \%Cu$$

$$Cr_{eq} = \%Cr + \%Mo + 1.5 \%Si$$

All the concentrations of the elements are expressed in weight percentages.

The results shown in Table 7.3 indicate that the ratio of Ni_{eq}/Cr_{eq} for super DSS SAF 2507 was higher than that for super DSS Zeron 100 and Ferralium 255. In addition, the ferrite content in SDSS SAF 2507 is lower than that in the other two alloys.

Material	Ni _{eq}	Cr _{eq}	Ni _{eq} / Cr _{eq}	Ferrite (Vol%)	Austenite (Vol%)	Ferrite mean grain size (µm)	Austenite mean grain size (µm)
Ferralium 255	13.4	29.7	0.45	52	48	16.7±11.4	10.6±5.3
SAF 2507	14.5	29.4	0.49	51	49	8.1±6.3	7.4±5
Zeron 100	13.6	29.3	0.46	52	48	12.7±7.5	9.2±5.6

Table 7.3: Summary of volume fraction and grain size for both ferrite and austenite grains in the longitudinal section for the three alloys

Correspondingly, figure 7.4 summarized effect of Cr and Mo expressed as PREN in each phase shows a slightly increasing trend with Ni_{eq}/Cr_{eq}. This is due to the composition difference in each phase of the alloy. The ferrite phase showed enrichment of Cr and Mo while the austenite phase showed enrichment in Ni and N. The results in figure 7.4 indicate that the Ni_{eq}/Cr_{eq} ratio increases slightly with increasing the ferrite PREN, although it is not clear that a correlation between these parameters would be expected.

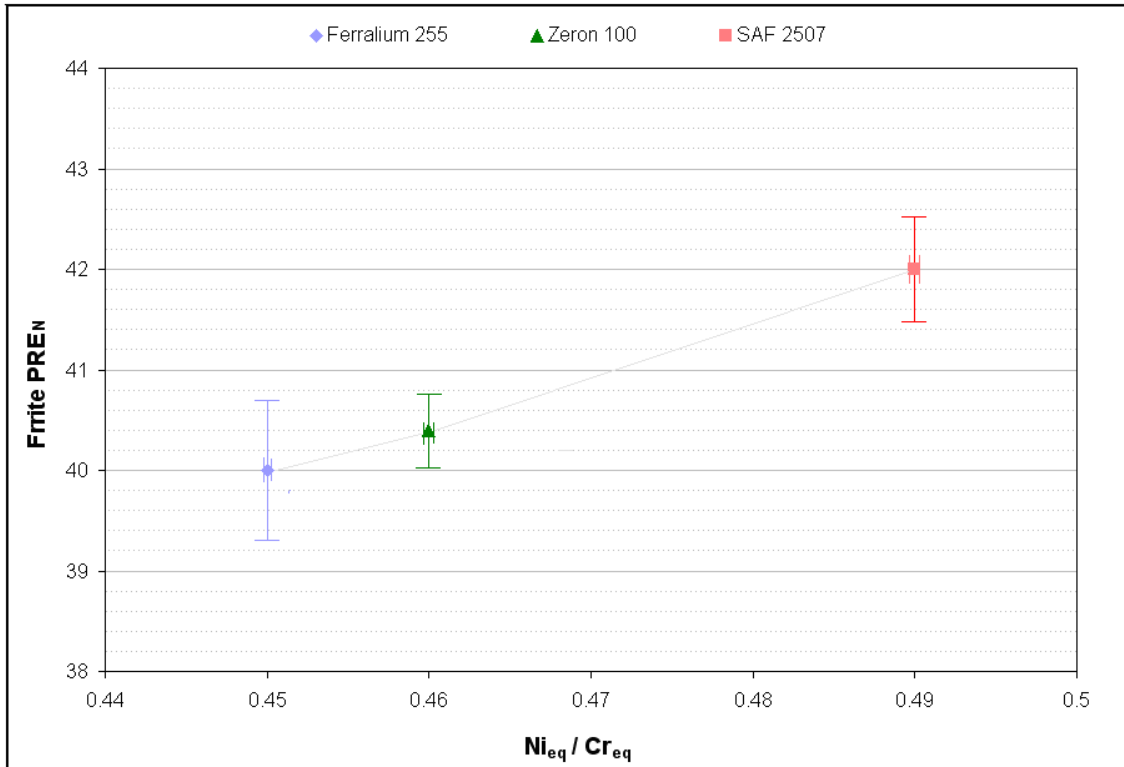


Figure 7.4: Effect of the alloy composition expressed as a ratio of Ni_{eq}/Cr_{eq} on the ferrite PREN number for the three alloys

7.5 Influence of Grain Size

The microstructure plays a role in terms of ferrite path (austenite spacing)¹⁵³. When this parameter decreases the material is more resistant¹⁵⁰. This is because austenite is able to arrest cracks. Large grain materials are also more susceptible than smaller grain materials. Taylor et al.¹⁵⁴ found the large grain size forging material to be also more susceptible to embrittlement than the small grain size material they used when tested under CP. Chou et al.¹⁵⁵ has also observed the same behaviour under cathodic applied potential in 26% NaCl for 22% Cr duplex stainless steels with two different grain sizes. His conclusion was the effective hydrogen diffusivity decreased with increasing the grain size (ferrite/austenite). Figure 7.5 shows the relationship between the ferrite grain size and the Ni_{eq}/Cr_{eq} ratio but there was not a significant difference between the three materials. The grain size is affected by other factors such as the

cooling rate. Maximum Ni_{eq}/Cr_{eq} ratio means higher volume of austenite phase. SAF 2507 has the maximum Ni_{eq}/Cr_{eq} ratio and austenite volume. The three alloys have different cooling treatment as shown in table 7.4.

Material	Heat Treatment
Ferrallium 255	Solution treated followed by water quenching (1060 ° C)
SAF 2507	Solution annealed – water (1100 ° C) for 2 hours
Zeron 100	Quenched / Solution annealed

Table 7.4: Heat treatment for the three tested super DSS

A recommendation was proposed in terms of microstructure considering the following ranking from more susceptible to less susceptible that can be applied to hydrogen embrittlement: forgings > rolled plates > hydrostatic hot pressed ¹⁵⁰

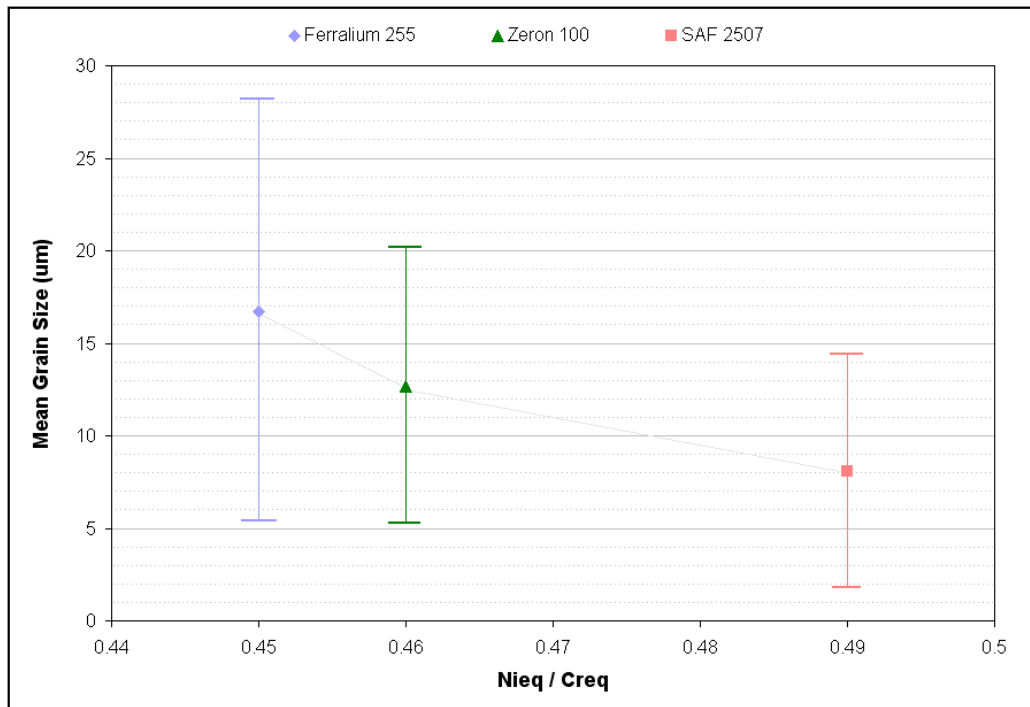


Figure 7.5: Effect of the alloy composition expressed as a ratio of Ni_{eq}/Cr_{eq} on mean grain size of the ferrite phase for the three alloys

7.6 Influence of Hydrogen Diffusion

Hydrogen diffusion through duplex stainless steel is a complicated process due to the existence of the two phases. The hydrogen diffusion through the austenite, FCC structure, is much slower than the ferrite, BCC structure. In addition, the hydrogen solubility in the austenite is higher than the ferrite grains. Thus austenite grains have different characteristics of hydrogen trapping. Some other factors should also be considered in terms of diffusivity such as the volume and shape of grains in the two phases.

The material which is susceptible to embrittlement is determined by three factors: susceptible microstructure, the presence of hydrogen, and stress. Highly ferritic microstructures, with body centred cubic structure (BCC), are considered susceptible because they have high strength, low toughness, high hydrogen diffusivity and low hydrogen solubility. Austenitic stainless steels, FCC structure, are known as insensitive to hydrogen embrittlement which is often attributed to their low hydrogen diffusion coefficient and high hydrogen solubility. Most of the failures that have occurred have been caused by one or a combination of the following: very high loads, large grain sizes, intermetallic phase or high ferrite content ^{150, 151}.

The susceptibility of DSS (austenite + ferrite) increases as ferrite content increases; therefore, it is necessary to have a properly controlled ferrite/austenite balance. The reason for this is that the diffusivity of hydrogen in austenite is significantly lower than in ferrite. The austenite can act as a partial sink for hydrogen. It is important to consider the differences in diffusivity for the ferrite and the austenite stainless steel at room temperature. The hydrogen diffusion coefficient of duplex is in the order of 10^{-10} cm²/s and is between the values for austenitic and ferritic stainless steels. Hutchings et al. ¹⁵² have analysed the permeation transients for super duplex stainless steel

Uranus with a range of austenite volumes and different grain orientations. A summary of their analysis are presented in Figure 7.6. Table 7.5 shows a summary of some published hydrogen diffusion values of the austenitic, ferritic and duplex stainless steels.

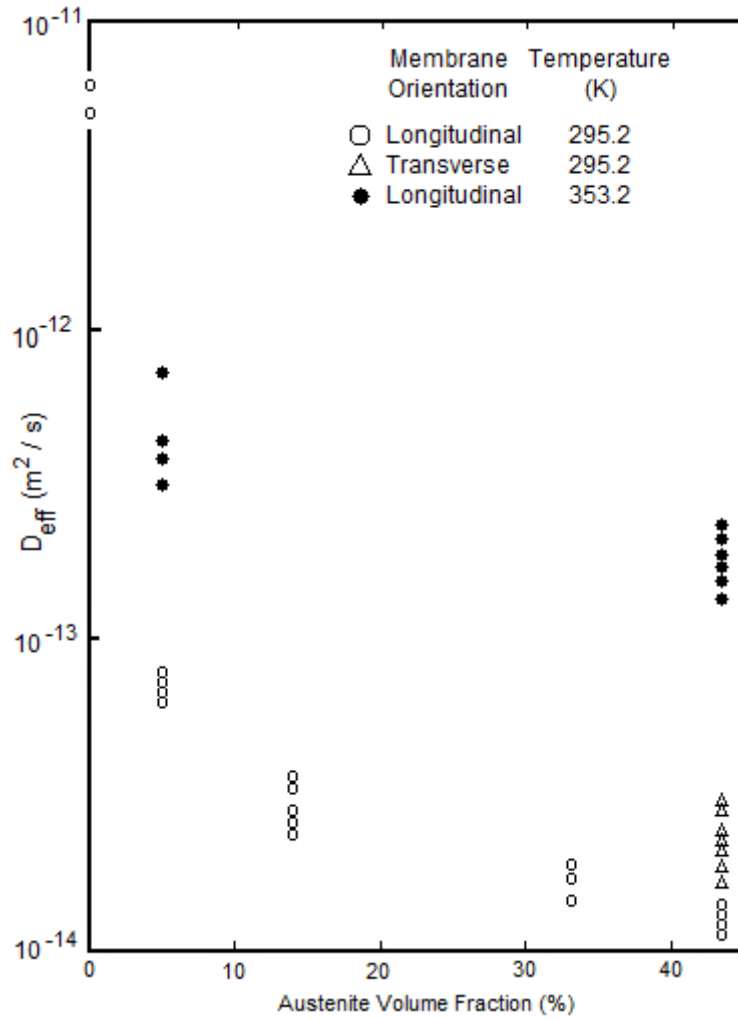


Figure 7.6 : Variation of the effective diffusion coefficient with volume fraction of Uranus B50 duplex stainless steel

Material Structure	D (cm ² /sec)	Reference
Austenitic SS (FCC)	2.15×10^{-12}	158
Duplex SS (FCC + BCC)	$10^{-9} - 10^{-10}$ (depending on the ferrite/austenite ratio)	159 - 163
Ferritic SS (BCC)	10^{-7}	159

Table 7.5: Diffusion coefficient of hydrogen in different structure of stainless steel

Trap sites in grain boundaries is one of the important effect influencing hydrogen embrittlement. Finer grains will allow hydrogen to be trapped in the grain boundaries and therefore less hydrogen will permeate the material, which can increase the time to failure in slow strain rate test ¹⁵⁵. In general sense, it can be argued that austenite phase can act as irreversible traps due to its low hydrogen diffusivity ¹⁵⁶.

Hydrogen can diffuse in the specimen in any direction to reach a point on a phase boundary of the ferrite/austenite. Figure 7.7 can be used to show the path that the hydrogen might take as a short circuit in the ferrite phase. It contained the austenite phase (bright area) embedded in a ferrite matrix (dark area). The volume fraction and the mean grain size of each phase in the longitudinal section, in each alloy, determined by using an image analyzer, are given in table 7.1. Clearly, the colony grain size (either austenite or ferrite) of super DSS Ferralium 255 was larger than that of SAF 2507 and Zeron 100.

Referring to figure 5.1 through 5.6, these micrographs show the banding effect of the Austenite and ferrite phase. The proportion of those two phases is similar for the three alloys (in the range of $50\% \pm 2$). However, the effect of the austenite and ferrite shape is the important geometrical factor. Hydrogen can diffuse quickly through the ferrite phases until it encounters an austenite island.

Reaching the austenite phase can slow down the diffusion due to its higher solubility level.

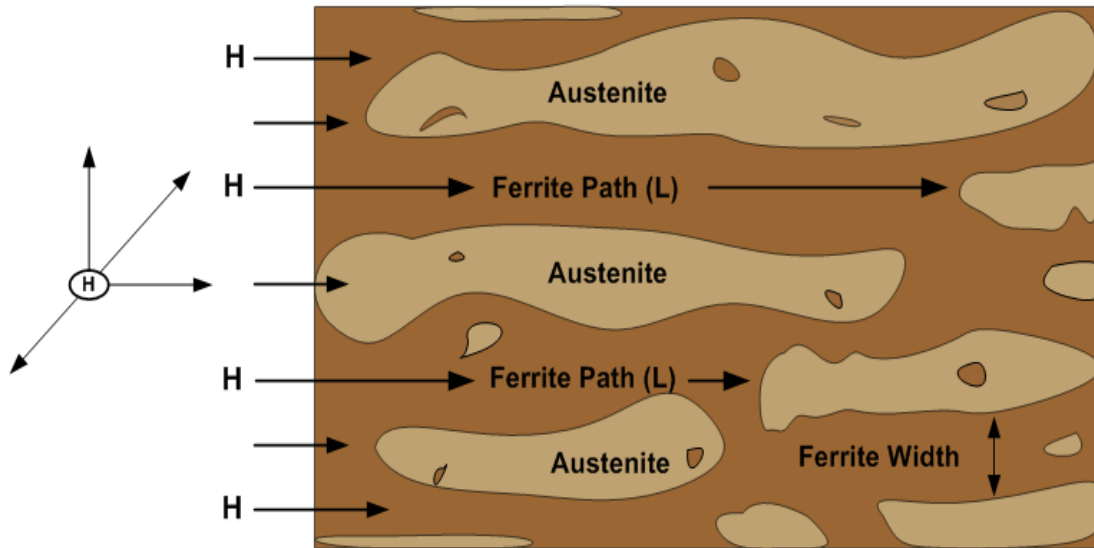


Figure 7.7: Illustrated graph showing the ferrite length path and width for the hydrogen atoms diffusion through a permeation membrane

The length and width of the ferrite path was measured using an image analyser and expressed as an average of 50 measurements for each alloy (Table 7.6). The ferrite path length and width of the specimen can effect and influence the diffusion coefficient value. A longer and wider ferrite path can give a higher chance for the hydrogen atoms to permeate the metal without being trapped by the austenite.

Material	Ferrite Path length (um)				Ferrite Width (um)			
	Mean	SD	Min	Max	Mean	SD	Min	Max
Ferratum 255	39	32	4	113	16.7	11.4	2.6	45.6
SAF 2507	22	28	1.8	118	8.1	6.3	1.5	37.4
Zeron 100	24.8	23	1	109	12.7	7.5	1.6	44.2

Table 7.6: Summary of the length and width of the ferrite phase in the longitudinal section for the three alloys

A question can be raised whether there is a relationship between the hydrogen embrittlement susceptibility and other factors such as chemical composition, ferrite/austenite ratio, size and grain distribution and segregation of alloying elements in each phase. Clearly, these factors could play an important role in the hydrogen effect.

By comparing the ferrite PREN and the diffusion coefficient value for the three alloys, SAF 2507 has the higher value for this phase as shown in figure 7.8.

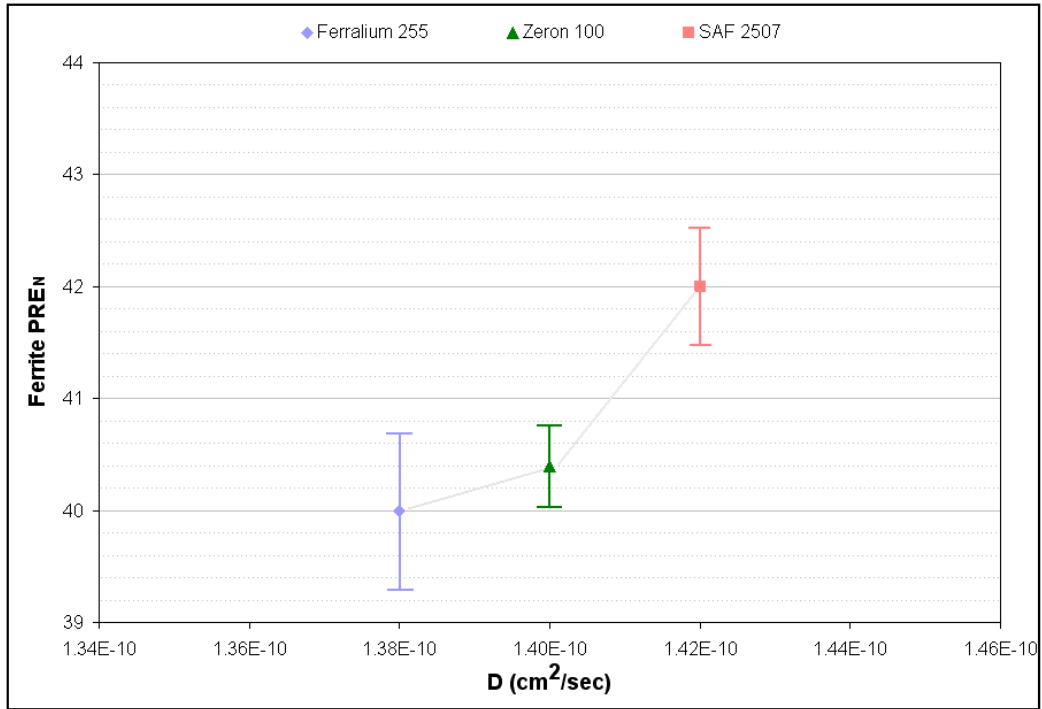


Figure 7.8: Effect of the ferrite PREN number on the hydrogen diffusion coefficient for the three alloys

Hydrogen transport in the alloy is an important factor in the tendency to hydrogen embrittlement. A lower hydrogen diffusion coefficient means less hydrogen should penetrate the alloy. Therefore, the hydrogen diffusion coefficient is an important property that can be associated with the extent of the hydrogen embrittlement for structural components. However, it is important to realise that measuring the hydrogen diffusion coefficient for super DSS is very difficult and may take much longer than for iron.

In this project, the susceptibility of super DSS to hydrogen embrittlement was determined in 3.5% NaCl solution at a temperature of 50°C over a range of cathodic potentials after a precharging period of 2 weeks using cylindrical specimens in a SSR testing technique. The determination of the hydrogen embrittlement index was based on the percentage of the reduction of area for the fractured specimens. The length of the brittle crack on the fracture surface was used to estimate the diffusion coefficient for each alloy for a particular test

condition. The cracking behaviour may be attributed to the synergistic effect of the absorbed hydrogen and the applied stress in the SSRT. Clearly, the embrittlement index was related to the length of the brittle crack which makes the diffusion coefficient an important factor.

At this point, a comparison between the embrittlement index (EI) and the hydrogen diffusion coefficient can be presented in figure 7.9. It can be observed that super DSS SAF 2507 has a higher hydrogen diffusion coefficient but lower embrittlement index. At the same time, SAF 2507 has the smallest grain size and the highest UTS. Higher strength steels are more sensitive to hydrogen embrittlement.



Figure 7.9: Comparison of hydrogen diffusion coefficient and the mean embrittlement index (%RA) for the three alloys

It is widely regarded that hydrogen embrittlement sensitivity is directly influenced by strength. Higher strength steels are more sensitive to hydrogen embrittlement. In addition, strength is related to microstructure which is linked to the chemical composition and heat treatment.

In agreement with Hall and Petch¹⁶⁴ SAF 2507 possess higher strength (figure 7.9) than the other two alloys as seen in the 0.2% proof stress and ultimate tensile strength results (Figure 6.72 and 6.73). Hall and Petch is a relation between the grain size and the yield point of a material. The larger the grain size of a material, the smaller its yield strength as described in the following relationship:

$$\sigma_y = \sigma_o + kd^{-\frac{1}{2}}$$

Where k is material constant, σ_y and σ_o are the yield stress and material constant for the starting stress for dislocation movement respectively, and d is the mean grain size.

The smaller grain sizes increase tensile strength, as shown in figure 7.10, by providing a greater number of boundaries per unit volume, hence creating more barriers to dislocation movement. It was expected that SAF 2507 with the smallest grain size would have the lowest diffusion coefficient. However, it appeared that SAF 2507 had the highest diffusion coefficient.

Figure 7.11 relates σ_y to grain size: which could be related to Hall & Petch effect. However, it does not explain higher diffusion coefficient in super DSS SAF 2507.

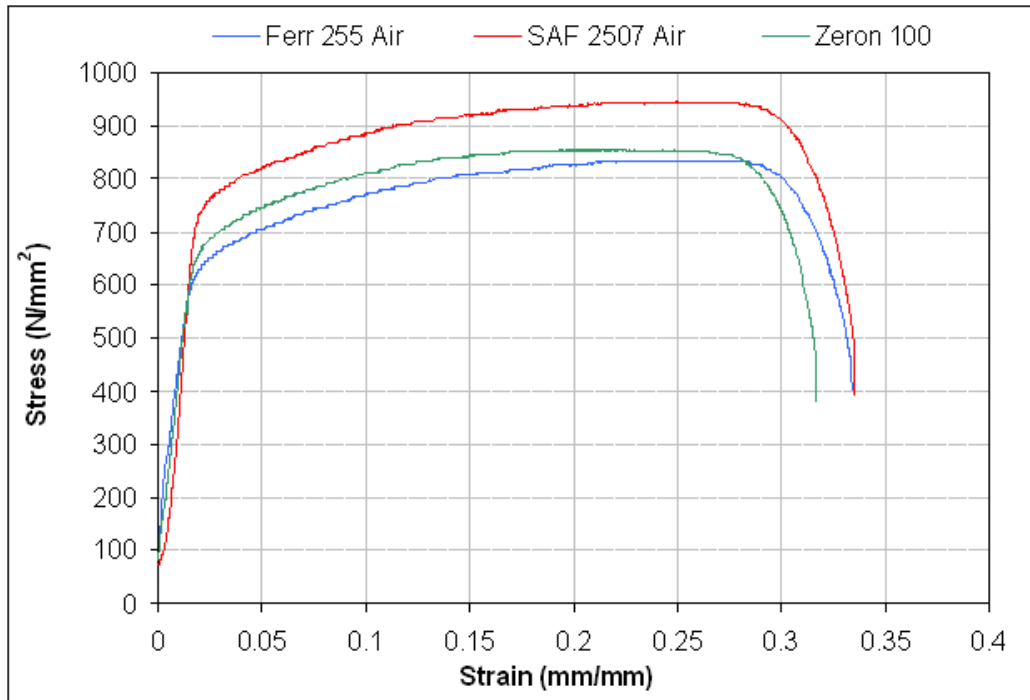


Figure 7.10: Comparison of SSRT of the three tested super DSSs in air test condition

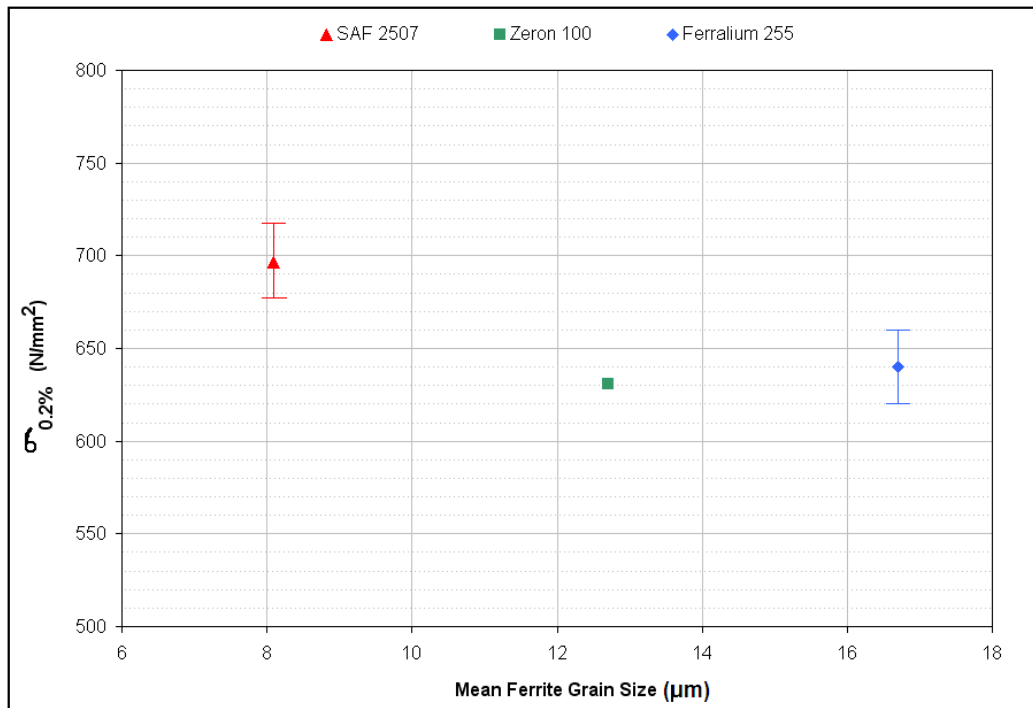


Figure 7.11: Effect of the grain size on the 0.2% Proof Stress

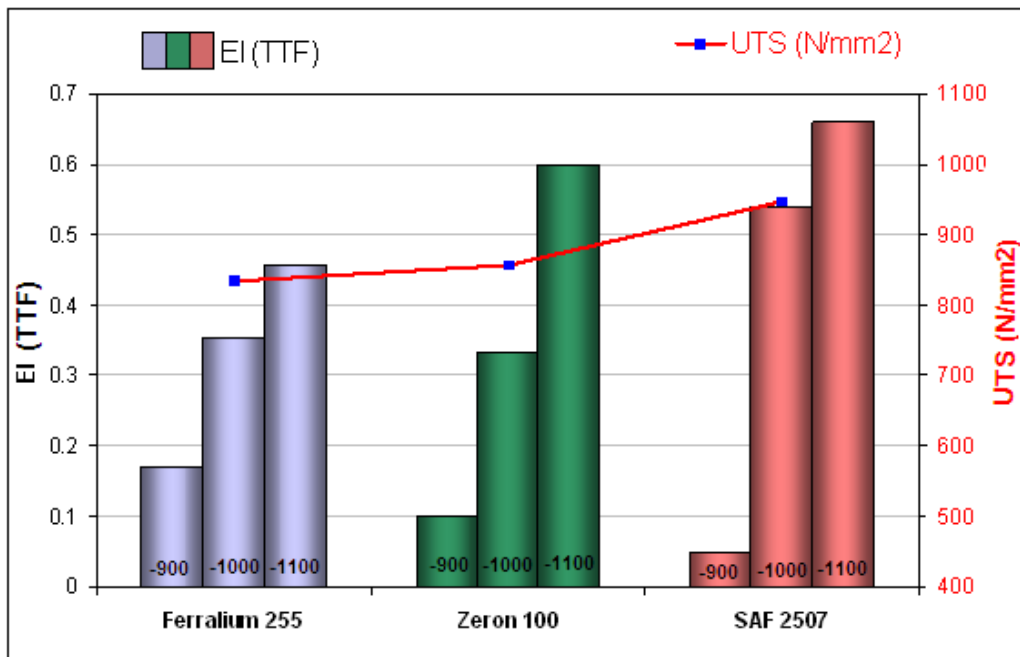


Figure 7.12: Comparison of the mean embrittlement index (TTF) for the three alloys at potentials of -900, -1000 and -1100 mV (SCE)

Based on the hydrogen embrittlement index calculated from time to failure (TTF) alone, it can be seen that Zeron 100 and Ferralium 255 have lower hydrogen embrittlement susceptibility in potentials of -800 and -900 mV (SCE). These potentials are less important range as embrittlement index is small as shown in figure 7.13. However, at over protection range of -1000 and -1100 mV (SCE) SAF 2507 has the highest hydrogen embrittlement susceptibility with a wider variation range. Also it has the highest diffusion coefficient and longest crack lengths.

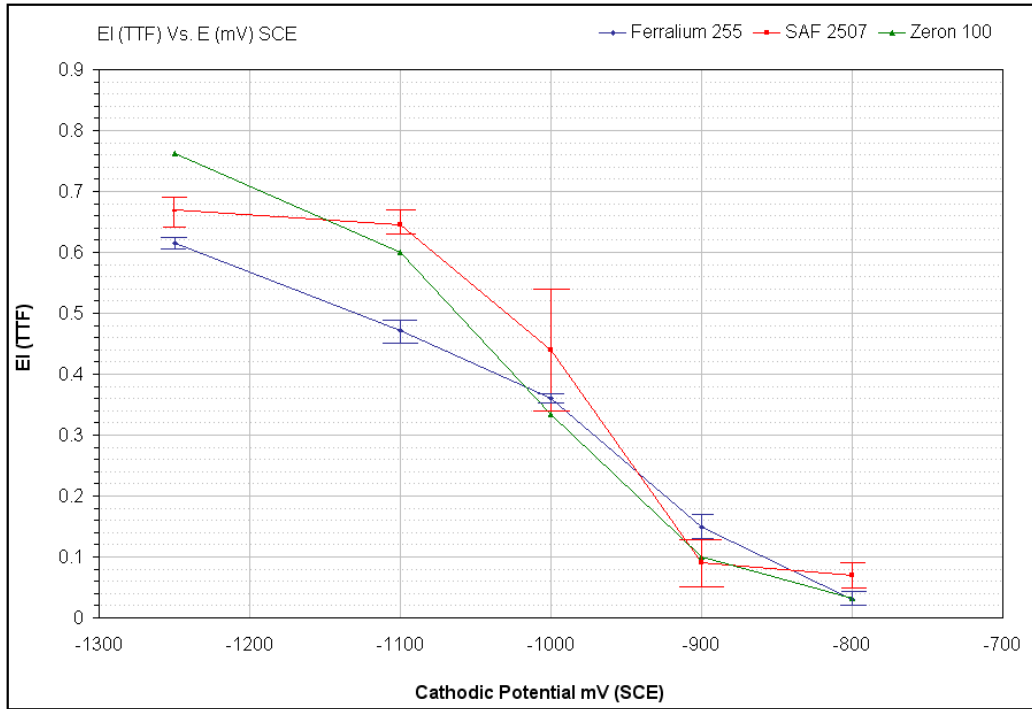


Figure 7.13: Comparison of Embrittlement Index (%RA) Vs. cathodic potentials from -1250 to -800 mV SCE after SSR testing for all three super DSSs

Similarly, a relation can be found between diffusion coefficient values and Ni_{eq}/Cr_{eq} ratio. Figure 7.13 shows that SAF 2507 has the highest diffusion coefficient value and Ni_{eq}/Cr_{eq} which suggests that higher Ni_{eq}/Cr_{eq} ratio will give higher austenite/ferrite ratio as show in figures 7.14 and 7.15

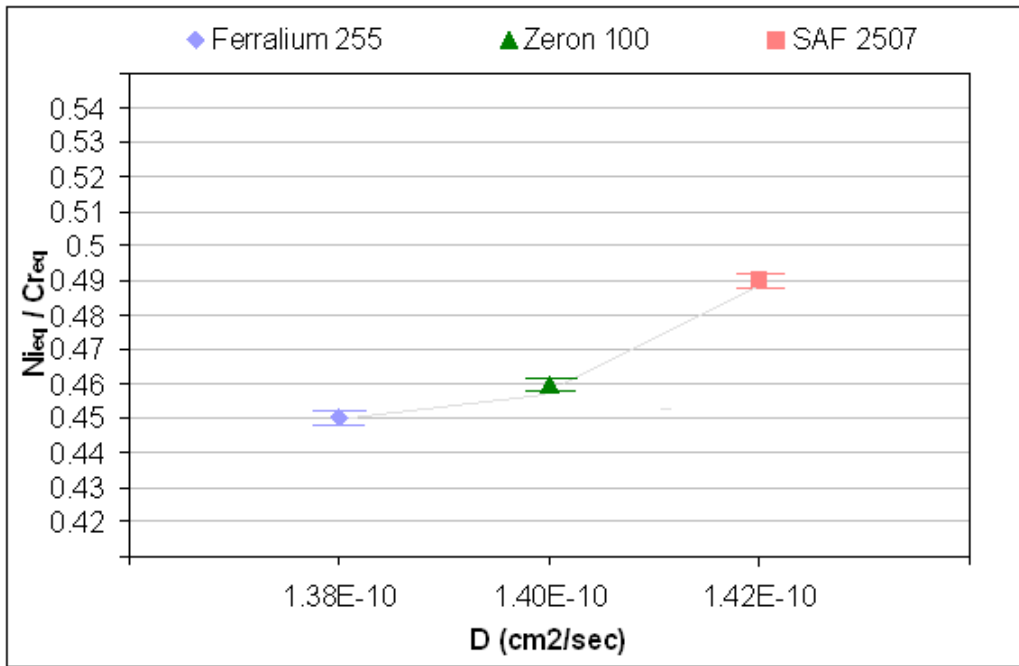


Figure 7.14: The relation between the diffusion coefficient values and Ni_{eq}/Cr_{eq} ratio.

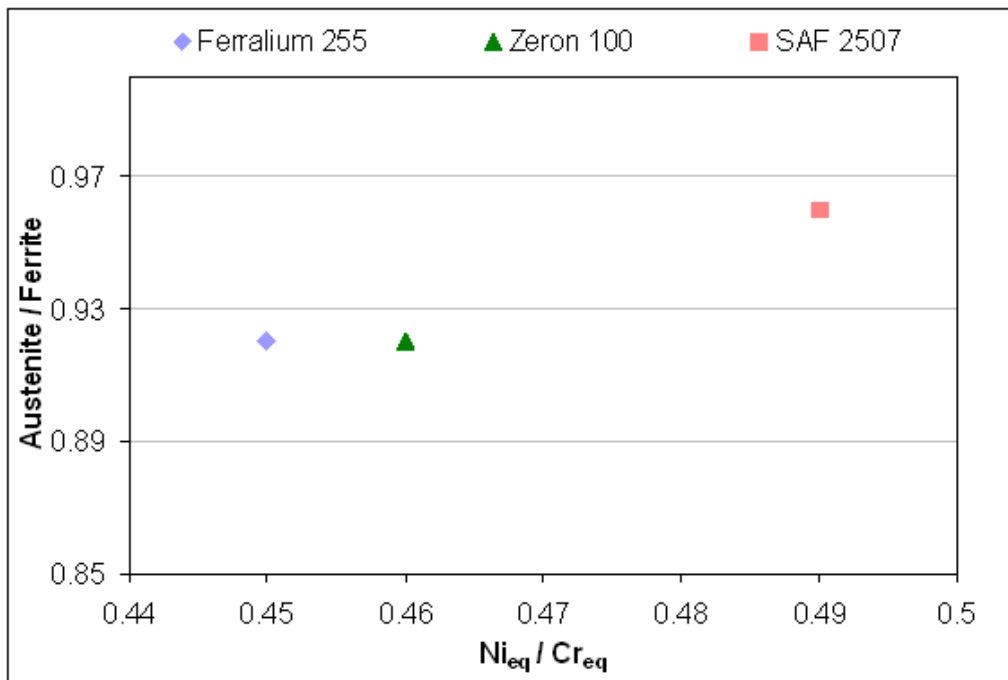


Figure 7.15: The relation between the austenite/ferrite ratio and Ni_{eq}/Cr_{eq} ratio.

The result through out this investigation can lead us to a general recommendation for which alloy is less susceptible to hydrogen embrittlement based on the laboratory tests. As mentioned previously, the cathodic protection for subsea applications are typically under potentials of -1000 or -1100 mV (SCE).

Based on the time to failure in slow strain rate tests, Ferralium 255, Zeron 100 displaced similar resistance to hydrogen embrittlement at a typical cathodic potential of -1000 mV (SCE). Using this criterion, SAF 2507 had the highest embrittlement and this correlated with the highest diffusion coefficient and the deepest cracks measured on the fractured surface. However, when assessed by the reduction of area criterion, the results are less clear and Ferralium 255 showed little higher embrittlement than the SAF 2507 and Zeron 100.

The correlation between composition and microstructure are essential to optimise alloy composition in development of the alloy or considering the condition of environment in field service. A low diffusion coefficient value is certainly the key factor for any material to be susceptible to hydrogen embrittlement. Lowering the diffusion coefficient means improving all other factors.

Without doubt, many factors can contribute to a better performance alloy. It is important to understand that those factors have a tendency to work together like links in a chain. Certainly, some factors have stronger influence than others. Therefore, the end result can not be better than the weakest link. Further more, when failure occurs, valuable time and work must be spent to determine the cause.

8 Conclusion

This investigation was aimed at elucidating the susceptibility of super DSS to HE in 3.5% NaCl at a temperature of 50° C. The pitting corrosion behaviour was determined by potentiodynamic polarization method. The susceptibility to HE behaviour was determined by SSR testing techniques, using cylindrical specimens. The effect of hydrogen on the cracking behaviour was evaluated under controlled cathodic potential. Fractographic and metallographic evaluations of the tested specimens were performed by SEM and optical microscopy, respectively. Hydrogen permeation and galvanostatic methods were used to calculate the hydrogen diffusion coefficient for the tested materials. The predicted model was successively used to estimate the diffusion coefficients for the three alloys based on the embrittled crack length of the fractured surface after SSR testing. The significant conclusions drawn from this investigation are summarized below.

1. Duplex stainless steels Ferralium 255, SAF 2507 and Zeron 100 exhibited two pitting potentials related to the two phase microstructure. The ferrite phase had more active pitting potential, whereas the austenite phase has the more noble potential.
2. The stability of the two phases, measured by potentiostatic tests in 3.5 % NaCl solution at room temperature, was shown to be related to the pitting resistance equivalent number (PREN). Austenite phase had higher PREN than the ferrite phase due segregation of alloying elements and nitrogen enrichments.
3. Scanning Electron Microscopy (SEM) was used to confirm segregation of the alloying elements between austenite and ferrite phases. Nickel and nitrogen enrichments occur in the austenite, whereas chromium and molybdenum segregate to the ferrite.
4. SSRT studies on super DSS specimens in air indicated that all the alloys undergo ductile fracture by elastic-plastic deformation. Without charging,

the effect of 3.5% NaCl at temperature of 50 ° C was minimal on percentage of elongation, TTF and the percentage of reduction area of the super DSSs.

5. Stress vs. strain plots for super DSSs FERRALIUM 255, SAF 2507 and Zeron 100 obtained from SSRT studies indicated a susceptibility of HE related to potential: more negative potential causing more embrittlement; although there was no significant effect on the maximum load (UTS).
6. Under charged conditions, the fracture surfaces showed features of hydrogen embrittlement. This indicated that hydrogen damage could occur on the three alloys during cathodic protection (C.P.) in service. The ferrite phase of super duplex stainless steel is the susceptible phase to be embrittled. The austenite phase provides resistance to the duplex microstructure against hydrogen embrittlement.
7. Pre-charged (-1250 mV SCE) super DSS specimens subject to SSRT indicated failure by brittle fracture with no necking. HE occurred in the ferrite phase whereas the austenite failed in a ductile manner. The austenite phase can arrest a crack propagating through the ferrite.
8. A 24 hours baking treatment was effective in reducing extent of embrittlement in hydrogen charged metal. Super DSS Ferralium 255 was shown a good recovery of the mechanical properties by the baking process. A 72 hours treatment was even more effective.
9. Super DSSs FERRALIUM 255, SAF 2507 and Zeron 100 can be susceptible to hydrogen embrittlement. HE susceptibility increases with decreasing CP potential to more negative values. All three alloys suffered a marked loss of ductility on charging at a potential of – 1250 mV (SCE) during SSRT.
10. Values of the hydrogen diffusion coefficient measured by the two-cell permeation technique of Devanathan-Stachursky were

$1.38 \pm 0.01 \times 10^{-10} \text{cm}^2/\text{s}$ and $1.42 \pm 0.12 \times 10^{-10} \text{cm}^2/\text{s}$ for the super DSSs Ferralium 255 and SAF 2507, respectively.

11. The predicted values for hydrogen diffusion coefficients were calculated from observed crack lengths on fracture surfaces to be $1.4 \pm 0.1 \times 10^{-10} \text{cm}^2/\text{s}$, $1.8 \pm 0.1 \times 10^{-10} \text{cm}^2/\text{s}$ and $1.4 \pm 0.1 \times 10^{-10} \text{cm}^2/\text{s}$ for super DSSs Ferralium 255, SAF 2507, and Zeron 100, respectively.
12. In ferritic-austenitic duplex stainless steels, hydrogen diffusivity and the degree of embrittlement depend on the austenite content, volume and size of grains. The austenite spacing can play an important role as this phase acts as an effective trap for hydrogen permeating the metals.
13. Based on the time to failure in slow strain rate tests, Ferralium 255 and Zeron 100 displayed similar resistance to hydrogen embrittlement at a typical cathodic potential of -1000 mV (SCE). Using this criterion, SAF 2507 had the highest embrittlement and this correlated with the highest diffusion coefficient and the deepest cracks measured on the fractured surface. However, when assessed by the reduction of area criterion, the results are less clear and Ferralium 255 and Zeron 100 showed higher embrittlement than the SAF 2507.

9 Future Work

There are several areas where additional investigations can be a natural extension of this thesis and provide valuable information. The recommendations for future work include:

- Further SSRT investigations should be performed at other solutions and temperatures (specific service condition). Perform SSRT at potentials of -850, -950 and -1050 mV (SCE). Coating and inhibitors can also be evaluated.
- Effect of cathodic protection in other forms of microstructure such as large forging and weld.
- Hydrogen permeation test can be performed on super DSS Zeron 100 to measure the diffusion coefficient since this test has not been done due to the time limitation and availability of the material. Investigate hydrogen permeation measurements on other super DSS membranes with different metallurgical and microstructure conditions.
- Use transverse specimen section for the hydrogen permeation test and compare the diffusion coefficient with the longitudinal specimen section.

10 REFERENCES

1. T. Ishihara, Microstructural effects of fatigue crack growth in a two-phase steel, *Journal of Materials Science* 18 (1983) 103-108.
2. K. Cho, J. Gurland, The law of mixtures applied to the plastic deformation of two-phase alloys of coarse microstructures, *Metallurgical and Materials Transactions A* 19 (1988) 2027-2040.
3. T. Wada, S. Hashimoto, Fatigue crack growth across the interphase boundaries in two-phase bicrystals, *Materials Science Forum* 294-196 (1999) 693-696.
4. H. Sakasegawa, T. Hirose, A. Kohyama, Y. Katoh, T. Harada, K. Asakura, Microstructural stability of reduced activation ferritic/martensitic steels under high temperature and stress cycling. *Fusion Engineering and Design* 61-62 (2002) 671-675.
5. N. Giel, Application of duplex stainless steel in the chemical process industry, *Proc. 5th World Duplex Stainless Steel Conference 1997*, Maastricht, The Netherlands, KCI Publishing D97-201 (1997) 9-16.
6. L. Smith, A guideline to the successful use of duplex stainless steels for flowlines. *Proc. Duplex America Conference*, Houston, USA, KCI Publishing DA_2-102 (2000) 17-29.
7. N. John, Digesters and pulp storage towers of duplex stainless steels-saving weight and costs, *ACOM, Avesta Sheffield AB 3* (1994) 1-8.
8. T. Alpo, Increased usage of duplex materials in manufacturing of pulping equipment, *Proc. Duplex America Conference*, Houston, USA, KCI Publishing DA2_061 (2000) 401-408.
9. T. H. Kang, D.M. Li, Y.D. Lee, C.S. Lee, Alloying and aging effects on the fatigue crack growth of duplex stainless steels, *Materials Science and Engineering A* 251 (1998) 192-199.
10. N. Akdut, Phase morphology and fatigue lives of nitrogen alloyed duplex stainless steels, *International Journal of Fatigue* 21 (1999) 97-103.
11. I. A. Alvarez-Armas, M. C. Marinelli, J.A. Malarria, S. Degallaix, A.F. Armas, Microstructure associated with crack initiation during low cycle

- fatigue in a low nitrogen duplex stainless steel, *International Journal of Fatigue* 29 (2007) 758-764.
12. T. Takemoto, K. Mukai, K. Hoshini, Effect of nitrogen on low cycle fatigue behaviour of austenitic stainless steel, *Transactions ISIJ* 26 (1986) 337-344.
 13. J.-B Vogt, K. Massol, J. Foct, Role of the microstructure on fatigue properties of 475°C aged duplex stainless steels, *International Journal of Fatigue* 24 (2002) 627-633.
 14. M. Pohl, A. Ibach, K.-H. Lange, Microstructure and Properties of Super-Duplex Stainless Steels, *Pract. Met.* 28 (1991) 333–349.
 15. T. S Taylor, T. Pendlington and R. Bird, "Foinaven Super Duplex Materials Cracking Investigation" Offshore Technology Conference 1999, paper No. 10965.
 16. S. Huisinga, B. Mcloughlin, I. Hannah, S. Paterson. BNW. Snedden. BNW. "Failure of a Subsea Super Duplex Manifold Hub by HISC and Implications for Design", Paper no. 06145, NACE Corrosion 2006 Conference, NACE International.
 17. L. E. Newton, R. H. Hausler, R. H. Methodology to Study Cost of Corrosion, *Corrosion Engineering, Science and Technology*, Vol. 40, No. 4 (Dec. 2005), University of Cantabria, Spain.
 18. M. G. Fontana, *Corrosion Engineering*. Third Edition, McGraw Hill, New York 1987.
 19. S. Bradford, *Corrosion Control*, Second Edition, Casti Publishing Inc. Alberta, Canada, 2003.
 20. Ocean International, Retrieved March 9, 2007, from www.oceanint.com/content/interior.asp?section=products&body=superduplex&title=prod&goto=superduplex.
 21. R. M. R. Davison, *Practical Guide to Using Duplex Stainless Steels. Material Performance*, 1990. 29(1):pp. 57-62.
 22. J.-O. Nilsson, P. Kangas, T. Karlsson, A. Wilson, Mechanical properties, microstructural stability and kinetics of σ -phase formation in 29Cr-6Ni-

- 2Mo-0.38N superduplex stainless steel, *Metallurgical and Materials Transactions A*. Vol. 31, No. 1, Jan, 2000, pp. 35-45.
23. S.D. Cramer, B. S. Covino, ed, ASM Handbook-corrosion: Materials. Vol. 13B. ASM International, Material Park, Ohio, 2005.
 24. S. D. Cramer, B. S. Covino, ed. ASM Handbook – Corrosion: Fundamentals, Testing and Protection. Vol. 13A. ASM International, Material Park, Ohio, 2003.
 25. L. F. Garfias-Mesias, J. M. Sykes, and C. D. S. Tuck, The Effect of Phase Composition on the Pitting Corrosion of 25 Cr Duplex Stainless Steel in Chloride Solutions, *Corrosion Science*, Vol. 38, No. 8, pp. 1319-1338.
 26. R. A. T. D. Sriram, *Pitting Corrosion of Duplex Stainless Steels*. *Corrosion*, 1989. 45(10): pp. 804-810.
 27. T. A. K. Ogawa, T.a.K., T., Effect of Composition Profiles on Metallurgy and Corrosion Behavior on Duplex Stainless Steel Weld Metals. *Welding Journal*, 1998. 68(5): pp. 181s-191s.
 28. M. Miura, M. Koso, T. Kudo, H. Tsuge, The Effects of Nickel and Nitrogen on the Microstructure and Corrosion Resistance of Duplex Stainless Steel Weldments. *Welding International*, 1990. 4(3): pp. 200-206.
 29. J. M. Nicholls, Corrosion Properties of Duplex Stainless Steels: General Corrosion, Pitting and Crevice Corrosion. in Duplex Stainless Steels, Conf. Proc. Duplex Stainless Steel '94, Glasgow, Scotland, 13-16 Nov. 1994, Gooch, T. G, (Ed), Pub: Abingdon, Cambridge, UK, 1995.
 30. Walker, R.A.a.G., T.G., Pitting Resistance of Weld Metal for 22Cr-5Ni Ferritic-Austenitic Stainless Steels. *British Corrosion Journal*, 1991. 26(1): pp. 51-59.
 31. H. Okamoto, Conf. Proc. Applications of Stainless Steel 1991, Vol.1 Stockholm, Jernkontoret, 1992, 360-369.
 32. J.O. Nilsson, Overview: Super Duplex Stainless Steels, *Material Science Technology*, V8, 1992, pp 685-700.

33. M. Yamashita, S. Matsumoto, N. Hirohata, Corrosion resistance and properties of duplex stainless steels. Duplex'07, Grado, Italy
34. P. Stenvall, M. Holmquist, Weld properties of Sandvik 2707HD. Duplex'07, Grado, Italy.
35. J. Charles, Super Duplex Stainless Steels: Structures and Properties, Proceedings of Duplex Stainless Steels, 1991, Les Editions de Physique, F-91944 Les Cedex, France, p.3.
36. R. W. K. Honeycombe, Steels: Microstructure and Properties, Metals Park, OH. American Society for Metals, 1981.
37. K. Hashimoto, K. Asami, K. Teramoto, "Corrosion Science" 1979, pp.3-14.
38. I. Varol, J. C. Lippold, W. A. Baeslack III, "Welding of Duplex Stainless Steels," Key Engineering Materilas, Vol. 69 & 70, 1992, pp. 217-252.
39. R. Gunn, ed. Duplex Stainless Steel – Microstructure, Properties and Applications. 1997, Abington Publishing: Cambridge, England.
40. R. Quarfort, "Critical Pitting Temperature Measurements of Stainless Steels with an Improved Electrochemical Method," *Corrosion Science*, Vol. 29, 1989, p. 987.
41. R. J. Brigham, E. W. Tozer, "Temperature as a Pitting Criterion," *Corrosion*, Vol. 29, No. 1, 1973, pp. 33-36.
42. P. Lau, S. Bernhardsson, *Electrochemical Techniques in Corrosion Engineering*, R. Baboian, Ed., NACE, Houston, TX, 1986, p. 281.
43. Honeycombe RWK. (1981) Steels - Microstructure and Properties, London: Edward Arnold.
44. T. Ogawa, T. Koseki, (1989) Effect of Composition Profiles on Metallurgy and Corrosion Behaviour of Duplex Stainless Steel Weld Metals. Welding Research Supplement. Vol. May, p. 181-91.
45. J. P. Potgieter, (1992) Influence of α -phase on General and Pitting Corrosion Resistance of SAF 2205 Duplex Stainless Steel. *British Corrosion J.* 1992, Vol. 27, p. 219-33.

46. S. Atamert, J.E. King (1991) Thermodynamic and Kinetic Analysis of Duplex Stainless Steels. In: Charles J, Bernhardsson S, eds. Duplex Stainless Steels'91. Beaune: Les Editions de Physique, p. 701-10.
47. H. D. Solomoq, T. M. Devine, Conf. Proc. "Duplex Stainless Steels", ed R. A. Lula, ASM, St. Louis (1983), p. 693
48. C. V. Roscoe, K. J. Gradwell, G. W. Lorimer, Conf. Proc. "Stainless Steels 18411, GdtebOrg, Publ. I. O. M., London (1984), p. 563.
49. J. O. Nilssen, Super Duplex Stainless Steels (overview) Material Science and Technology, Vol. 8 (1992), p. 685-700.
50. J. Charles, Super Duplex Stainless Steels: Structure and Properties. In: Duplex Stainless Steels 1991. Beaune, France, p. 151-68.
51. J. Charles. (1994) Structure and Mechanical Properties of Duplex Stainless Steel In: Gooch TG, ed. Fourth Intern. Conference in Duplex Stainless Steels. Glasgow: Abington Publishing, p. Paper KI
52. C. S. Huang, C.C. Shih, Effects of Nitrogen and High Temperature Aging on σ -phase Precipitation of Duplex Stainless Steel, Material. Science Engineering A, 402 (2005) 66-75.
53. B. Josefsson, J. O. Nilsson, A. Wilson, (1991) Phase Transformations in Duplex Steels and the Relation Between Continuous Cooling and Isothermal Heat Treatment. Duplex Stainless Steels'91. Beaune: France, 1991, p. 67-78.
54. T. Thorvaldsson, H. Eriksson, J. Kutka, A. Salwén, Influence of Microstructure on Mechanical Properties of a Duplex Stainless Steel, Stainless Steel '84, Göteborg, Sweden, 1 (1984) 101-105.
55. T. H. Chen, J. R. Yang, Effects of solution treatment and continuous cooling on σ -phase precipitation in a 2205 duplex stainless steel, Mater. Sci. Eng. A, 311 (2001) 28-41.
56. D. Figueroa, Hydrogen Embrittlement Susceptibility of Ultra High Strength Steels. 2003, Cranfield University.
57. Johnson, W. H. Proc. Roy. Sco., Vol. 23 (1875) p.168.

58. R. W. Revie, H. H. Uhlig, Corrosion and Corrosion Control: An Introduction to Corrosion Science and Engineering, John Wiley & Sons, Inc. New Jersey, USA. 2008, p100.
59. G.P Halada, C.R Clayton, J.D Fritz, D. Kim, Corrosion 95, Orlando, NACE, paper 95531.
60. H. Nagano, T. Kudo, Y. Inaba, M. Harada, Highly Corrosion Resistance Duplex Stainless, *Metaux Corrosion Industrie*, Vol. 667, Mar. 1981, pp. 81-88.
61. K. N. Adhe, V. Kain, K. Madangopal, H. S. Gadiyar, "Influence of Sigma-Phase Formation on the Localized Corrosion Behavior of a Duplex Stainless Steel," *Journal of Materials Engineering and Performance*, 1996. 5(4): pp. 500-506.
62. T.A.K. Ogawa, "Effect of Composition Profiles on Metallurgy and Corrosion Behavior of Duplex Stainless Steel Weld Metals," *Welding Journal*, 1998. 68(5): pp. 181s-191s.
63. M. Miura, M. Koso, T. Hudo, H. Tsuge, "The Effects of Nickel and Nitrogen on the Microstructure and Corrosion Resistance of Duplex Stainless Steel Weldments," *Welding International*, 1990. 4(3): pp. 200-206.
64. P. Yunan, K. Ibrahim, W.B. Wan Nik, Effect of pH and Chloride Concentration on the Corrosion of Duplex Stainless Steel, *The Arabian Journal for Science and Engineering*, Dec. 2009, Vol. 34. Number 2C.
65. D. J. Kotecki, T. A. Siewert, "WRC-1992 Constitution Diagram for Stainless Steel Weld Metals: A Modification of the WRC-1988 Diagram," *Welding Journal*, 71(5), 1992, pp. 171s-178s.
66. J. Charles, Duplex Stainless Steel, Proc conf *Duplex Stainless Steels '94*, Glasgow, Scotland, TWI, Abington, Cambridge, England, 1994, Vol. 1, paper K1.
67. J. Charles, How to Improve Super Duplex Stainless Steel Properties with Addition. In 6th World Duplex Stainless Steels. 2000. Venezia, Italy.
68. Y.C. Lu, R. Bandy, CR, Clayton R.C Newman, "Electrochemical Society.,"n1983, p.1774.

69. A. G. Hynes, Duplex and High Alloy Corrosion Resistance Steels, Paper No. 6, London, Lloyd's Register Technical Association, Report 000245 session 1990-91.
70. I. Varol, J. C. Lippold, W. A Baeslack III, W. A., Welding of Duplex Stainless Steels. Key Engineering Materials, 1992. 69&70: p. 217-252.
71. J. O. Nilsson, A. Wilson, T. Huhtala, L. Karlsson, P. Jonsson, "Structural Stability of Super Duplex Stainless Weld Metals and Its Dependence on Tungsten and Copper," Metallurgical and Materials Transactions A, 27A (8), Aug. 1996, pp. 2196-2208.
72. H. Okamoto, Conference Proceedings Applications of Stainless Steel 92, Stockholm Jernkontoret 1992, Vol.1, p. 360-369
73. K. Ogawa, H. Okamoto, M. Ueda M, Igarashi, T. Mori, " Effects of Tungsten on Pitting Corrosion Resistance and Impact Toughness in the HAZ of Duplex Stainless Steel – Study of Weldability of High – Tungsten Duplex Stainless Steel (1st Report)," Welding International, 10(6), 1996, p.466-472.
74. H. Okamoto, Effect of Tungston and Molybdenum on Performance of Super Duplex Stainless Steel, Conf. proc. Applications of Stainless Steel' 92, Stockholm, Sweden, Pub: Jernkontoret, 1992, Vol 1, 360-369.
75. J. O Nilsson, P. Jonsson, A. Wilson, Formation Of Secondary Austenite in Super Duplex Stainless Steel Weld Metal and its Dependence on Chemical Composition, Conf. Proc. Duplex Stainless Steel '94, Glasgow, Scotland, 13-16 Nov. 1994, Gooch, T. G, (Ed), Pub: Abington, Cambridge, UK, 1995.
76. P. Soullignac, F. Dupoirion, Stainless Steel Europe, 1990, pp. 18-21.
77. Taylor R, "Duplex Stainless Steel Production," SFSA T&O conference, 1994
78. R. A. Farrar, The Importance of Microstructural Transformations for Welding and the Stability of Long Term Service Properties, Welding in the World, Vol. 36, 1995, pp. 143-151
79. S. Bernhardsson, Proceeding Conference: Duplex Stainless Steels '91, Beaune Bourgogne, France, 1991.

80. L. Bela, Avesta Sheffield AB, Stainless Steel and their Properties 2nd revised edition, Stockholm, 1998.
81. DNV Report No. 2004-3471, rev.01 Draft-Duplex Stainless Steel- Field Failure and Acceptance Criteria Data.
82. Recommended Practice DNV-RP-F112 "Design Guideline for Duplex Stainless Steel Used for Subsea Equipment Exposed to Cathodic Protection" (Det Norske Veritas, October 2008).
83. M. W. Mucek M. W. Detection, Repair, and Mitigation of Wet H₂S Cracking: An overview of RP0296, Corrosion '99. The NACE Annual Conference and Corrosion Show, NACE International; 1999. paper No. 416.
84. P. F. Timmins, Solutions to Hydrogen Attack in Steels. ASM International; 1997.
85. P. Domzalicki P, E. Lunarska, J. Birn J. Effect of Cathodic Polarisation and Sulphate Reducing Bacteria on Mechanical Properties of Different Steels in Synthetic Seawater. Mater. Corros. 2007;58: p.413–419.
86. F. Zucchi, V. Grassi, C. Monticelli, G. Trabanelli, Hydrogen Embrittlement of Duplex Stainless Steel Under Cathodic Protection in Acidic Artificial Seawater in the Presence of Sulphide Ions. Corrosion Science, 2006; Vol. 48 p. 522–530.
87. J. Charles, Super Duplex Stainless Steels: Structure and properties, Duplex Stainless Steel '91, Beaune, France, 2 (1991) 3-48.
88. D. William, J. Callister. Materials Science and Engineering an Introduction. John Wiley and Sons, Inc. New York. USA, 1999.
89. C. A. Zappfe, C. D. Sims, Hydrogen Embrittlement, Internal Stress and Defects in Steel. IN: Beachem, C.D. (ed). Hydrogen Damage. Ohio: American Society of Metals, 1979, pp 13.
90. G. G. Hancock, H. H. Johnson, Trans., TMS-AIME, 224, 1962, p. 775-783.
91. N. J. Petch, Stables P. Delayed Fracture of Metals Under Static Load. IN: Beachem, C.D. (ed). Hydrogen Damage. Ohio: American Society of Metals, 1979, pp 93

92. E. N. Pugh, 'A Post Conference Evaluation of our Understanding of the Failure Mechanisms', Stress Corrosion Cracking and Hydrogen Embrittlement of Iron Base Alloys, Editors R.W. Staehle, J. Hochmann, R.D. Mc.Cright and J.E. Slater, Conf. Proc. Unieux-Firminy, 12-16 June 1973, NACE-5, 37-51, 1977.
93. A. R. Troiano, The Rule of Hydrogen and Other Interstitials in Mechanical Behaviour of Metals. IN: Beachem, C.D. (ed). Hydrogen Damage. Ohio: American Society of Metals, 1979, pp 151.
94. E. A. Taqi, R. A. Cottis, reported in P. Marcus & J. Oudar, Corrosion Mechanisms in Theory and Practice. 2nd addition, 2002, Marcel Dekker, Inc. New York, p 434.
95. A. Zaki, Principles of Corrosion Engineering and Corrosion Control, Elsevier Ltd. 2006, p.215.
96. C. O. A. Olsson. D. Landolt, Passive Films on Stainless Steel-Chemistry, Structure and Growth, Electrochemica Acta, April 2003, Vol. 48, Issue 9, p. 1093-1104.
97. S. Bernhardsson, The Corrosion Resistance of Duplex Stainless Steel. In Duplex Stainless Steel 91. 1991.
98. J. C. Scully, Corrosion Failure and Attack. In The Fundamentals of Corrosion, Oxford: Pergamon, 1990, pp 181, pp. 192.
99. A. Turnbull, Corrosion Science, 23 (1983). p. 833.
100. Retrieved December 2009, From http://www.substech.com/dokuwiki/doku.php?id=pitting_corro
101. K. Sugimoto, S. Matsuda, Passive and Transpassive Films on Fe-Cr Alloys in Acid and Neutral Solutions. Mat. Science and Engineering, 1980, Vol. 42, p. 181-189.
102. W. P. Yang, D. Costa, and P. Marcus, Oxide Films on Metals and Alloys (B. MacDougall, R. S. Alwitt, T. A. Ramanarayanan, eds.) Proceedings Vol. 92–22, The Electrochemical Society, Princeton, NJ, 1992, p. 516.
103. P. Marcus and J. M. Herbelin, The entry of chloride ions into passive films on nickel studied by spectroscopic (ESCA) and nuclear (³⁶Cl radiotracer) methods, Corrosion. Science. 34:1123 (1993).

104. D.D. Macdonald, S. Biaggio and H. Song, Steady-State Passive Films Interfacial Kinetic Effects and Diagnostic Criteria, *Journal of Electrochemical Society*, Volume 139, Issue 1, pp. 170-177 (January 1992).
105. D.D. Macdonald, The Point Defect Model for the Passive State, *Journal of Electrochemical Society*, Vol. 139, Issue 12, pp. 3434-3449, Dec. 1992.
106. A. S. Jin, Passive Films on Stainless Steels in Aqueous Media, *Applied Physics A: Materials Science & Processing*, Vol. 50, No.3, pp 287-300, March, 1990.
107. P. Heimgartner and H. Böhni, Mechanistic Aspects of Pit Growth on Nickel in Diluted Chloride Solutions, *Corrosion*. Vol. 41, no. 12, pp. 715-719. Dec. 1985.
108. A. A. Seys , A. A. van Haute , M. J. Brabers, On the Initiation Process of Pitting Corrosion on Austenitic Stainless Steel in Chloride Solutions, *Materials and Corrosion*, Vol. 25, Issue 9 , pp 663 – 669, Nov. 2004.
109. V. Vignal, C. Valot, R. Oltra, M. Verneau and L. Coudreuse, Analogy between the effects of a mechanical and chemical perturbation on the conductivity of passive films, *Corrosion Science*, Vol. 44, Issue 7, July 2002, pp 1477,.
110. A. Shahryari, S. Omanovic, Improvement of Pitting Corrosion Resistance of a Biomedical Grade 316LVM Stainless Steel by Electrochemical Modification of the Passive Film Semiconducting Properties, *Electrochemistry Communications*, Vol. 9, Issue 1, January 2007, pp 76-82.
111. A. Conde, D.E. Williams, Crevice Corrosion and Pitting Detection on 304 Stainless Steel Using Electrochemical Noise, *Materials and Corrosion*, Vol. 50, Issue 10 , pp. 585 – 590, Oct 1999.
112. Z. Szklarska-Smialowska, Pitting Corrosion of Metals, NACE, 1986.
113. G. S. Eklund, *J. Electrochemical Soc.*, Vol 121, 1974, p 467.
114. G. Wranglén, *Corrosion Science*, Vol 14, 1973, p 331.

115. D. A. Jones, Principles and Prevention of Corrosion, Macmillan Publishing Company, p. 125 (1992).
116. O. A. J. Sedriks, Corrosion of Stainless Steels, John Wiley & Sons, Inc., 1979.
117. U. R. Evans, (1960). The Corrosion and Oxidation of Metals, Arnold & Co., London.
118. M.A.V. Devanathan and Z. Stachurski, Journal of Electrochemical Soc., Vol. 111, No.5, p. 619 (1964).
119. C. J. Wen Ho, C. B. A. Boukamp, 'Use of Electrochemical Methods to Determine Chemical-Diffusion Coefficients in Alloys: Application to LiAl', International Metals Reviews, No.5, 253-668, 1981.
120. P. A. Sundaram, E. Wessel, *et al*, 'Determination of the Diffusion Coefficient of Hydrogen in Gamma Titanium Aluminides During Electrolytic Charging', Acta Materialia, No.48, 1005-1019, 2000
121. D. Figueroa, M.J. Robinson, Hydrogen transport and embrittlement in 300 M and AerMet100 ultra high strength steels, Corrosion Science, Vol.52 (2010) p. 1593–1602.
122. J. Charles, Super Duplex Stainless Steels: Structures and Properties, Proceedings of Duplex Stainless Steels, 1991, Les Editions de Physique, F-91944 Les Cedex, France, p.3 .
123. M.A.V. Devanathan, A.W.Stachursky, Proc. Royal Soc. A270, (1962), p90-102.
124. A. Turnbull A, EL. Beylegaard R. B. Hutchings, Hydrogen Transport in SAF 2205 and SAF 2507 Duplex Stainless Steels. In: Hydrogen transport and Cracking in Metals, Conference Proceedings, The Institute of Materials; 1994. p. 268–79.
125. R. B. Hutchings, A. Turnbull, A. T. May, Measurement of Hydrogen Transport in a Duplex Stainless Steel. Scripta Metallurgica et Matialia, Vol. 25, 1991, p. 2657-2662.
126. J. Sakai, Matsushima, Y. Kamemura, M. Tanimura, T. Osuka, (1982) Proceeding of Inter. Conference of Duplex Stainless Steels, The USA, Paper (8201-010), p. 211.

127. C. V. Roscoe, K. J. Gradwell, (1986) Proceeding of Inter. Conference of Duplex Stainless Steels, The Netherlands, Paper 34, p. 126.
128. P. Guha, C. A. Clark, (1982) Proceeding of Inter. Conference of Duplex Stainless Steels, The USA, Paper 8201-018, p. 355.
129. U. R. Evans (1960) The corrosion and Oxidation of Metals, Arnold & Co. London.
130. T. T. Wen, M. T. Kuen, L. Chang-jian Lin, Corrosion NACE, 2003, Paper # 03398.
131. I-H Hsuang Lo, Y. Fu. J.T. Chang, T. T. Wen, Corrosion Science. Vol. 48 (2006) pp. 696-708.
132. E. A. M. Hussain, M. J. Robinson, Errosion- Corrosion of 2205 Duplex Stainless Steel in Flowing Seawater Containing Sand Particles, Corrosion Science, Vol. 49, Issue 4, 2007, P. 1737-1754.
133. Horng- Yih Liou, Yeong-Tsuen Pan, Rong-luan Hsieh, Wen-Ta Tsai, J. Materials Engineering and Performance. 10 (2001) 231–241.
134. M. T. Chuan, Y. L. Horng, T. T. Wen, Metallurgical and Materials Transactions A: Physical Metallurgy and Material Science. Vol. 34, Issue 1, (2003) p.95–103.
135. J. Charles, Proc. Conf., Duplex Stainless Steel, Beaune, France. 1991, p.3.
136. M. Hagen, W. Bollinger, W. Schoffer, "Sulzer Pumps", Internal Report, 1997, pp. 1-15.
137. S. A. J. Sedriks, conf proc stainless steel 1984, Goteborg, institute of metals 1985.
138. W. Hume-Rothery, (1968), The Structures of the Iron Alloys, Edgard Blucher Ltda, Saõ Paulo, Brazil.
139. M. Hagen, W. Bolliger, W. Schoffer, (1997), "Sulzer pumps", Internal Report, pp. 1-15
140. E. M. K. Hillier, and M.J. Robinson, Hydrogen embrittlement of high strength steel electroplated with zinc-cobalt alloys. Corrosion science, Vol.46, Issue3, March 2004, pages 715-727.

141. ASM Handbook, Vol. 11, Failure Analysis and Prevention, ASM Int., 1986.
142. N. Eliaz, A. Shachar, B. Tal, D. Eliezer, Characteristic of hydrogen embrittlement, stress corrosion cracking and tempered martensite embrittlement in high-strength steels, *Engineering Failure Analysis* 9 (2002) 176-184.
143. J. Crank, *The mathematics of Diffusion*. Oxford: Clarendon Press, 1975.
144. W. Beck, J.O'M. Bockris, J. McBreen and L.Nanis, 'Hydrogen permeation in metals as a function of stress, temperature and dissolved hydrogen concentration'. *Proceedings of the Royal Society, London*, Vol. 290A, (1966), 220–235.
145. T. Zakroczymski, 'The effects of straining on the transport of hydrogen in iron, nickel and stainless steel'. *Corrosion–NACE*, Vol.41, (1985), 485–489.
146. B. Robert, *Nace corrosion engineer's Reference book* third edition, NACE Press 2002.
147. F. B. Pickering. *Physical Metallurgy of Stainless Steel Developments. Int. Metals Rev.* 21 (1976), p. 227
148. A. Iris, A. Alvarez, D. Suzanne, *Duplex Stainless Steel*, ISTE Ltd. 2009.
149. R. Sabina, J. Anna, K. Ulf, *Hydrogen Embrittlement of Duplex Stainless Steels Testing of Different Product Forms at Low Temperature*, *Corrosion NACE International 2007*, March 11 - 15, 2007, Nashville, Tennessee, paper No. 07498.
150. T. Cassagne, F. Busschaert, *A Review on Hydrogen Embrittlement of Duplex Stainless Steels*, *Corrosion NACE International 2005*, April 3 - 7, 2005 , Houston, Tx, paper No. 05098.
151. *Design Guideline to Avoid Hydrogen Induced Stress Cracking in Subsea Duplex Stainless Steel*, *NORSOK Workshop Agreement M-WA-01*, Rev.1 October 2005.
152. R. B. Hutchings, A. Turnbull, A. T May, *MEASUREMENT OF HYDROGEN TRANSPORT IN A DUPLEX STAINLESS STEEL*, *Scripta Metallurgica*, 1991, Vol. 25, pp. 2657-2662.

153. P. Woollin, A. Gregory, "Avoiding HESC of Ferritic Austenitic Stainless Steels under Cathodic Protection", Proceedings of OMEA 2004, Paper 51203, (Vancouver, Canada, June 2004).
154. T.S. Taylor, T. Pendlington, R. Bird, "Foinaven Super Duplex Materials Cracking Investigation ", Offshore Technology Conference, (Houston, TX, May 1999) 467.
155. S. L. Chou, W. T. Tsai, Effect of Grain Size of the Hydrogen-assisted Cracking in Duplex Stainless Steels, Material Science and Engineering, A270 (1999), p. 219.
156. V. Olden, C. Thaulow, R. Johnsen, Modelling of hydrogen diffusion and hydrogen in induced cracking in supermartensitic and duplex stainless steels. Material & Design, Vol. 29, Issue 10, Dec 2008. p. 1934-1948.
157. A. A. El-Yazgi and D. Hardie, "Effect of heat treatment on susceptibility of Duplex Stainless Steel embrittlement by hydrogen', Mater. Sci. Tech. Ser., 16 (200) 506.
158. L. Smith, M. Celant and A. Pourbaix, in "Duplex America 2000 Conference" Proceedings, Stainless Steel world, DA 2 – 102, p. 17 – 29, 2000.
159. P. Olsson, A.D. Bauer and H. Eriksson, in "Duplex Stainless Steels 97, 5th World Conference" Proceedings, pp. 607 – 618, 1997.
160. P. Woollin and M. Maligas, CORROSION 2003, Houston, TX, USA, NACE International, 2003, paper No. 3132.
161. R. Oltra and C. Bouillot, , in "Hydrogen Transport and Cracking in Metals", A. Turnbull eds., Proceedings of Conference held at The National Physical Laboratory Teddington, UK, 13 – 14 April, 1994, p.17 – 26.
162. A. J. Griffiths and A. Turnbull. Corrosion Science, Vol. 37, No. 11, pp. 1879 –1881,1995.
163. R. Hutchings, D. Ferris, A. Turnbull, British Corrosion Journal vol.28, No. 4, p. 309, 1993.
164. R. W. K. Honeycombe, (1995), Steel: Microstructure and Properties, (2nd edition) Butterworth-Heinemann, Oxford.

APPENDICES

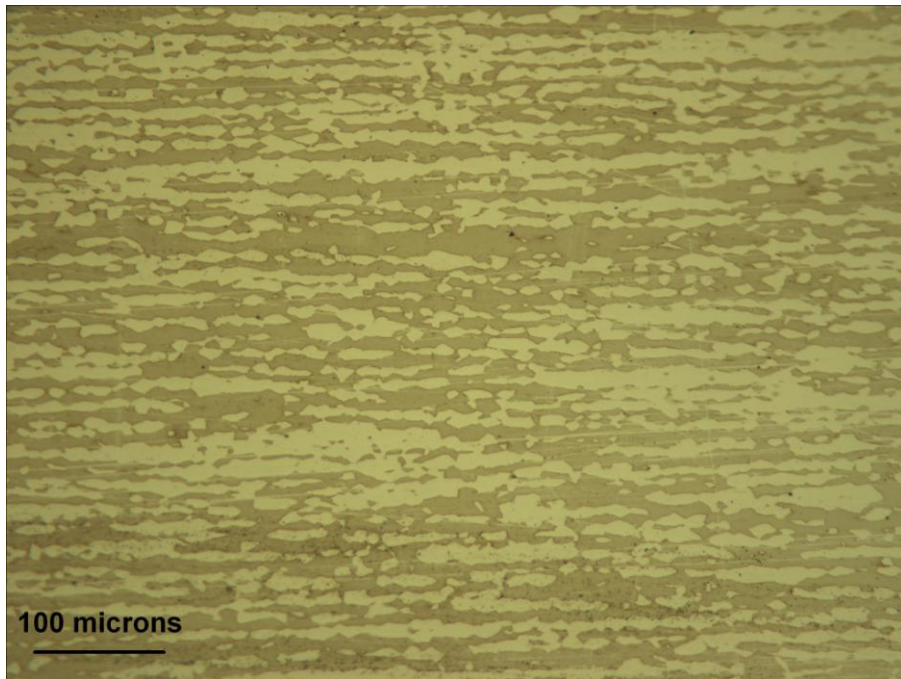


Figure 10.1: Cross section of the 3mm gauge length of the super DSS Ferralium
255

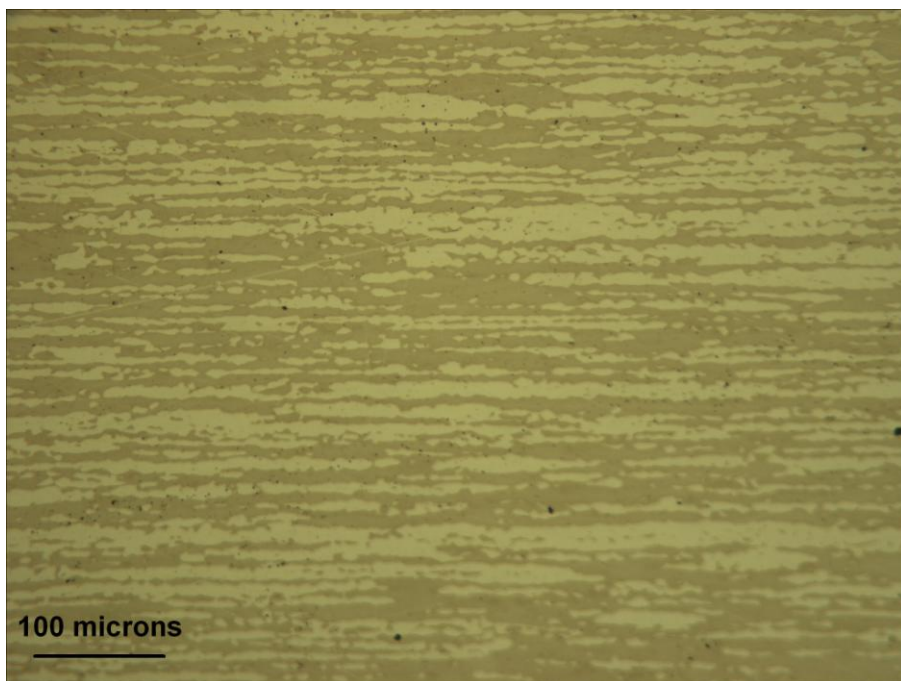


Figure 10.2: Cross section of the 3mm gauge length of the super DSS SAF
2507

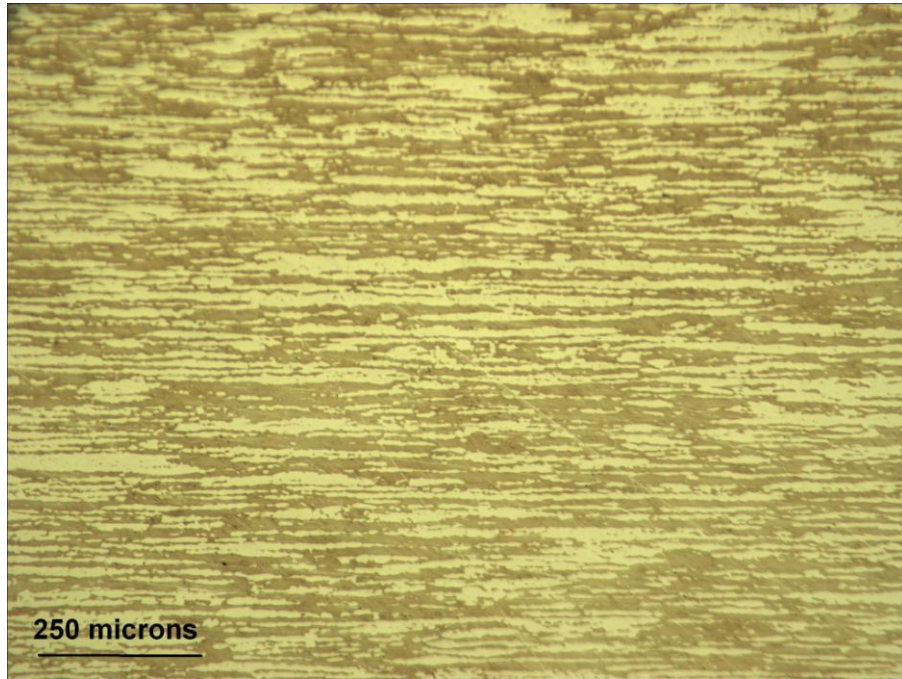


Figure 10.3: Cross section of the 3mm gauge length of the super DSS Zeron

100

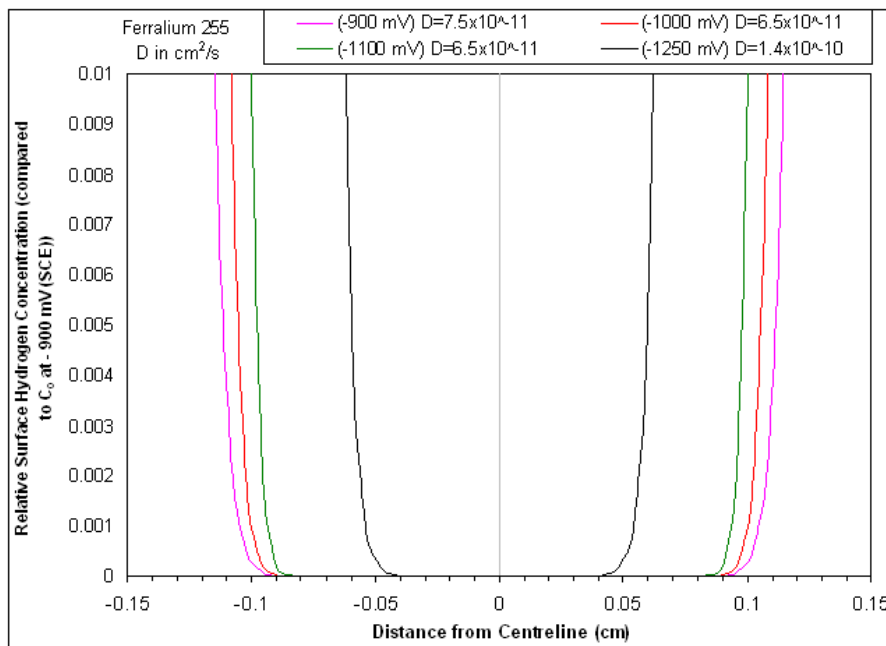


Figure 10.4: Profile of hydrogen concentration modelling in a 3 mm gauge length for the tensile specimen of super DDS Ferralium 255 at a range of applied cathodic potentials for a period of 2 weeks showing D value

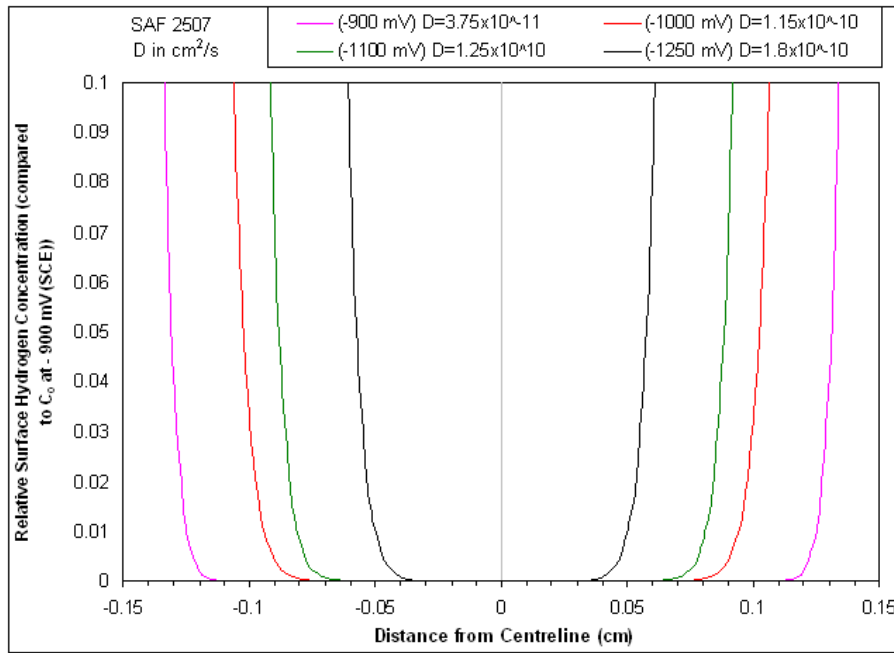


Figure 10.5: Profile of hydrogen concentration modelling in a 3 mm gauge length for the tensile specimen of super DDS SAF 2507 at a range of applied cathodic potentials for a period of 2 weeks Showing D value

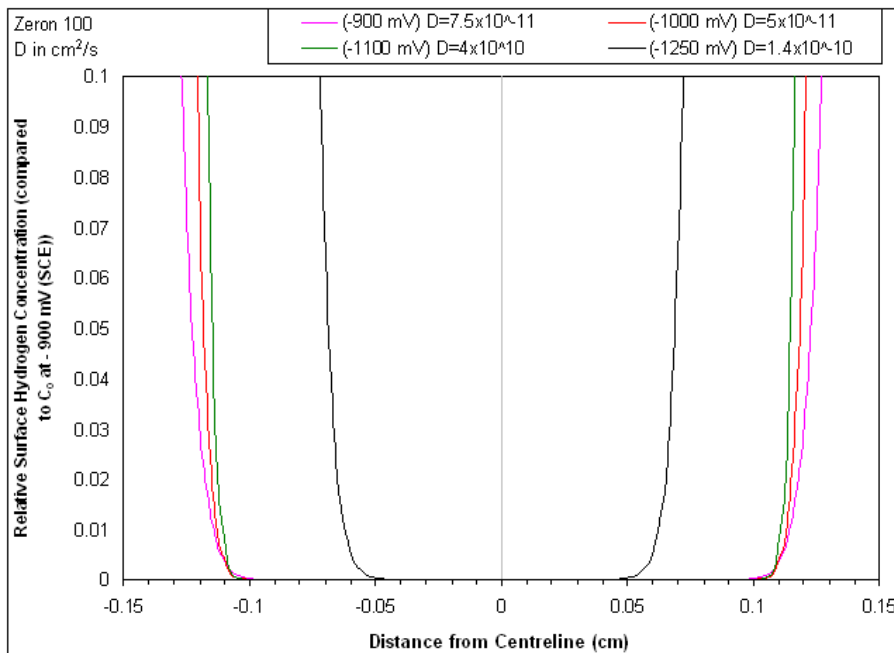


Figure 10.6: Profile of hydrogen concentration modelling in a 3 mm gauge length for the tensile specimen of super DDS Zeron 100 at a range of applied cathodic potentials for a period of 2 weeks Showing D value

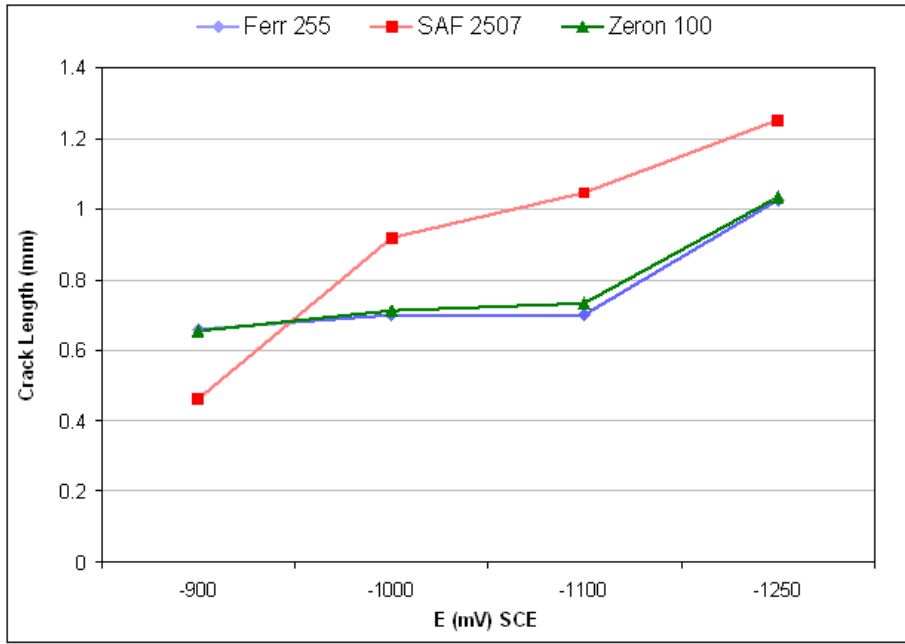


Figure 10.7: Measured crack length of the fracture surface after SSRT for tested materials